



Integrity monitoring applied to the reception of GNSS signals in urban environments

Carlos Daniel Salós Andrés

► To cite this version:

Carlos Daniel Salós Andrés. Integrity monitoring applied to the reception of GNSS signals in urban environments. Signal and Image processing. Institut National Polytechnique de Toulouse - INPT, 2012. English. NNT : 2012INPT0047 . tel-04243160

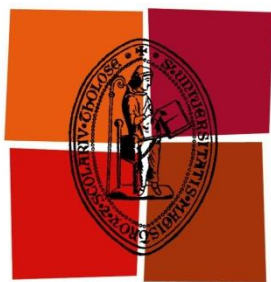
HAL Id: tel-04243160

<https://theses.hal.science/tel-04243160>

Submitted on 16 Oct 2023

HAL is a multi-disciplinary open access archive for the deposit and dissemination of scientific research documents, whether they are published or not. The documents may come from teaching and research institutions in France or abroad, or from public or private research centers.

L'archive ouverte pluridisciplinaire **HAL**, est destinée au dépôt et à la diffusion de documents scientifiques de niveau recherche, publiés ou non, émanant des établissements d'enseignement et de recherche français ou étrangers, des laboratoires publics ou privés.



Université
de Toulouse

THÈSE

En vue de l'obtention du
DOCTORAT DE L'UNIVERSITÉ DE TOULOUSE

Délivré par :

Institut National Polytechnique de Toulouse (INP Toulouse)

Discipline ou spécialité :

Signal, Image, Acoustique et Optimisation

Présentée et soutenue par :

Carlos Daniel Salós Andrés

le: mardi 3 juillet 2012

Titre :

Contrôle d'intégrité appliqué à la réception des signaux GNSS en
environnement urbain

Integrity monitoring applied to the reception of GNSS signals in urban
environments

Ecole doctorale :

Mathématiques Informatique Télécommunications (MITT)

Unité de recherche :

Ecole Nationale de l'Aviation Civile (ENAC), Laboratoire TELECOM, Groupe de Recherche
en Traitement du Signal et GNSS

Laboratoire des Télécommunications Spatiales et Aéronautiques (TéSA)

Directeurs de Thèse :

Christophe Macabiau et Anaïs Martineau

Rapporteurs :

Washington Ochieng et Philippe Bonnifait

Membres du jury :

Professeur Jaume Sanz Subirana

Professeur Washington Ochieng

Professeur Philippe Bonnifait

Docteur Christophe Macabiau

Docteur Damien Kubrak

Monsieur Bernard Bonhoure

Abstract

Global Navigation Satellite Systems (GNSS) integrity is defined as a measure of the trust that can be placed in the correctness of the information supplied by the navigation system. Although the concept of GNSS integrity has been originally developed in the civil aviation framework as part of the International Civil Aviation Organization (ICAO) requirements for using GNSS in the Communications, Navigation, and Surveillance / Air Traffic Management (CNS/ATM) system, a wide range of non-aviation applications need reliable GNSS navigation with integrity, many of them in urban environments.

GNSS integrity monitoring is a key component in Safety of Life (SoL) applications such as aviation, and in the so-called liability critical applications like GNSS-based electronic toll collection, in which positioning errors may have negative legal or economic consequences. At present, GPS integrity monitoring relies on different augmentation systems (GBAS, SBAS, ABAS) that have been conceived to meet the ICAO requirements in civil aviation operations. For this reason, the use of integrity monitoring techniques and systems inherited from civil aviation in non-aviation applications needs to be analyzed, especially in urban environments, which are frequently more challenging than typical aviation environments.

Each application has its own requirements and constraints, so the most suitable integrity monitoring technique varies from one application to another. This work focuses on Electronic Toll Collection (ETC) systems based on GNSS in urban environments. Satellite navigation is one of the technologies the EU recommends for the European Electronic Toll Service (EETS), and it is already being adopted: as of 2012, toll systems for freight transport that use GPS as primary technology are operational in Germany and Slovakia, and France envisages to establish a similar system from 2013.

This dissertation begins presenting first the concept of integrity in civil aviation in order to understand the objectives and constraints of existing GNSS integrity monitoring systems.

The derivation of the GNSS integrity requirements and the appropriate integrity monitoring techniques capable to meet them needs a deep knowledge of the targeted application and of its needs and constraints. Consequently, a thorough analysis of GNSS-based ETC systems and of GNSS navigation in urban environments is done in Chapter 2 with the aim of identifying the most suitable road toll schemes, GNSS receiver configurations and integrity monitoring mechanisms. In this case, the need of integrity is not given by safety reasons as in civil aviation, but rather as requirements of economic nature (overcharging and undercharging). Geo-fencing is selected as the method for developing GNSS-based ETC systems over a given area or road network, dividing the tolled region in geo-objects which are the basic pricing sections. A simple user detection (geo-object recognition) algorithm is proposed to charge a user the price of a section whenever it is detected inside it. Receiver autonomous integrity monitoring (RAIM) is chosen among other integrity monitoring systems due to its design flexibility and adaptability to urban environments. Finally, the most promising GNSS receivers are retained, giving special emphasis to dual constellation GPS & Galileo users. The use of SBAS corrections is optionally considered for reducing pseudorange errors.

An accurate pseudorange measurement model is a key input in the derivation of the GNSS integrity requirements and the evaluation of RAIM performance. A nominal pseudorange measurement model suitable for integrity-driven applications in urban environments has been obtained following a methodology similar to that of civil aviation, splitting the total pseudorange error into five independent error sources which can be modeled independently: broadcasted satellite clock corrections and

ephemeris errors, ionospheric delay, tropospheric delay, receiver thermal noise (plus interferences) and multipath. Nominal errors are modeled as zero-mean Gaussian variables, which is consistent with the error models and integrity monitoring systems used in civil aviation, as well as with SBAS corrections. In this work the fault model that includes all non-nominal errors consists only of major service failures.

Once the ETC scheme and the fault model are known, the GNSS integrity requirements with which design the RAIM can be calculated. First, the top level requirements of toll applications are defined in terms of maximum allowable probabilities of missed and false geo-object recognition. Afterwards, the relationship between positioning failures and incorrect geo-object recognition is studied, resulting in maximum allowed probabilities of missed and false alarm values that depend on the number of independent positions with available RAIM employed to decide whether the user is or not inside a pricing section.

Two RAIM algorithms are studied. The first of them is the Weighted Least Squares Residual (WLSR) RAIM, widely used in civil aviation and usually set as the reference against which other RAIM techniques are compared. Since one of the main challenges of RAIM algorithms in urban environments is the high unavailability rate because of the bad user/satellite geometry, a new RAIM is proposed. The novel algorithm, based on the WLSR RAIM, is designed with the premise of providing a trade-off between the false alarm probability and the RAIM availability in order to maximize the probability that the RAIM declares valid a fault-free position.

Finally, simulations have been carried out to study the performance of the different RAIM and ETC systems in rural and urban environments. Electronic toll collection by means of GNSS in urban environments with geo-objects shorter than 500 m and road topologies that allow a Horizontal Alert Limit (HAL) of 25 or 50 meters has been demonstrated to be feasible with certain signal combinations of dual constellation GPS & Galileo users. Single constellation users only attain the requirements in rural environments with some receiver configurations. In all cases, the availability obtained with the novel RAIM improve those of the standard WLSR RAIM.

The main contributions of this thesis are a detailed analysis of GNSS-based ETC systems, a numerical pseudorange nominal error model due to ionospheric delay in Galileo single-frequency receivers, a pseudorange nominal error model due to multipath in urban environments suitable for applications with GNSS integrity, the failure tree that leads to geo-object misleading positions, the derivation of the P_{MD} and P_{FA} of fault detection RAIM algorithms for GNSS-based ETC in the case of a threat model consisting on major service failures, a novel RAIM, based on the WLSR RAIM, that increments the number of valid positions within the integrity requirements in urban environments, the derivation of the analytical expression of the chi-squared non-centrality parameter in the WLSR RAIM and the derivation of the null correlation between the test statistic and the navigation solution error in the WLSR RAIM.

Résumé

L'intégrité des signaux GNSS est définie comme la mesure de la confiance qui peut être placée dans l'exactitude des informations fournies par le système de navigation. Bien que le concept d'intégrité GNSS a été initialement développé dans le cadre de l'aviation civile comme une des exigences standardisées par l'Organisation de l'Aviation Civile Internationale (OACI) pour l'utilisation du GNSS dans les systèmes de Communication, Navigation, et Surveillance / Contrôle du Trafic Aérien (CNS/ATM), un large éventail d'applications non aéronautiques ont également besoin de navigation par satellite fiable avec un niveau d'intégrité garanti. Beaucoup de ces applications se situent en environnement urbain.

Le contrôle d'intégrité GNSS est un élément clé des applications de sécurité de la vie (SoL), telle que l'aviation, et des applications exigeant une fiabilité critique comme le télépéage basé sur l'utilisation du GNSS, pour lesquels des erreurs de positionnement peuvent avoir des conséquences juridiques ou économiques. Chacune de ces applications a ses propres exigences et contraintes, de sorte que la technique de contrôle d'intégrité la plus appropriée varie d'une application à l'autre. Cette thèse traite des systèmes de télépéage utilisant GNSS en environnement urbain. Les systèmes de navigation par satellite sont l'une des technologies que l'UE recommande pour le Service Européen de Télépéage Electronique (EETS). Ils sont déjà en cours d'adoption: des systèmes de télépéage pour le transport poids lourd utilisant GPS comme technologie principale sont opérationnels en Allemagne et en Slovaquie, et un système similaire est envisagé en France à partir de 2013.

À l'heure actuelle, le contrôle d'intégrité GPS s'appuie sur des systèmes d'augmentation (GBAS, SBAS, ABAS) conçus pour répondre aux exigences de l'OACI pour les opérations aviation civile. C'est la raison pour laquelle cette thèse débute par une présentation du concept d'intégrité en aviation civile afin de comprendre les performances et contraintes des systèmes hérités.

La thèse se poursuit par une analyse approfondie des systèmes de télépéage et de navigation GNSS en milieu urbain qui permet de dériver les techniques de contrôle d'intégrité GNSS les plus adaptées. Les algorithmes autonomes de type RAIM ont été choisis en raison de leur souplesse et leur capacité d'adaptabilité aux environnements urbains.

Par la suite, le modèle de mesure de pseudodistances est élaboré. Ce modèle traduit les imprécisions des modèles de correction des erreurs d'horloge et d'éphéméride, des retards ionosphériques et troposphériques, ainsi que le bruit thermique récepteur et les erreurs dues aux multitrajets.

Les exigences d'intégrité GNSS pour l'application télépéage sont ensuite dérivées à partir de la relation entre les erreurs de positionnement et leur effets dans la facturation finale.

Deux algorithmes RAIM sont alors proposés pour l'application péage routier. Le premier est l'algorithme basé sur les résidus de la solution des moindres carrés pondérés (RAIM WLSR), largement utilisé dans l'aviation civile. Seulement, un des principaux défis de l'utilisation des algorithmes RAIM classiques en milieux urbains est un taux élevé d'indisponibilité causé par la mauvaise géométrie entre le récepteur et les satellites. C'est pour cela que un nouvel algorithme RAIM est proposé. Cet algorithme, basé sur le RAIM WLSR, est conçu de sorte à maximiser l'occurrence de fournir un positionnement intègre dans un contexte télépéage.

Les performances des deux algorithmes RAIM proposés et des systèmes de télépéage associés sont analysés par simulation dans différents environnements ruraux et urbains. Dans tous les cas, la disponibilité du nouvel RAIM est supérieure à celle du RAIM WLSR.

Les contributions principales de cette thèse sont: l'analyse détaillée des systèmes de télépéage utilisant GNSS, un modèle numérique d'erreur nominale sur les mesures de pseudodistance due au retard ionosphérique pour des récepteurs Galileo monofréquence, un modèle d'erreur nominale sur les mesures de pseudodistance à cause dues aux multitrajets dans des environnements urbains adapté aux applications de télépéage utilisant GNSS, l'arbre de défaillance pour des applications de télépéage ainsi que la dérivation de la configuration des algorithmes RAIM pour ce type d'applications, un nouvel algorithme RAIM qui augmente la disponibilité en milieu urbain, la dérivation de l'expression analytique du paramètre de non centralité chi-carré pour l'algorithme RAIM WLSR, et la démonstration de la corrélation nulle entre le test statistique et l'erreur de position dans l'algorithme RAIM WLSR.

Acknowledgments

This work has been carried out in the GNSS and Signal Processing Group of the TELECOM Lab at the ENAC. I gratefully acknowledge the CNES and Thales Alenia Space for funding this thesis, and the TéSA Lab for managing it.

I would like to specially thank my thesis directors Christophe Macabiau and Anaïs Martineau for all their time, enthusiasm and support during these years. I would like to thank as well Bernard Bonhoure and Damien Kubrak for their advices all along this work.

I am grateful to Washington Ochieng and Philippe Bonnifait for accepting to review the thesis, and to Jaume Sanz Subirana for accepting to be part of the jury.

Last but not least, I would like to thank my colleagues at the lab throughout these years for always creating such a good atmosphere.

Table of Contents

ABSTRACT	III
RESUME	V
ACKNOLEDGMENTS	VII
TABLE OF CONTENTS	IX
LIST OF FIGURES	XV
LIST OF TABLES	XIX
CHAPTER 1 INTRODUCTION	1
1.1. MOTIVATION OF THE WORK	1
1.2. ORGANIZATION OF THE DISSERTATION	2
CHAPTER 2 GNSS INTEGRITY MONITORING IN CIVIL AVIATION	5
2.1. INTRODUCTION	5
2.2. GNSS SIGNAL-IN-SPACE PERFORMANCE REQUIREMENTS	5
2.2.1. ICAO SARPS ANNEX 10	7
2.2.2. CAT-II AND CAT-III PRECISION APPROACHES	7
2.3. GNSS INTEGRITY MONITORING WITH AUGMENTATION SYSTEMS	8
2.3.1. GPS SPS PERFORMANCE AND NEED OF AUGMENTATION SYSTEMS	8
2.3.2. PROTECTION LEVELS AND INTEGRITY MONITORING AVAILABILITY	10
2.3.3. GROUND BASED AUGMENTATION SYSTEM (GBAS)	11
2.3.4. SATELLITE BASED AUGMENTATION SYSTEM (SBAS)	11
2.3.5. AIRCRAFT BASED AUGMENTATION SYSTEM (ABAS)	12
2.3.5.1. Fault Detection and Exclusion (FDE)	12
2.4. CONCLUSIONS	14
CHAPTER 3 GNSS-BASED ELECTRONIC TOLL COLLECTION	15
3.1. INTRODUCTION	15
3.2. CURRENT STATE OF GNSS-BASED ETC SYSTEMS	16
3.3. GNSS INTEGRITY	17
3.3.1. LIABILITY	17
3.3.2. GNSS INTEGRITY MONITORING SYSTEMS	18
3.3.3. ABAS SCHEME	20
3.4. ROAD SEGMENTATION	21
3.5. ON-BOARD GNSS RECEIVER	25
3.5.1. GNSS SIGNALS	25
3.5.2. NAVIGATION SOLUTION	30
3.6. GEO-OBJECT RECOGNITION	31
3.6.1. MAP-MATCHING ALGORITHMS	31
3.6.2. VALID ESTIMATED POSITIONS FOR ETC	31
3.6.3. INDEPENDENT POSITIONS	33

3.6.4. GEO-OBJECT RECOGNITION ALGORITHM	33
3.7. CONCLUSIONS	35
<u>CHAPTER 4 PSEUDORANGE MEASUREMENT MODEL</u>	<u>37</u>
4.1. INTRODUCTION	37
4.2. MEASUREMENT EQUATION SYSTEM	37
4.3. NOMINAL ERROR MODEL	38
4.3.1. ERROR SOURCES	39
4.3.2. SATELLITE CLOCK AND EPHEMERIS ERRORS	40
4.3.2.1. GPS	40
4.3.2.2. Galileo	42
4.3.2.3. SBAS	42
4.3.3. IONOSPHERIC RESIDUAL ERROR	43
4.3.3.1. Single-frequency GPS corrections	44
4.3.3.2. Single-frequency Galileo corrections	47
4.3.3.3. SBAS ionospheric corrections	51
4.3.3.4. Dual-frequency iono-free measurements	52
4.3.4. TROPOSPHERIC RESIDUAL ERROR	53
4.3.5. THERMAL NOISE AND INTERFERENCES	55
4.3.6. MULTIPATH	57
4.3.6.1. Urban Channel Model	58
4.3.6.2. Receiver tracking loops	60
4.3.6.3. Lock Detector	64
4.3.6.4. Error overbounding	65
4.3.6.5. Final Pseudorange Error due to Multipath	67
4.3.6.6. Conclusions and scope of the multipath model	68
4.3.7. TOTAL PSEUDORANGE NOMINAL MEASUREMENT ERROR MODEL	68
4.3.8. NOMINAL MODEL OF THE EXTERNAL ALTITUDE INFORMATION	73
4.4. FAULT MODEL	74
4.5. ERROR CORRELATION TIME	75
4.6. CONCLUSIONS	76
<u>CHAPTER 5 INTEGRITY REQUIREMENTS OF GNSS-BASED ELECTRONIC TOLL COLLECTION SYSTEMS</u>	<u>77</u>
5.1. INTRODUCTION	77
5.2. EXAMPLES OF ETC REQUIREMENTS AND PERFORMANCE	77
5.3. GEO-OBJECT RECOGNITION REQUIREMENTS	78
5.3.1. RELATIONSHIP BETWEEN INVOICE ACCURACY AND GEO-OBJECT REQUIREMENTS	78
5.3.1.1. Undercharging	78
5.3.1.2. Overcharging	80
5.3.2. CONCLUSIONS AND PROPOSITION OF GEO-OBJECT LEVEL REQUIREMENTS	83
5.4. GNSS INTEGRITY REQUIREMENTS	84
5.4.1. DEFINITIONS	85
5.4.2. FAILURE TREE OF GEO-OBJECT MISLEADING POSITIONS (GOMP)	86
5.4.3. SCENARIO DESCRIPTION	89

5.4.4. PROBABILITY OF MISSED DETECTION (P_{MD}) AND PROBABILITY OF FALSE ALARM (P_{FA})	91
5.4.4.1. False geo-object recognition (Road segment overcharging)	91
5.4.4.1.1. Nominal scenario (no pseudorange failures)	92
5.4.4.1.2. Faulty scenario (major service failure)	93
5.4.4.2. Missed geo-object recognition (road segment undercharging)	96
5.4.4.2.1. Nominal scenario (no pseudorange failure)	97
5.4.4.2.2. Faulty scenario (major service failure)	101
5.4.4.3. Performance for a particular user trajectory throughout successive road segments	102
5.5. CONCLUSIONS	102
CHAPTER 6 RAIM ALGORITHMS	105
6.1. INTRODUCTION	105
6.2. WLSR RAIM	105
6.2.1. ALGORITHM DESIGN	106
6.2.1.1. Navigation solution and pseudorange measurement models	106
6.2.1.2. Test Statistic	107
6.2.1.3. Detection Threshold	108
6.2.1.4. Minimum detectable failures	109
6.2.1.5. Relationship between test statistic and position errors	110
6.2.1.5.1. Deterministic component (Slope)	111
6.2.1.5.2. Statistic component	112
6.2.1.6. Horizontal protection level	113
6.2.2. IMPLEMENTATION	116
6.2.2.1. Availability check and fault detection	116
6.2.2.2. Fault exclusion	117
6.2.3. LIMITATIONS	117
6.2.3.1. Assumptions made during the algorithm design	117
6.2.3.2. Pseudorange detection and probability of false detection	117
6.2.3.3. Minimum allowable HAL	118
6.3. WLSR RAIM WITH A VARIABLE P_{FA}	119
6.3.1. MOTIVATION AND RATIONALE	119
6.3.2. ALGORITHM DESIGN	121
6.3.3. IMPLEMENTATION	123
6.3.4. COMPARISON AGAINST THE WLSR RAIM USED IN CIVIL AVIATION	123
6.3.5. LIMITATIONS	125
6.4. CONCLUSIONS	125
CHAPTER 7 SIMULATION RESULTS OF GNSS-BASED ETC SYSTEMS	127
7.1. INTRODUCTION	127
7.2. DESCRIPTION AND CONFIGURATION OF THE SIMULATIONS	127
7.2.1. SCENARIO	127
7.2.2. GNSS RECEIVER CONFIGURATION	128
7.2.3. NOMINAL PSEUDORANGE ERROR MODEL AND USER LOCATION	128
7.2.4. SATELLITE CONSTELLATIONS	128
7.2.5. RAIM ALGORITHMS	128

7.2.6.	POSITIONING ERROR CORRELATION TIME	129
7.2.7.	GEO-OBJECT DETECTION ALGORITHM	129
7.2.8.	HAL	129
7.2.9.	TRAJECTORY DURATION	129
7.3.	SATELLITE VISIBILITY	129
7.4.	HORIZONTAL POSITIONING ERROR	133
7.5.	RAIM PERFORMANCE	135
7.5.1.	MAXIMUM SLOPE	135
7.5.2.	VARIABLE HPL (WLSR RAIM WITH CONSTANT P_{FA})	136
7.5.3.	VARIABLE P_{FA} (WLSR RAIM WITH CONSTANT HPL)	139
7.5.4.	ALTERNATIVE RECEIVERS	139
7.5.5.	FAULT EXCLUSION MODULE	142
7.6.	ROAD TOLL PERFORMANCE	142
7.6.1.	SEGMENT RECOGNITION ALGORITHM AND RAIM CONFIGURATION	142
7.6.2.	PROBABILITY OF MISSED GEO-OBJECT RECOGNITION	144
7.6.3.	ALTERNATIVE RECEIVERS	149
7.6.4.	A NOTE ON THE PERFORMANCE IN THE FAULTY CASE	149
7.7.	CONCLUSIONS	149
CHAPTER 8	CONCLUSIONS AND FUTURE WORK	151
8.1.	CONCLUSIONS	151
8.2.	ORIGINAL CONTRIBUTIONS	153
8.3.	PERSPECTIVES FOR FUTURE WORK	154
REFERENCES		157
ACRONYMS		163
APPENDIX B.	DERIVATION OF THE LINEAR PSEUDORANGE MEASUREMENT EQUATION	167
B.1.	LINEARIZATION	167
B.2.	POSITIONING IN THE USER GEOGRAPHIC FRAME	168
B.3.	BIDIMENSIONAL POSITIONING	169
B.4.	DUAL-CONSTELLATION RECEIVERS	169
B.5.	EXTERNAL ALTITUDE INFORMATION	170
APPENDIX C.	OVERBOUNDING GAUSSIAN OF A UNIFORM DISTRIBUTION	173
C.1.	CDF OVERBOUNDING OF A UNIFORM DISTRIBUTION	173
APPENDIX D.	WEIGHTED LEAST SQUARES ESTIMATOR (WLSE)	175
D.1.	MEASUREMENT EQUATION	175
D.2.	WLS NAVIGATION SOLUTION ESTIMATION	175
D.3.	WLS ESTIMATION ERROR VECTOR	176
D.4.	ESTIMATION ERROR COVARIANCE MATRIX	176
D.5.	HORIZONTAL POSITIONING ESTIMATION ERROR	177
D.6.	PSEUDORANGE RESIDUALS	177
D.7.	UNCORRELATION BETWEEN RESIDUAL AND POSITION ERROR VECTORS	178
D.8.	WLSE AS THE LSE OF A NORMALIZED SYSTEM	179

D.8.1.	NORMALIZED PSEUDORANGE MEASUREMENT EQUATION SYSTEM	179
D.8.2.	LSE PROPERTIES	180
APPENDIX E.	WLSR RAIM RELATED SUBJECTS	181
<hr/>		
E.1.	DERIVATION OF THE NON-CENTRALITY PARAMETER	181
E.2.	UNCORRELATION BETWEEN THE TEST STATISTIC AND THE ESTIMATION ERROR VECTOR	182
E.3.	DEMONSTRATION OF MATRIX EXPRESSIONS	184
E.3.1.	DEMONSTRATION 1	184
E.3.2.	DEMONSTRATION 2	185
E.4.	LSR RAIM DESIGN WITH THE PARITY MATRIX METHOD	185
APPENDIX F.	SIMULATION RESULTS (I): RAIM PERFORMANCE	187
<hr/>		
F.1.	WLSR RAIM UNAVAILABILITY	187
APPENDIX G.	SIMULATION RESULTS (II): MISSED ROAD SEGMENT RATE	205
<hr/>		
G.1.	MINIMUM TRAJECTORY DURATION	205
G.2.	PROBABILITY OF ZERO VALID POSITIONS	214

List of Figures

Figure 2.1. Total System Error.....	6
Figure 2.2. Relationship between alert and protection levels: a) available integrity monitoring system, b) unavailable integrity monitoring system.....	11
Figure 2.3. Diagram of possible FDE events [RTCA, 2006]	13
Figure 3.1. Different interpretations of the HPL.	22
Figure 3.2. Examples of the relationship between geo-object boundaries, the estimated position and the HAL when the real position can be anywhere inside the geo-object.....	22
Figure 3.3. Example of geo-object defined as the area of points closer to the road segment than to any other.....	23
Figure 3.4. Example of HAL computation in a road network (Positions 1 and 2). Example of undetected positioning failure (Position 3).....	23
Figure 3.5. Geo-object that allows a constant HAL.	24
Figure 3.6. Segment length histogram and CDF of German and Slovak freight transport ETC.	25
Figure 3.7. Segment length histogram and CDF of German and Slovak freight transport ETC (zoom).	25
Figure 3.8. Spectra of GNSS signals.	26
Figure 3.9. Scheme of the possible outputs of the GNSS positioning & integrity system at a given instant, indicating when an estimated position is declared valid to be used in the geo-object recognition algorithm.	32
Figure 3.10. Examples of user trajectories and GNSS positioning & integrity data provided.	34
Figure 3.11. Creation of the position set used in the geo-object recognition algorithm.....	34
Figure 4.1. Map of the UDRE obtained with EGNOS.	43
Figure 4.2. Comparison of the mapping functions F and F_{SBAS}	45
Figure 4.3. Graphical view of $\sigma_{iono,v} = \max(0.2 \cdot \Delta_{KL,v}, \tau_v)$	46
Figure 4.4. Ionospheric residual error model for single-frequency GPS L1.	47
Figure 4.5. Geomagnetic latitude.	49
Figure 4.6. Example of VTEC daily and long term variations.....	49
Figure 4.7. Percentiles of $E1 \sigma_{iono,v}$ obtained with all VTEC data.	50
Figure 4.8. Worst GIVE obtained for EGNOS during 24 hours.....	52
Figure 4.9. Residual tropospheric error model standard deviation.....	54
Figure 4.10. Pseudorange error model due to thermal noise for various receiver configurations.	56
Figure 4.11. Scheme followed to calculate the multipath error model.....	58
Figure 4.12. Normalized autocorrelation function of total and partial PRN codes. Example of L1 C/A and E1B.....	63
Figure 4.13. Example of CDF of simulated pseudorange error and its overbounding function.....	65
Figure 4.14. Example of CDF of simulated pseudorange error and its overbounding function.....	66
Figure 4.15. Example of error percentiles of simulated pseudorange error and its overbounding function.....	66
Figure 4.16. Multipath nominal error model with an integration time of 20 ms.	67
Figure 4.17. Multipath nominal error model with an integration time of 100 ms.	68
Figure 4.18. Nominal pseudorange measurement error model σ_{PSR} of single frequency, standalone GPS receivers.	70
Figure 4.19. Nominal pseudorange measurement error model σ_{PSR} of single frequency, standalone Galileo receivers.....	70

Figure 4.20. Nominal pseudorange measurement error model σ_{PSR} of single frequency GPS and Galileo receivers with SBAS corrections.	71
Figure 4.21. Nominal pseudorange measurement error model σ_{PSR} of dual frequency GPS and Galileo receivers.	71
Figure 4.22. Contribution of the error sources to the total nominal pseudorange measurement error model σ_{PSR}^2 . Example of a single frequency L1 BOC(1,1) receiver.	72
Figure 4.23. Contribution of the error sources to the total nominal pseudorange measurement error model σ_{PSR}^2 . Example of a single frequency L1 BOC(1,1) receiver with SBAS corrections.	72
Figure 4.24. Contribution of the error sources to the total nominal pseudorange measurement error model σ_{PSR}^2 . Example of a dual frequency receiver with L1/E1 BOC(1,1) and L5/E5a BPSK(10) signals.	73
Figure 5.1. Probability of missed geo-object recognition needed for different invoice requirements.	80
Figure 5.2. Probability of false geo-object recognition needed for different invoice requirements.	82
Figure 5.3. Diagram of events for snapshot fault detection RAIM algorithms.	84
Figure 5.4. Examples of Undetected Positioning Failures (UPF) and Geo-object Misleading Positions (GoMP).	86
Figure 5.5. Failures that lead to a Geo-object Misleading Position (GoMP).	89
Figure 5.6. Events that lead to a false geo-object recognition.	92
Figure 5.7. Example of scenario susceptible to false geo-object recognition without pseudorange failures.	92
Figure 5.8. Example of scenario susceptible to false geo-object recognition affected by a major service failure.	94
Figure 5.9. Probability of false recognized geo-object due to positioning failures caused by pseudorange failures with $P_{\text{MD}}=10^{-3}$ in the presence of a major service failure.	95
Figure 5.10. Maximum allowable probability of missed detection P_{MD} that meets the false geo-object recognition requirement $p\{N_{\text{GoMP (PSR)}} \geq N_{\text{Th}} \mid \text{Faulty Scenario}\} \leq 3.8 \cdot 10^{-3}$	95
Figure 5.11. Failure tree that leads to a missed geo-object recognition.	97
Figure 5.12. Example of scenario susceptible to missed geo-object recognition without pseudorange failures.	98
Figure 5.13. Probability of missed geo-object recognition due to false detections with $P_{\text{FA}} = 10^{-3}$	100
Figure 5.14. Maximum allowable probability of false alarm P_{FA} that meets the missed geo-object recognition requirement $p\{N_{\text{valid pos IN}} < N_{\text{Th}} \mid \text{Nominal Scenario}\} \leq 5 \cdot 10^{-5}$	100
Figure 5.15. Example of missed geo-object recognition in the faulty scenario (major service failure).	101
Figure 6.1. Derivation of the detection threshold (Th).	109
Figure 6.2. Derivation of the minimum detectable non-centrality parameter (λ_{det}).	110
Figure 6.3. Examples of the slope as the relationship between the test statistic non-centrality (λ) and the bias projection $ b_{\text{H}} $	112
Figure 6.4. Examples of bidimensional pdf in the plane square root(t) vs. $ e_{\text{H}} $ in the a) fault free case, b) faulty case.	113
Figure 6.5. Relationship between the test statistic and the position error in different stages of the WLSR RAIM design. a) Derivation of the detection threshold. b) Computation of the minimum detectable non-centrality parameter. c) Estimation of the HAL.	115
Figure 6.6. WLSR RAIM algorithm.	116
Figure 6.7. HAL exceeded by nominal horizontal positioning errors with a probability P.	119
Figure 6.8. Effect of the P_{FA} in the WLSR RAIM.	121
Figure 6.9. Design of the WLSR RAIM that maximizes the number of valid positions.	122
Figure 6.10. WLSR RAIM fault detection that maximizes the number of valid positions.	123

Figure 6.11. Comparison of fault detection events in the classic and novel WLSR RAIM algorithms.	124
Figure 6.12. Probability of not declaring valid a fault free position as a function of the ratio $HAL/slope_{MAX}$ and the number of chi-squared degrees of freedom k . Example with $P_{MD}=10^{-3}$ and $P_{FA}=10^{-5}$.	125
Figure 7.1. Measured probability that at a given epoch there is a minimum number of visible satellites (x).	131
Figure 7.2. Measured distribution of visible GPS and Galileo satellites according to their elevation angle.	132
Figure 7.3. Measured distribution of visible GPS and Galileo satellites according to their azimuth with respect to the street axis (set in the line $0^\circ - 180^\circ$).	132
Figure 7.4. Distribution of the visible satellites in the urban environment.	133
Figure 7.5. Measured PDF of σ_{major} and σ_{minor} in the urban scenario. Receiver: dual constellation, dual frequency receiver L1/E1 BOC(1,1) - L5/E5a BPSK(10). Navigation solution: 3D position and receiver/GNSS time shift.	134
Figure 7.6. Mean, 5% and 95% percentiles of the measured σ_{major} and σ_{minor} as a function of the number of visible satellites. Receiver: dual constellation, dual frequency receiver L1/E1 BOC(1,1) - L5/E5a BPSK(10). Navigation solution: 3D position and receiver/GNSS time shift.	134
Figure 7.7. Measured distribution of the relative angle between the positioning error major axis and the street axis. Receiver: dual constellation, dual frequency receiver L1/E1 BOC(1,1) - L5/E5a BPSK(10). Navigation solution: 3D position and receiver/GNSS time shift.	134
Figure 7.8. Measured CDF of the slopeMAX in the fault detection RAIM (fault-free case). Receiver: dual constellation L1/E1 BOC(1,1); dual frequency with L5/E5a BPSK(10). Navigation solution: 3D position and receiver/GNSS time shift.	136
Figure 7.9. CDF of the HPL obtained in the fault detection civil aviation WLSR RAIM (fault-free case). Receiver: dual constellation L1/E1 BOC(1,1); dual frequency with L5/E5a BPSK(10). Navigation solution: 3D position and receiver/GNSS time shift.	137
Figure 7.10. CDF of the HPL obtained in the fault detection module of the civil aviation WLSR RAIM for hybrid receivers with external altitude with an error model σ_{alt} . Receiver: dual constellation, dual frequency L1/E1 BOC(1,1) - L5/E5a BPSK(10). Navigation solution: 3D position and receiver/GNSS time shift. RAIM configuration: $P_{MD} = 5 \cdot 10^{-5}$, $P_{FA} = 5 \cdot 10^{-3}$.	138
Figure 7.11. CDF of the P_{FA} obtained in the fault detection module of the variable- P_{FA} WLSR RAIM (fault-free case). Receiver: dual constellation L1/E1 BOC(1,1); dual frequency with L5/E5a BPSK(10). Navigation solution: 3D position and receiver/GNSS time shift.	140
Figure 7.12. CDF of the P_{FA} obtained in the fault detection module of the variable- P_{FA} WLSR RAIM for hybrid receivers with external altitude with an error model σ_{alt} . $HAL=50$ meters. Receiver: dual constellation, dual frequency L1/E1 BOC(1,1) - L5/E5a BPSK(10). Navigation solution: 3D position and receiver/GNSS time shift.	141
Figure 7.13. Probability that, in the fault-free case, the number of valid positions inside the geo-object is lower than the segment recognition threshold for different N_{Th} and P_{MD} . $HAL=50$ meters. Variable- P_{FA} WLSR RAIM. Receiver: dual constellation L1/E1 BOC(1,1); dual frequency with L5/E5a BPSK(10). Navigation solution: 3D position and receiver/GNSS time shift.	143
Figure 7.14. Probability of zero valid positions during a user trajectory trough a geo-object in the fault-free case. Environment: urban. Receiver: dual constellation L1/E1 BOC(1,1); dual frequency with L5/E5a BPSK(10). Navigation solution: 3D position and receiver/GNSS time shift.	146
Figure 7.15. Probability of zero valid positions during a user's trajectory trough a geo-object in the fault-free case. Environment: urban. Receiver: dual constellation L1/E1 BOC(1,1); dual frequency	

with L5/E5a BPSK(10); hybridization with external altitude $\sigma_{\text{alt}} = 5$ m. Navigation solution: 3D position and receiver/GNSS time shift.	147
Figure 7.16. Probability of zero valid positions during a user's trajectory trough a geo-object in the fault-free case. Environment: rural. Receiver: dual constellation L1/E1 BOC(1,1); dual frequency with L5/E5a BPSK(10). Navigation solution: 3D position and receiver/GNSS time shift.	148

List of Tables

Table 2.1. GNSS signal-in-space performance requirements for civil aviation [ICAO, 2006].	9
Table 3.1. Characteristics of augmentation systems for ETC applications.	20
Table 3.2. Characteristics of the considered GNSS signals.	26
Table 3.3. Single frequency receiver configurations.	28
Table 3.4. Single frequency GPS receivers under study.	29
Table 3.5. Dual frequency GPS receivers under study.	29
Table 3.6. Single frequency Galileo receivers under study.	29
Table 3.7. Dual frequency Galileo receivers under study.	29
Table 3.8. Single frequency dual constellation GPS/Galileo receivers under study.	30
Table 3.9. Dual frequency dual constellation GPS/Galileo receivers under study.	30
Table 3.10. Minimum number of range measurements needed for various GNSS receiver types according to their navigation solution unknowns.	30
Table 3.11. Events related to the Fault Detection process.	33
Table 4.1. Iono-free coefficients for different frequency pairs.	53
Table 4.2. Recommended channel model sampling period T_s (ms).	59
Table 4.3. Maximum multipath error model standard deviation (σ_{mp}) obtained at any elevation angle.	67
Table 5.1. Maximum probability of missed geo-object recognition (P_{MGoR}) for different invoice requirements in the worst case.	80
Table 5.2. Probability of missed detection P_{MD} that meets the overcharging requirement in the worst-case scenario.	96
Table 7.1. Building generation pattern of urban and rural environments.	127
Table 7.2. Percentage of epochs with a number of visible GPS satellites enough for running a RAIM algorithm.	130
Table 7.3. Percentage of epochs with a number of visible Galileo satellites enough for running a RAIM algorithm.	130
Table 7.4. Percentage of epochs with a number of visible GPS & Galileo satellites enough for running a RAIM algorithm.	130
Table 7.5. Minimum user trajectory that meets the undercharging requirement. Urban environment. Receiver: GPS & Galileo L1/E1 BOC(1,1); iono-free with L5/E5a BPSK(10). Navigation solution: 3D position and receiver/GNSS time shift.	145
Table 7.6. Minimum user trajectory that meets the undercharging requirement. Rural environment. Receiver: GPS & Galileo L1/E1 BOC(1,1); iono-free with L5/E5a BPSK(10). Navigation solution: 3D position and receiver/GNSS time shift.	145

Chapter 1

Introduction

1.1. Motivation of the work

Civil aviation navigation is a Safety of Life (SoL) application that needs reliable navigation aids in which integrity plays a major role, defined as a measure of the trust that can be placed in the correctness of the information supplied by the total system, including the ability of providing alerts to the user when the requirements are not assured to be met. The concept of GNSS integrity has been originally defined in the civil aviation framework as part of the International Civil Aviation Organization (ICAO) specifications required to use GNSS in the Communications, Navigation, and Surveillance / Air Traffic Management (CNS/ATM) system. Since current standalone GPS cannot meet the civil aviation requirements, and in particular does not provide integrity as specified by the ICAO, several augmentation systems able to monitor GNSS integrity have been developed: GBAS, SBAS and ABAS. Most of the existing GNSS integrity monitoring systems, techniques and algorithms have been conceived to support civil aviation SoL operations within the ICAO specifications.

Reliability in GNSS is defined as the ability of a Standard Positioning System (SPS) Signal in Space (SIS) to perform its required functions over a specified time interval [DoD, 2008]. The applications that actually have a need of a reliable GNSS navigation with integrity monitoring are not restricted to the civil aviation field, and a number of them take place in urban environments. These integrity-driven applications are classified as SoL if undetected navigation errors may endanger life, and as liability-critical if positioning errors may have negative legal or economic consequences. Studies like [RacalTracs, 2000] have addressed the use of GNSS integrity in different sectors. Examples of these applications are train control, surveying the transport of dangerous or valuable goods, emergency calls, tracking bracelets, etc. Each application needs a GNSS integrity monitoring technique adapted to its specific requirements.

The targeted application in this thesis is the Electronic Toll Collection by means of GNSS (GNSS ETC) in rural and urban environments. The reason of this choice is that GNSS ETC are highly flexible, free-flow toll systems with a reduced quantity of roadside infrastructure; these advantageous characteristics make GNSS an interesting alternative to other road pricing mechanisms, and satellite navigation is one of the technologies recommended by the EU for the European Electronic Toll Service (EETS) [EU, 2004]. GPS is already used as the primary technology to toll freight transport in German and Slovak highways and certain national roads, reaching a toll collection efficiency of 99.75% and 98.99% respectively [TollCollect, 2008], [NDSAS, 2010], [Toll Collect, 2011 (a)], [SkyToll, 2011 (b)]. France will establish from 2013 a mileage-based eco-tax for heavy goods vehicles in the national road network relying on satellite navigation [MEEDAT, 2009].

The main equipment required in GNSS-ETC systems is an on-board unit (OBU) installed at each vehicle, capable to perform GNSS navigation and to communicate with the central unit that manages

the toll invoices of the different users. Compared to other technologies used in electronic toll like Dedicated Short Range Communications (DSRC), which require roadside infrastructure to monitor the presence of users at different checkpoints distributed along the tolled road network or area, GNSS ETC equipment is limited, generally resulting in lower installation and maintenance costs per tolled kilometre. The absence of roadside infrastructure confers a high flexibility that allows to quickly update or modify the tolled area. For instance, around 30 monthly modifications were made to the German toll network [TollCollect, 2008], and the deployment of a pilot GNSS-ETC covering more than 250 km. of national roads in Czech Republic took only 16 days [SkyToll, 2010].

Since GNSS integrity requirements and monitoring techniques have been originally defined and developed in the civil aviation framework, they have to be reformulated and adapted to satisfy the particular needs of urban toll applications. The derivation of the GNSS integrity requirements and the most suitable integrity monitoring techniques needs a deep knowledge of the targeted application scheme its needs. In particular, since electronic toll is a liability critical application, its top level integrity requirements is not a target level of safety as in civil aviation, but rather a maximum quantity of missed revenues (undercharging) and incorrectly high invoices that may cause user complaints (overcharging).

From the possible augmentation systems capable of monitoring GNSS integrity, this work focuses on ABAS because it is proven to be the most appropriate one for electronic toll applications. ABAS provides user autonomous integrity monitoring for the estimated position based on redundant information provided by the range measurements. The use of SBAS augmentation will be considered, not for integrity monitoring, but as a means of correcting and reducing pseudorange errors.

To sum up, the aim of this thesis is to provide the GNSS integrity requirements and integrity monitoring techniques for electronic toll collection applications in rural and urban environments. This objective needs a thorough analysis of GNSS ETC systems and of GNSS navigation in urban environments, in order to identify their needs and constraints to which adapt the integrity concepts and systems originally conceived for civil aviation.

1.2. Organization of the dissertation

This PhD dissertation is organized as follows.

Chapter 1 contains the motivation and objective of the thesis and a brief explanation of each chapter.

Chapter 2 introduces the concept of GNSS integrity in civil aviation in order to set the objectives and constraints with which have been designed the existing integrity monitoring solutions. The GNSS Signal-in-Space (SIS) requirements standardized by the ICAO for various operations are shown, and the different augmentation systems (GBAS, SBAS, ABAS) are presented with emphasis in their integrity monitoring capability.

Chapter 3 presents the main characteristics of Electronic Toll Collection systems based on GNSS. Existing toll systems are analyzed and the road network segmentation into pricing areas using the geofencing method is defined. The impact of the road network topology on the integrity requirements is studied. Finally, the toll system under study is defined, which includes the identification of the most suitable GNSS receivers (signals, receiver configuration, hybridization of external data), GNSS integrity monitoring system, and the algorithm that charges a pricing section using GNSS positioning data.

Chapter 4 establishes the pseudorange measurement error model in road urban environments for the GNSS signals and receivers configurations selected in the previous chapter. First, the nominal error model is obtained splitting the total pseudorange error into independent error sources that can be modeled individually. Afterwards, the correlation time of the nominal errors is presented for different receiver types. Finally, the faulty model is presented, which in this thesis consists only of major service failures.

Chapter 5 calculated the GNSS integrity requirements needed in the design of the integrity monitoring algorithms for ETC systems. These specifications are derived from the top level requirements of the toll system, i.e. the overcharging and undercharging ratios, directly related to the revenues and potential user complaints due to erroneous charges.

Chapter 6 addresses the design of RAIM algorithms. First the WLSR RAIM, a well known algorithm frequently used in civil aviation is presented including the rationale of its design and limitations. The second part of the chapter introduces a novel algorithm based on the WLSR RAIM, explaining its motivation and its suitability to toll applications in urban environments, as well as the justification of its design and limitations.

Chapter 7 presents the results of the simulations run in MATLAB to evaluate the toll system performance in rural and urban environments. First, the statistics of certain parameters such as positioning errors or satellite visibility and position are shown. Afterwards, the RAIM performance and the overall toll system performance are analyzed with different GNSS receivers.

Finally, Chapter 8 summarizes the main results obtained along this PhD thesis and lists the original contributions. Several propositions of continuation of the present work conclude the manuscript.

Chapter 2

GNSS Integrity Monitoring in Civil Aviation

2.1. Introduction

GNSS worldwide positioning has been identified by the International Civil Aviation Organization (ICAO) as one of the possible navigation aids of the Communications, Navigation, and Surveillance / Air Traffic Management (CNS/ATM) system [ICAO, 2002], [ICAO, 2006].

Civil aviation navigation is a safety-of-life (SoL) application, meaning that large and undetected positioning errors may lead to unsafe situations. Therefore, it needs accurate and strongly reliable navigation aids. The ICAO is the authority responsible of setting the standards that radio navigation systems, including GNSS, must fulfill in order to be suitable for civil aviation applications. This is the framework in which the concept of GNSS integrity has been developed, defined as a measure of the trust that can be placed in the correctness of the information supplied by the total system, including the ability of providing alerts to the user when the requirements are not assured to be met [RTCA, 2006].

Since standalone GPS does not meet the ICAO requirements, different augmentation systems have been developed to fulfill them. In particular, all augmentation systems provide GNSS integrity services. Consequently, most of the integrity monitoring systems, techniques and algorithms have been designed to support civil aviation operations within the ICAO specifications.

Before dealing with integrity monitoring systems in other applications and environments, this chapter introduces the GNSS integrity in the civil aviation framework in order to understand the objectives and constraints with which have been designed the existing integrity monitoring solutions. First, the ICAO requirements for GNSS navigation are defined; afterwards, the different integrity monitoring systems are presented.

2.2. GNSS Signal-in-Space Performance Requirements

The Area Navigation (RNAV) method allows aircraft operation on any desired flight path within the coverage of station-referenced navigation aids or within the limits of the capability of self-contained navigation aids, or a combination of these [RTCA, 2003]. The Performance Based Navigation (PBN) specifies the aircraft RNAV system performance requirements needed for the proposed operations in a particular airspace.

The Required Navigation Performance (RNP) is the statement of the navigation performance necessary for operation within a defined airspace. GNSS is the primary navigation system to support currently defined RNP standards.

The RNP is a set of requirements on the Total System Error (TSE), which is made of the Path Definition Error (PDE), Flight Technical Error (FTE) and the Navigation System Error (NSE) (Figure 2.1).

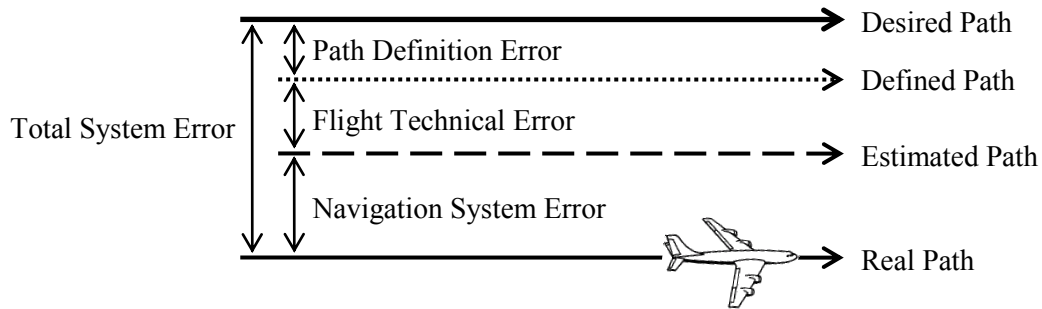


Figure 2.1. Total System Error.

The entire set of GPS code-plus-data sequences and carriers is referred to as the Precise Positioning Service (PPS) Signal in Space (SIS) [DoD, 2008]. A subset of the PPS SIS, the Standard Positioning Service (SPS) SIS, comprises only the 1.023 MHz code-plus-data sequence on the L1 carrier. Collectively, the PPS SIS and the SPS SIS are known as the satellite's navigation signals (or navigation SIS or GPS SIS). The GNSS Signal-in-Space (SIS) performance requirements, responsible of the Navigation System Error, are standardized by the ICAO. Civil aviation standards define GNSS SIS performance requirements for different operations in terms of accuracy, integrity, continuity and availability [ICAO, 2006] [RTCA, 2006]:

- **Accuracy:** The accuracy of a navigation system is a measurement of the degree of conformance between estimated and true positions, i.e. the position error. Accuracy requirements are given as the maximum allowable 95% percentile of the position error. If the position error is modelled with a zero-mean normal distribution, the accuracy is approximately twice the maximum allowable standard deviation (2σ).
- **Availability:** The availability of a navigation system is the ability of the system to provide usable service within the specified coverage area, i.e. the ability to provide the required function and performance at the initiation of the intended operation. Signal availability is the percentage of time that navigational signals transmitted from external sources are available for use. Availability is a function of both the physical characteristics of the environment and the technical capabilities of the transmitter facilities.
- **Continuity:** The continuity of a system is the ability of the total system (comprising all elements necessary to maintain aircraft position within the defined airspace) to perform its function without interruption during the intended operation. More specifically, continuity is the probability that the specified system performance will be maintained for the duration of a phase of operation, presuming that the system was available at the beginning of that phase of operation and was predicted to operate (to exist) throughout the operation.
- **Integrity:** The integrity is a measure of the trust that can be placed in the correctness of the information supplied by the total system. Integrity includes the ability of a system to provide timely and valid warnings to the user (alerts). Integrity requirements consist of four terms:
 - **Integrity Risk (P_{int}):** The integrity risk is the probability of providing a position that is out of tolerance without warning the user within the time-to-alert.

- **Horizontal Alert Limit (HAL):** The HAL is the radius of a circle in the horizontal plane (the local plane tangent to the WGS-84 ellipsoid), with its center being at the true position, that describes the region that is required to contain the indicated horizontal position with the required probability for a particular navigation mode (e.g. 10^{-7} per flight hour for en route), assuming the probability of a GPS satellite integrity failure being included in the position solution is less than or equal to 10^{-4} per hour.
- **Vertical Alert Limit (VAL):** The VAL is half the length of a segment on the vertical axis (perpendicular to the horizontal plane of WGS-84 ellipsoid), with its center being at the true position, that describes the region that is required to contain the indicated vertical position with a probability of $1 - 2 \cdot 10^{-7}$ per approach, for a particular navigation mode, assuming the probability of a GPS satellite integrity failure being included in the position solution is less than or equal to 10^{-4} per hour.
- **Time to Alert (TTA):** The TTA is the maximum allowable elapsed time from the onset of a positioning failure until the equipment annunciates the alert.

2.2.1. ICAO SARPS Annex 10

The ICAO SARPS Annex 10 [ICAO, 2006] specifies that the combination of GNSS elements and a fault-free receiver shall meet the SIS performance requirements contained in Table 2.1 for different operations. A fault-free receiver is assumed to have no failures that affect the integrity, availability and continuity performance, so the requirements concern only to GNSS failures.

Ranges of continuity values are given for some operations because this requirement is dependent upon several factors including the intended operation, traffic density, complexity of airspace and availability of alternative navigation aids. The lower value given is the minimum requirement for areas with low traffic density, while higher values are appropriate for areas with higher traffic density.

Ranges of availability values are given because this requirement is dependent upon several factors including the frequency of operations, weather environments, the size and duration of the outages, availability of alternate navigation aids, radar coverage, traffic density and reversionary operational procedures. With the lowest availability values, GNSS is considered to be practical but not adequate to replace non-GNSS navigation aids, while higher values are adequate for GNSS to be the only navigation aid for en-route navigation.

2.2.2. Cat-II and Cat-III Precision Approaches

Cat-II and Cat-III approaches are GBAS-based precision approaches, currently under development, that provide Decision Heights (DH) between 60 m in the case of Cat-II down to 0 m in the case of Cat-III C [ICAO, 2001]. The GBAS Approach Service Type D (GAST D) described in [RTCA, 2008], supports Cat-II/III approaches enabling the user to compute an accurate differentially corrected position solution, including the definition of a reference path so that the airborne equipment can compute guidance information (deviations) relative to the reference path. The GAST D vertical alert limit is a function of the Final Approach Segment Vertical Alert Limit (FASVAL). GAST D has been evaluated with an integrity risk of 0.5×10^{-7} per approach and a FASVAL of 10 meters [Dautermann et al., 2011].

2.3. GNSS Integrity Monitoring with Augmentation Systems

2.3.1. GPS SPS Performance and need of Augmentation Systems

The accuracy and integrity levels guaranteed by standalone single-frequency L1 C/A are defined in the GPS SPS performance standard [DoD, 2008]:

- The 95% global average code User Range Error (URE) during normal operations over all ages of data (AODs) is lower than or equal to 7.8 m. This performance standard is statistically equivalent to a ≤ 4.0 m rms SPS SIS URE performance standard, assuming a normal distribution with zero mean.
- The probability over any hour of the SPS SIS instantaneous URE exceeding the not-to-exceed tolerance of $4.42 \cdot \text{URA}$ without a timely alert during normal operations is lower or equal to 10^{-5} .

Standalone GPS capabilities as captured in the GPS SPS performance standard cannot meet certain civil aviation signal-in-space performance requirements like the accuracy for precision approaches or integrity monitoring for any operation. For this reason different augmentation systems have been implemented to enhance GPS performance and allow its use in civil aviation operations within the ICAO requirements. Among other services, augmentation systems provide GNSS integrity monitoring.

Augmentation systems are classified into three types according to the source from which the user receives the augmentation information:

- **Ground Based Augmentation System (GBAS):** the augmentation information is sent from a ground-based transmitter
- **Satellite Based Augmentation System (SBAS):** the augmentation information sent is from a satellite-based transmitter
- **Aircraft Based Augmentation System (ABAS):** the augmentation information is autonomously calculated within the aircraft equipment

Table 2.1. GNSS signal-in-space performance requirements for civil aviation [ICAO, 2006].

Typical operation	Accuracy (95%)		Integrity				Continuity	Availability
	Horizontal	Vertical	P _{int}	HAL	VAL	TTA		
En-route	3.7 km	N/A	$10^{-7}/h$	7.4 km (oceanic) 3.7 km (continental)	N/A	5 min	$1 - 10^{-4}/h$ to $1 - 10^{-8}/h$	0.99 to 0.99999
En-route, terminal	0.74 km	N/A	$10^{-7}/h$	1.85 km	N/A	15 s	$1 - 10^{-4}/h$ to $1 - 10^{-8}/h$	0.99 to 0.99999
Initial approach, Intermediate approach, Non-precision Approach (NPA), Departure	220 m	N/A	$10^{-7}/h$	556 m	N/A	10 s	$1 - 10^{-4}/h$ to $1 - 10^{-8}/h$	0.99 to 0.99999
Approach Operations with vertical Guidance (APV-I)	16 m	20 m	$2 \cdot 10^{-7}$ in any approach	40 m	50 m.	10 s	$1 - 8 \cdot 10^{-6}$ per 15 s	0.99 to 0.99999
Approach Operations with vertical Guidance (APV-II)	16 m	8 m	$2 \cdot 10^{-7}$ in any approach	40 m	20 m.	6 s	$1 - 8 \cdot 10^{-6}$ per 15 s	0.99 to 0.99999
Category I Precision Approach	16 m	6 m to 4 m	$2 \cdot 10^{-7}$ in any approach	40 m	35 m to 10 m	6 s	$1 - 8 \cdot 10^{-6}$ per 15 s	0.99 to 0.99999

2.3.2. Protection Levels and Integrity Monitoring Availability

Integrity monitoring techniques currently employed in civil aviation check the compliance with the integrity requirements calculating statistical bounds of the position error denoted protection levels [RTCA, 2006]:

- **Horizontal Protection Level (HPL):** The HPL is the radius of a circle in the horizontal plane (the local plane tangent to the WGS-84 ellipsoid), with its center being at the true position, that describes the region assured to contain the indicated horizontal position.

When autonomous fault detection is used (ABAS), the HAL is a horizontal region where the missed alert and the false alert are met for the chosen set of satellites. It is a function of the user geometry and the expected error characteristics: it is not affected by actual measurements. Its value is predictable given reasonable assumptions regarding the expected error characteristics.

When the HAL is based upon the error estimates provided by SBAS, it is the horizontal region where the missed alert requirement can be met.

- **Vertical Protection Level (VPL):** The VPL is half of the length of a segment on the vertical axis (perpendicular to the horizontal plane of WGS-84 ellipsoid), with its center being at the true position, that describes the region assured to contain the indicated vertical position.

When autonomous fault detection is used (ABAS), the VAL defines the vertical region where the missed alert and the false alert are met for the chosen set of satellites.

When the VAL is based upon the error estimates provided by SBAS, it defines the vertical region where the missed alert requirement can be met.

The system assures that, in the absence of an integrity alert, the estimated position is within the volume defined by the HPL and VPL in compliance with the integrity risk:

$$p\{(|e_H| > HAL) \text{ or } (|e_V| > VAL)\} \text{ and [no alert]} \leq P_{int} \quad (2.1)$$

where e_H and e_V are the horizontal and vertical positioning errors.

When any of the protection levels exceeds the alert limit, the integrity monitoring system is declared unavailable because it is not able to assure that the estimated position is within the volume defined by the HAL and VAL specified in the SIS requirements (Figure 2.2):

$$(HPL \leq HAL) \text{ and } (VPL \leq VAL) \Rightarrow \text{available integrity monitoring} \quad (2.2)$$

$$(HPL > HAL) \text{ or } (VPL > VAL) \Rightarrow \text{unavailable integrity monitoring} \quad (2.3)$$

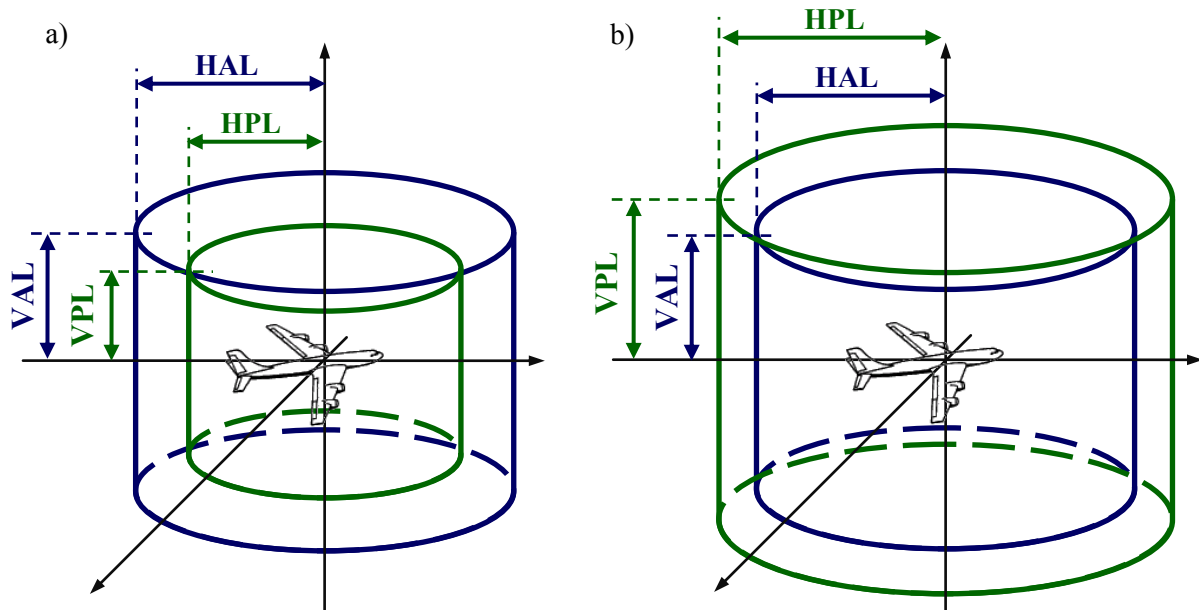


Figure 2.2. Relationship between alert and protection levels: a) available integrity monitoring system, b) unavailable integrity monitoring system.

2.3.3. Ground Based Augmentation System (GBAS)

GBAS is a local-area safety-critical system that enhances standalone GNSS to support civil aviation operations in the airport area (within a recommended 23-mile coverage radius), in which the user receives the augmentation information directly from a ground-based transmitter. It must support at least Cat-I approaches. An example of GBAS is the Local Area Augmentation System (LAAS) deployed in the USA.

GBAS infrastructure is composed of a ground subsystem installed at the airport premises (reference receivers, a ground station and a VHF transmitter), and an on-board subsystem capable to receive and process the augmentation information.

GBAS integrity monitoring relies on local-area differential corrections computed thanks to the reference receivers, and it is transmitted to the users by the ground transmitter in the VHF-NAV band (108 MHz – 118 MHz). Apart from integrity monitoring, GBAS provides additional information like path definition and local-area differential pseudorange corrections.

2.3.4. Satellite Based Augmentation System (SBAS)

SBAS is a wide-area safety-critical system that enhances standalone GNSS in which the user receives the augmentation information from a satellite-based transmitter.

Various SBAS have been deployed to augment GPS civil signals in order to allow civil aviation operations over different regions: WAAS in USA, EGNOS in Europe and MSAS in the Asia and Pacific region. EGNOS is operational for civil aviation since March 2011 and will support all ICAO Performance Based Navigation (PBN) applications with a decision minima compared to conventional non-precision approaches [Eurocontrol, 2011].

SBAS is divided into three subsystems: the ground subsystem, composed of a reference station network, master stations and ground transmitters, the space subsystem, comprising geostationary satellites, and the user subsystem.

SBAS augmentation information relies on differential measurements calculated with the reference station network and the master stations. The ground transmitters send these data to the GEO satellites, that finally broadcast the augmentation information over the coverage area.

Among other data, the augmentation information contains pseudorange differential corrections and integrity flags that indicate faulty satellites. With this information, users estimate the position and compute the protection levels.

2.3.5. Aircraft Based Augmentation System (ABAS)

ABAS is an augmentation system that uses exclusively information available on board the aircraft. It may employ only GNSS information or provide a hybridized navigation solution that integrates other sensors like barometric altimeters or inertial navigation systems (INS).

The ABAS integrity monitoring scheme, denoted fault detection and exclusion (FDE), is a set of algorithms that autonomously monitors integrity using redundant range measurements. The FDE performs two separate functions: first, the fault detection process detects the presence of unacceptable large position errors; second, the fault exclusion algorithm isolates and eliminates the source of the error, allowing the navigation service to continue within the required performances without interruption.

Autonomous integrity monitoring techniques are classified as receiver autonomous integrity monitoring (RAIM) when they use exclusively GNSS information, and as aircraft autonomous integrity monitoring (AAIM) if they include additional on-board sensors [ICAO, 2006]. Nevertheless, the term RAIM may also refer to the fault detection process of the FDE [RTCA, 2006].

2.3.5.1. Fault Detection and Exclusion (FDE)

The following events, depicted in Figure 2.3, can occur throughout the FDE process [RTCA, 2006]:

- A **positioning failure** occurs whenever the difference between the true position and the estimated position exceeds the applicable alert limit:

$$(|e_H| > HAL) \text{ or } (|e_H| > VAL) \Rightarrow \text{Positioning Failure} \quad (2.4)$$

If the equipment is not aware of the alert limit, a positioning failure is defined to occur whenever the difference between the true position and the estimated position exceeds the applicable protection level (HPL, VPL).

- A **false detection** is defined as the detection of a positioning failure when a positioning failure has not occurred.
- A **missed detection** occurs whenever a positioning failure is not detected.
- A **failed exclusion** occurs whenever a true position failure is detected and the detection condition is not eliminated within the time-to-alert (from the onset of the positioning failure). A failed exclusion would cause a navigation alert.

- A **wrong exclusion** is defined to occur when a detection occurs, and a positioning failure exists but is undetected after exclusion.
- A **missed alert** is a positioning failure that is not annunciated as an alert within the time-to-alert are defined to. Both missed detection and wrong exclusion can cause missed alerts after the time-to-alert expires.
- A **false alert** is defined as the indication of a positioning failure when a positioning failure has not occurred (a result of false detection). A false alert would cause a navigation alert.

The probability of the previous events, specially the probability of missed and false alert, define the FDE performance. In order to meet the ICAO specifications, the FDE must have a maximum probability of missed alert of $P_{MA} = 10^{-3}$ per test and a maximum probability of false alert of $P_{FA} = 3.33 \cdot 10^{-7}$ per test for operations from en-route to NPA, while APV operations require $P_{FA} = 1.6 \cdot 10^{-5}$ per test [RTCA, 2006].

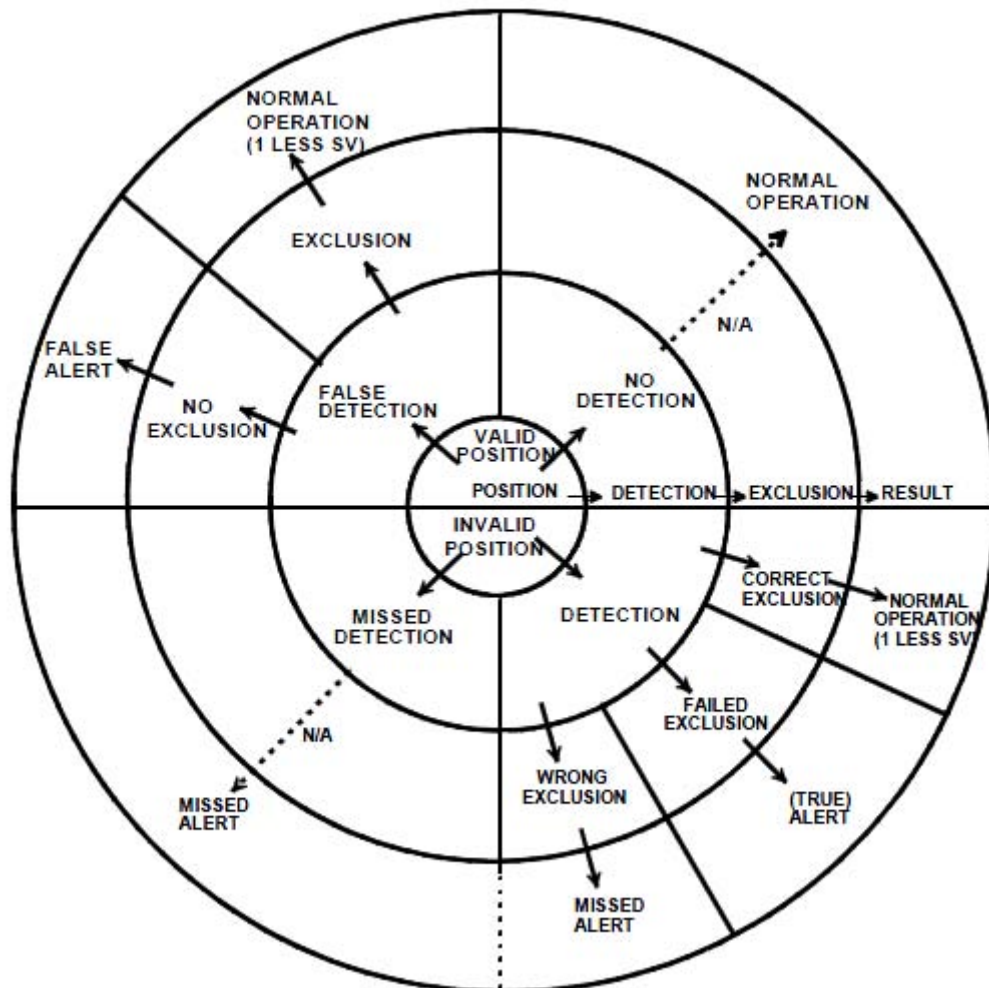


Figure 2.3. Diagram of possible FDE events [RTCA, 2006]

2.4. Conclusions

Civil aviation is a safety-of-life application that needs reliable navigation aids with performance within the requirements standardized by the ICAO.

The concept of GNSS integrity, defined as a measure of the trust on the correctness of the information supplied by the navigation system, has been originally defined in the framework of civil aviation. Consequently, the integrity monitoring systems have been conceived to meet the ICAO specifications.

Standalone GPS does not meet the requirements, so three different types of augmentation systems (GBAS, SBAS, ABAS) have been developed with the aim of allowing the use of GNSS positioning in civil aviation applications. GBAS and SBAS rely on local and wide area differential measurements, while ABAS is calculated with equipment on board the aircraft.

The integrity monitoring information the user computes thanks to augmentation systems consists of horizontal and, if applicable, vertical protection levels, which are statistical bounds of the position error, and integrity alerts or flags.

Chapter 3

GNSS-based Electronic Toll Collection

3.1. Introduction

A number of applications that take place in urban environments need reliable navigation by means of GNSS integrity monitoring: route guidance for special vehicles (ambulances, police, etc.), transport of dangerous or very valuable goods, bracelet trackers, emergency calls, electronic toll collection (ETC), etc. The most appropriate GNSS integrity monitoring technique and its required performance must be adapted to the application needs, so the scope of this work focuses on one particular application: GNSS-based ETC (GNSS ETC).

Most of European states are deploying ETC systems. In order to assure the interoperability among them, the EU Directive 2004/52/EC [EU, 2004] establishes a European Electronic Toll Service (EETS) where new ETC are recommended to use GNSS and/or 5.8 GHz Dedicated Short-Range Communications (DSRC), together with GSM-GPRS mobile communication technologies.

Electronic toll collection systems based on GNSS positioning (GNSS-ETC) have been studied in numerous projects [Racal Tracs, 2000] [ARS, 2006] [MEEDAT, 2009] [Gutierrez-Lanza et al., 2011] and are already operational in non-urban environments [TollCollect, 2008] [NDSAS, 2010].

Because of these reasons, the chosen target application is GNSS-ETC in urban environments. This chapter presents the characteristics of this type of electronic toll systems.

Charging road infrastructures is a tool used for controlling traffic congestion and pollution, as well as for generating revenues, usually reinvested in road infrastructure. The different road pricing mechanisms include tolls, fuel taxes, etc.

Among the various road pricing methods, road user charging (RUC) systems are responsible for collecting the fee that vehicles pay for using tolled areas or roads. Various implementations are possible: tollbooths, number plate recognition cameras, tachometer logs, dedicated short-range communications (DSRC), satellite navigation, etc. Systems relying on electronic technologies are also called electronic toll collection (ETC) or electronic fee collection (EFC) systems.

Satellite navigation provides a worldwide positioning service independent from the ETC infrastructure, which gives GNSS-ETC some advantageous properties. One of the most important is the fact that the quantity of roadside infrastructure is reduced in comparison with other toll collection mechanisms. Indeed, the main equipment needed is an on-board unit (OBU) installed at the vehicle, whose principal component is a GNSS receiver, so the investment and maintenance cost per kilometre of tolled road is reduced. This results in a highly flexible system, where updates of the tolled road network or of the toll rates can be made simply and fast because they do not require modifying or installing new roadside infrastructure. It is also possible to cover any area, even where setting up infrastructure would be difficult or unpractical. Moreover, the toll system is free-flow and does not

require users to slow down or drive in specific lanes at any moment. Additionally, GNSS positioning information obtained for ETC may be also used in other services like emergency calls, distance-based insurance or car rental applications, etc.

The OBU may contain, in addition to a GNSS receiver, the means for calculating the toll from the positioning data, as well as a communication link with the central invoice managing centre.

The structure of the chapter is the following. First, GNSS-ETC projects and already operational systems are presented. The need of GNSS integrity and the most adequate monitoring systems are studied afterwards. Then, the geo-fencing technique is explained, and the OBU characteristics are derived. Finally, an appropriate road segment detection algorithm is proposed.

3.2. Current state of GNSS-based ETC systems

Satellite navigation technologies are already being used in electronic road toll systems. As of 2011, two ETC systems for freight transport vehicles using GPS are already deployed in Germany and Slovakia, and several road toll projects envisage relying on GNSS. Moreover, some ETC whose primary technology is not satellite navigation use it as support.

Toll Collect GmbH operates the electronic toll system for heavy commercial vehicles on German federal motorways and certain roads since 1 January 2005 [TollCollect, 2008]. The levied toll is a function of the distance travelled and the vehicle characteristics like weight, number of axes or the emission category.

Vehicles are equipped with an on-board unit (OBU) which has stored in memory the digital map of more than 13000 km of motorways and tolled roads divided in more than 2800 segments, as well as the toll rates in force. The digital map includes non-tolled roads running within a 250 m distance from the motorway, which represent critical areas where user monitoring mechanisms must be specially reliable in order not to incorrectly charge users circulating on non-tolled road.

All along the trajectory, the OBU estimates user's position with GPS and compares it with the digital map to detect whether the vehicle is on a tolled road segment and determine which segments have been used. Around 60 support radio beacons have been installed to guarantee correct positioning in critical areas where GNSS may not be sufficient for a trustful vehicle detection, like long tunnels or sectors with non-toll roads running parallel to the motorway. Portable support beacons can be temporarily installed at specific points, for instance, during road works.

Once toll charges have reached a certain amount or a specific time period has elapsed, the OBU transmits the collected information to the computing centre via GSM. Finally, the toll collection centre assigns the charges to the user according to the vehicle license plate number and sends him the corresponding monthly toll statement.

Since 1st September 2011, Toll Collect and the Austrian operator ASFINAG provide a cross-system ETC service that allows truck drivers to pay tolls in Germany and Austria with the same OBU installed in the vehicle. ETC in Austria is based on microwave technology; thus, the OBU uses GPS in Germany and DSRC in Austria. Toll invoices by the two companies remain separate [TollCollect, 2011 (b)].

Slovakia has also deployed a freight transport toll system based on GNSS which follows a similar approach as the implemented in Germany, consisting on comparing GPS positioning information with a digital map of the segmented road network [NDSAS, 2010]. SkyToll operates the ETC for heavy vehicles on Slovak federal motorways and certain roads since 1 January 2010. The toll is computed

upon the distance driven and the vehicle characteristics. The system covers more than 2300 km of motorways and national roads divided into more than 1600 segments, and user monitoring and toll computation rely on GPS positioning computed by the OBU installed in the trucks.

Flexibility is one of the key features of GNSS-supported ETC: toll network and fee updates are possible without additional roadside infrastructure. Flexibility ensures quick adaptation to new scenarios and ETC feasibility in national road networks more intricate than motorway ones. Examples of the flexibility advantages are the around 30 modifications made to the German toll network per month, including the addition of federal roads [TollCollect, 2008], and the deployment of a pilot ETC covering more than 250 km. of national roads in Czech Republic in 16 days [SkyToll, 2010].

France will establish from 2013 a mileage-based eco-tax for heavy goods vehicles in the national road network [AFIFT, 2011]. The ETC must be compatible with the future European Electronic Toll System defined in the EU directive 2004/52/EC and technologically will rely on GNSS, DSRC, or a combination of both [MEEDAT, 2009]. The road network, comprising between 10000 and 15000 km of national roads, will be split into pricing sections, each one controlled by a pricing point. The pricing sections are defined as segments of taxed route between two consecutive intersections with other roads. The passage of a vehicle by a charging point is the trigger that charges the user the fee corresponding to the predetermined length of the segment. About 3000 segments are envisaged, with an average length from 4 to 5 km. Nevertheless, a taxed road with intersections close to each other will be divided into much shorter sections, more challenging to detect. In order to avoid an excessive complex detection system with a cost disproportional to the generated revenues, the law permits joining several adjacent charging sections.

Dutch authorities studied to charge on a driven distance basis all vehicles on the whole national road network with a toll system using GNSS [Tierolf, 2010]. Nevertheless, the government discontinued the project in October 2010 in favour of investigating the effects of general fuel tax raise.

Switzerland's ETC uses satellite navigation as support technology. The performance-related heavy vehicle fee HVF, also known by its acronym in German LSVA, levies a distance-based toll to freight transport vehicles on all public highways in Switzerland since 1st January 2001 [FDF, 2011]. Vehicles' mileage is directly read from the vehicle's tachometer, connected to the OBU, while GPS and motion sensors are used as support technologies to control if the tachometer signal is interrupted or manipulated. The mileage counter is automatically switched on or off thanks to DSRC radio beacons installed at the highway borders.

3.3. GNSS Integrity

3.3.1. Liability

GNSS liability-critical applications are defined by the fact that excessive and uncontrolled positioning errors may have negative legal or economic consequences. In these type of applications, as in safety-of-life (SoL) ones, error control by means of GNSS integrity monitoring modules plays a major role.

ETC is considered a liability-critical application because erroneous positioning may lead to an incorrect toll computation. According to their effects, wrong toll invoices are classified in two groups, undercharging and overcharging:

- **Undercharging** is defined to occur when the levied toll is lower than it should. It is directly translated as a loss of revenue of the toll system operator.

- **Overcharging** is defined to occur when the levied toll is higher than it should. It may cause user claims and their associated legal and economic implications.

Toll systems are usually designed with specifications that limit the maximum allowable overcharging and undercharging, which implicitly requires monitoring of positioning errors.

For this reason, GNSS integrity monitoring is a key element in ETC that assures that position errors, and the consequent equivalent toll computation errors, are within the allowed limits.

3.3.2. GNSS integrity monitoring systems

Integrity monitoring systems have been originally designed for civil aviation, which requirements may be different from those of urban electronic toll services. Suitable integrity monitoring mechanisms for ETC applications should have the following characteristics: first, they must be flexible in order to tune their performance to the ETC requirements; second, they have to operate properly in urban environments. This means that they must attain acceptable availability rates even in challenging urban scenarios with limited satellite visibility, and should be able to deal with failures of different origins, including those caused by the user's local environment, like non-line-of-sight (NLOS) multipath. Only integrity in the user's horizontal plane is considered.

The level of integrity provided in current standalone GPS by means of the user range accuracy (URA) is insufficient for SoL and liability critical applications, which require GNSS integrity monitoring services based on augmentation systems. The application of the three augmentation systems inherited from civil aviation (GBAS, SBAS and ABAS) to electronic toll applications is studied. Integrity services that may offer future standalone GNSS are not considered because of their immature development stage.

1) GBAS

GBAS has been originally conceived to support aviation operations in the airport vicinity, transmitting integrity information and local area differential corrections computed by the ground subsystem installed at the airport. For that reason, GBAS integrity information is limited to an area within about 20 miles from the ground infrastructure.

Current GBAS systems augment GPS L1 signals, although a future extended service to other frequencies and GNSS is expected.

Because of its limited coverage area, toll systems should deploy several GBAS ground segments - composed of reference receivers, a ground station and a VHF emitter - in order to provide integrity throughout the whole road network. All this roadside infrastructure would increment the cost and reduce the flexibility of the toll system. Moreover, differential corrections only apply to errors that affect equally to GBAS reference receivers and the user, so they cannot deal with failures generated by the user's immediate environment, like multipath.

In consequence, GBAS-like local area augmentation systems are not recommended for urban ETC applications.

2) SBAS

SBAS broadcasts augmentation information that allows error correction and integrity monitoring in a wide area, typically a continent. Any user with an SBAS receiver can obtain the augmentation

information throughout the coverage area. Toll systems just need to equip vehicles with the adequate receiver to be able to use SBAS corrections and integrity, without any additional infrastructure.

SBAS satellites are typically in a geostationary orbit, which results in relatively low elevation angles at high latitudes like those of the European territory. This fact may cause signal masking in scenarios with important obstacles such as urban environments. This problem of satellite visibility is solved with technologies like SISNeT that uses internet as a complementary transmission link of EGNOS messages, allowing the access to augmentation information in environments where SBAS satellites are likely to be blocked. In this case the receiver is not required to receive the SBAS signals, being enough with an internet connexion.

Current SBAS systems augment only GPS L1 signals, although SBAS evolution studies point towards enhanced services based on dual frequency, multi-constellation navigation solutions [EU-UE CSN, 2010].

SBAS integrity as defined in [RTCA, 2006] has been conceived under civil aviation requirements and assumptions. For example, because the shape of residual error distributions strongly depends on the SBAS system architecture and algorithms and no general overbounding method has been identified, the SBAS system designer is responsible of providing a method to compute UDRE and GIVE variances in compliance with the civil aviation integrity risk of $P_{\text{int}} = 2 \cdot 10^{-7}$ /approach [Roturier, 2001]. Furthermore, SBAS integrity monitoring cannot detect failures generated in the user's immediate environment, NLOS multipath for example, because it relies on differential corrections computed by a network of reference stations.

The conclusion is that it is not recommended to apply directly SBAS integrity in urban ETC applications, but SBAS error corrections and their residual error models are still applicable. If SBAS corrections are used for applications with integrity requirements different from the civil aviation ones, their residual error distributions are assumed to overbound always the real error (and not to be designed only to assure the civil aviation integrity risk).

3) ABAS

ABAS integrity monitoring involves algorithms, run at the receiver, that process redundant GNSS measurements and, optionally, information from other sensors installed in the vehicle. Following the ICAO notation, RAIM denotes the particular case where only GNSS signals are used, and AAIM the hybridized solution with other on-board sensors.

ABAS presents a number of characteristics that make it an appropriate integrity monitoring scheme for ETC. First, toll systems do not need additional roadside infrastructure because integrity is monitored at the receiver via software and, if sensors are used, these are on board the vehicle. Second, ABAS deals directly with GNSS user's measurements which procure information about all errors and failures affecting vehicle positioning, including those that cannot be detected by other systems based on reference receivers. Third, ABAS performance can be easily tuned to ETC needs modifying the algorithm run at receiver. Finally, ABAS can be easily adapted to multi-constellation receivers and to signals broadcasted in any frequency band.

Hence, autonomous integrity monitoring algorithms of the type RAIM (or AAIM) are suitable for electronic road applications.

Table 3.1 summarizes the key characteristics of the integrity monitoring provided by each augmentation systems concerning the needs of ETC applications.

Table 3.1. Characteristics of augmentation systems for ETC applications.

Characteristics	Augmentation system		
	GBAS	SBAS	ABAS
Flexible integrity performance (integrity monitoring adapted to ETC requirements)	✗	✗	✓
Flexible toll system (no additional roadside infrastructure)	✗	✓	✓
Deal with all kind of failures (including those generated by the user's local environment)	✗	✗	✓
Extensible to multi-constellation receivers and to different frequency bands	✗	✗	✓

The conclusion is that autonomous integrity monitoring schemes like RAIM or AAIM is chosen for GNSS-ETC systems, with the possible aid of SBAS pseudorange error corrections.

3.3.3. ABAS scheme

An ABAS can be constituted by different combinations of sensors and FD or FDE algorithms.

Hybrid positioning systems merge satellite navigation with other sensors with the aim of improving the performance of standalone GNSS, specially in environments of reduced satellite visibility. Different sensors can be included in a hybrid system: inertial sensors, odometer, pressure sensors that estimate the altitude, laser, cameras, etc. Inertial measurement units (IMU), composed of accelerometers and gyroscopes, are one of the most common sensors used in civil aviation, road and urban applications. There are several hybridization techniques for integrating GNSS with the external sensors; depending on the type of data used and the stage of the positioning process where the information is merged, they can be divided into loose, tight and ultra-tight coupling. Loose coupling techniques correct sensor measurements with user positions estimated using exclusively GNSS data. They do not increment positioning availability because they need standalone GNSS positioning, and usually require a sensor set capable of estimating the user position by itself, like an IMU. Tight coupling combine GNSS raw measurements (pseudoranges in our case) and sensor measurements to estimate the position. Ultra-tight coupling uses more basic data from the GNSS receiver structure like the tracking loops, which may not be accessible in commercial receivers.

Hybridization techniques are usually implemented with Kalman filters, which are recursive loops. Although they are a powerful tool for integrating data from different sensors, integrity analysis with Kalman filters are complicated because once a faulty measurement with a large error enters the system, it contaminates the rest of the measurements and remains in the recursive loops. This fact makes difficult to predict the performance of the integrity monitoring system at a given instant.

In order to have full control on the performance of the integrity monitoring algorithm at each instant, including the capability of predicting it, a receiver structure with no Kalman filter is chosen. The navigation solution is calculated applying the weighted least squares (WLS) estimator to the pseudorange linear measurement model. This fact limits the sensors that can be hybridized.

Height information issued from sensors can be expressed as the equivalent pseudorange measured from a satellite situated at the user's zenith. Thus, height sensors can be introduced in the WLS estimator in a tight coupling scheme. Height information can be obtained from a barometer or a digital map.

RAIM algorithms may be sequential or snapshot. Snapshot algorithms monitor integrity using only current measurements, while sequential RAIM also uses data of previous epochs. In order to avoid recursive loops, a snapshot algorithm will be chosen in this study.

3.4. Road segmentation

The tolled road network is segmented into sections that constitute the basic charging units: each road segment has an associated price that the toll system charges to users for crossing it. Then, the trajectory of any user can be expressed as the list of crossed road segments, and the total levied toll can be computed as the sum of the price of the segments in the trajectory. If road segments are defined as road portions between consecutive intersections, with only one entrance and one exit, their charge can be proportional to the distance travelled by the user, leading to a distance-based toll where the distance is the sum of the predefined lengths of the road segments the vehicle has traversed. The toll rates can also be adapted to the daytime, traffic density, vehicle type, etc. Road segmentation in pricing sections is being used in the German and Slovak GNSS-ETC systems, and is the proposed approach for the French EcoTax.

Toll systems based on DSRC technologies usually monitor the use of road segments with a checkpoint scheme in which each segment is managed by a control point equipped with a DSRC transceiver. Users are charged the whole segment's price when they cross the control point. The checkpoint scheme is the result of the need of installing dedicated roadside infrastructure with limited coverage area (microwave transceivers) at each road segment.

GNSS positioning has worldwide coverage and does not need additional roadside infrastructure. This fact allows to monitor road segment crossings by means of user positions calculated along their whole trajectory and not only at fixed checkpoints. Moreover, GNSS positioning may be unavailable at certain locations and instants in urban scenarios because of the reduced satellite visibility; a system capable of detecting segment crossings with user positions estimated all along its trajectory throughout the segment contributes to overcome the problem of punctual satellite outages.

For these reasons, the use of road segments in GNSS-ETC will be managed following a geo-fencing method. This approach assigns each road segment a virtual perimeter, called geo-object. Geo-objects are defined in a way that, if a user's estimated position (\hat{x}_H) lies inside it, the true position (x_H) is assured to be inside the road segment with a probability equal to or higher than $(1 - P_{MD})$, where P_{MD} is the probability of missed detection of the RAIM. This relationship is done thanks to the HPL associated to \hat{x}_H by the GNSS integrity monitoring system, and the HAL derived from the geo-object boundaries. Considering only horizontal positions:

$$\begin{aligned} p\{x_H \text{ inside road segment} \mid (\hat{x}_H \text{ inside geo object}) \& (HPL \leq HAL) \& (\text{no integrity alert})\} \\ &\geq 1 - P_{MD} \end{aligned} \quad (3.1)$$

The toll system is allowed to use an estimated position only if the GNSS integrity system does not rise an alert and the HPL is lower than or equal to the HAL:

$$\hat{x}_H \text{ valid for the toll system} \Leftrightarrow (\text{HPL} \leq \text{HAL}) \ \& \ (\text{no integrity alert}) \quad (3.2)$$

The geo-object boundaries and \hat{x}_H determine the HAL. Before deriving the value of the HAL, let us recall the relationship between the position error and the HPL:

$$p\{(|x_H - \hat{x}_H| > \text{HPL}) \ \& \ (\text{no alert})\} \leq P_{MD} \quad (3.3)$$

Civil aviation standards define the HPL as the radius of the circle in the horizontal plane centred at x_H , which is assured to contain \hat{x}_H with a probability equal to or higher than $(1 - P_{MD})$ when the RAIM has not detected a failure (Figure 3.1-a). The HPL can be equivalently interpreted as the radius of the circle centred at \hat{x}_H , which is assured to contain the true horizontal position x_H with a probability equal to or higher than $(1 - P_{MD})$ when the RAIM has not detected a failure (Figure 3.1-b).

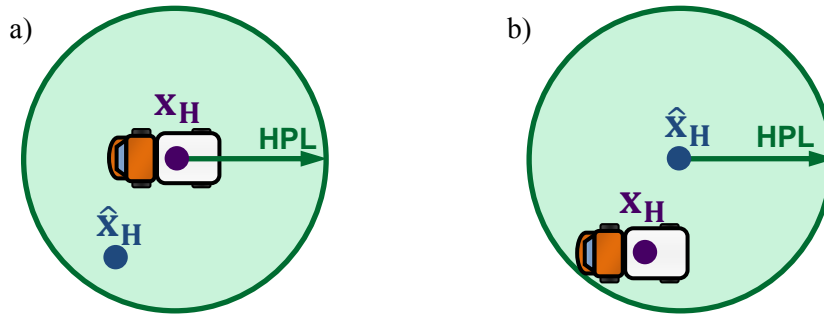


Figure 3.1. Different interpretations of the HPL.

When the true position x_H can be anywhere within the geo-object, the HAL associated to an estimate \hat{x}_H that is inside the geo-object is the distance to the closest geo-object's boundary, so the circle centred at \hat{x}_H that is assured to contain x_H is contained inside the geo-object. (Figure 3.2). The HAL decreases as \hat{x}_H approaches the geo-object's limits, being null on the perimeter. When the HPL is larger than the HAL, the geo-object is not assured to contain x_H with the required probability.

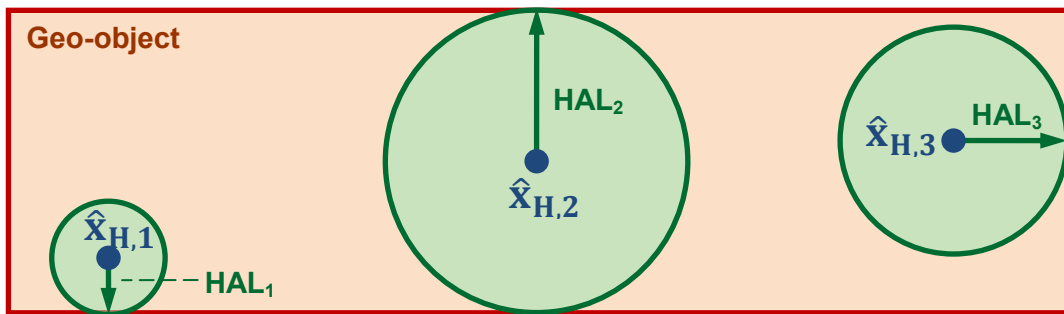


Figure 3.2. Examples of the relationship between geo-object boundaries, the estimated position and the HAL when the real position can be anywhere inside the geo-object.

Let us consider the case of a road network where vehicles are restricted to circulate on the roads. Although estimated positions \hat{x}_H can lie anywhere, even where users cannot drive (e.g. in a building),

acceptable values of x_H are limited to be inside the road segment. In this case, the geo-object boundaries can be established as the lines equidistant to the closest road limits (Figure 3.3).

In other words, the geo-object of a road segment can be defined as the area comprising all the points that are closer to the associated road segment than to any other. Any estimate \hat{x}_H inside the geo-object with an appropriate value of HPL assures that the real position x_H lies on the road segment. In this case, the HAL can be defined as the distance between the estimated position and the closest segment (Figure 3.4). Thus, the HAL becomes zero at the intersections with other road segments. Additionally, when the circle defined by the HPL and \hat{x}_H does not include the road segment, it can be deduced that a missed detection has occurred.

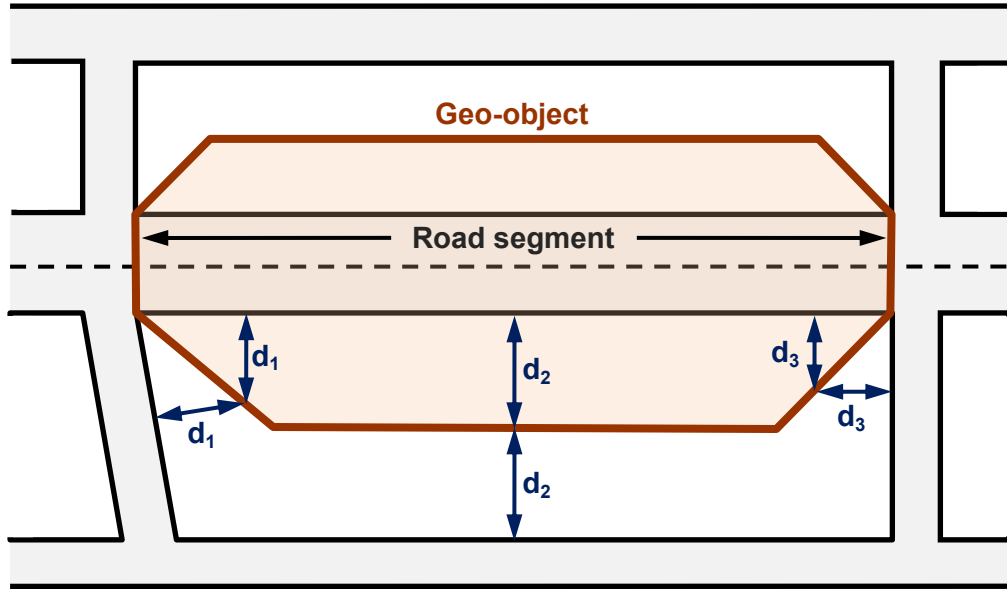


Figure 3.3. Example of geo-object defined as the area of points closer to the road segment than to any other.

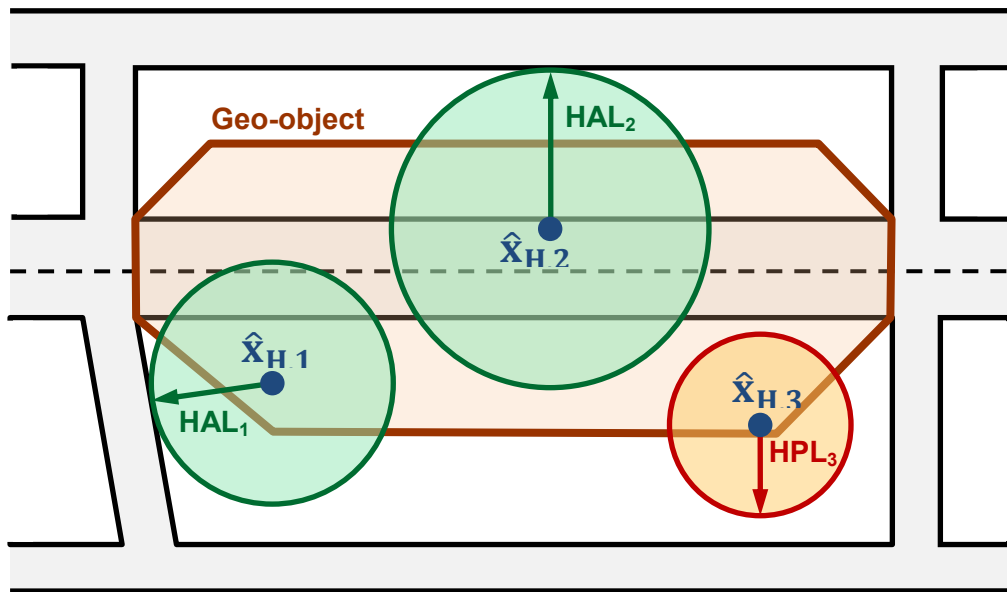


Figure 3.4. Example of HAL computation in a road network (Positions 1 and 2). Example of undetected positioning failure (Position 3).

This method obtains the maximum possible HAL for each \hat{x}_H and attains the highest availability rate of the integrity monitoring system, that is, the maximum number of estimated positions that are valid for being used by the toll system. Nevertheless, its computation is somewhat laborious, must be recalculated for each \hat{x}_H and needs the exact map of the adjacent roads, regardless they are part of the tolled network or not. In order to simplify the process, a constant HAL independent from \hat{x}_H and the neighbouring roads is proposed. With that purpose, the geo-object is redefined as the region situated at distance equal to or lower than the desired HAL from the road segment, and at a distance higher than the HAL to any other segment (Figure 3.5).

Then, any \hat{x}_H lying within the geo-object boundaries assures that x_H is inside the road segment if the HPL is lower than the fixed HAL. The HAL value is a design parameter that depends on the road pattern, but generally a suitable choice is half of the distance from the road segment to the closest road that runs approximately parallel to it. Note that a constant HAL is provided at the expense of reducing the area covered by the geo-object, i.e. the zone that contains the estimated positions that can be processed by the toll system, and reducing in most cases the HAL, which decreases the availability of the integrity monitoring system.

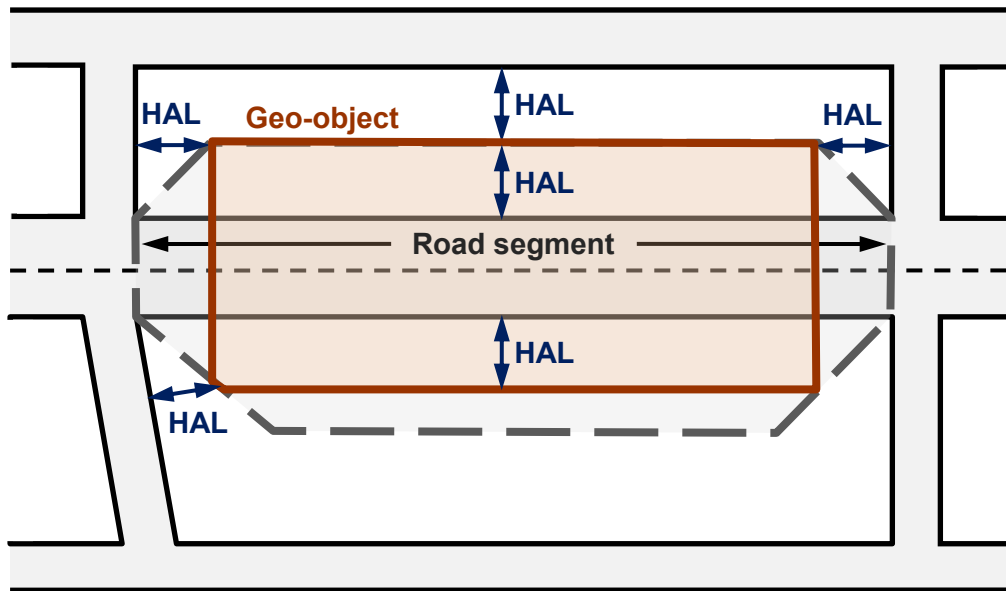


Figure 3.5. Geo-object that allows a constant HAL.

The process of deciding whether a vehicle has driven throughout a road segment or not will be denoted geo-object recognition or segment recognition. The size of the segment is one of the main parameters that affect the performance of the geo-object recognition process. Long segments where users have longer trajectories are more robust against unavailability of GNSS positioning and integrity monitoring systems.

The segment size depends on the route type: motorways with spaced exits are likely to be divided in long segments, while national roads with frequent crossroads require short segments. For example, motorways represent the majority of the German ETC network, and national roads predominate in the Slovak one. As a consequence, the Slovakian ETC has to deal with shorter segments (Figure 3.6, Figure 3.7). For example, road segments shorter than 300 meters represent 20% of the Slovakian ETC network, and less than 3% of the German one. Urban road networks are expected to be segmented in short sections with numerous intersections.

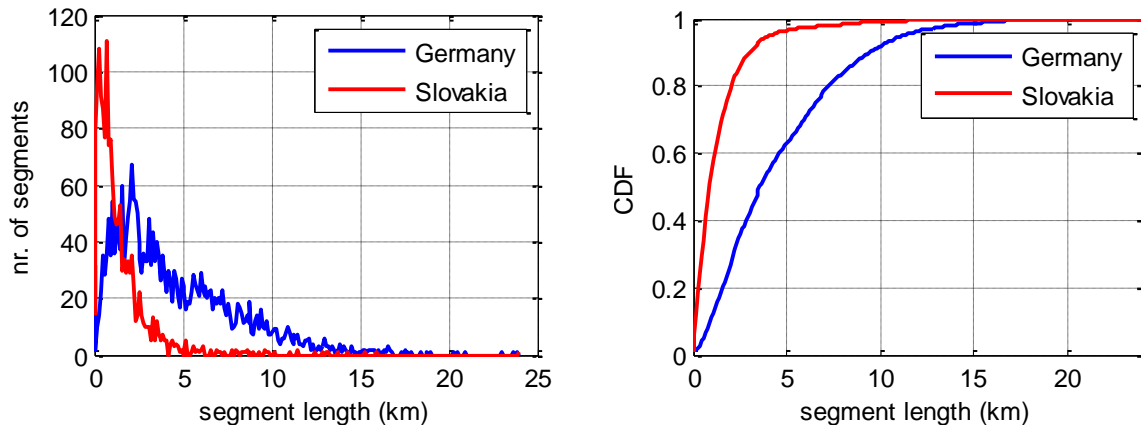


Figure 3.6. Segment length histogram and CDF of German and Slovak freight transport ETC.

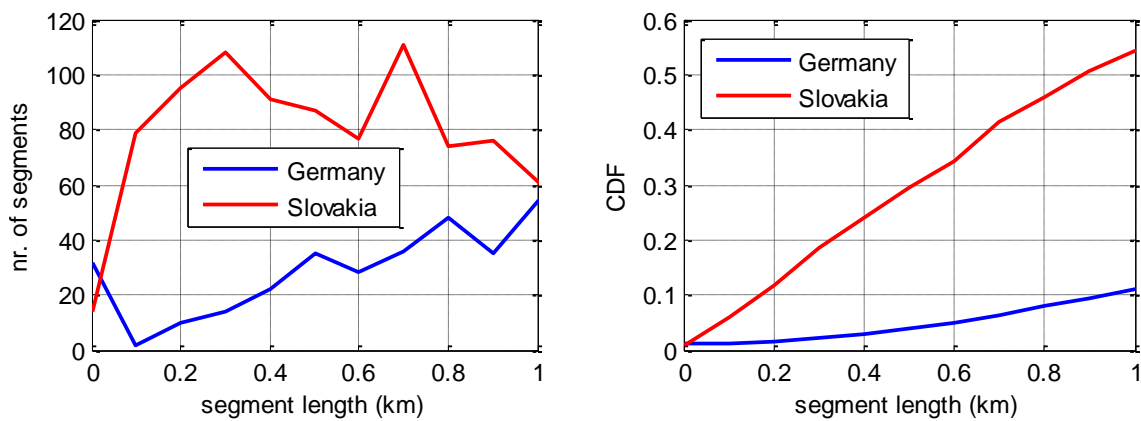


Figure 3.7. Segment length histogram and CDF of German and Slovak freight transport ETC (zoom).

In general, geo-fencing is a versatile technique that can also be applied in other ETC schemes apart from mileage-based tolled roads, like area-based tolls established around city centre perimeters or specific infrastructures such as bridges.

3.5. On-board GNSS receiver

The GNSS receiver is the main element of the on-board unit installed at each vehicle. This section identifies the characteristics of suitable GNSS receivers for GNSS-ETC systems, that is, the GNSS signals to be tracked and the receiver configuration.

3.5.1. GNSS signals

The following receiver types are studied according to the type and number of tracked signals:

- Single constellation GPS, single constellation Galileo and dual constellation GPS/Galileo.
- Single and dual-frequency receivers.

Current and future civil signals are studied. GPS and Galileo will broadcast various signals with different modulations at several frequency bands. The main characteristics of current and future GPS and Galileo signals are summarized in Table 3.2, and their baseband power spectral density are depicted in Figure 3.8. The Galileo commercial service is not considered.

Table 3.2. Characteristics of the considered GNSS signals.

GNSS	Signal	F (MHz)	BW (MHz)	ARNS Band	Modulation	
GPS	L1 C/A	1575.42	20.46	Yes	BPSK(1)	
	L1Cd		30.69		BOC(1,1)	
	L1Cp				MBOC(6,1,1/11) (25% L1Cd, 75% L1Cp)	
	L2C	1276.6	20.46	No	BPSK(1) with Time Division Multiplexing (TDM) of Civilian Moderate (CM) and Civilian Long (CL) codes	
	L5-I L5-Q	1176.45	24	Yes	BPSK(10) BPSK(10)	QPSK (50%)
Galileo	E1B E1C	1575.42	24.552	Yes	CBOC(6,1,1/11,+) CBOC(6,1,1/11,-)	MBOC(6,1,1/11) (50%)
	E5a-I E5a-Q	1176.45	20.46	Yes	BPSK(10) BPSK(10)	QPSK (50%)
	E5b-I E5b-Q	1207.14	20.46	Yes	BPSK(10) BPSK(10)	QPSK (50%)
	E5	1191.795	51.15	Yes	AltBOC(15,10)	

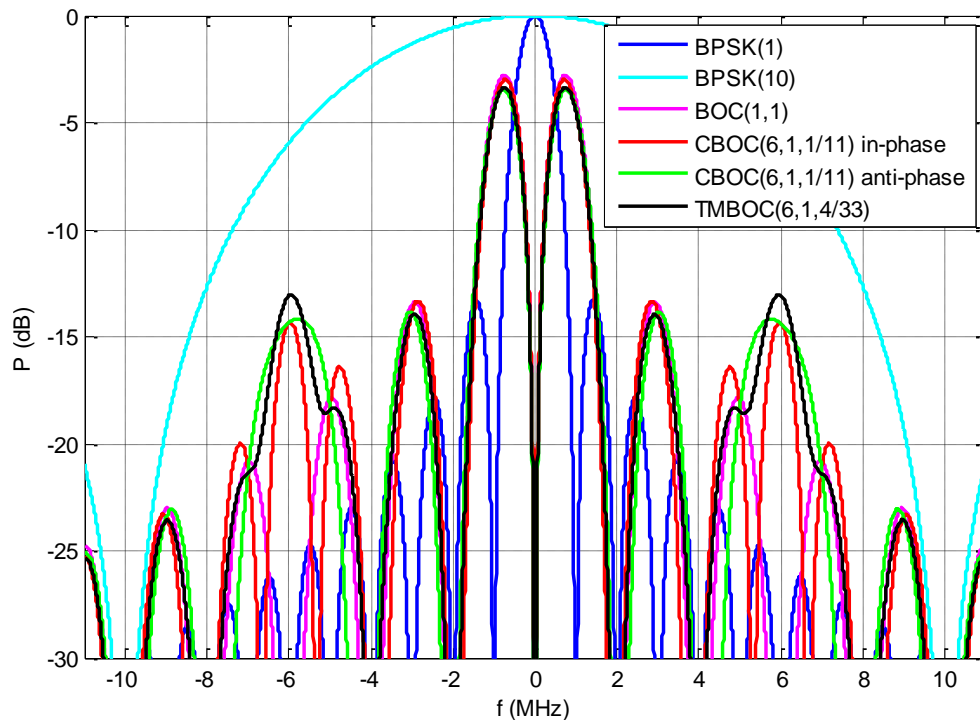


Figure 3.8. Spectra of GNSS signals.

All frequency bands except GPS L2C are aeronautical radio navigation system (ARNS) bands and are regulated by the stringent aviation requirements. ARNS bands limit the in-band interference environment because any new system generating in-band emissions has to go through interference studies supervised by an aviation regulatory authority.

Since RAIM is based on redundant range information, it needs at least one visible satellite more than the minimum necessary to estimate the navigation solution. As it is proven in Chapter 7, dual constellation receivers are needed to attain acceptable rates of visible satellites in urban environments with high probability of signal masking. For this reason, only signals adequate for dual constellation GPS/Galileo receivers will be considered.

Modernized GPS and Galileo signals transmitted in the frequency bands L1/E1 and L5/E5a are compatible and interoperable, so they can be easily received and processed by multi-constellation equipments. Consequently, L1/E1 and L5/E5a are the a selected frequency bands for GNSS receivers in GNSS-ETC applications, and the use of GPS L2C, Galileo E5b and E5 AltBOC will not be further studied.

Modernized L1/E1 and L5/E5a signals are transmitted in phase-quadrature (I-Q) pairs. Only one signal of the pair, the data component, contains the navigation message. This fact allows to receive the dataless signal, known as pilot, with longer integration periods and thus a better tracking performance. Nevertheless, processing pilot signals requires the navigation message, which could be obtained from the data component or by means of assisted GPS (AGPS) services, for instance.

The GPS L1C pair is composed of the data component L1Cd, which has a BOC(1,1) modulation and 25% of the total power of the pair, and the pilot component L1Cp, which has a TMBOC(6,1,4/33) modulation and the remaining 75% of the power. The modulation TMBOC(6,1,4/33) is a time division multiplex of BOC(1,1) and BOC(6,1) chips in a way that the last ones represent 4/33 of the signal power [SAIC, 2008].

The Galileo E1 pair divides equally the power between the data component E1B, which has a CBOC(6,1,1/11,+) modulation, and the pilot component E1C, which has a CBOC(6,1,1/11,-) modulation. The modulation CBOC(6,1,1/11) adds BOC(1,1) and BOC(6,1) chips in a way that the last ones represent 1/11 of the signal power. CBOC(6,1,1/11,+) introduces BOC(6,1) chips in phase, and CBOC(6,1,1/11,-) in anti-phase [EU, 2010].

GPS L5 [ARINC, 2005] and Galileo E5 signals have a BPSK(10) modulation.

Apart from the selected signals because of their interoperability in dual constellation GPS/Galileo receivers, GPS L1 C/A signals are also considered with the aim of studying the performance attainable in GNSS-ETC systems with current GPS receivers.

The same signal can be received and processed with different receiver configurations, resulting in diverse degrees of performance, complexity and computation costs. The main parameters to be tuned are the front-end bandwidth (BW) and the discriminator chip spacing (C_s). A receiver configuration is defined to receive each signal modulation except for L1 C/A signals, for which two receiver configurations are proposed (Table 3.3):

- 1) A narrowband BPSK(1) receiver with $BW = 2$ MHz that only processes the main lobe. A value of $C_s = 1$ chips is chosen; even if a narrower chip spacing would be possible, it would not offer significant improvements because only the main lobe is being tracked.
- 2) A wideband BPSK(1) receiver with $BW = 16$ MHz capable of processing the main and secondary lobes. A narrow chip spacing of $C_s = 0.1$ is chosen.

- 3) A BPSK(10) receiver with $BW = 20$ MHz that only processes the main lobe. A value of $C_s = 0.25$ chips is chosen; narrower values would not offer significant improvements because only the main lobe is being tracked.
- 4) A BOC(1,1) receiver with $BW = 4$ MHz that only processes the main lobe. The discriminator chip spacing is $C_s = 0.2$ chips. The value of C_s is located distant from the nulls of the autocorrelation function that could lead to false lock situations and, consequently, erroneous pseudorange measurements. Narrower C_s would not provide significant improvements because only the main lobe is being tracked.
- 5) A TMBOC/CBOC receiver with $BW = 14$ MHz that processes up to the main lobe of the BOC(6, 1) component. The value of $C_s = 0.1$ has been chosen because it is situated in a suitable point of the autocorrelation function, distant from the nulls.

The selected values of BW and C_s for each modulation are similar to those typically proposed in other applications like civil aviation.

The best tracking performance of TMBOC and CBOC signals is obtained with receivers that generate the local replica of the code corresponding to their modulation [Julien et al., 2007]. These receivers require a minimum bandwidth of 14 MHz in order to receive the primary lobe of the BOC(6,1) component, which require a high computational rate. Nevertheless, their BOC(1,1) component can be filtered and processed with a BOC(1,1) receiver, which is more simple and has a narrower bandwidth. The drawback of this technique is the lost of the useful signal power allocated to the BOC(6,1) component.

Dual constellation GPS/Galileo receivers are necessary in urban scenarios with degraded satellite visibility. However, single constellation receivers will be also studied because they are practical in less stringent environments like rural areas or highways.

Table 3.4 - Table 3.9 are a wrap-up of the selected GNSS receivers to be studied in GNSS-ETC systems.

Table 3.3. Single frequency receiver configurations.

Receiver configuration	Local replica	Two-sided front-end bandwidth BW (MHz)	Two-sided chip spacing C_s (chips)
narrowband BPSK(1)	BPSK(1)	2	1
wideband BPSK(1)	BPSK(1)	16	0.1
BPSK(10)	BPSK(10)	20	0.25
BOC	BOC(1,1)	4	0.2
TMBOC/CBOC	TMBOC(6,1,4/33)	14	0.1
	CBOC(6,1,1/11, -)		
	CBOC(6,1,1/11, +)		

Table 3.4. Single frequency GPS receivers under study.

Single frequency GPS receivers			
Receiver type	Signal	Modulation	Receiver configuration
Narrowband L1 C/A	L1 C/A	BPSK(1)	narrowband BPSK(1)
Wideband L1 C/A	L1 C/A	BPSK(1)	wideband BPSK(1)
GPS L1 BOC	L1Cd	BOC(1,1)	BOC
	L1Cp	TMBOC(6,1,4/33)	
GPS L1 TMBOC	L1Cp	TMBOC(6,1,4/33)	TMBOC/CBOC
GPS L5 BPSK(10)	L5-I	BPSK(10)	BPSK(10)
	L5-Q		

Table 3.5. Dual frequency GPS receivers under study.

Dual frequency GPS L1/L5 receivers		
Dual frequency Receiver	Receiver L1	Receiver L5
GPS L1/L5 narrowband C/A	narrowband L1 C/A	GPS L5 BPSK(10)
GPS L1/L5 wideband C/A	wideband L1 C/A	GPS L5 BPSK(10)
GPS L1/L5 BOC	GPS L1 BOC	GPS L5 BPSK(10)
GPS L1/L5 TMBOC	GPS L1 TMBOC	GPS L5 BPSK(10)

Table 3.6. Single frequency Galileo receivers under study.

Single frequency Galileo receivers			
Receiver type	Signal	Modulation	Receiver configuration
Galileo E1 BOC	E1B	CBOC(6,1,1/11,+)	BOC
	E1C	CBOC(6,1,1/11,-)	
Galileo E1 CBOC+	E1B	CBOC(6,1,1/11,+)	TMBOC/CBOC
Galileo E1 CBOC-	E1C	CBOC(6,1,1/11,-)	TMBOC/CBOC
Galileo E5a BPSK(10)	E5a-I	BPSK(10)	BPSK(10)
	E5a-Q		

Table 3.7. Dual frequency Galileo receivers under study.

Dual frequency Galileo E1/E5a receivers		
Dual frequency Receiver	Receiver E1	Receiver E5a
Galileo E1/E5a BOC	Galileo E1 BOC	Galileo E5a BPSK(10)
Galileo E1/E5a CBOC+	Galileo E1 CBOC+	Galileo E5a BPSK(10)
Galileo E1/E5a CBOC-	Galileo E1 CBOC-	Galileo E5a BPSK(10)

Table 3.8. Single frequency dual constellation GPS/Galileo receivers under study.

Single frequency GPS/Galileo receivers		
GPS/Galileo Receiver	Receiver GPS	Receiver Galileo
L1/E1 BOC	GPS L1 BOC	Galileo E1 BOC
L1/E1 TMBOC/CBOC+	GPS L1 TMBOC	Galileo E1 CBOC+
L1/E1 TMBOC/CBOC-	GPS L1 TMBOC	Galileo E1 CBOC-
L5/E5a BPSK(10)	GPS L5 BPSK(10)	Galileo E5a BPSK(10)

Table 3.9. Dual frequency dual constellation GPS/Galileo receivers under study.

Dual frequency GPS/Galileo receivers		
GPS/Galileo Receiver	Receiver GPS	Receiver Galileo
L1/L5a - E1/E5a BOC	GPS L1/L5 BOC	Galileo E1/E5a BOC
L1/L5a TMBOC- E1/E5a CBOC+	GPS L1/L5 TMBOC	Galileo E1/E5a CBOC+
L1/L5a TMBOC- E1/E5a CBOC-	GPS L1/L5 TMBOC	Galileo E1/E5a CBOC-

3.5.2. Navigation solution

Four receiver types are envisaged according to their navigation solution (Table 3.10). The first one estimates a 2D position plus the time shift between the receiver and the GNSS time. This model applies to single constellation receivers and dual constellation receivers with known inter-system time shift.

Estimating the navigation solution requires a minimum number of range measurements equal to the number of unknowns, whereas one or two additional measurements are needed to attain the redundancy required for RAIM fault detection (FD) and exclusion (FDE) respectively. Generally, the higher is the additional number of range measurements, the better is the positioning and RAIM performance. Therefore, receivers with the lowest number of unknowns are expected to have the best performance.

Table 3.10. Minimum number of range measurements needed for various GNSS receiver types according to their navigation solution unknowns.

		Navigation solution unknowns			
		<ul style="list-style-type: none"> • 2D position • $T_{rcx}/GNSS$ 	<ul style="list-style-type: none"> • 2D position • T_{rcx}/GPS • $T_{rcx}/Galileo$ 	<ul style="list-style-type: none"> • 3D position • $T_{rcx}/GNSS$ 	<ul style="list-style-type: none"> • 3D position • T_{rcx}/GPS • $T_{rcx}/Galileo$
N_{min}	\hat{x}	3	4	4	5
	FD	4	5	5	6
	FDE	5	6	6	7

3.6. Geo-object Recognition

One of the main tasks of GNSS toll systems consists in deciding whether a user has driven through a road segment or not in order to charge him. This decision, known as segment detection or geo-object recognition, is taken using exclusively vehicle GNSS horizontal positioning data, augmented with integrity monitoring, and the segmented road map.

3.6.1. Map-matching algorithms

Map-matching algorithms are techniques commonly used in road transportation systems to identify the correct road link on which a vehicle is travelling, combining positioning data with cartographic information. They can additionally estimate the user's position on the link.

According to their approach, map-matching algorithms can be classified into geometric, topological, probabilistic and based on other advanced techniques [Quddus et al., 2007]. Geometric algorithms use the geometric information of the spatial road network data by considering only the shape of the links, while topological ones also take into account the connectivity and contiguity between links. The probabilistic algorithms rely on a confidence region around the position fix obtained from a navigation sensor, and other map-matching algorithms rely in other advanced techniques like fuzzy logic.

Only a few map-matching algorithms offer an indicator of the trust that can be placed on the provided user position [Velaga et al., 2012] [Jabbour et al., 2008] [Fouque et al., 2008] [Quddus et al., 2006]. The techniques proposed to measure the trust of the map-matching solution include the use of classic RAIM algorithms with positions estimated integrating GNSS and GIS in a tight-coupling scheme (simplifying road links by their centre lines), the comparison between the user heading against the road link direction (which suffers from noisy user heading estimates at low velocity), and the difference between the distance of consecutive map-matched fixes on the link and the real distance travelled by the user obtained from its speed.

The most performing algorithms commonly hybridize GNSS with external sensors and make use of other information like user velocity and heading, road links connectivity, proximity or turn restrictions according to a number of criteria based on empirical studies. The use of this amount of non-GNSS data makes difficult to assure the positioning integrity at each instant. Furthermore, road segments are simplified by their centre lines and the map-matching algorithms assume that the user is always on one of these road links, which is not the case. For these reasons, instead of using map-matching algorithms designed for road navigation, this work proposes a geo-object recognition algorithm for GNSS-based toll collection systems relying exclusively on the geo-objects and the estimated positions, checked by a RAIM algorithm.

3.6.2. Valid Estimated Positions for ETC

GNSS receivers installed at each vehicle estimate the user position at each epoch. Afterwards, the integrity monitoring system (the RAIM algorithm) decides whether an estimate is valid for being used in the geo-object recognition process or not, in order to discard unacceptably large errors. The RAIM is assumed to perform only fault detection (it has no fault exclusion capabilities). An estimate \hat{x}_H is declared valid for ETC when, according to the RAIM, meets the GNSS integrity requirements:

$$\hat{x}_H \text{ is valid for ETC} \Leftrightarrow (HPL \leq HAL) \& \text{ (no alert)} \quad (3.4)$$

That is, valid estimates are those positions in which the RAIM has not detected a horizontal positioning failure (PF). Recalling the civil aviation definition of horizontal positioning failure:

$$\text{Positioning Failure} \Leftrightarrow |e_H| = |x_H - \hat{x}_H| > HAL \quad (3.5)$$

Integrity monitoring systems cannot detect 100% of the positioning failures, so there is a probability, lower than the probability of missed detection P_{MD} specified during the RAIM design, that an estimated position containing a positioning failure is declared valid. Valid positions can be classified as reliable positions when $|e_H| \leq HAL$, and as undetected positioning failures if $|e_H| > HAL$.

An estimate \hat{x}_H can be declared non-valid for two reasons: RAIM unavailability and integrity alerts. When the RAIM is not available, \hat{x}_H has no integrity information associated and cannot be guaranteed to be free of positioning failures. Integrity alerts indicate that the estimate is likely to contain a positioning failure, so \hat{x}_H must be discarded.

In environments with reduced visibility the number of tracked satellites may not be sufficient to provide GNSS positioning at certain instants. In that cases, the user's position cannot be estimated and no data is provided to the geo-object recognition algorithm.

The scheme followed to select the estimated positions valid for geo-object recognition is summarized in Figure 3.9.

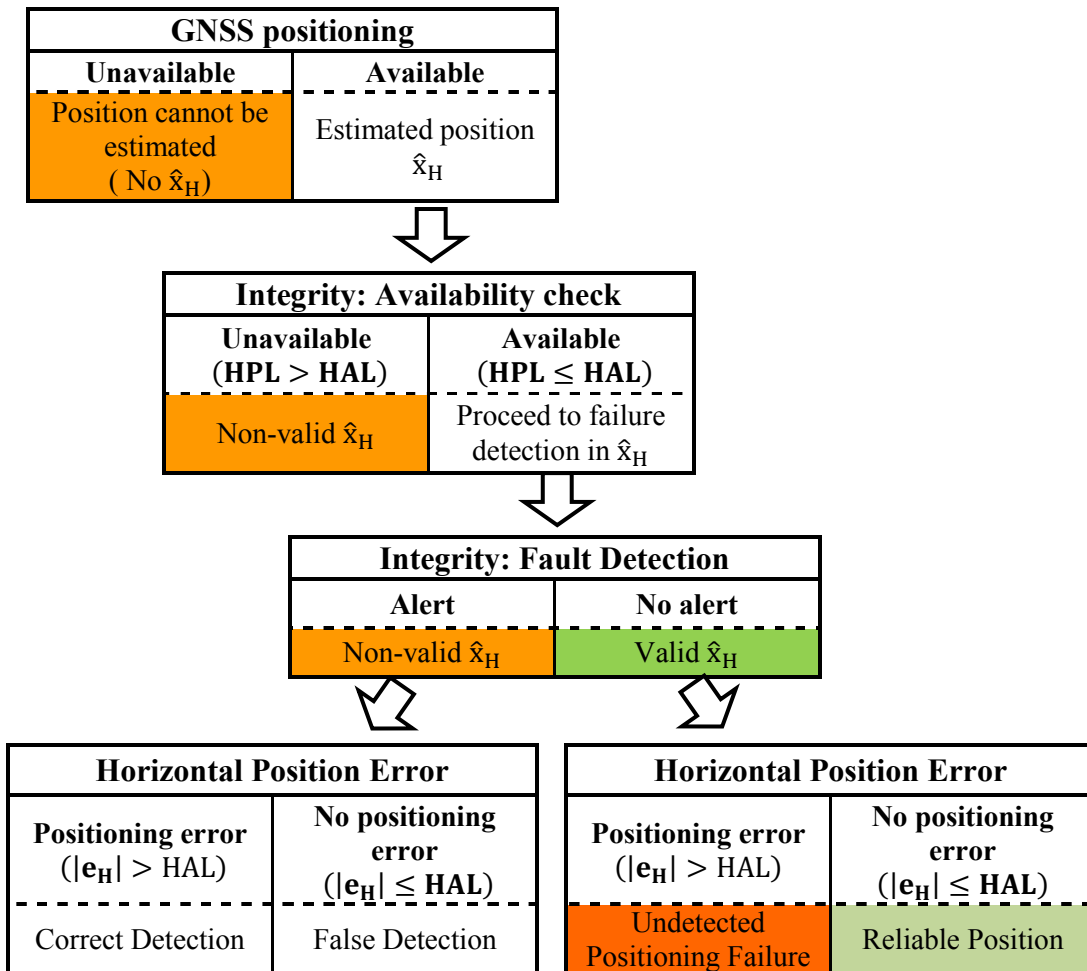


Figure 3.9. Scheme of the possible outputs of the GNSS positioning & integrity system at a given instant, indicating when an estimated position is declared valid to be used in the geo-object recognition algorithm.

3.6.3. Independent positions

Positioning errors have a certain correlation time (T_c) that depends on the correlation time of pseudorange measurement errors ($T_{c,PSR}$) and the satellite/user geometry, which may vary in time. Consequently, the outputs of the RAIM fault detection (FD) algorithm are also correlated.

Depending on the position error, FD outputs give place to four possible events: correct detection, false detection, correct non-detection and missed detection (Figure 2.3). The occurrence of this events have a correlation time derived from the position error correlation.

In the context of this work, two estimated positions are independent if they provide independent RAIM outputs.

Correlated positions do not provide additional information. Thus, geo-object recognition algorithms only process independent positions.

Table 3.11. Events related to the Fault Detection process.

		FD output	
		No Detection	Detection
Positioning Error	No Positioning failure ($ e_H \leq HAL$)	Correct Non-Detection	False Detection
	Positioning failure ($ e_H > HAL$)	Missed Detection	Correct Detection

3.6.4. Geo-object Recognition Algorithm

The inputs of the segment detection algorithm are the estimated positions with their integrity information and a digital map with the geo-object boundaries.

Figure 3.10 represents the two cases the algorithm has to deal with: detecting users when they cross a road segment, and not charging them for unused segments even when they drive close to them. In both cases, estimated positions can be declared valid or non-valid by the RAIM and may contain positioning failures that can mislead the recognition algorithm.

The geo-object recognition algorithm will use only positions declared valid by the RAIM. This selection process assures that the probability that a chosen sample contains an undetected position failure is below a certain limit. The following detection rule is proposed. The algorithm decides that a user has been inside the road segment if the number of independent positions declared valid by the RAIM inside the geo-object ($N_{\text{valid positions IN}}$) is equal to or higher than a threshold:

$$\text{user inside route segment} \Leftrightarrow N_{\text{valid positions IN}} \geq N_{Th} \quad (3.6)$$

where the threshold N_{Th} is tuned according to the application requirements. Indeed, incrementing the N_{Th} decreases the probability of false segment recognition, but increments the probability of missed detection, as more valid positions are needed.

In this algorithm, an valid position inside a geo-object triggers the recognition process. Then, all the independent valid positions lying inside the geo-object, that can be considered from the same trajectory of the user through the road segment, are collected in a position set (Figure 3.11). When the position set is closed because next estimated positions cannot be considered of the same user trajectory along the road section under study, the number of positions in the set is compared with the threshold to decide whether the user has been inside the road segment or not.

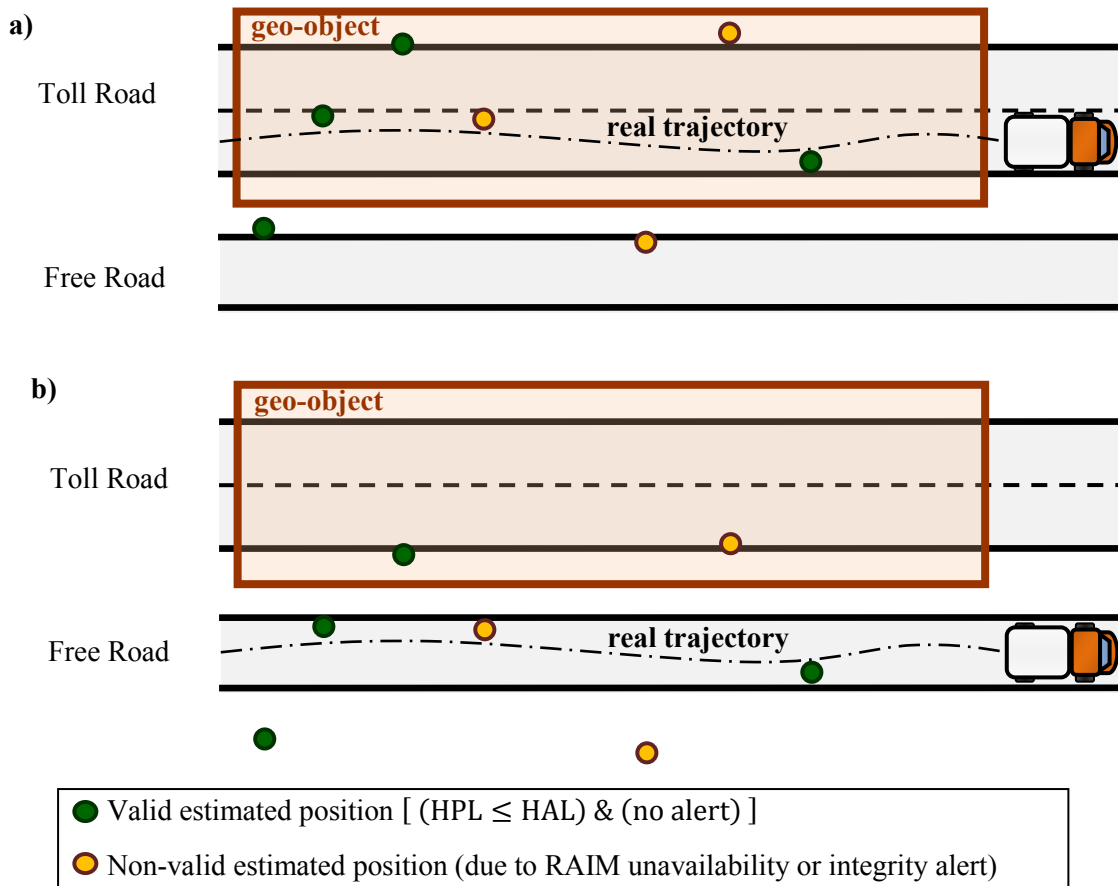


Figure 3.10. Examples of user trajectories and GNSS positioning & integrity data provided.

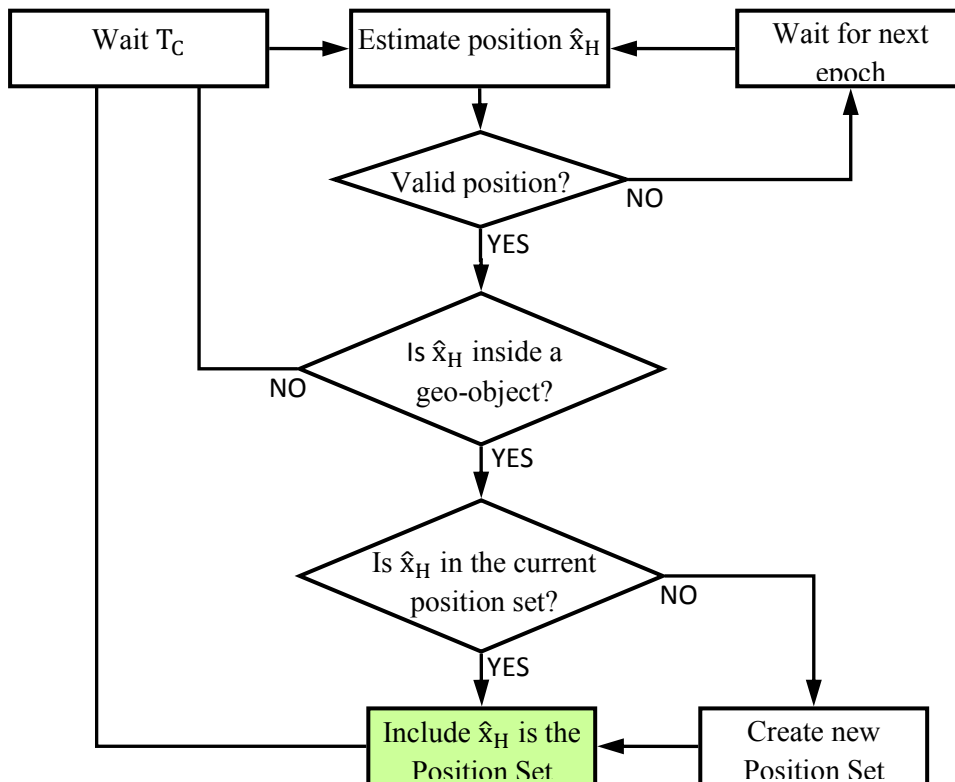


Figure 3.11. Creation of the position set used in the geo-object recognition algorithm.

The probability of a missed or false geo-object recognition depends on the probability of positioning failures and upon the number of independent valid positions per segment, which in turns depends on the user trajectory, the positioning error correlation time, the RAIM algorithm and the user/satellite geometry.

Other geo-object recognition algorithms could be proposed, for example:

$$\text{user inside route segment} \Leftrightarrow \begin{cases} N_{\text{valid pos IN}} \geq N_{\text{Th,in}} \\ N_{\text{valid pos OUT}} < N_{\text{Th,out}} \end{cases} \quad (3.7)$$

Nevertheless, algorithm (3.7) poses the problem of proving which estimated positions can be included in the position set used in the recognition process of a given road segment. For instance, the positions estimated between the first and last ones lying inside the geo-object could be taken, but this method could lose some valid samples outside the geo-object.

Other algorithms could integrate other information like direction of the vehicle, route segments previously used, etc.

The road segment recognition algorithm of eq.(3.6) is chosen because of its versatility due to the possibility of adapting the threshold to the application needs, and the simple selection of the positions used by the recognition process.

3.7. Conclusions

Different applications need different GNSS integrity monitoring techniques and requirements; therefore, a general GNSS integrity solution for any application in urban environments cannot be provided. Electronic toll collection systems based on GNSS positioning (GNSS-ETC) in urban environments has been chosen as the target application of this work because of the interest that has attracted, as proves the EU Directive 2004/52/EC that establishes the bases of European Electronic Toll Services (EETS).

GNSS-ETC is a liability critical application that needs GNSS integrity in order to limit the effects of undercharging and overcharging toll invoices.

The different augmentation systems capable of providing GNSS integrity monitoring have been analyzed, concluding that ABAS is the most adequate because it is easily extensible to multi-constellation receivers, it does not require additional infrastructure, and it is capable of detecting failures generated in the user's immediate environment.

A snapshot WLS navigation solution estimator with snapshot RAIM algorithms are chosen in this thesis in order to avoid recursive loops and to assure full control of the integrity monitoring process at each instant. External altitude information can be incorporated by means of a barometer or cartographic information. Although SBAS integrity as defined in civil aviation standards will not be directly used in the electronic toll application, SBAS corrections are still applicable.

The toll computation is based on a segmentation of the road network, so the total amount charged to a user is the sum of the price of the segments contained in its trajectory. Geo-fencing has been proven to be a suitable segmentation technique. The relation between the road network, the geo-object boundaries and the HAL has been explained.

A dual constellation GPS/Galileo receiver is proposed for urban environments. Single constellation receivers are also considered in less stringent scenarios. Different GNSS signals and several suitable receiver configurations have been proposed, including single and dual frequency receivers.

Geo-object recognition is one of the main tasks of GNSS toll systems, consisting in deciding whether a user has driven through a road segment or not in order to charge it. The RAIM decides which estimated positions are valid to be used in the algorithm in order to obtain reliable segment recognitions. A geo-object recognition algorithm based on the number of independent positions inside the geo-object is proposed.

Chapter 4

Pseudorange Measurement Model

4.1. Introduction

The pseudorange measurement model is a mathematical description of pseudorange measurements that characterizes their nominal errors and faults. The measurement model is a key input in the design of GNSS integrity monitoring mechanisms and their posterior performance prediction.

Pseudorange measurement degradations are classified into two categories: nominal errors and faults. Nominal errors are those present when all GNSS segments are working according to their specifications and the magnitudes of other external error sources are within their typical range. Faults are those errors not considered in the nominal case. For example, pseudorange errors due to residual ionospheric delays within their regular values (the ionosphere is not disturbed, for instance, by a magnetic storm) are nominal errors, while pseudorange biases caused by a satellite clock malfunctions are faults.

Pseudorange measurements are expected to be constantly contaminated by nominal errors, while pseudorange faults are punctual events.

This chapter presents a pseudorange measurement model suitable for integrity applications in urban road environments. First, the linear equations that link pseudorange measurements with the navigation solution are presented. Afterwards, nominal errors are presented and derived. Finally, the faulty measurement case is described.

4.2. Measurement Equation System

The relationship between pseudorange measurements and the navigation solution at a given instant is non-linear, but can be approximated with the following linear equation system (Appendix A):

$$\Delta Y = H \cdot \Delta X + E \quad (4.1)$$

where:

- ΔY : pseudorange measurement vector after linearization [$N \times 1$]
- ΔX : navigation solution vector after linearization [$N_u \times 1$]
- H : observation matrix [$N \times N_u$]
- E : pseudorange measurement error vector [$N \times 1$]

with:

- N : number of pseudorange measurements
- N_u : number of unknowns in the navigation solution

Pseudorange measurement errors are the addition of nominal errors and other faults not included in the nominal model:

$$E = \varepsilon + B \quad (4.2)$$

where

- ε : nominal error vector $[N \times 1]$
- B : fault vector $[N \times 1]$

The observation matrix H is a function of the user/satellite geometry and the navigation solution vector (Appendix A). It can be designed to describe the user position either in latitude, longitude and height coordinates, or in the north, east and up coordinates of the user's local frame.

4.3. Nominal Error Model

The nominal error model characterizes the pseudorange measurement errors that are present when all GNSS segments are working according to their specifications and the magnitudes of other external error sources have typical values.

Nominal errors are modelled as zero-mean independent Normal distributions in civil aviation standards, and GNSS integrity mechanisms are commonly designed under this assumption. For instance, residual pseudorange error models provided by SBAS describe zero-mean Gaussian distributions. Nominal errors in urban environments will also be modelled as zero-mean independent normal distributions because of the following reasons: first, the reliability of this type of model has been validated with the stringent requirements of civil aviation, so it is suitable for integrity applications; second, it is the assumed error distribution of civil aviation integrity monitoring systems; third, it is compatible with SBAS residual error models. Therefore, the mathematical model of nominal errors in urban environments is:

$$\varepsilon \sim N(0, \Sigma) \quad (4.3)$$

where

$$\Sigma = \text{cov}(\varepsilon) = \begin{pmatrix} \sigma_1^2 & 0 & \dots & 0 \\ 0 & \sigma_2^2 & & \vdots \\ \vdots & & \ddots & 0 \\ 0 & \dots & 0 & \sigma_N^2 \end{pmatrix} \quad (4.4)$$

Because nominal pseudorange errors are not exactly described by zero-mean normal random variables, the model provides instead a conservative normal distribution, obtained with overbounding techniques, that bounds the real error distribution. For instance, the definition of a CDF overbounding distribution is [De Cleene, 2000]:

$$\begin{aligned} \text{cdf}_o(x) &\geq \text{cdf}_e(x) & \forall x \leq 0 \\ \text{cdf}_o(x) &\leq \text{cdf}_e(x) & \forall x \geq 0 \end{aligned} \quad (4.5)$$

where cdf_0 is the overbounding CDF (zero-mean normal distribution) and cdf_e is the real CDF of the error. CDF overbounding requires the original error distribution to be symmetric and unimodal.

Summarizing, the nominal pseudorange error model consist of independent, overbounding zero-mean normal distributions, so it can be described by the variance. For the i^{th} pseudorange measurement:

$$\varepsilon_{ii} \sim N(0, \sigma_i^2) \quad (4.6)$$

4.3.1. Error Sources

Following a similar approach as in civil aviation [RTCA,2006], pseudorange nominal errors are formulated as the result of various independent error sources that can be analyzed separately.

Five error sources have been identified in road urban environments in the nominal case: inaccuracy of the broadcasted satellite clock corrections and ephemeris errors, ionospheric delay, tropospheric delay, receiver thermal noise (plus interferences) and multipath. The error sources are independent from each other because of their different nature.

The pseudorange errors caused by each independent source are modelled with a zero-mean normal distribution that overbounds the real error distribution. For the i^{th} satellite:

$$\varepsilon_{\text{clk \& eph},i} \sim N(0, \sigma_{\text{clk \& eph},i}^2) \quad (4.7)$$

$$\varepsilon_{\text{iono},i} \sim N(0, \sigma_{\text{iono},i}^2) \quad (4.8)$$

$$\varepsilon_{\text{tropo},i} \sim N(0, \sigma_{\text{tropo},i}^2) \quad (4.9)$$

$$\varepsilon_{\text{noise},i} \sim N(0, \sigma_{\text{noise},i}^2) \quad (4.10)$$

$$\varepsilon_{\text{mp},i} \sim N(0, \sigma_{\text{mp},i}^2) \quad (4.11)$$

where:

- $\varepsilon_{\text{clk \& eph},i}$ is the model of pseudorange errors at the i^{th} satellite due to the inaccuracy of the broadcasted satellite clock and ephemeris, with variance $\sigma_{\text{clk \& eph},i}^2$
- $\varepsilon_{\text{iono},i}$ is the model of pseudorange errors at the i^{th} satellite due to the ionospheric delay residual error, with variance $\sigma_{\text{iono},i}^2$
- $\varepsilon_{\text{tropo},i}$ is the model of pseudorange errors at the i^{th} satellite due to the tropospheric delay residual error, with variance $\sigma_{\text{tropo},i}^2$
- $\varepsilon_{\text{noise},i}$ is the model of pseudorange errors at the i^{th} satellite due to thermal noise and interferences, with variance $\sigma_{\text{noise},i}^2$
- $\varepsilon_{\text{mp},i}$ is the model of pseudorange errors at the i^{th} satellite due to multipath, of variance $\sigma_{\text{mp},i}^2$

The total pseudorange nominal error is the convolution of the five independent error sources, so its model is an overbounding zero-mean normal distribution of variance equal to the sum of the variances of each error component. The nominal error model of the i^{th} satellite is:

$$\varepsilon_{ii} = \varepsilon_{\text{clk \& eph},i} * \varepsilon_{\text{iono},i} * \varepsilon_{\text{tropo},i} * \varepsilon_{\text{noise},i} * \varepsilon_{\text{mp},i} \quad (4.12)$$

$$\varepsilon_{ii} \sim N(0, \sigma_{\text{PSR},i}^2) \quad (4.13)$$

$$\sigma_{\text{PSR},i}^2 = \sigma_{\text{clk \& eph},i}^2 + \sigma_{\text{iono},i}^2 + \sigma_{\text{tropo},i}^2 + \sigma_{\text{noise},i}^2 + \sigma_{\text{mp},i}^2 \quad (4.14)$$

The different error sources are studied in the following subsections in order to obtain the total pseudorange error model.

Certain nominal error sources identified in urban environments are also present in aviation and have standardized models in the civil aviation framework. In these cases, the aviation models will be applied because they have been thoroughly tested for safety-of-life applications.

Other nominal error sources depend on the environment or on the receiver characteristics and need to be modeled specifically for urban road applications.

4.3.2. Satellite Clock and Ephemeris Errors

The inaccuracy of data provided by the GNSS space and control segments, principally of the satellite clock corrections and the ephemeris, constitute a nominal pseudorange error source. Despite the use of high performance clocks on board of satellites, clock drifts cause discrepancies between the GNSS time estimated by the user and the real one. Satellite clock corrections supplied in the navigation message contribute to reduce this time error, although a residual error remains. Moreover, satellite trajectories calculated by users from the ephemeris broadcasted in GNSS navigation messages are not exact. The error model $\varepsilon_{\text{clk \& eph}}$ describes pseudorange errors due to the joint effect of inexact ephemeris and satellite clock residual errors.

The accuracy of the ephemeris and satellite clock corrections depends on the GNSS, which in this study can be GPS or Galileo. Besides, GNSS ground and space segments performance is expected to improve in time, so different modernization levels have different error models. Additionally, SBAS provides corrections to reduce ephemeris and satellite clock errors.

Thus, the error model has to be adapted to the following three cases:

- 1) GPS (different modernization stages)
- 2) Galileo
- 3) SBAS corrections

4.3.2.1. GPS

The User Range Accuracy (URA) is a statistical measure of the GPS range errors for which the space and control segments are responsible, excluding errors due to the user equipment and transmission media [ARINC, 2006], [ARINC, 2005], [SAIC, 2008]. It is broadcasted in the GPS navigation message for each satellite. In particular, the URA is a one-sigma (1σ) estimate of the satellite's signal-in-space (SIS) user range error (URE), applicable to every signal transmitted by the satellite. GPS sends an alert flag whenever the URA may be worse than indicated.

The GPS SPS SIS integrity standard concedes the URA certain integrity significance. In particular, the SIS URE of single frequency C/A code measurements from healthy satellites are assured to surpass the not-to-exceed (NTE) tolerance, without a timely warning during any hour of normal operations,

with a probability lower than 10^{-5} /hour/satellite. The NTE tolerance is defined to be ± 4.42 times the upper bound of the currently transmitted URA [DoD, 2008]:

$$p\{\text{SIS URE} > \pm 4.42 \cdot \text{URA}\} \leq 10^{-5}/\text{hour/satellite} \quad (4.15)$$

Future GPS-III will reduce the probability to 10^{-8} /hour/satellite with a NTE tolerance of $\pm 5.73 \cdot \text{URA}$ and a TTA of 5.2 seconds [Kovach, 2008].

The URA of modernized GPS signals has been interpreted as the standard deviation of the zero-mean normal distribution that overbounds the satellite's range error up to the $1 - 10^{-5}$ quantile [Lee and McLaughlin, 2007]. In fact, the probability that a zero-mean normal variable exceeds ± 4.42 times its standard deviation is 10^{-5} , and to exceed ± 5.73 times its standard deviation is 10^{-8} :

$$x \sim N(0, \sigma^2) \Rightarrow p\{|x| > 4.42 \cdot \sigma\} = 10^{-5}; p\{|x| > 5.73 \cdot \sigma\} = 10^{-8} \quad (4.16)$$

For these reasons, the standard deviation of the pseudorange error model due to satellite clock and ephemeris inaccuracies is set to be equal to the satellite's URA.

A URA index indicating a URA range is transmitted for each satellite. Sixteen pre-fixed intervals have been defined for current L1 C/A signals, being the lowest one $0.0 < \text{URA} \leq 2.4$ m. Since the error model must overbound the real error distribution, the upper bound is taken. Therefore, the minimum possible error model of current L1 C/A receivers is $\sigma_{\text{clk} \& \text{eph}} = 2.4$ metres.

Modernized GPS signals broadcast satellite clock URA and ephemeris URA independently. In order to account for improved ranging performance, 16 new segments below 2.4 metres have been added to the segments already defined for L1 C/A, being the lowest one $0.0 < \text{URA} \leq 0.01$.

The user is assumed to use the most recent clock corrections, so additional parameters that degrade clock-URA according to the time elapsed since the last correction are neglected.

The nominal error is used to design the RAIM algorithm and to predict its performance, so it should depend on nominal values of the URA and not on the particular value assigned to a satellite at a given instant.

Several nominal values of URA have been proposed in various studies. A nominal URA of 3.9 metres has been proposed for RAIM analysis with current L1 C/A signals [Have, 2003]. A URA of 1.5 metres has been derived from the modernized GPS specifications [Kovach, 2000]. The GPS evolutionary architecture study (GEAS) used URA values between 1 and 0.3 metres to predict the performance of RAIM in the future [Lee and McLaughlin, 2007]. Assuming that modernized GPS and Galileo performance will be equivalent, the standard deviation of the model is set to be equal to 0.85 metres, the maximum allowed Galileo SISA (although URA and SISA definitions are somewhat different).

Summing up, the standard deviation of the nominal error model is:

$$\sigma_{\text{clk} \& \text{eph}} = \begin{cases} 3.9 \text{ m.} & \text{in current GPS} \\ 1.5 \text{ m.} & \text{in early modernization stage} \\ 0.85 \text{ m.} & \text{in advanced modernization stage} \end{cases} \quad (4.17)$$

4.3.2.2. Galileo

The Galileo integrity concept defines the SISA (Signal In Space Accuracy) as the predicted minimum standard deviation of the normal distribution that overbounds the SISE (Signal In Space Error) distribution for fault-free SIS [Oehler et al., 2004].

Although Galileo OS navigation messages have the capability of transmitting the SISA, a SISA for Galileo OS has not been defined yet. Despite this fact, Galileo OS performance will be assumed to be described by the SISA.

The SISA accounts for ephemeris and satellite clock errors, so the standard deviation of the pseudorange error model due to satellite clock and ephemeris inaccuracies is set to be equal to the satellite's SISA.

The SISA must be lower than 0.85 metres in order to meet the Galileo RAMS (Reliability, Availability, Maintainability, and Safety) requirements [Oehler et al., 2004]. Thus, the standard deviation of the nominal error model is:

$$\sigma_{\text{CLK \& eph}} = 0.85 \text{ m} \quad (4.18)$$

4.3.2.3. SBAS

SBAS provides satellite clock and ephemeris corrections denoted as fast and long term corrections. The fast corrections apply to rapidly changing satellite clock errors, and the long term corrections refer to slower changing errors in the ephemeris and to the long term satellite clock errors.

SBAS broadcasts, together with the corrections, parameters to calculate a zero-mean normally distributed residual error model. The error variance is defined by the UDRE (user differential range error), transmitted at least once every 6 seconds, and degradation parameters that modify the model according to the time elapsed since the applicability instant of the used data. Assuming the user employs the most recent corrections, the standard deviation of the error model is equal to the UDRE.

The nominal value of the UDRE has been calculated with an EGNOS simulator at ENAC. Other SBAS are understood to have similar performance. The UDRE has been calculated along the trajectory of each satellite with a 1-minute temporal step during 24 hours, approximately the rotation period of GPS satellites (Figure 4.1). In general, the UDRE of most of the satellites visible from the EGNOS operational area is 0.3 m. Hence, the standard deviation of the nominal error model is:

$$\sigma_{\text{clk \& eph}} = 0.3 \text{ m.} \quad (4.19)$$

SBAS provides corrections for GPS. The same result will be extended to Galileo in order to analyze the potential of hypothetical modernized SBAS.

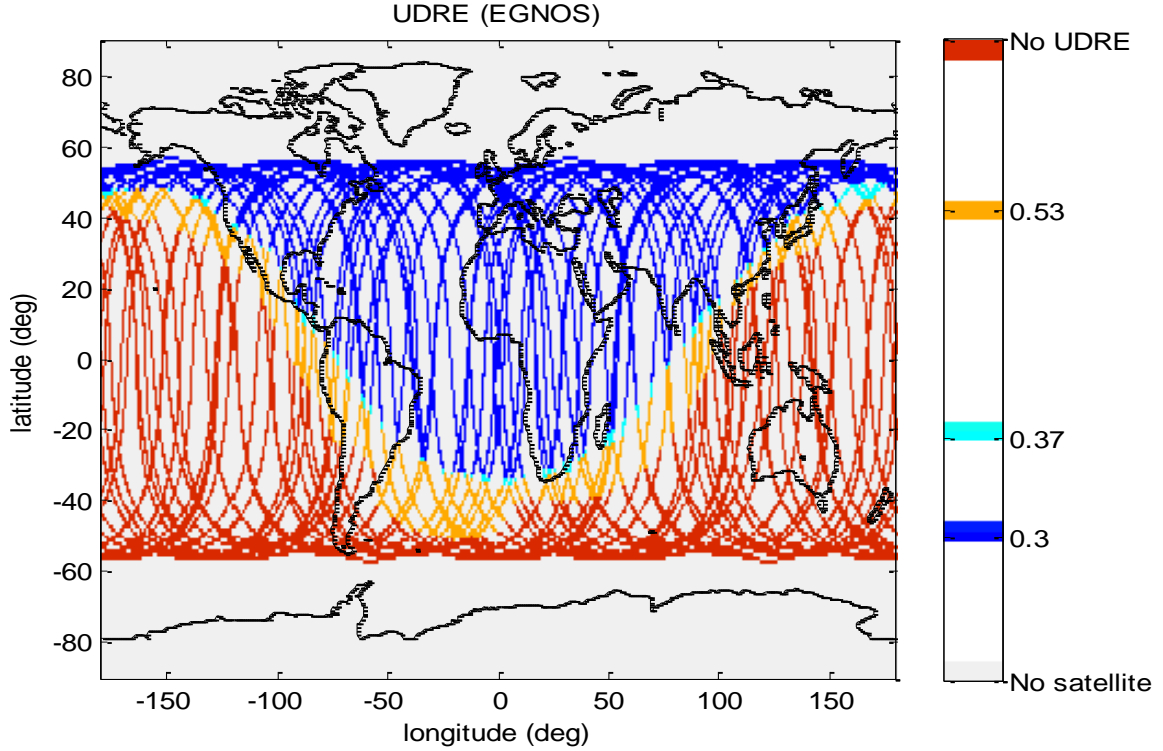


Figure 4.1. Map of the UDRE obtained with EGNOS.

4.3.3. Ionospheric Residual Error

The ionosphere is a dispersive medium, i.e. signals traversing it are delayed according to their frequency. The ionosphere has an opposite effect in the signal's code and phase delay, resulting in a group delay Δ (code delay) and a phase advance Δ_ϕ of the same magnitude and opposite sign. The first order model of the ionospheric delay is:

$$\Delta = -\Delta_\phi \approx \frac{40.3}{f^2} \cdot 10^4 \cdot \text{TEC} \quad [\text{m}] \quad (4.20)$$

where:

- f : signal frequency [MHz]
- TEC (Total Electron Content): electron density integrated along the ionospheric path followed by the signal [TECu; 1 TECu = $10^{16} \text{ e}^-/\text{m}^2$].

TEC measurements are denoted vertical TEC (VTEC) when the signal arrives at the user's zenith, and slant TEC (STEC) if the signal arrival angle is different to 90° .

GNSS receivers systematically apply correction algorithms to reduce the pseudorange errors introduced by the ionospheric delay. Different correction strategies are established in dual- and single-frequency receivers. Single-frequency receivers apply algorithms that predict the ionospheric delay with the ionospheric parameters supplied by the GNSS in the navigation message. Each system (GPS, Galileo, SBAS) has a different ionospheric correction algorithm with its own residual error. Dual-frequency receivers combine two pseudoranges measured from the same satellite to obtain a range measurement in which the first order ionospheric delay has been eliminated.

Thus, the error model has to be adapted to the following four cases:

- 1) GPS ionospheric corrections (Klobuchar model)
- 2) Galileo ionospheric corrections (NeQuick model)
- 3) SBAS ionospheric corrections
- 4) Dual-frequency receivers

Pseudorange errors due to ionospheric delay are identical in aviation and in urban environments, so the residual error models defined in civil aviation standards can be directly applied to urban applications.

4.3.3.1. Single-frequency GPS corrections

All GPS civil signals apply the Klobuchar ionospheric model to correct the ionospheric delay in single-frequency receivers, which is estimated to reduce at least 50 % of the single-frequency ionospheric delay RMS error [Klobuchar, 1987], [ARINC, 2006], [ARINC, 2005], [SAIC, 2008].

Let us depart from the residual error model standardized for civil aviation GPS L1 C/A airborne equipment when SBAS corrections are not available [RTCA, 2006]. The standard deviation of the error model is defined as 20% of the ionospheric delay predicted by the Klobuchar model, or a minimum error that depends on the user's latitude, whichever is larger:

$$\sigma_{iono} = \max(0.2 \cdot c \cdot T_{KI}, F_{SBAS} \cdot \tau_v) \quad (4.21)$$

where:

- c : the speed of the light in a vacuum ($2.99792458 \cdot 10^8$ m/s)
- T_{KI} : ionospheric delay correction calculated with the Klobuchar model from the GPS navigation message (s)
- F_{SBAS} : mapping function defined for SBAS corrections, see eq.(4.23).
- τ_v : minimum standard deviation of vertical errors (m)

$$\tau_v = \begin{cases} 9 \text{ m.} & 0 \leq |\phi_m| \leq 20 \\ 4.5 \text{ m.} & 20 \leq |\phi_m| \leq 55 \\ 6 \text{ m.} & 55 < |\phi_m| \end{cases} \quad (4.22)$$

where ϕ_m is the user's geomagnetic latitude.

The mapping function scales the ionospheric delay estimated for signals arriving at the user's zenith to other elevation angles. The following mapping function is defined in SBAS corrections:

$$F_{SBAS} = \left[1 - \left(\frac{R_e \cos \theta}{R_e + h_I} \right)^2 \right]^{-1/2} \quad (4.23)$$

where:

- θ : satellite's elevation angle
- R_e : approximate radius of the Earth's ellipsoid, $R_e = 6378.1363$ km
- h_I : height of the maximum electron density, $h_I = 350$ km

The mapping function F used in the Klobuchar corrections, as well as in the Galileo ionospheric residual error model, is different from that used in SBAS:

$$F = 1 + 16 \cdot \left(0.53 - \frac{\theta}{180}\right)^3 \quad (4.24)$$

The difference between F and F_{SBAS} is less than 3% for elevation angles higher than 3° (Figure 4.2).

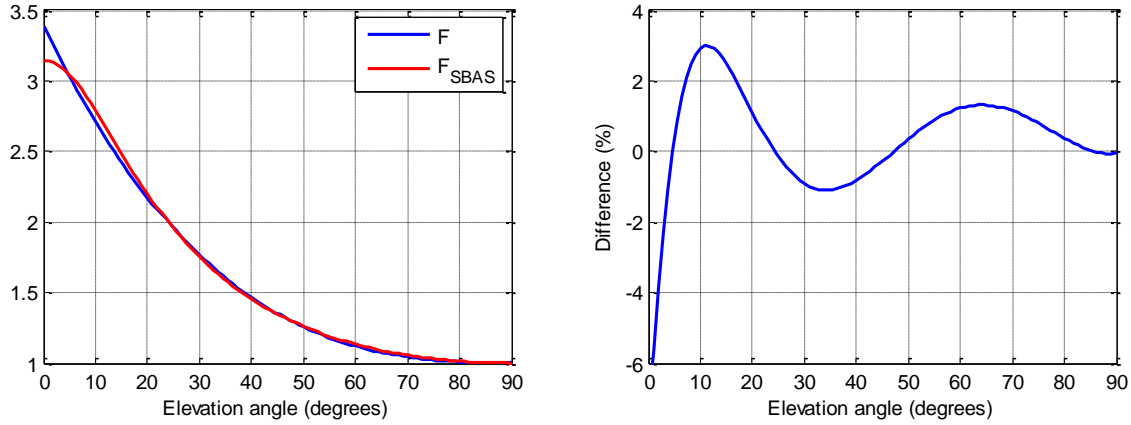


Figure 4.2. Comparison of the mapping functions F and F_{SBAS} .

Substituting F_{SBAS} by F in the original model (4.21):

$$\sigma_{\text{iono}} = F \cdot \max(0.2 \cdot \Delta_{\text{Kl},v}, \tau_v) = F \cdot \sigma_{\text{iono},v} \quad (4.25)$$

where $\Delta_{\text{Kl},v}$ is the vertical ionospheric delay estimated with the Klobuchar model in meters:

$$\Delta_{\text{Kl},v} = c \cdot T_{\text{Kl},v} = \frac{c \cdot T_{\text{Kl}}}{F} \quad (4.26)$$

Developing eq.(4.25):

$$\sigma_{\text{iono}} = \begin{cases} F \cdot \max(0.2 \cdot \Delta_{\text{Kl},v}, 9) & 0 \leq |\phi_m| \leq 20 \\ F \cdot \max(0.2 \cdot \Delta_{\text{Kl},v}, 4.5) & 20 \leq |\phi_m| \leq 55 \\ F \cdot \max(0.2 \cdot \Delta_{\text{Kl},v}, 6) & 55 < |\phi_m| \end{cases} \quad (4.27)$$

The error model depends on the value of the ionospheric correction currently applied by the user, which is a function of the correction parameters transmitted in the GPS navigation message, the user's position and time.

Expression (4.25) allows $\sigma_{\text{iono},v}$ to be obtained directly by comparing $\Delta_{\text{Klob},v}$ with τ_v . A historical series of vertical ionospheric corrections will be analyzed with the aim of setting a simplified, worst-case error model independent from the data currently used by the receiver.

Suitable values of $\Delta_{\text{Klob},v}$ have been obtained using the ionospheric corrections database prepared by the CTUP (Czech Technical University in Prague). It contains the ionospheric correction coefficients α and β broadcasted in GPS navigation messages since 1994, with a variable update rate of every several days, sufficient for following their temporal changes. The IGS (International GNSS Service) database also provides daily updated corrections parameters since 1997, but some inconsistencies were detected in the data from the years 1999-2001 and the wider time span covered by the CTUP database, the use of the latter has been preferred. Outside the 1999-2001 period, CTUP and IGS correction databases are similar.

GPS ionospheric corrections depend on the instant of the day, with a maximum at 14:00 local time. The daily maximum vertical ionospheric correction ($\Delta_{\text{Kl},v,\text{MAX}}$) has been obtained with the CTUP database and a 1-degree-step geomagnetic magnitude vector. For each geomagnetic latitude interval in which τ_v is defined, the highest correction magnitude is compared to the corresponding τ_v (Figure 4.3). During the studied time period, τ_v always exceeded the 20% of the maximum daily correction.

Thus, the residual ionospheric error model for single-frequency GPS L1 is in effect (Figure 4.4):

$$\sigma_{\text{iono}} = F \cdot \tau_v = \begin{cases} F \cdot 9 & 0 \leq |\phi_m| \leq 20 \\ F \cdot 4.5 & 20 \leq |\phi_m| \leq 55 \\ F \cdot 6 & 55 < |\phi_m| \end{cases} \quad (4.28)$$

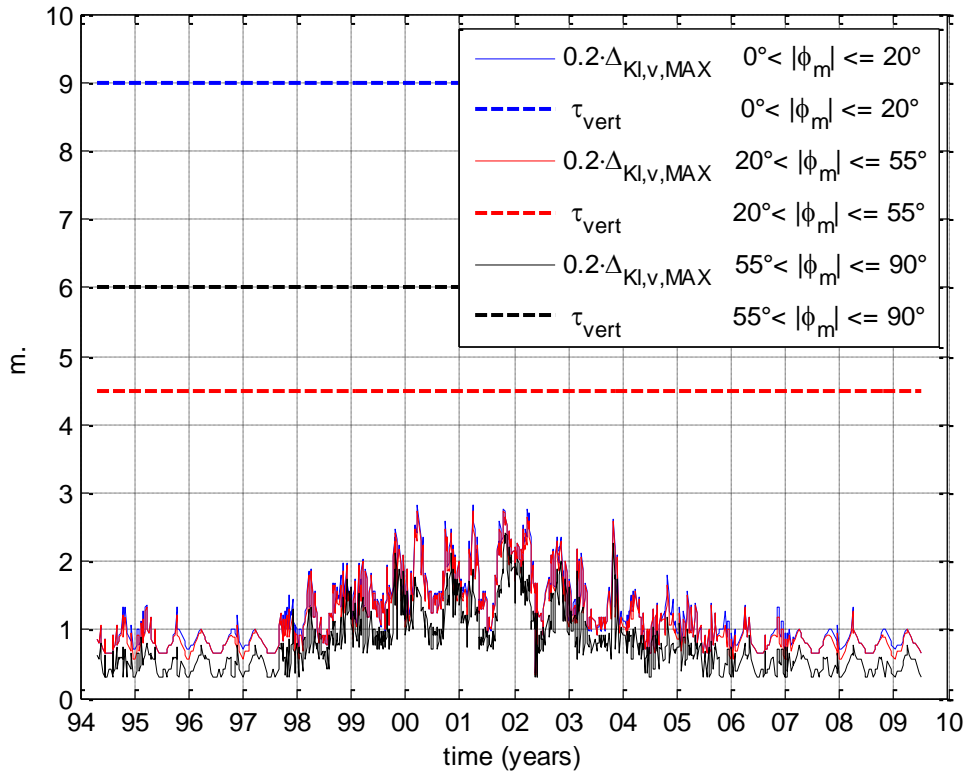


Figure 4.3. Graphical view of $\sigma_{\text{iono},v} = \max(0.2 \cdot \Delta_{\text{Kl},v}, \tau_v)$.

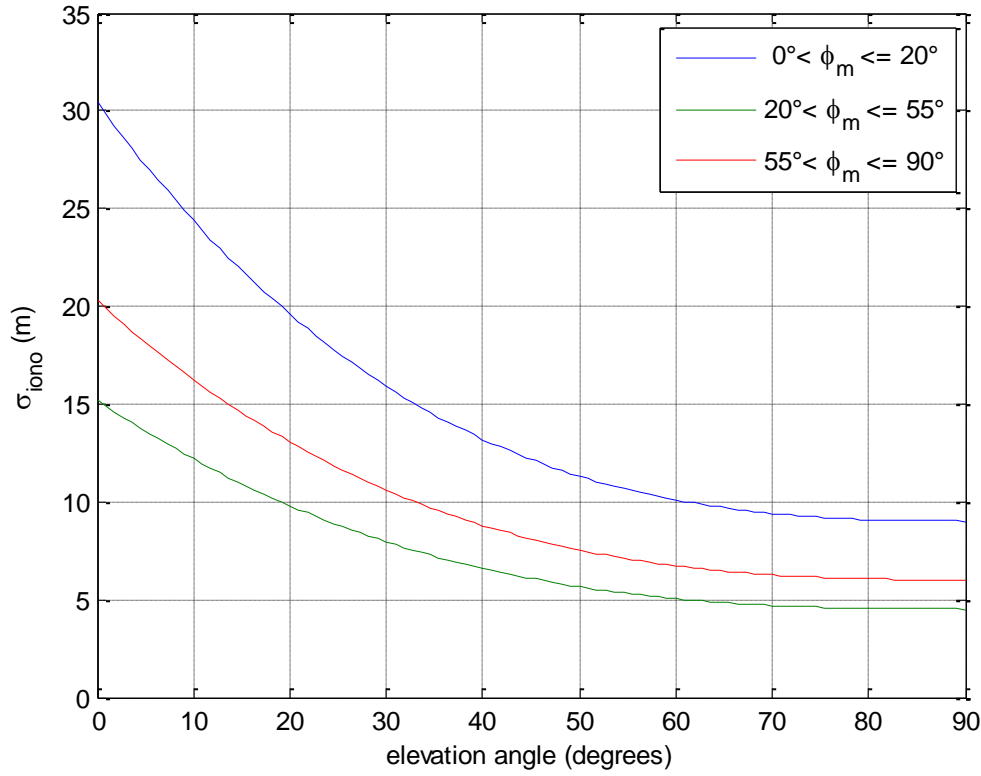


Figure 4.4. Ionospheric residual error model for single-frequency GPS L1.

Ionospheric corrections for L5 signals are obtained scaling the L1 corrections by $(f_{L1}/f_{L5})^2$, so the single-frequency residual ionospheric error model for GPS L5 is:

$$\sigma_{iono,L5} = \left(\frac{f_{L1}}{f_{L5}}\right)^2 \cdot \sigma_{iono,L1} = 1.79 \cdot \sigma_{iono,L1} \quad (4.29)$$

4.3.3.2. Single-frequency Galileo corrections

All Galileo OS signals will broadcast the same single-frequency ionospheric corrections based on the NeQuick model, assumed to correct at least 70 % of the ionospheric delay [Arbesser, 2006], [EU, 2010].

Civil aviation standards do not provide yet a ionospheric residual error model for single-frequency Galileo receivers. The Galileo TUSREQ (Test User Receiver Requirements) specifies that the residual error standard deviation of single-frequency receivers must not exceed 30% of the correction magnitude, or the equivalent first order delay of a 20-TECu STEC, whichever is larger [Arbesser, 2006]:

$$\sigma_{iono} = \max\left(0.3 \cdot \Delta_{NQ}, \frac{40.3}{f^2} \cdot 20 \cdot 10^4\right) \quad (4.30)$$

where:

- f : carrier frequency [MHz]

- Δ_{NQ} : NeQuick ionospheric delay estimation applied by the user, defined as the first order ionospheric delay calculated with the STEC estimated by the NeQuick algorithm [m]:

$$\Delta_{\text{NQ}} = \frac{40.3}{f^2} \cdot 10^4 \cdot \text{STEC}_{\text{NQ}} \quad (4.31)$$

The error model depends on the value of the ionospheric correction currently applied by the user. Historical series of Δ_{NQ} could be analyzed with the aim of setting a simplified, worst-case error model independent from the data currently used by the receiver. Nevertheless, as of year 2011, Galileo correction coefficients are not being transmitted yet and the use of historical databases is not possible. Thus, in order to estimate a data series of previous values of Δ_{NQ} , the STEC_{NQ} will be approximated as the VTEC scaled by the mapping function of (4.24). The advantage of this expression resides in the fact that VTEC is a well studied parameter with available databases of historical data:

$$\text{STEC}_{\text{NQ}} \approx F \cdot \text{VTEC} \quad (4.32)$$

The alternative ionospheric residual error model results:

$$\sigma_{\text{iono}} = \frac{40.3}{f^2} \cdot 10^4 \cdot \max(0.3 \cdot F \cdot \text{VTEC}, 20) \quad (4.33)$$

Equivalently:

$$\sigma_{\text{iono}} = \begin{cases} \frac{40.3}{f^2} \cdot 10^4 \cdot 0.3 \cdot F \cdot \text{VTEC}, & \text{if } \text{STEC} = F \cdot \text{VTEC} \geq 66.7 \\ \frac{40.3}{f^2} \cdot 10^4 \cdot 20, & \text{if } \text{STEC} = F \cdot \text{VTEC} < 66.7 \end{cases} \quad (4.34)$$

The model of eq.(4.33) has been satisfactorily assessed in [Rogers et al., 2005].

The IGS VTEC database has been used to compute the historical σ_{iono} series that would have been obtained in the previous years. The IGS provides worldwide VTEC data since 1998, approximately covering the 11-year solar period, updated every 2 hours with a 0.1 TECu accuracy [Hernández-Pajares et al., 2008].

First, the VTEC database position grid is converted from geographic into geomagnetic latitude, which describes better the ionospheric delay. The following conversion formula is applied [Klobuchar, 1987]:

$$\sin(\phi_m) = \sin(\phi) \cdot \sin(78.3^\circ) + \cos(\phi) \cdot \cos(78.3^\circ) \cdot \cos(\lambda - 291^\circ) \quad (4.35)$$

where ϕ_m is the geomagnetic latitude, ϕ the geographic latitude, and λ the longitude. Most of Europe is located between $40^\circ < \phi_m \leq 65^\circ$ (Figure 4.5).

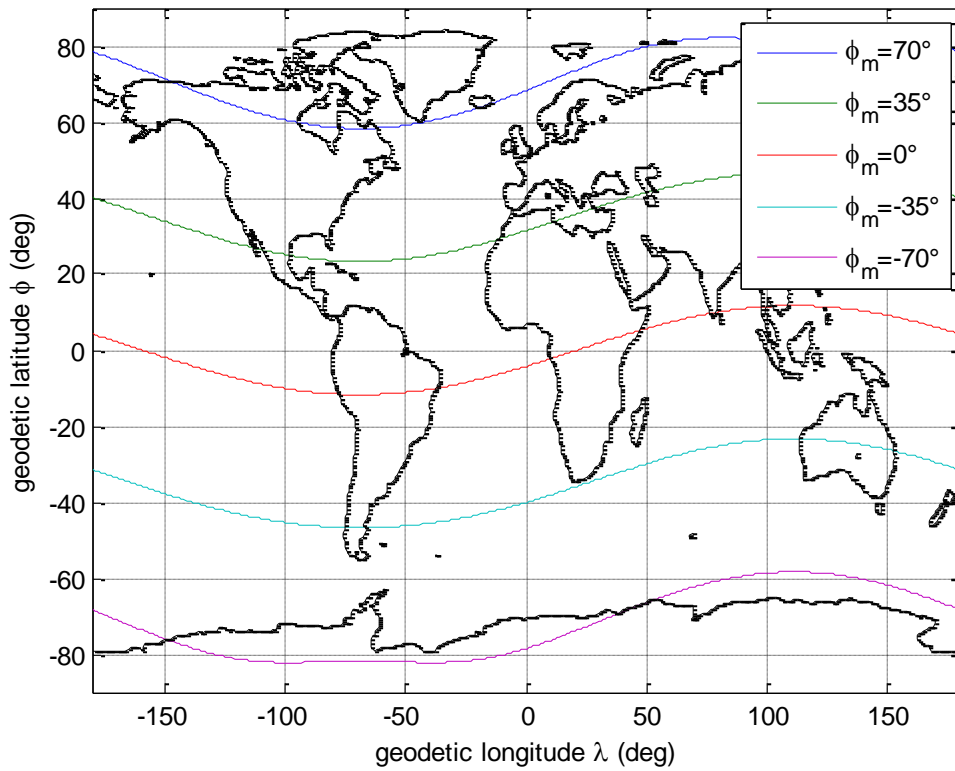


Figure 4.5. Geomagnetic latitude.

The VTEC presents daily variations with the maximum peak during day time and the minimum at night, as well as long term variations that depend on several factors, like the current phase of the solar cycle (Figure 4.6).

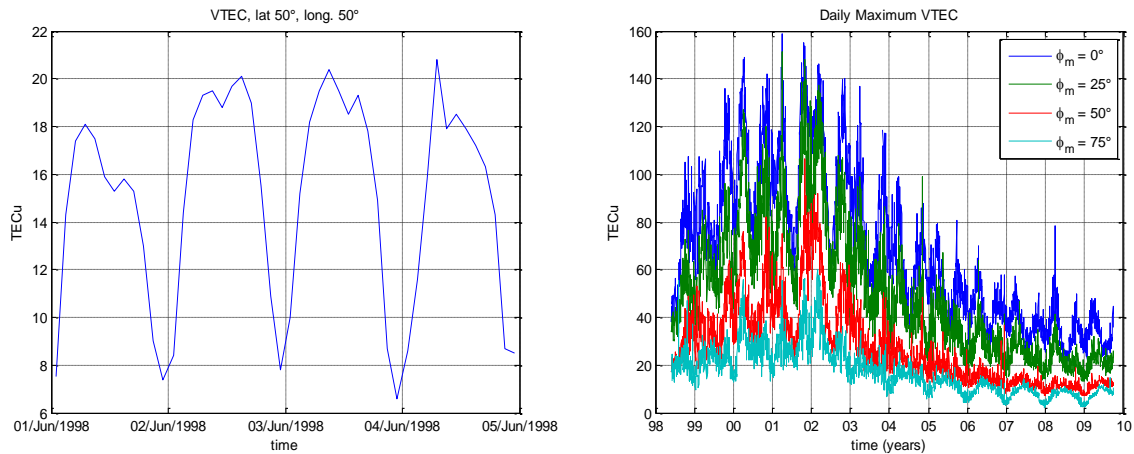


Figure 4.6. Example of VTEC daily and long term variations.

According to the historical data series, a tight model of σ_{iono} would be tailored to the time of the day or to the solar cycle. Nevertheless, a more general error model independent from the time is preferred, so it could be used in integrity analysis that would be valid regardless the instant of application. Thus, a function of σ_{iono} dependent only on $|\phi_m|$, the elevation angle and the carrier frequency is proposed.

Several percentile curves of the σ_{iono} for E1 signals received at the user's zenith have been obtained with the IGS VTEC database (Figure 4.7). The percentile 100% cannot be directly used because it includes sporadic VTEC magnitude spikes originated by multiple causes, like electromagnetic storms or possible data errors, that cannot be considered within the nominal case. The appropriate percentile depends on the application needs.

The proposed Galileo E1 residual ionospheric error model that bounds that of eq.(4.33) consists of the vertical error component $\sigma_{iono,v}$, obtained from the percentile 99.999% of Figure 4.7 at the user's geomagnetic latitude, scaled by the mapping function:

$$\sigma_{iono} = F \cdot \sigma_{iono,v} \quad (4.36)$$

The chosen percentile 99.999% means that at a given instant, the probability that the selected $\sigma_{iono,v}$ is lower than the true one is 0.001%. Let us remember that this percentage has been calculated with all the VTEC measurements included in the IGS database since 1998, so it is not restricted to nominal errors.

The ionospheric residual error of E5a signals is obtained scaling the model for E1:

$$\sigma_{iono,E5} = \left(\frac{f_{E1}}{f_{E5a}} \right)^2 \cdot \sigma_{iono,E1} = 1.79 \cdot \sigma_{iono,E1} \quad (4.37)$$

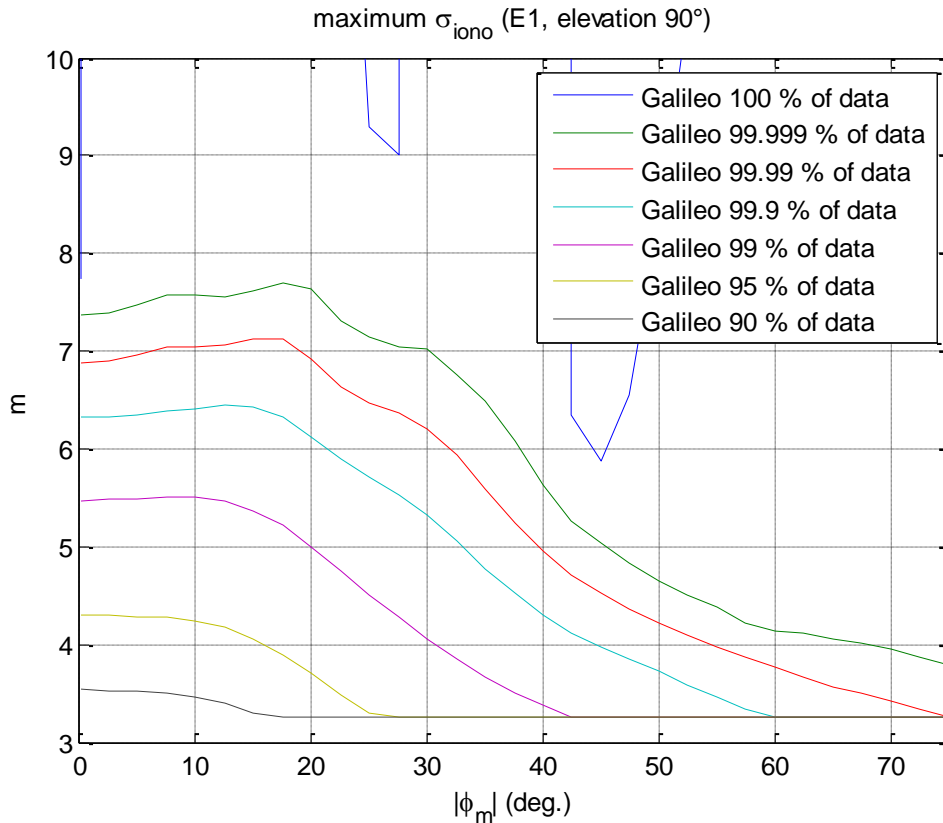


Figure 4.7. Percentiles of E1 $\sigma_{iono,v}$ obtained with all VTEC data.

4.3.3.3. SBAS ionospheric corrections

SBAS provides GPS L1 ionospheric delay corrections at fixed ionospheric grid points (IGP). It also supplies users with the GIVE (Grid Ionosphere Vertical Error), the standard deviation of the overbounding zero-mean normally distributed residual error model that remains after applying the corrections to signals received at the zenith of each IGP. Additional degradation parameters that adapt the error model when the user fails to use the most recent GIVE will be neglected in this study because the user is assumed to use the most recent corrections. In general, users are not exactly located on an IGP, and interpolate the GIVEs of neighbouring IGPs to calculate the vertical error model at their own position, called UIVE (User Ionosphere Vertical Error). Finally, the UIVE is scaled by the mapping function (F_{SBAS}) to include the effect of the satellite's elevation angle in order to obtain the UIRE (User Ionosphere Range Error), which is the standard deviation of the residual ionospheric residual error:

$$\text{UIRE} = F_{\text{SBAS}} \cdot \text{UIVE} \quad (4.38)$$

where F_{SBAS} is the mapping function defined in eq.(4.23):

$$F_{\text{SBAS}} = \left[1 - \left(\frac{R_e \cos \theta}{R_e + h_I} \right)^2 \right]^{-1/2}$$

The worst GIVE provided by EGNOS during a 24-hour period (approximately the ground track period of GPS satellites) has been calculated with an EGNOS simulator available at ENAC (Figure 4.8). Other SBAS have similar performance. The GIVE has been calculated with a 1-minute temporal step. The circles on Figure 4.8 represent EGNOS ground stations and red areas indicate the places where GIVE cannot be continuously provided. In general, the service is continuously available in most of Europe with:

$$\text{GIVE} = 0.46 \text{ m.} \quad (4.39)$$

Since worst case GIVE is the same all over Europe, the worst case UIVE is equal to the worst case GIVE. Thus, the standard deviation of the SBAS ionospheric residual error model is:

$$\sigma_{\text{iono}} = F_{\text{SBAS}} \cdot \text{UIVE} \quad (4.40)$$

$$\text{UIVE} = 0.46 \text{ m.} \quad (4.41)$$

SBAS provides corrections for GPS L1 signals. The same result will be extended to other frequency bands and GNSS (Galileo) to analyze the potential of hypothetical modernized SBAS.

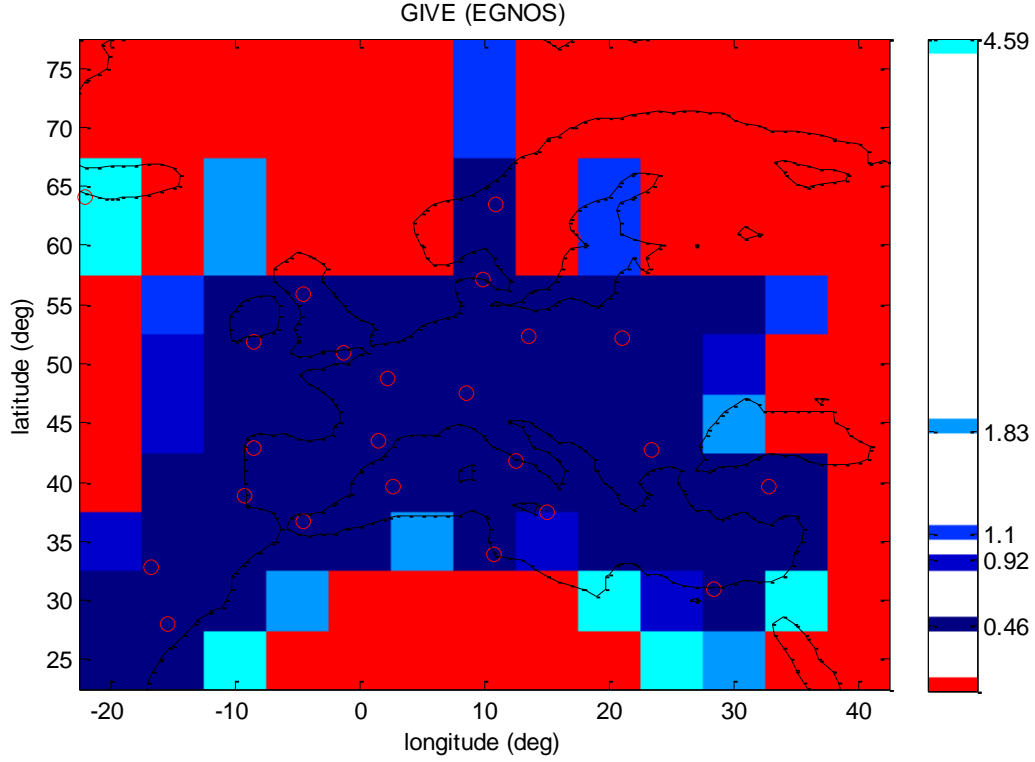


Figure 4.8. Worst GIVE obtained for EGNOS during 24 hours.

4.3.3.4. Dual-frequency iono-free measurements

Dual-frequency receivers measure the pseudorange to each satellite at two different frequencies and combine them to build a iono-free pseudorange measurement that removes the first order ionospheric delay. For a receiver working at the frequency bands A and B, the iono-free pseudorange is:

$$y_{\text{iono-free}} = k_A \cdot y_A + k_B \cdot y_B \quad (4.42)$$

where:

- $y_{\text{iono-free}}$: iono-free pseudorange combination
- y_A, y_B : pseudoranges measured at the frequency band A and B, respectively
- k_A, k_B : combination coefficients

$$k_A = \frac{f_A^2}{f_A^2 - f_B^2} \quad (4.43)$$

$$k_B = \frac{f_B^2}{f_B^2 - f_A^2} \quad (4.44)$$

- f_A : carrier frequency of the frequency band A
- f_B : carrier frequency of the frequency band B

Dual-frequency pseudorange combinations remove the first order ionospheric delay, but higher order errors remain. Nonetheless, their magnitude is insignificant compared to other error sources: for example, typical second order ionospheric delays are around 0 and 2 cm at the zenith, and the third

order ones, between 0 and 2 mm [Mainul-Hoque et al., 2007]. Thus, ionospheric effects of order higher than one are neglected:

$$\sigma_{\text{iono}} = 0 \quad (4.45)$$

The main drawback of iono-free pseudoranges is the amplification of the errors caused by thermal noise and multipath. Assuming these two error sources are independent at each frequency:

$$\sigma_{\text{noise,iono-free}}^2 = k_A^2 \cdot \sigma_{\text{noise,A}}^2 + k_B^2 \cdot \sigma_{\text{noise,B}}^2 \quad (4.46)$$

$$\sigma_{\text{mp,iono-free}}^2 = k_A^2 \cdot \sigma_{\text{mp,A}}^2 + k_B^2 \cdot \sigma_{\text{mp,B}}^2 \quad (4.47)$$

Noise amplification makes (L1, L2) and (L1/E1, L5/E5a,) and (E1,E5b) the only practical frequency pairs to build dual-frequency iono-free measurements (Table 4.1).

Table 4.1. Iono-free coefficients for different frequency pairs.

f_A	f_B	k_A^2	k_B^2
L₁ (1575.42 MHz)	L₂ (1227.6 MHz)	6.48	2.39
L₁, E₁ (1575.42 MHz)	L₅, E_{5a} (1176.45 MHz)	5.11	1.59
E₁ (1575.42 MHz)	E_{5b} (1207.14 MHz)	5.87	2.02
L₂ (1227.6 MHz)	L₅ (1176.45 MHz)	150.19	126.68
E_{5b} (1207.14 MHz)	E_{5a} (1176.45 MHz)	396.80	357.96

4.3.4. Tropospheric Residual Error

Tropospheric delay is a local phenomenon caused by tropospheric refraction. Therefore, neither standalone GNSS (GPS, Galileo), nor SBAS provide tropospheric delay corrections in the navigation messages. Instead, the user segment is responsible of estimating and correcting its own tropospheric delay. The tropospheric residual error only depends on the correction model applied by the user, which is independent from the GNSS or SBAS used. A suitable model should provide low residual error standard deviation with a low computational burden.

The UNB3 (University of New Brunswick) tropospheric delay model has been proven to provide the lowest residual error standard deviation among the most representative models proposed for GNSS applications [Collins, 1999]. Originally conceived for civil aviation WAAS receivers, the UNB3 is based on the zenith delay algorithms of Saastamoinen, the mapping functions of Niell and a table of atmospheric parameters extracted from the U.S. 1966 Standard Atmosphere Supplements (years 1987 – 1996).

The tropospheric delay model currently specified in [RTCA, 2006] for civil aviation GPS/WAAS airborne equipment is based on the UNB3, replacing the Niell mapping function by the computationally less exigent Black and Eisner (B&E) one. This change reduces the computational

burden at the expense of a delay over-prediction that could reach 30 cm. at elevation angles of 5° [Collins and Langley, 1999].

The tropospheric delay correction algorithm chosen for integrity urban applications is the standardized for civil aviation because of its compromise between residual error magnitude and computational cost.

The residual error model is a vertical error standard deviation of 12 cm. scaled by a mapping function [RTCA, 2006]. Therefore it is exclusively dependent upon the satellite's elevation angle θ (Figure 4.9):

$$\sigma_{\text{tropo}} = F_{\text{tropo}} \cdot \sigma_{\text{tropo},v} \quad (4.48)$$

where:

$$F_{\text{tropo}} = \begin{cases} \frac{1.001}{\sqrt{0.002001 + \sin^2 \theta}} & \text{for } \theta \geq 4^\circ \\ \frac{1.001}{\sqrt{0.002001 + \sin^2 \theta}} (1 + 0.015 \cdot (4^\circ - \theta)^2) & \text{for } 2^\circ \geq \theta > 4^\circ \end{cases} \quad (4.49)$$

$$\sigma_{\text{tropo},v} = 0.12 \text{ meters} \quad (4.50)$$

The overbounding capacity of the model (4.48) has been satisfactorily assessed in [Collins and Langley, 1999].

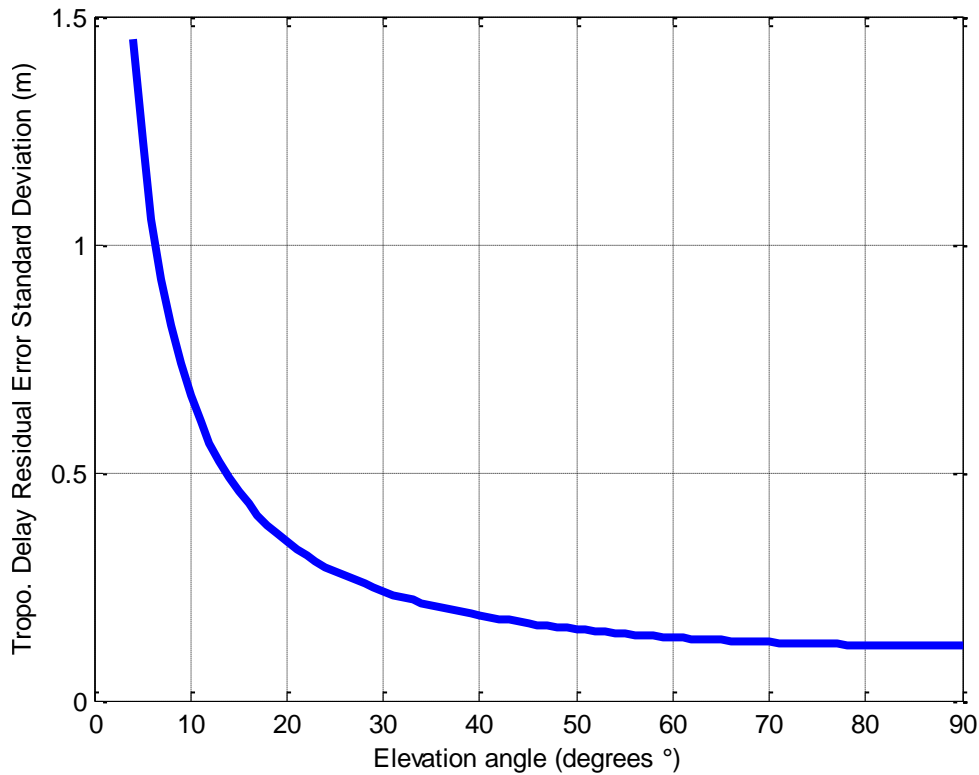


Figure 4.9. Residual tropospheric error model standard deviation.

4.3.5. Thermal noise and interferences

GNSS receivers must first acquire and track the signal broadcast by the GNSS satellite in order to measure its pseudorange. The signal acquisition mechanism computes a rough frequency and delay estimation of the received signal, while the tracking loops perform a fine estimation and follow the temporal signal variations. During the first stage of the tracking process, the PLL (Phase Lock Loop) or FLL (Frequency Lock Loop) wipe off the carrier of the incoming signal. Afterwards, the DLL (Delay Lock Loop) synchronizes the local code replica with the received one and computes the pseudorange.

The DLL's discriminator compares the Early, Late and Prompt correlator outputs to synchronise the code. Coherent discriminators only use the in-phase correlators, assuming a perfect phase alignment between the received and locally generated carrier. Non coherent discriminators use in-phase and quadrature components. Two non-coherent discriminators are widely used, Early minus Late Power (Δ_{E-L}) and Dot Product (Δ_{DP}).

Noise present at the receiver front-end perturbs the tracking process and causes pseudorange errors. The code tracking error variance of a limited bandwidth receiver with an E-L discriminator due to white Gaussian noise at its input is given by [Betz and Kolodziejewski, 2000]:

$$\sigma_{E-L}^2 = c^2 \cdot \frac{B_L(1 - 0.5 \cdot B_L T_I) \cdot \int_{-B/2}^{B/2} G_S(f) \sin^2(\pi f d) \cdot df}{\frac{C_S}{N_0} \left(\int_{-B/2}^{B/2} 2\pi f \cdot G_S(f) \sin(\pi f d) \cdot df \right)^2} \cdot \left[1 + \frac{\int_{-B/2}^{B/2} G_S(f) \cos^2(\pi f d) \cdot df}{\frac{C_S}{N_0} T_I \left(\int_{-B/2}^{B/2} G_S(f) \cos(\pi f d) \cdot df \right)^2} \right] \quad (4.51)$$

For a DLL with a DP discriminator, the code tracking error variance is given in [Julien, 2005]:

$$\sigma_{DP}^2 = c^2 \cdot \frac{B_L(1 - 0.5 \cdot B_L T_I) \cdot \int_{-B/2}^{B/2} G_S(f) \sin^2(\pi f d) \cdot df}{\frac{C_S}{N_0} \left(\int_{-B/2}^{B/2} 2\pi f \cdot G_S(f) \sin(\pi f d) \cdot df \right)^2} \cdot \left[1 + \frac{1}{\frac{C_S}{N_0} T_I \left(\int_{-B/2}^{B/2} G_S(f) \cdot df \right)^2} \right] \quad (4.52)$$

In both equations:

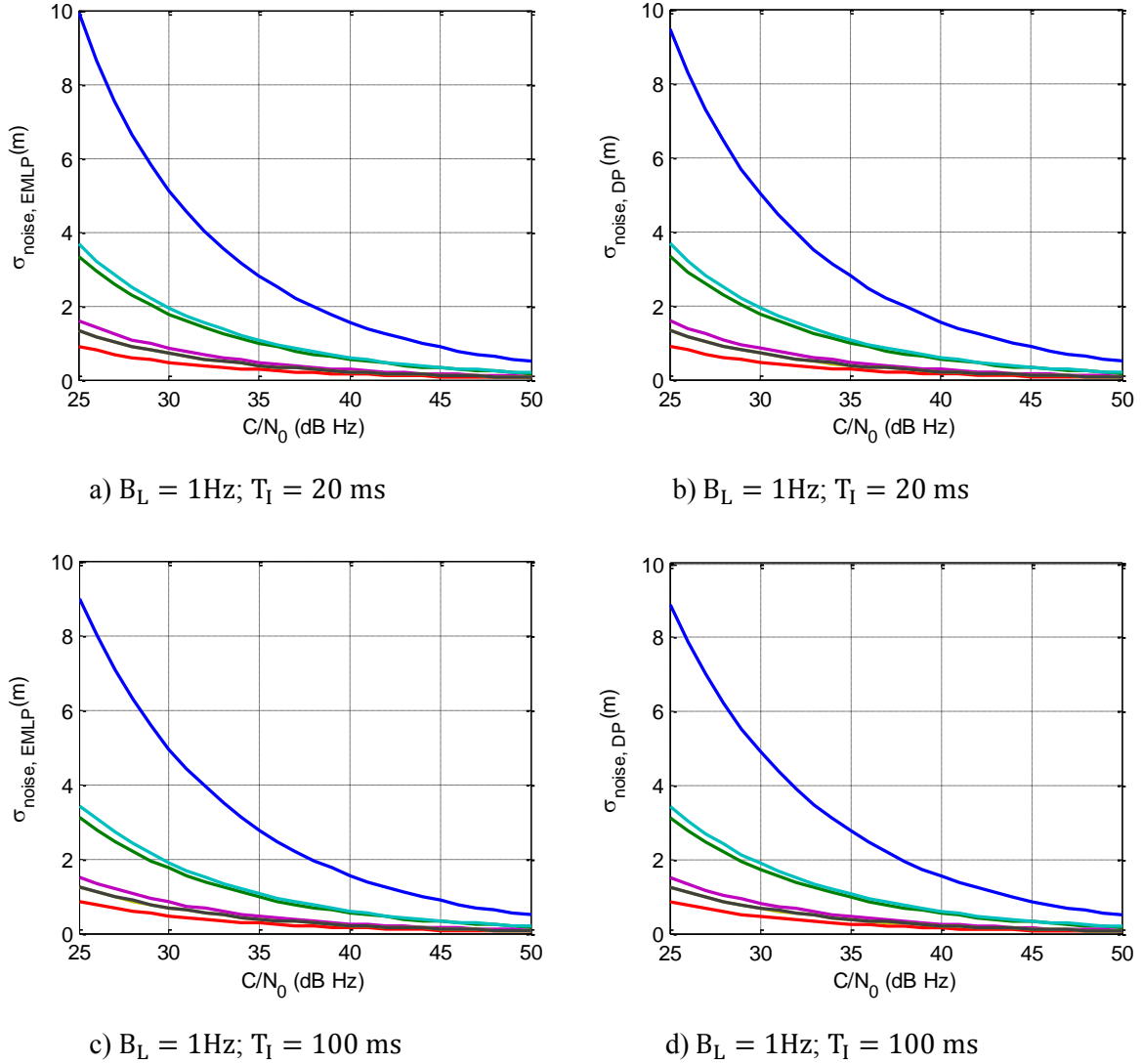
- B_L : is the one-sided equivalent rectangular bandwidth of the DLL [Hz]
- T_I : integration time [s]
- $G_S(f)$: signal power spectral density (PSD)
- C_S/N_0 : signal to noise ratio
- d : two-sided early-late spacing [chips]
- B : two-sided front-end bandwidth [Hz]
- c : speed of the light in the vacuum [m/s²]

The previous models are adequate when the digital tracking loops are derived from the analog loop model using an approximate analog-to-discrete transform. If they are designed directly in the digital domain, the term $(1 - 0.5 \cdot B_L T_I)$ is omitted.

Thus, the pseudorange error model due to noise and interferences depends on the discriminator:

$$\sigma_{\text{noise}} = \begin{cases} \sigma_{\text{E-L}} & \text{with an Early minus Late discriminator} \\ \sigma_{\text{DP}} & \text{with a Dot Product discriminator} \end{cases} \quad (4.53)$$

The standard deviation of the error model of different receiver types is plotted in Figure 4.10 as a function of C/N_0 , T_I and B_L .



— BPSK(1);	BW = 2 MHz;	$C_S = 1\text{ chip}$
— BPSK(1);	BW = 16 MHz;	$C_S = 0.1\text{ chip}$
— BPSK(10);	BW = 20 MHz;	$C_S = 0.25\text{ chip}$
— BOC(1,1);	BW = 4 MHz;	$C_S = 0.2\text{ chip}$
— CBOC(6,1,1/11,+);	BW = 14 MHz;	$C_S = 0.1\text{ chip}$
— CBOC(6,1,1/11,-);	BW = 14 MHz;	$C_S = 0.1\text{ chip}$
— TMSOC(6,1,4/33);	BW = 14 MHz;	$C_S = 0.1\text{ chip}$

Figure 4.10. Pseudorange error model due to thermal noise for various receiver configurations.

Pseudorange errors present a similar magnitude regardless the discriminator type, E-L or DP. In general, a narrower DLL bandwidth, or a longer integration time decreases the error. Concerning the signal performance, the most robust signals against noise effects are those that allocate the highest amount of power in higher frequencies, i.e. BPSK(10) followed by TMBOC and CBOC. After them, wideband BPSK(1) and BOC(1,1) receivers provide a similar standard deviation, approximately twice as the TMBOC or CBOC ones. As expected, 2MHz-band BPSK(1) receivers provide the poorest performance in terms of thermal noise effects.

The effect of interferences can be simulated with the thermal noise obtained by setting the C/N_0 at the loss-of-lock threshold of the tracking loops. As example, the lowest C/N_0 allowed in civil aviation vary between 29 dB and 36.5 dB.

4.3.6. Multipath

Urban environments typically present a high number of obstacles and reflecting surfaces, being scenarios rich in multipath, signal blocking and fading. This chapter describes a novel model of pseudorange error due to multipath for integrity-oriented vehicular applications in urban environments.

The error model has been calculated analysing, via Monte Carlo simulations, the pseudorange errors obtained by a GNSS receiver simulator processing signals that have been modified by the effects generated with a GNSS urban channel model. The subsequent scheme has been followed (Figure 4.11):

- 1) A database of the characteristics of received signal rays in urban environments has been calculated with an urban channel model specifically designed for GNSS users in an urban road scenario. The generated database consists of time series of the power, phase and delay of each LOS and NLOS rays of the signal received from a satellite situated at different elevation and azimuth angles.
- 2) The database of received rays is processed with a module that implements the receiver tracking loops and correlator to provide the pseudorange error and additional data like the PLL and DLL outputs. All the data are obtained before the coherent integration, at the same sampling rate as the channel database.
- 3) A lock detector based in PLL error and C/N_0 estimations decides which pseudorange error samples after the coherent integration correspond to instants in which the receiver is tracking the signal or not.
- 4) Finally, the pseudorange error samples selected by the lock detector are used to compute the standard deviation of the overbounding function.

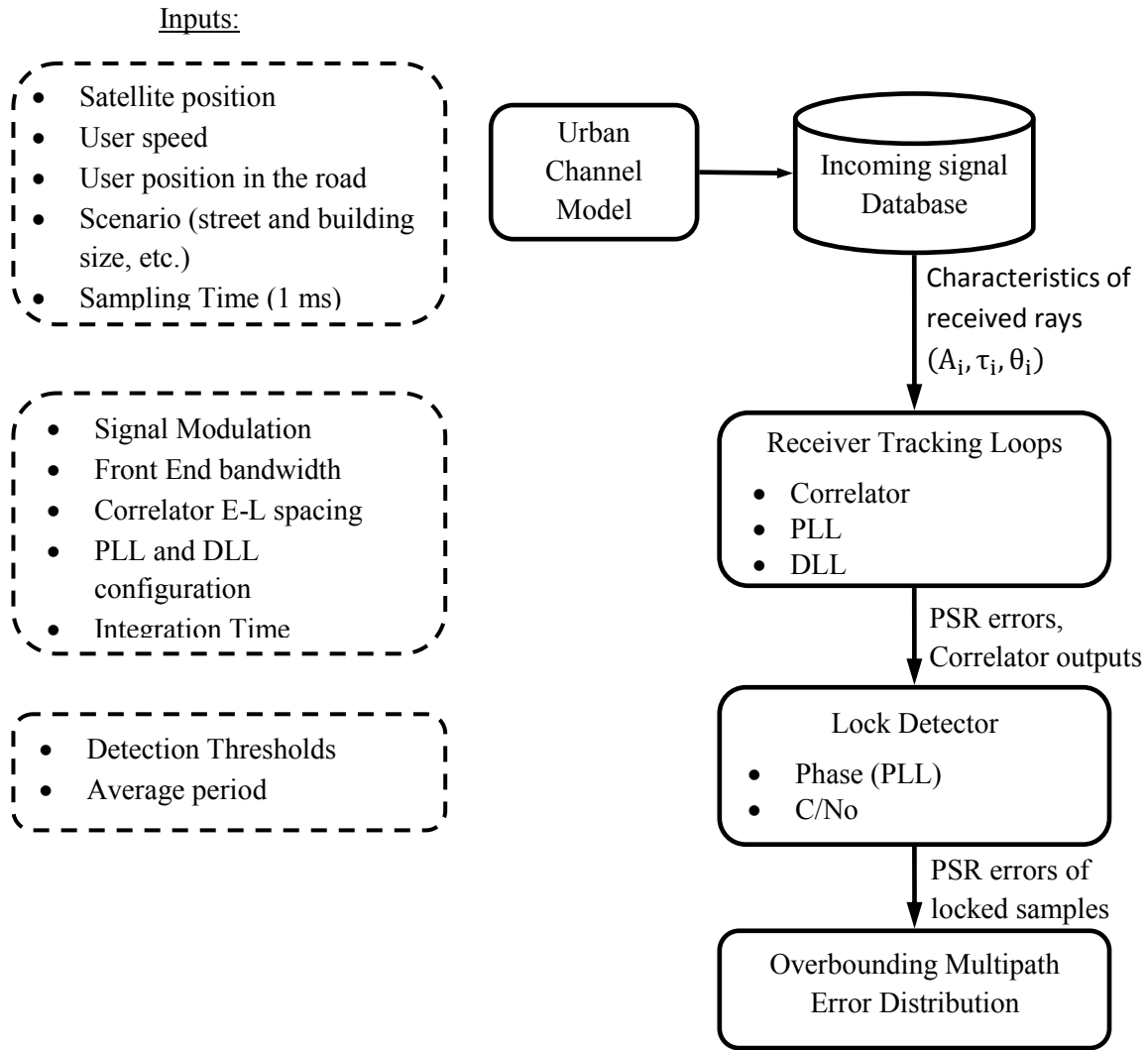


Figure 4.11. Scheme followed to calculate the multipath error model.

4.3.6.1. Urban Channel Model

A channel model specifically developed for GNSS applications in urban environments has been used to generate delay (τ_i), amplitude (A_i) and phase (θ_i) time series of each LOS and reflected ray received by the user [Lehner and Steingass, 2005], [Steingass and Lehner, 2004].

The simulated scenario consists of a vehicle moving at a constant speed along a street with three sort of obstacles: buildings, trees and lampposts. Only one satellite at a constant azimuth and elevation angle is simulated at a time. The street width is constant and the distance between the vehicle and the road centre is fixed by the user. The size of the buildings and other obstacles, as well as of the gaps between them, changes along the simulation time according to a Gaussian distribution.

The direct ray follows a deterministic model determined by the house fronts, trees and lampposts found in its trajectory. House front diffraction is modelled by a knife edge model, the trees as an attenuating cylinder plus a statistical fading process, and the lampposts by a double knife edge model.

The reflected rays are generated one by one. Each multipath ray is associated with a reflector that is generated following a statistical model based on measured data: the number of simultaneous reflectors, their position in the scenario, their mean power according to their location and their lifespan follow

statistical distributions obtained from data obtained in a measurement campaign. The excess delay and phase (Doppler) of each reflected ray is computed geometrically from the relative position between the satellite, the reflector and the user while the receiver moves. That is, the model does not use statistical distributions neither for the excess delay nor for the Doppler spectrum.

Scenario parameters

The scenario has been set to reproduce a typical city centre street:

- The user is assumed to be a vehicle progressing along the road axis at a speed (v) of 50 km/h with the GNSS antenna situated at a height of 1.5 metres.
- The street is assumed to be 20 meters wide. The width of the buildings follows a normal distribution $W_B \sim N(20 \text{ m.}, 25\text{m.})$ subject to $W_B \geq 10 \text{ m.}$ The height of the buildings follows a normal distribution $H_B \sim N(15 \text{ m.}, 3\text{m.})$ subject to $4 \text{ m.} \leq H_B \leq 25 \text{ m.}$ A gap between buildings appears with a probability $p_G = 0.15$. The width of the gaps follows a normal distribution $W_G \sim N(15 \text{ m.}, 25\text{m.})$ subject to $W_G \geq 10 \text{ m.}$
- Trees have a constant height of 8 m. and a diameter of 5 m. Tree trunks have a constant length of 2 m. a diameter of 0.2 m. Leaflets are assumed to cause an attenuation of 1.1 dB/m. The distance between the trees and the buildings is 2 m. The distance between trees follows a normal distribution $d_T \sim N(20 \text{ m.}, 2\text{m.})$ subject to $d_T \geq 1 \text{ m.}$
- Lampposts have a constant height of 10 m. and a diameter of 0.2 m. The distance between lampposts follows a normal distribution $d_L \sim N(10 \text{ m.}, 2\text{m.})$ subject to $d_L \geq 1 \text{ m.}$
- All reflected rays up to a maximum attenuation of -60 dB are taken into account.

Sampling period

The sampling period that typically gives enough resolution of urban channel models is [Pérez-Fontán et al., 2001]:

$$T_s = \frac{\lambda}{8 \cdot v} \quad (4.54)$$

- λ : carrier wavelength (m)
- v : user speed (m/s)

The adequate sampling period for different GNSS frequency bands and user velocities are of the order of the millisecond, between 0.95 ms and 2.3 ms (Table 4.2). The multipath database has been generated with a frequency period of $T_s = 1 \text{ ms.}$

Table 4.2. Recommended channel model sampling period T_s (ms).

		Frequency band			
		L1/E1	L2	L5/E5a	E5b
v (km/h)	50	1.7	2.2	2.3	2.2
	90	0.95	1.2	1.3	1.2

Satellite position

The database contains the time series of received rays from a satellite at different positions. The elevation angle goes from 10° to 90° in 10° steps, and the azimuth from 0° to 90° in 10° steps, considering the street axis as azimuth 0°.

Number and length of simulations

Sixty simulations with a duration of ten seconds have been performed for each satellite's azimuth and elevation angle pair. The number and length of the simulations has been chosen according to criteria of computation time, output data size and accuracy of the model.

4.3.6.2. Receiver tracking loops

Once the received signals have been obtained with the urban channel model, they are processed by GNSS receiver tracking loops. A typical loop configuration suitable for urban scenarios has been used. The PLL is of 3rd order with a 10-Hz bandwidth and a Q discriminator, aided by a 15-Hz bandwidth FLL to improve the tracking of phase changes. The DLL is of 1st order, with a 1-Hz bandwidth and a dot product discriminator.

The delay of the signal without multipath is known at each instant of the database, so the computation of the pseudorange error due to multipath from the delay estimated by the DLL is straightforward.

The correlator and the tracking loops are implemented in a simple and computationally efficient way, where the only inputs are the channel model time series ($\{A_i\}$, $\{\tau_i\}$, $\{\theta_i\}$) and the power spectral density of the modulated signal.

First, the GNSS receiver wipes off the carrier multiplying the incoming signal by a local carrier with the phase estimated by the PLL followed by a low pass filter. This process may be done in one or several steps using intermediate frequencies. The analytical result is the incoming code signal scaled by the cosine of the difference between the phase of the incoming signal and the phase estimated by the PLL in the in-phase branch (I), and by the sine in the quadrature (Q) one. Let us take the in-phase branch as an example:

$$r_I(t) = \sum_{i=1}^{N_{mp}} A_i \cdot \tilde{c}(t - \tau_i) \cdot \cos(\theta_i - \hat{\theta}) \quad (4.55)$$

where:

- $r_I(t)$: received signal after the carrier wipe-off process in the in-phase branch
- N_{mp} : number of multipath rays
- \tilde{c} : modulated signal code filtered by the front-end filter
- A_i , τ_i and θ_i : are the amplitude, delay and phase of the i^{th} received ray
- $\hat{\theta}$: carrier phase estimated by the PLL

Afterwards, the correlator multiplies the incoming code signal by a local code replica with the delay estimated by the DLL plus the delay Δ_{corr} corresponding to the correlator gate, that is, $\Delta_{\text{corr}} = 0$ for the prompt, $\Delta_{\text{corr}} = C_s/2$ for the early and $\Delta_{\text{corr}} = -C_s/2$ for the late gate, where C_s is the discriminator

chip-spacing. This product is integrated to compute the correlator outputs that are fed into the DLL and PLL. As example, the analytical expression of the in-phase prompt is:

$$I_p = \int_t^{t+T_I} \left[\sum_{i=1}^{N_{mp}} A_i \cdot \tilde{c}(t - \tau_i) \cdot \cos(\theta_i - \hat{\theta}) \right] \cdot c(t - \hat{\tau}) \cdot dt \quad (4.56)$$

where:

- T_I : correlator integration time
- $\hat{\tau}$: code delay estimated by the DLL.
- c : modulated PRN code (not filtered by the front-end because it is the code replica generated by the receiver)

In order to reduce the computational burden of eq.(4.56), the filtered PRN code autocorrelation function is introduced:

$$\tilde{K}_c(\tau_i - \hat{\tau}) = \int_t^{t+T_I} \tilde{c}(t - \tau_i) \cdot c(t - \hat{\tau}) \cdot dt \quad (4.57)$$

The filtered PRN code autocorrelation function is the result of the convolution between the front-end filter impulse response ($h_{\text{front-end}}$) and the PRN code autocorrelation function (K_c):

$$\tilde{K}_c = h_{\text{front-end}} * K_c \quad (4.58)$$

Assuming modulated PRN codes are wide-sense stationary (WSS), their autocorrelation function can be obtained with the Wiener-Kinchin theorem:

$$\tilde{K}_c = \text{TF}^{-1} \{ \text{PSD}(\tilde{c}) \} \quad (4.59)$$

where TF^{-1} means inverse Fourier transform and PSD is the power spectral density.

An alternative computation approach of I_p is obtained introducing eq.(4.57) into (4.56):

$$I_p = \sum_{i=1}^{N_{mp}} A_i \cdot \tilde{K}_c(\tau_i - \hat{\tau}) \cdot \cos(\theta_i - \hat{\theta}) \quad (4.60)$$

The use of \tilde{K}_c reduces considerably the computational complexity needed to calculate the correlator outputs, but makes the following assumptions:

- 1) the channel parameters (N_{mp} , $\{A_i\}$, $\{\tau_i\}$, $\{\theta_i\}$) and the PLL and DLL estimations ($\hat{\theta}$, $\hat{\tau}$) remain constant during the integration time T_I .
- 2) the integration time T_I is equal or longer than the whole PRN code, in order to consider the signal approximately white noise. In particular, the signal must satisfy the two following properties:
 - 2.1) the autocorrelation function is approximately a delta centred at the 0-chip lag:

$$\tilde{K}_c(\tau_i - \hat{\tau}) \approx 0 \text{ if } |\tau_i - \hat{\tau}| > T_{\text{chip}}$$

2.2) the signal is WSS, so the Wiener-Kinchin theorem is applicable:

$$\tilde{K}_c = \text{TF}^{-1}\{\text{PSD}(\tilde{c})\}$$

The integration time T_I is longer than the channel sampling period $T_s = 1$ ms (see Table 4.2), so the signal parameters are not constant. To solve this, the integral (4.56) is split between $M = T_I/T_s$ intervals of T_s length, in order to accommodate the signal update rate caused by channel changes. Continuing with I_p as example:

$$I_p = \sum_{j=1}^M \left(\int_{t+(j-1)T_s}^{t+jT_s} \left[\sum_{i=1}^{N_{\text{mp},j}} A_{i,j} \cdot \tilde{c}(t - \tau_{i,j}) \cdot \cos(\theta_{i,j} - \hat{\theta}_j) \right] \cdot c(t - \hat{\tau}_j) \cdot dt \right) \quad (4.61)$$

where:

- $N_{\text{mp},j}$: number of signal rays received during the j^{th} interval
- $A_{i,j}$, $\tau_{i,j}$ and $\theta_{i,j}$: amplitude, delay and phase of the i^{th} received ray during the j^{th} interval
- $\hat{\theta}_j$ and $\hat{\tau}_j$: carrier phase and code delay estimates during the j^{th} interval

Introducing \tilde{K}_c :

$$I_p = \frac{1}{M} \sum_{j=1}^M \left(\sum_{i=1}^{N_{\text{mp},j}} A_{i,j} \cdot \tilde{K}_c(\tau_{i,j} - \hat{\tau}_j) \cdot \cos(\theta_{i,j} - \hat{\theta}_j) \right) \quad (4.62)$$

This new formula fulfils the first assumption: the signal parameters remain constant during each T_s interval. It also meets the second assumption if the PRN is shorter than $T_s = 1$ ms. Nevertheless, Galileo E1B and E1C and GPS L1C signals have PRN lengths of 4 ms and 10 ms respectively, all of them at a chip rate of 1023 chips per ms.

Any 1-ms portion of these PRN codes has white noise properties, so eq.(4.62) is applicable to each signal considered. To prove that $\tilde{K}_c(\tau_i - \hat{\tau}) \approx 0$ if $|\tau_i - \hat{\tau}| > T_{\text{chip}}$, the circular autocorrelation of every 1023-chip segments of each E1B and E1C codes have been calculated, showing that they can still be approximated by a delta centred at the 0-chip lag. As an example, Figure 4.12 compares the normalized circular autocorrelation of the PRN #1 of the whole E1B PRN (of duration 4 ms), a 1023-chip segment of it (of duration 1 ms), and the complete L1 C/A. The entire E1B PRN has the lowest correlation values at lags larger than 0 chips, so its approximation to a delta is the most accurate. Nevertheless, partial E1B code has similar correlation values at lags different to 0 chips than L1 C/A, so the \tilde{K}_c approach is valid.

Several statistical measures, apart from the autocorrelation function, have been obtained for any partial code segment of 1023-chip length, presenting approximately white noise characteristics. Therefore 1 ms portions of any code can be assumed to be WSS, even for PRN codes with duration longer than 1 ms.

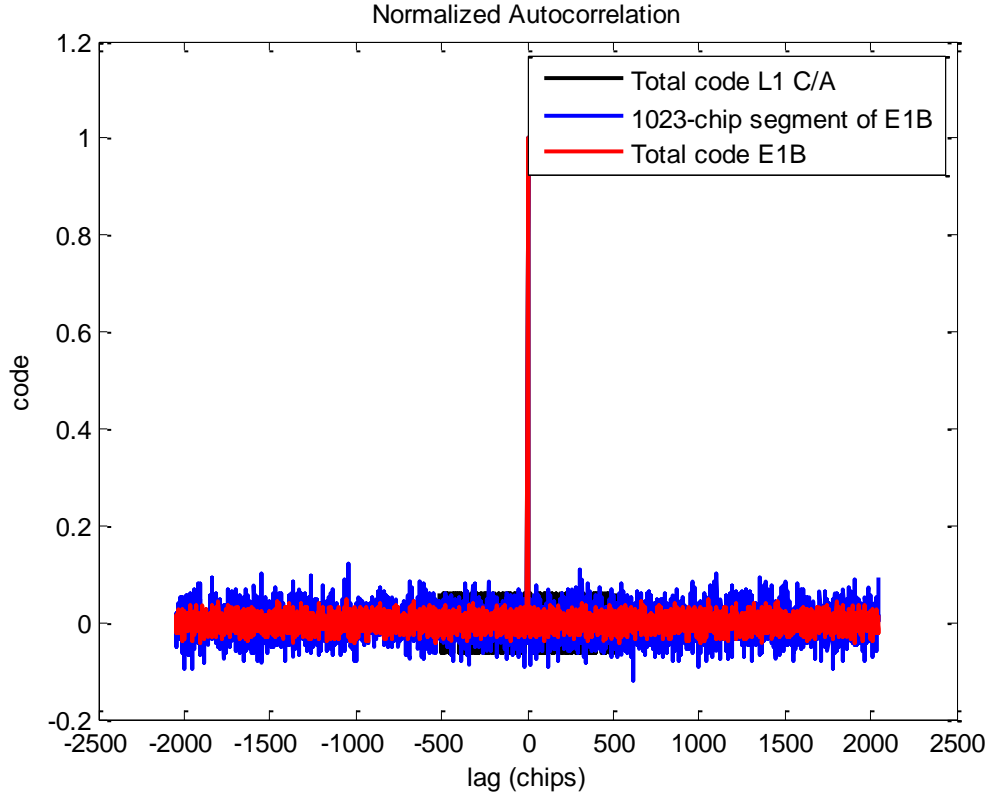


Figure 4.12. Normalized autocorrelation function of total and partial PRN codes. Example of L1 C/A and E1B.

Finally, operating as for I_p , the correlator outputs result:

$$I_p = \frac{1}{M} \sum_{j=1}^M \left(\sum_{i=1}^{N_{mp,j}} A_{i,j} \cdot \tilde{K}_c(\tau_{i,j} - \hat{\tau}_j) \cdot \cos(\theta_{i,j} - \hat{\theta}_j) \right) \quad (4.63)$$

$$Q_p = \frac{1}{M} \sum_{j=1}^M \left(\sum_{i=1}^{N_{mp,j}} A_{i,j} \cdot \tilde{K}_c(\tau_{i,j} - \hat{\tau}_j) \cdot \sin(\theta_{i,j} - \hat{\theta}_j) \right) \quad (4.64)$$

$$I_E = \frac{1}{M} \sum_{j=1}^M \left(\sum_{i=1}^{N_{mp,j}} A_{i,j} \cdot \tilde{K}_c(\tau_{i,j} - \hat{\tau}_j + C_s/2) \cdot \cos(\theta_{i,j} - \hat{\theta}_j) \right) \quad (4.65)$$

$$Q_E = \frac{1}{M} \sum_{j=1}^M \left(\sum_{i=1}^{N_{mp,j}} A_{i,j} \cdot \tilde{K}_c(\tau_{i,j} - \hat{\tau}_j + C_s/2) \cdot \sin(\theta_{i,j} - \hat{\theta}_j) \right) \quad (4.66)$$

$$I_L = \frac{1}{M} \sum_{j=1}^M \left(\sum_{i=1}^{N_{mp,j}} A_{i,j} \cdot \tilde{K}_c(\tau_{i,j} - \hat{\tau}_j - C_s/2) \cdot \cos(\theta_{i,j} - \hat{\theta}_j) \right) \quad (4.67)$$

$$Q_L = \frac{1}{M} \sum_{j=1}^M \left(\sum_{i=1}^{N_{mp,j}} A_{i,j} \cdot \tilde{K}_c(\tau_{i,j} - \hat{\tau}_j - C_s/2) \cdot \sin(\theta_{i,j} - \hat{\theta}_j) \right) \quad (4.68)$$

The instantaneous pseudorange error is calculated every $T_s = 1$ ms. as the difference between the delay estimated by the DLL and the real LOS delay. Finally, the number of samples is reduced averaging the errors obtained during the integration time. Integration times of 20 ms and 100 ms are studied.

4.3.6.3. Lock Detector

The GNSS receiver may not be able to track the signal during the whole simulation period because of signal masking or multipath. A lock detector has been implemented to exclude data obtained with unlocked tracking loops from the set of pseudorange errors used to calculate the nominal error model. A single outlier can have a strong influence on the overbounding algorithm and increment the final σ_{mp} . Thus, the lock detector plays a key role discarding the large pseudorange errors caused by unlocked tracking loops that would amplify artificially σ_{mp} .

The lock detector consists of a PLL lock detector in parallel with a C/N_0 estimator. This double check is necessary because the PLL lock detector cannot detect 25 Hz offset false locks. Although this fault is usually overcome with the navigation message parity check, a C/N_0 estimator is used to solve the problem faster and without the navigation message.

The following PLL lock detector has been implemented [Parkinson et al., 1996]:

$$C2\phi = \frac{NBD}{NBP} \quad (4.69)$$

where:

- $C2\phi$: estimated $\cos(2\varepsilon_\theta)$
- NBD: Narrow Band Difference

$$NBD = \left(\sum_{i=1}^M I_i \right)^2 - \left(\sum_{i=1}^M Q_i \right)^2$$

- NBP: Narrow Band Power

$$NBP = \left(\sum_{i=1}^M I_i \right)^2 + \left(\sum_{i=1}^M Q_i \right)^2$$

where M is the number of averaged correlator outputs. The total average time of the lock detector is $T_{\text{Lock Detector}} = M \cdot T_I$.

A carrier phase error threshold of 30° has been taken; signals with $\varepsilon_\theta > 30^\circ$ are considered not locked. This gives a lock detector threshold of $C2\phi = 0.5$.

The implemented C/N_0 estimator is:

$$C/N_0 = \frac{\text{mean}(I_p)}{\text{var}(I_p)} \quad (4.70)$$

The mean and the variance of I_p are computed during a period equal to the averaging time of the PLL lock detector. The detector decides the tracking loops are locked when the estimated C/N_0 is at least 23 dB. This threshold has been chosen because it is the C/N_0 that produces an equivalent effect on the PLL lock detector of eq.(4.69) equivalent to a 30° carrier phase error [Parkinson et al., 1996].

The averaging time $T_{\text{Lock Detector}}$ drives the lock detector performance. Various averaging times have been tested; in general, the longer the averaging time, the lower the number of outliers included in the computation of the error distribution. An averaging time of 500 ms has been chosen because it provides good performances for all studied receiver configurations.

4.3.6.4. Error overbounding

The set of pseudorange errors selected by the lock detector do not exactly follow a normal distribution. For this reason, the CDF overbounding technique of eq.(4.5) is applied in order to obtain a conservative Gaussian distribution suitable for the nominal error model:

$$\text{cdf}_o(x) \geq \text{cdf}_e(x) \quad \forall x \leq 0$$

$$\text{cdf}_o(x) \leq \text{cdf}_e(x) \quad \forall x \geq 0$$

where cdf_o is the overbounding CDF (zero-mean normal distribution), cdf_e is the original CDF of the error database and x is the error magnitude.

The CDF overbounding method requires the measured distribution to be zero-mean, symmetric and unimodal. As the measured distribution has been obtained with Monte Carlo simulations, it does not exactly fulfil these conditions, but approximately does (the measured mean is of the order of millimeters). Then, the mean has been displaced in order to center the measured CDF around the case of no error, $\text{cdf}_e(0) = 0.5$. Doing this the overbounding definition (4.5) can be applied directly.

Figure 4.13 provides an example of CDF overbounding, where the accumulated probability axis is in gaussian scale and the error is normalized by the overbounding standard deviation, so normal distributions follow straight lines. A comparison between the measured and overbounding error distributions shows how the latest redistributes the probability towards larger error magnitudes (Figure 4.14, Figure 4.15).

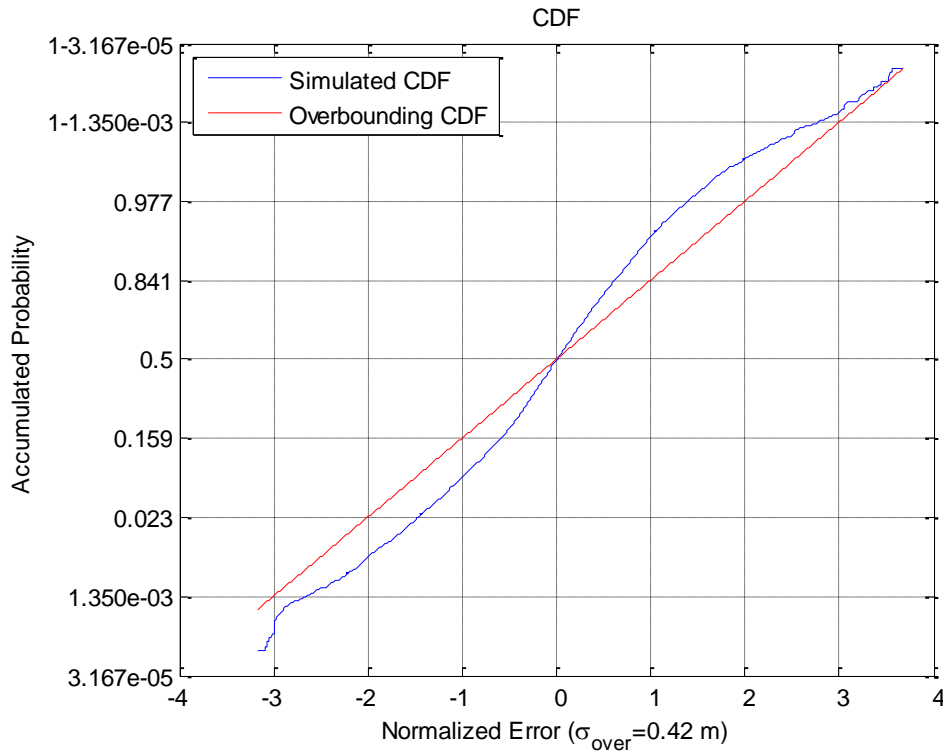


Figure 4.13. Example of CDF of simulated pseudorange error and its overbounding function.

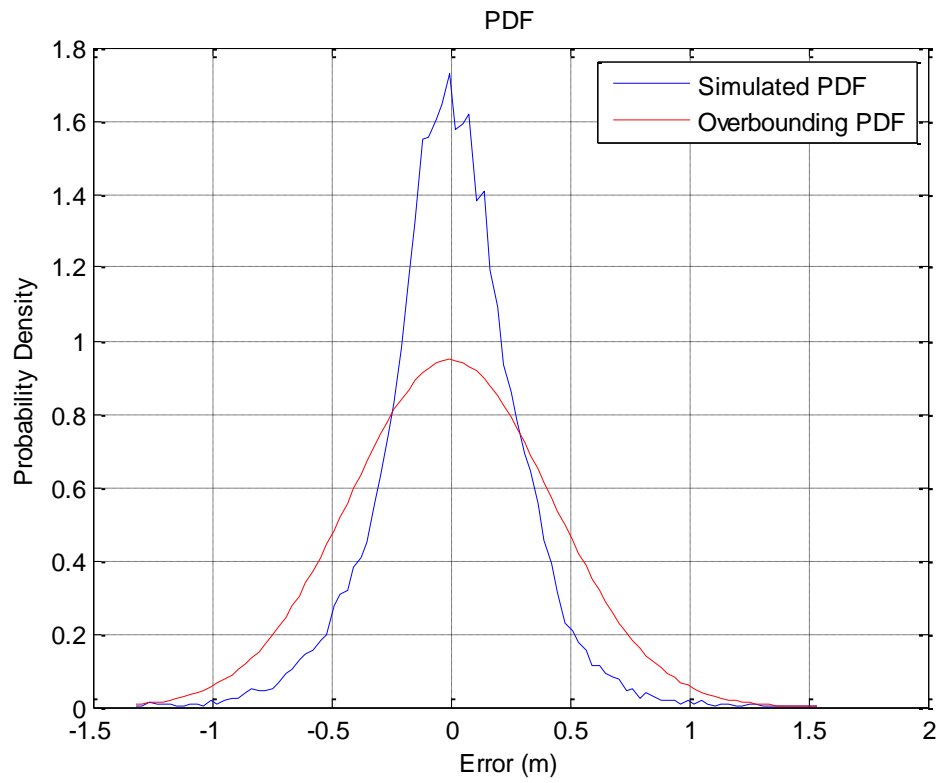


Figure 4.14. Example of CDF of simulated pseudorange error and its overbounding function.

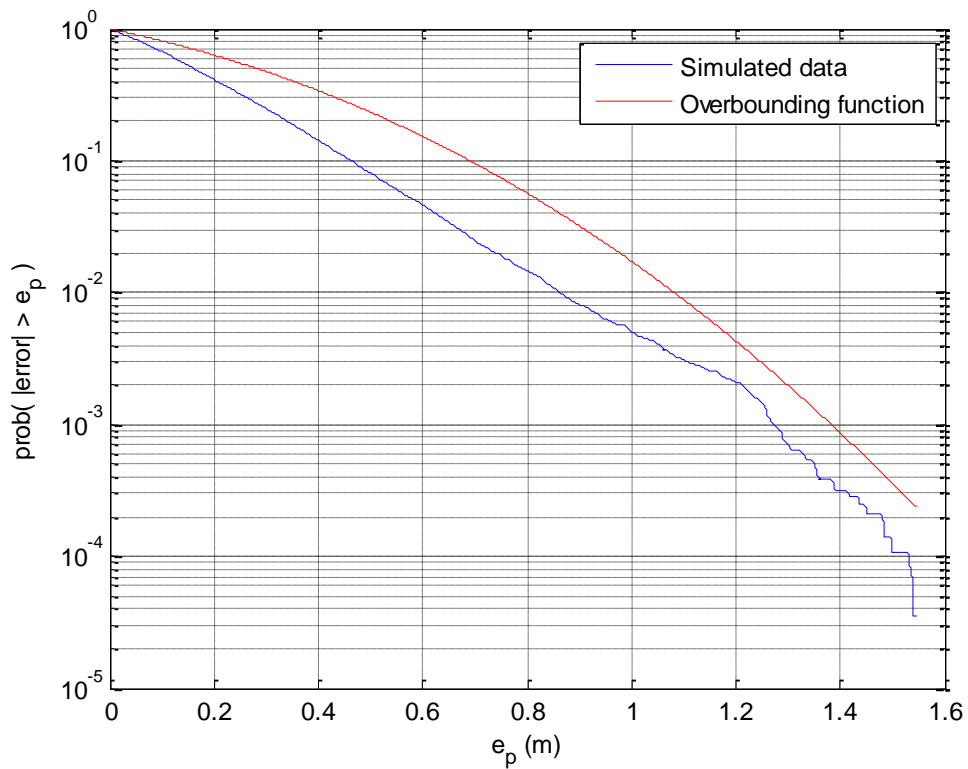


Figure 4.15. Example of error percentiles of simulated pseudorange error and its overbounding function.

4.3.6.5. Final Pseudorange Error due to Multipath

A multipath error model dependent only on the elevation angle is proposed for the receiver configurations of Table 3.3 with $T_I = 20$ ms. and $T_I = 100$ ms. (Figure 4.16, Figure 4.17). The modulation CBOC(6,1,1/11,-) has been taken as representative of TMBOC(6,1,4/33) and CBOC(6,1,1/11,+), which provide similar results. As expected, the most robust signal against multipath is BPSK(10), followed by CBOC(6,1,1/11,-). The next performing signals are wideband BPSK(1) and BOC(1,1), while narrowband BPSK(1) receivers provide the poorest performance against multipath effects.

Except for narrowband L1 C/A receivers, σ_{mp} is relatively independent from the elevation angle. The variations between the values at different elevation angles, of the order of centimetres, are explained because they are the result of different Monte Carlo simulation runs. For those signals, an simplified model independent from the elevation angle can be used taking the maximum σ_{mp} obtained at any elevation angle (Table 4.3).

Table 4.3. Maximum multipath error model standard deviation (σ_{mp}) obtained at any elevation angle.

T_I	Receiver type			
	Wideband L1 C/A	BPSK(10)	BOC(1,1)	CBOC(6,1,1/11,-)
$T_I = 20$ ms	0.41	0.22	0.53	0.29
$T_I = 100$ ms	0.39	0.15	0.51	0.23

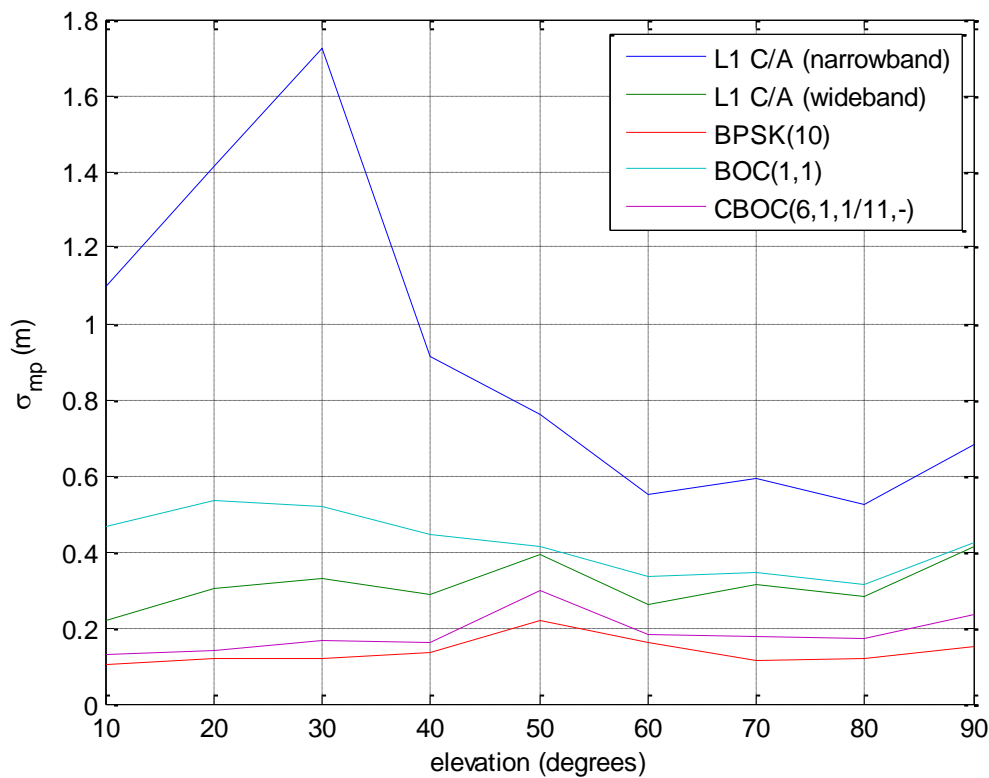


Figure 4.16. Multipath nominal error model with an integration time of 20 ms.

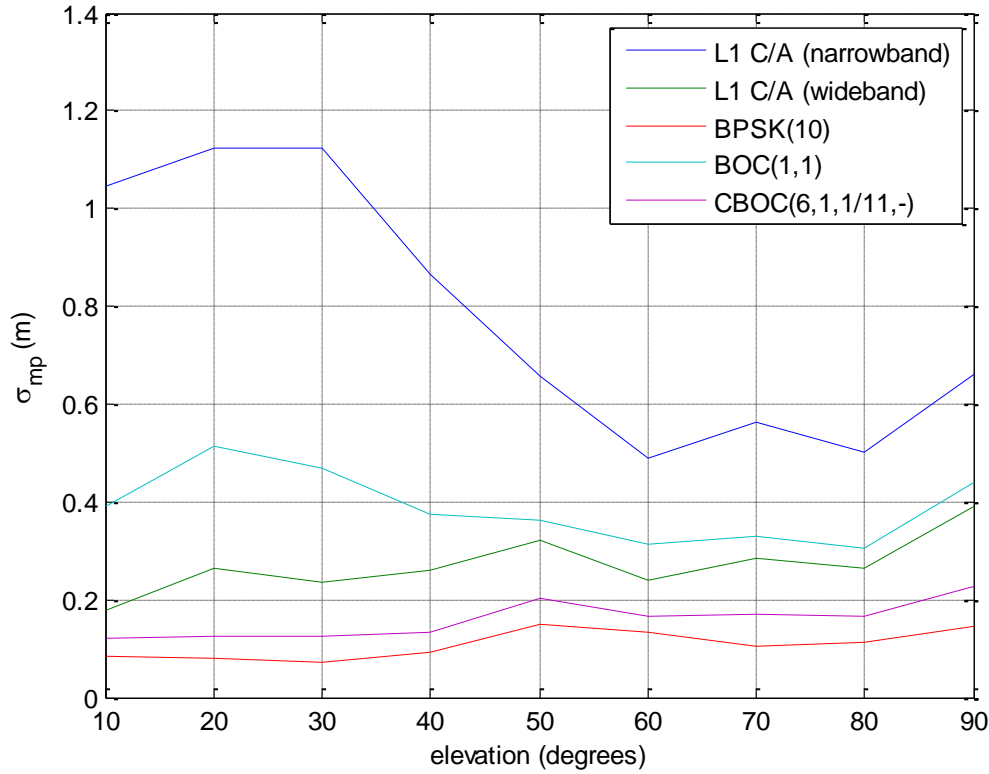


Figure 4.17. Multipath nominal error model with an integration time of 100 ms.

4.3.6.6. Conclusions and scope of the multipath model

The nominal error model shown in Figure 4.16 and Figure 4.17 describes the pseudorange errors due to multipath rays that are always present and disturb constantly the reception of the useful signal. The nominal model does not include NLOS multipath with large delays that occur only at specific times. For this reason, the magnitude of σ_{mp} is of the order of tens of centimetres. Indeed, the significant phase shift of high power NLOS multipath made the tracking loops to lose track, eliminating these samples from the model calculation.

Representative scenarios and receiver configurations of electronic toll collection systems in urban environments have been simulated to derive the multipath nominal error model. Nevertheless, the model may vary in other scenarios or receiver configurations different from the studied case.

4.3.7. Total pseudorange nominal measurement error model

Recalling equation (4.14), the variance of the total pseudorange nominal error is:

$$\sigma_{PSR}^2 = \sigma_{clk \& eph}^2 + \sigma_{iono}^2 + \sigma_{tropo}^2 + \sigma_{noise}^2 + \sigma_{mp}^2$$

The standard deviation σ_{PSR} has been computed for standalone, SBAS and dual frequency receivers (Figure 4.18 - Figure 4.21). The receiver configuration depends on the tracked signal as set in Table 3.3. In all cases the receiver tracking loops employ a DP discriminator, a DLL with an equivalent 1-sided bandwidth of $B_L = 1$ Hz and a correlator with an integration time of $T_I = 20$ ms. The signal to noise ratio is fixed to $C/N_0 = 30$ dB. The user is located in the south of France at the coordinates

$[\phi = 42^\circ 41', \lambda = 2^\circ 53']$. A modernized GNSS infrastructure is considered so that $\sigma_{clk \& eph} = 0.85$ m.

Standalone single-frequency receivers have the largest values of σ_{PSR} , with a strong effect of the satellite elevation angle (Figure 4.18, Figure 4.19). High performance BPSK(1) and TMBOC/CBOC receivers provide the best results with σ_{PSR} values between 5 and 15 meters, while BOC(1,1) signals offer a slightly poorer performance. Despite its robustness against noise and multipath, BPSK(10) receivers have the largest nominal error because of the higher ionospheric residual error at the L5/E5a frequency band. In general, σ_{PSR} is higher in Galileo than in GPS because the residual error model obtained for NeQuick corrections predicts bigger errors at the user's location than the one for Klobuchar corrections. At the studied location, the difference is of 30 cm. for an elevation angle of 90° , and up to one meter for an elevation of 5° .

SBAS corrections significantly reduce the ionospheric errors and provide lower values of σ_{PSR} , which are less sensitive to the satellite elevation angle (Figure 4.20). The SBAS corrections are assumed to be available and with the same performance for GPS and Galileo, and for the L1/E1 and L5/E5a frequency bands. The best performance, with σ_{PSR} between 0.5 and 2 meters, is provided by BPSK(10) signals, followed by TMBOC and CBOC. The Wideband BPSK(1) and CBOC have an intermediate performance with σ_{PSR} between 2 and 3 meters, while narrowband BPSK(1) receivers have values of σ_{PSR} between 5 and 5.5 meters.

Dual frequency L1/E1 & L5/E5a receivers eliminate the ionospheric residual error and provide a σ_{PSR} considerably lower than the one of standalone receivers, but higher than that obtained with SBAS corrections (Figure 4.21). The reason is the amplification effect that the iono-free pseudorange combination has on the errors due to noise and multipath, which are already large due to the low C/N_0 and the urban environment. All receivers use the same BOC(10) modulation in the L5/E5a frequency and only differ in the L1/E1 signals. The magnitude of the σ_{PSR} , approximately independent from the satellite elevation angle, is around 2 meters with TMBOC and CBOC signals, 4.5 meters for BOC and wideband BPSK(1), and 12 meters for narrowband BPSK(1).

An analysis of the contribution of each error source to the total pseudorange nominal error helps to understand the different performances of standalone, SBAS and dual-frequency receivers (Figure 4.22 - Figure 4.24). The total pseudorange error in single-frequency standalone receivers is largely dominated by the ionosphere (Figure 4.22). Therefore, when it is reduced with SBAS corrections or eliminated with dual frequency measurements, the total error is significantly reduced (Figure 4.23). The second most important contribution is the error due to thermal noise, which is even larger than the ionospheric residual error when SBAS corrections are applied, in part because of the low C/N_0 . For that reason, the noise amplification makes the dual-frequency pseudorange error larger than that of SBAS single-frequency receivers (Figure 4.24). SBAS corrections in dual-frequency receivers would only mitigate the effect of satellite clock and ephemeris errors, decreasing $\sigma_{eph \& clk}$ from 0.85 to 0.3 meters, so the improvement is practically insignificant.

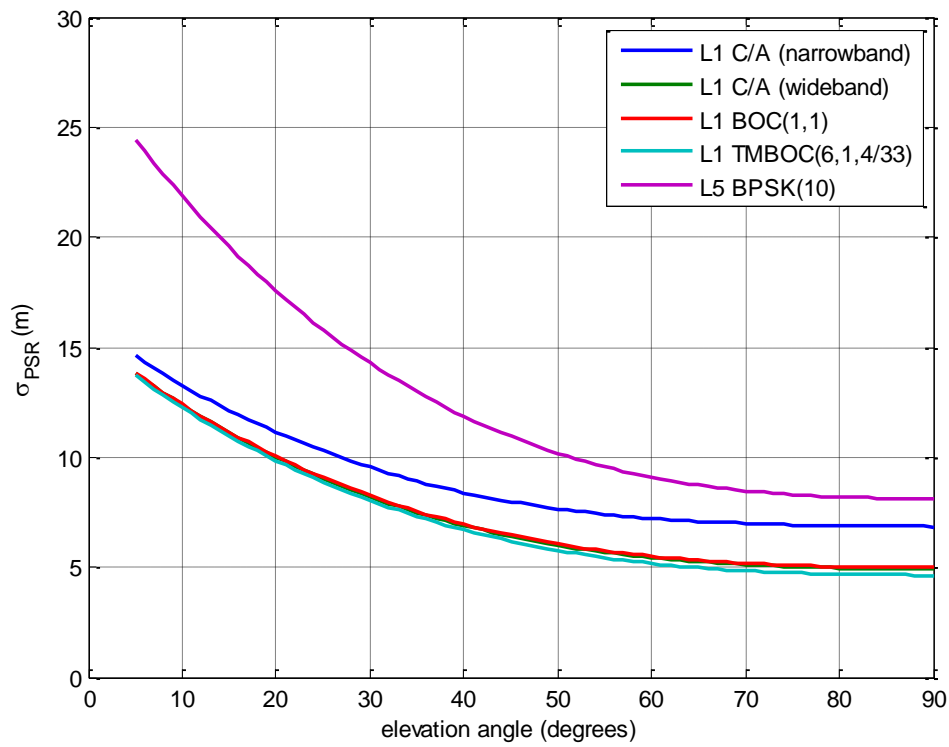


Figure 4.18. Nominal pseudorange measurement error model σ_{PSR} of single frequency, standalone GPS receivers.

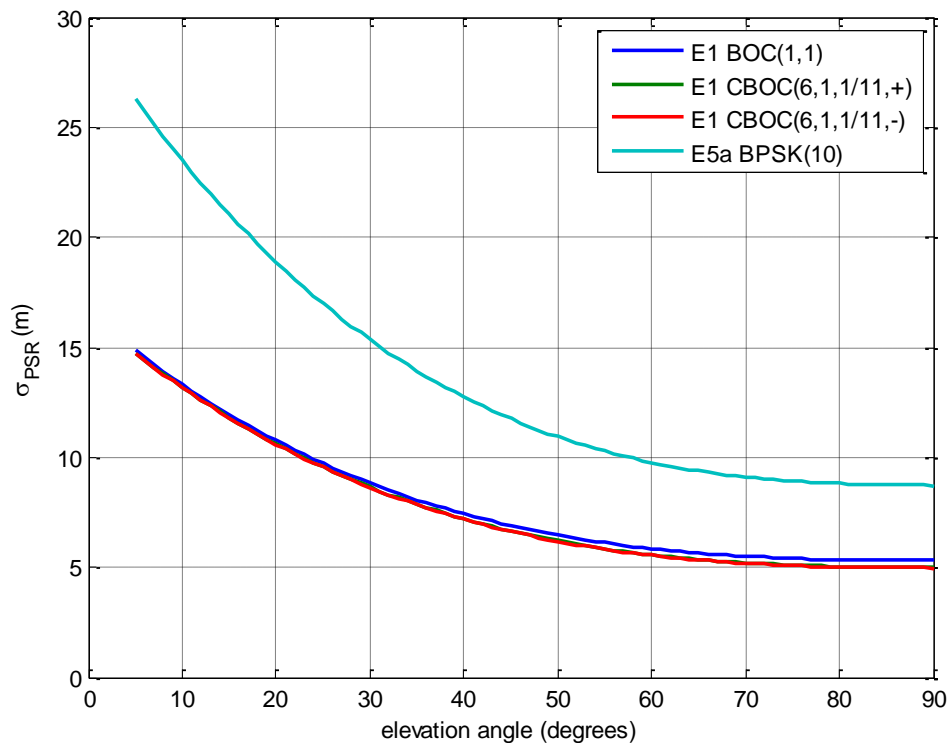


Figure 4.19. Nominal pseudorange measurement error model σ_{PSR} of single frequency, standalone Galileo receivers.

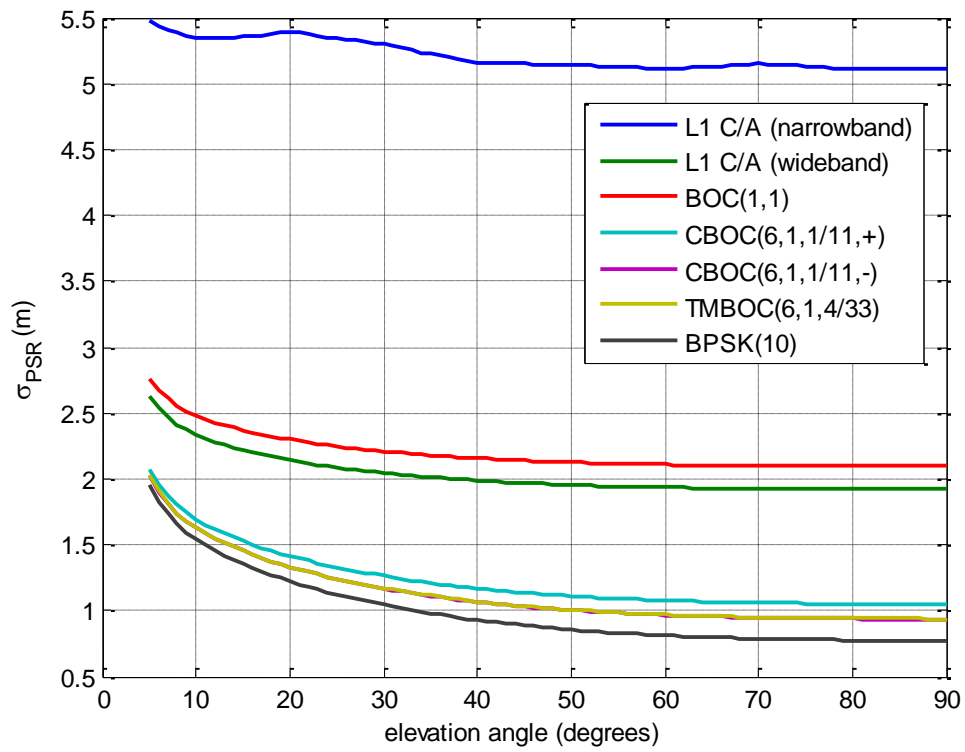


Figure 4.20. Nominal pseudorange measurement error model σ_{PSR} of single frequency GPS and Galileo receivers with SBAS corrections.

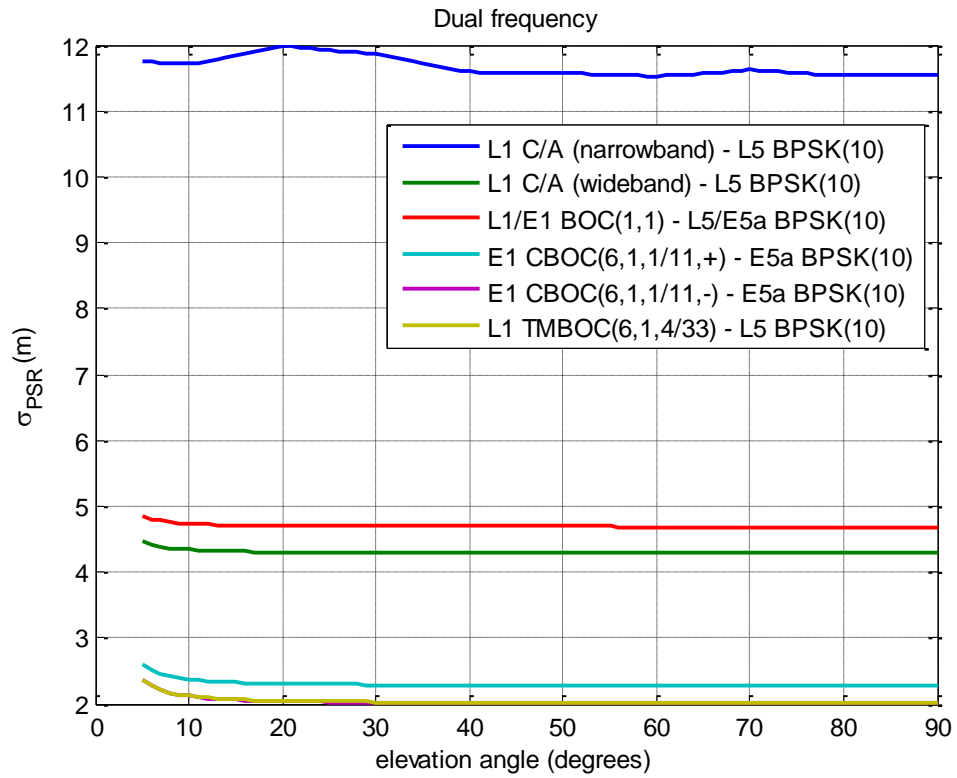


Figure 4.21. Nominal pseudorange measurement error model σ_{PSR} of dual frequency GPS and Galileo receivers.

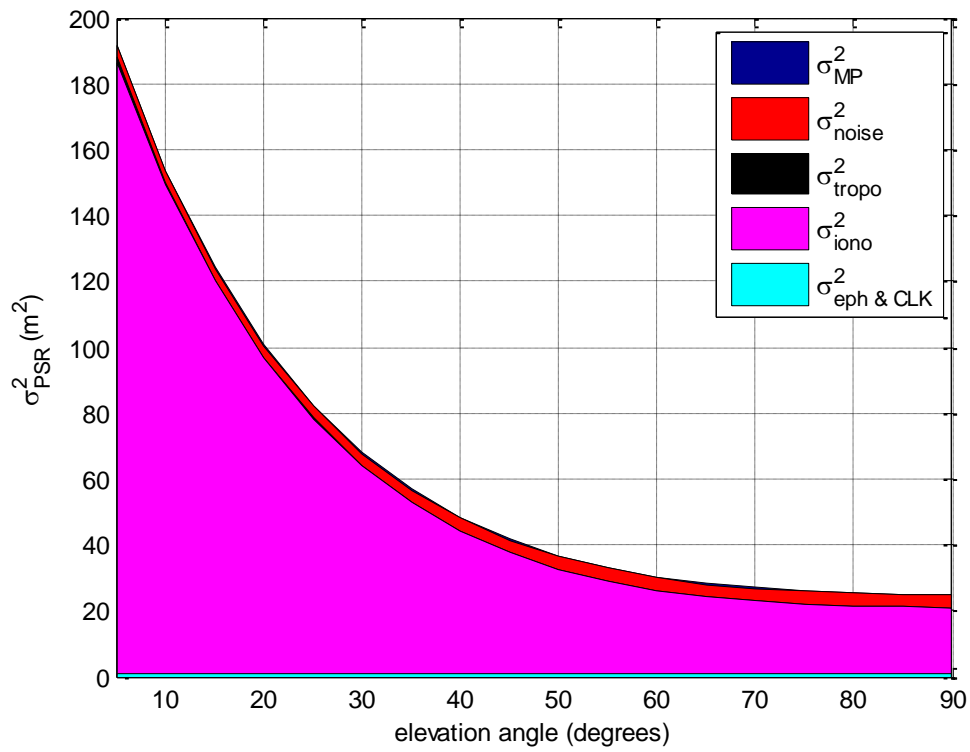


Figure 4.22. Contribution of the error sources to the total nominal pseudorange measurement error model σ_{PSR}^2 . Example of a single frequency L1 BOC(1,1) receiver.

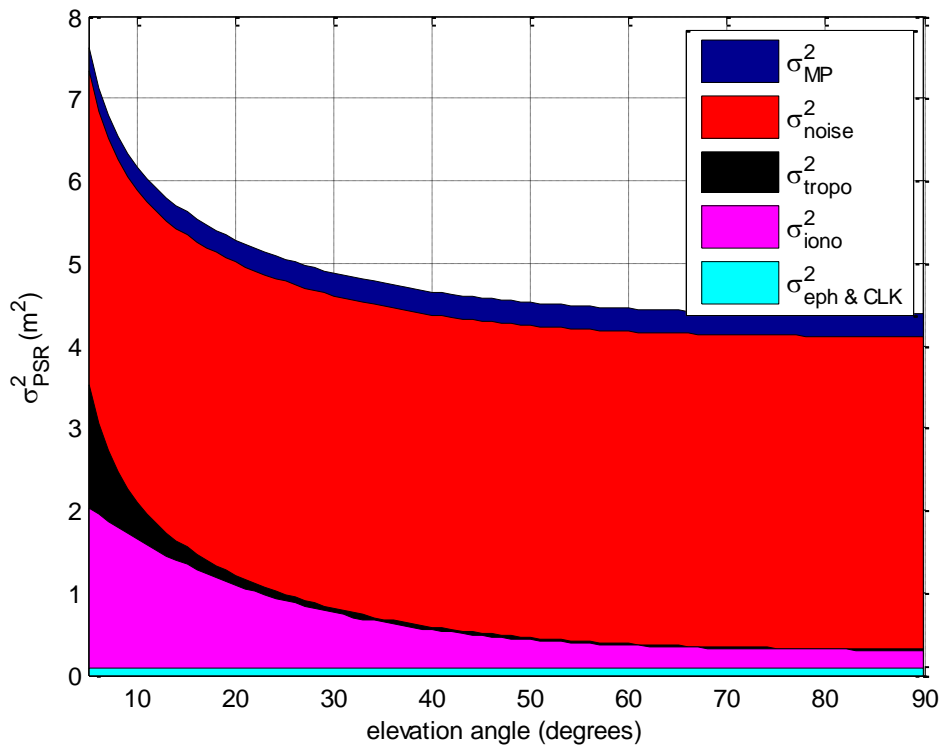


Figure 4.23. Contribution of the error sources to the total nominal pseudorange measurement error model σ_{PSR}^2 . Example of a single frequency L1 BOC(1,1) receiver with SBAS corrections.

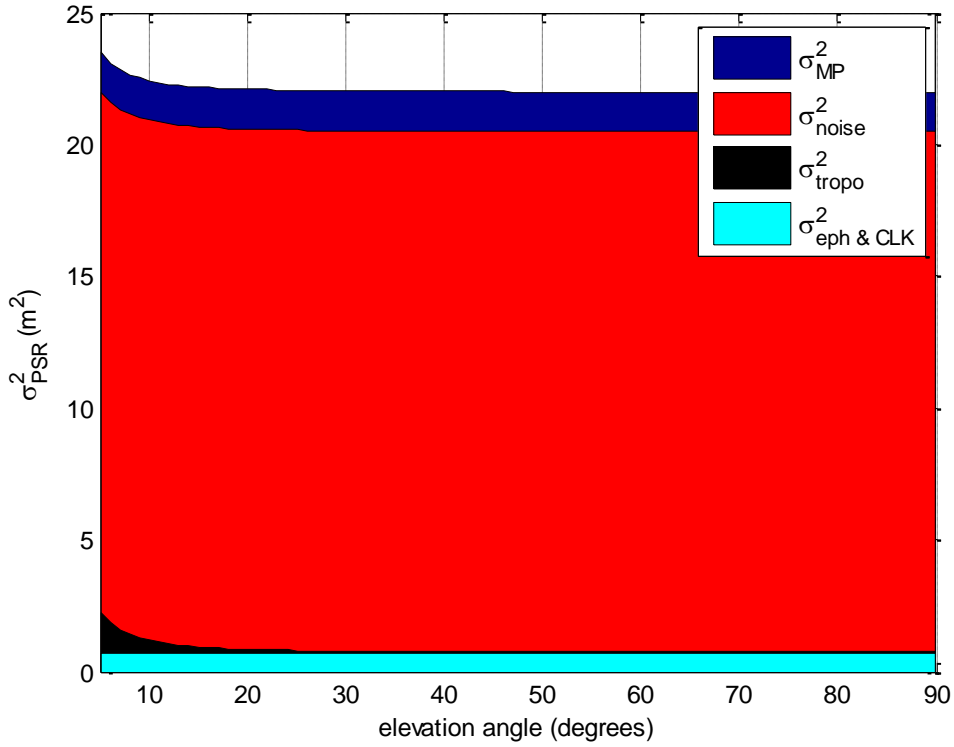


Figure 4.24. Contribution of the error sources to the total nominal pseudorange measurement error model σ_{PSR}^2 . Example of a dual frequency receiver with L1/E1 BOC(1,1) and L5/E5a BPSK(10) signals.

4.3.8. Nominal model of the external altitude information

3D positioning can be aided by altitude information provided by external sensors such as barometers or digital maps supports. Nominal errors of this external altitude information are modeled by a zero-mean normal distribution characterized by its variance σ_{alt}^2 . This assures their integration with GNSS signals in RAIM algorithms that require Gaussian range measurement errors.

Once the user is assured to be within a given area, its altitude information can be obtained from a digital map. If the user's altitude is uniformly distributed between the minimum and maximum altitude values in the zone, the error is uniformly distributed between $[-e_{h,\text{MAX}}, e_{h,\text{MAX}}]$ and the standard deviation of the overbounding Gaussian function is (Appendix B):

$$\sigma_{\text{alt}} = \sqrt{2/\pi} \cdot e_{h,\text{MAX}} \quad (4.71)$$

Four different values of σ_{alt} are considered in order to cover the use of different sensors with different performances:

$$\sigma_{\text{alt}} = 2, 5, 10, 25 \text{ meters} \quad (4.72)$$

4.4. Fault Model

The fault model characterizes the errors not included in the nominal case. Pseudorange faults are modelled as a bias added to the nominal error:

$$\mathbf{b} = [b_1, b_2, \dots, b_{N_{\text{sat}}}]^T \quad (4.73)$$

Faults may have different origins: a satellite clock malfunction, high power and large NLOS multipath, large and punctual ionospheric delays (due to magnetic storms, for instance), etc. One of the key properties of the fault model used in RAIM design is the probability of occurrence of the failures. Unfortunately, the only failure sufficiently characterized for integrity applications is the GPS major service failure (MSF). This characterization is assumed to be also applicable to Galileo. For this reason, the fault model will consider only pseudorange failures due to major service failures. This choice requires GNSS receivers to have robust protection mechanisms against other failures like NLOS multipath.

A major service failure is defined to occur whenever a healthy SPS SIS's instantaneous URE exceeds the SIS URE not-to-exceed (NTE) tolerance without a timely alert (alarm or warning) being provided [DoD, 2008]. The NTE tolerance is defined to be ± 4.42 times the upper bound of the currently transmitted URA. A previous version of standard limits the MSF to be higher than 30 metres [DoD, 2001]:

$$|b_{\text{MSF}}| \geq \max(4.42 \cdot \text{URA}, 30 \text{ m.}) \quad (4.74)$$

The SPS SIS integrity standard specifies the maximum probability of MSF per hour:

$$p_{\text{MSF},h} = 10^{-5} / \text{satellite/h.} \quad (4.75)$$

This probability assumes that an MSF was not present at the start of the hour. When an MSF occurs, the GNSS will detect and alert it with a worst case delay of 6 hours. Nevertheless, realistic maximum alert delays are around 1 hour, and are expected to improve in the future [Martineau, 2008]. Therefore, the probability that a satellite has an MSF at a given instant is the probability that the MSF had begun during the previous hour:

$$P_{\text{MSF (1 hour)}} = 1 \text{ hour} \cdot p_{\text{MSF},h} = 10^{-5} / \text{satellite} \quad (4.76)$$

The probability p_{MSF} is small enough to neglect the probability of multiple simultaneous MSF. Thus, the faulty model considers only one biased pseudorange at a time:

$$\mathbf{b} = [0, \dots, 0, b_i, 0, \dots, 0]^T \quad (4.77)$$

The probability that a position calculated with N_{sat} satellites contains a MSF is:

$$P_{\text{F,PSR}} = N_{\text{sat}} \cdot P_{\text{MSF (1 hour)}} \cdot (1 - P_{\text{MSF (1 hour)}})^{N_{\text{sat}}-1} < N_{\text{sat}} \cdot P_{\text{MSF (1 hour)}} \quad (4.78)$$

4.5. Error Correlation Time

As explained in sections 3.6.3 and 3.6.4, the toll charging algorithm may depend on the number of independent positions estimated along the user's trajectory through a road segment, where two positions are considered independent if they provide independent RAIM outputs. The time elapsed between independent positions is related to the temporal correlation of positioning errors, which in turn depends on the user/satellite geometry and on the magnitude and temporal correlation of pseudorange errors.

Nominal pseudorange errors are modelled with an autoregressive model derived from a 1st order Markov process. With a 1-second positioning sampling period, $T_s = 1$ s:

$$\varepsilon(k+1) = a \cdot \varepsilon(k) + \sqrt{1 - a^2} \cdot w(k) \quad (4.79)$$

where:

- ε : nominal pseudorange error
- $w \sim N(0, \sigma^2)$: white Gaussian noise
- a : autoregressive coefficient:

$$a = 1 - \exp\left(-\frac{1}{T_c}\right) \quad (4.80)$$

The term $\sqrt{1 - a^2}$ is the normalization coefficient that makes ε to have variance σ^2 .

The nominal pseudorange error correlation time is derived analyzing each independent error source identified in the nominal measurement model. Their correlation time has already been defined in civil aviation standards [RTCA, 2006]. The following values of T_c are considered for urban scenarios:

- Ionospheric residual errors: The civil aviation model is adopted (International Ionosphere Reference 2001), with typical values around $T_{c,iono} = 30$ minutes.
- Tropospheric residual errors: The civil aviation model is adopted, with $T_{c,tropo} = 30$ minutes, which is representative of a typical storm passing by.
- Satellite clock and ephemeris errors: The civil aviation model is adopted, with $T_c = 2$ hours. Nevertheless, it can be reduced to $T_{c,clk \& eph} = 1$ hour, based on the average satellite visibility.
- Thermal noise and multipath errors: Values around $T_{c,noise \& mp} = 1$ second have been obtained analyzing the multipath model. Additionally, a DLL bandwidth of 1 Hz indicates a thermal noise correlation close to 1 second. Thus, a correlation time of a few seconds can be taken.

The correlation time of the total pseudorange error depends on the magnitude and the correlation time of each error source. In general, ionospheric errors, thermal noise and multipath are the largest error sources and dominate the final correlation time. Pseudorange errors in single frequency receivers without SBAS corrections are driven by the ionospheric one, resulting in a correlation time close to 30 minutes. On the other hand, dual-frequency receivers present an error correlation of a few seconds, mainly driven by the thermal noise and multipath. The dominant error source in SBAS single frequency receivers depends on the signal-to-noise ratio and on the GNSS signal robustness against noise and multipath. Nevertheless, in civil aviation applications using SBAS, two estimated positions are considered to be independent when the time elapsed between them is at least 120 seconds, which is the period of the smoothing filter.

The error correlation also depends on the variations of the user/satellite geometry. The longest correlation time corresponds to the scenario in which the same satellites are used during the whole pseudorange correlation time. In that case, the correlation period of the position error can be as long as the pseudorange one. On the other hand, when a satellite is excluded from or included within the position estimation, it is likely to be less correlated with the previous estimate.

Considering the time elapsed between consecutive independent positions is equal to the pseudorange error correlation time, single frequency users with long T_c dominated by the ionospheric residual delay are likely to have only one independent position per geo-object, while dual frequency users with shorter T_c are likely to have several positions.

4.6. Conclusions

The linear approximated relationship between pseudorange measurements and the navigation solution of equation (4.1) is used.

The pseudorange measurement errors are divided in two components, fault-free (nominal) and faulty case. Nominal errors are present when all GNSS segments are working according to their specifications, and faults are the rest of errors not included in the nominal case. The nominal error model and the fault model are important because they are a key input in the design of GNSS integrity monitoring mechanisms and their posterior prediction of performance.

Nominal errors are modeled by zero-mean independent normal distributions, which variance is the result of five independent error sources that can be analyzed separately: residual satellite clock errors and inaccurate ephemeris, ionospheric delay, tropospheric delay, thermal noise and multipath. A pseudorange error model has been obtained for each error source for different types of GNSS receivers.

The faulty case only considers major service failures because they are sufficiently characterized for integrity applications. This assumption requires the GNSS receiver to use reliable protection mechanisms against other possible failures like NLOS multipath. The probability of occurrence and the minimum size of major service failures are defined in the GPS SPS integrity standard [DoD, 2008]. The probability of a failure is low enough to assume that, at a given instant, only one of the pseudoranges used to estimate a position may be affected by major service failure.

The temporal correlation of nominal errors has been studied. Pseudorange errors in single frequency receivers are dominated driven by the ionospheric error and have long correlation times, close to 30 minutes. On the other hand, dual-frequency receivers present an error correlation of a few seconds, mainly driven by the thermal noise and multipath. Civil aviation applications using SBAS take a temporal correlation of 120 seconds, which is the period of the smoothing filter.

Chapter 5

Integrity requirements of GNSS-based Electronic Toll Collection Systems

5.1. Introduction

GNSS-based ETC systems periodically charge users an amount equal to the sum of the price associated to the route segments in which the user has been detected during the invoice period. Different failures in the toll system may cause charging errors, which are classified as overcharging when a user is levied a higher charge than the real one, and as undercharging when a user is levied a lower charge than the real one.

ETC requirements are set to bound the impact of over- and undercharging errors. These specifications are usually defined either at service level, for example as the required invoice accuracy, or at geo-object level. In this thesis, the maximum allowable probabilities of missed geo-object recognition (p_{MGoR}) and of false geo-object recognition (p_{FGoR}) are proposed.

In order to meet the ETC specifications, GNSS positioning integrity is monitored with RAIM algorithms which design parameters, i.e. the maximum allowed probabilities of missed detection (P_{MD}) and false alert (P_{FA}), are derived from the geo-object recognition requirements.

First, some examples of ETC requirements and measured performances are presented. Second, the relationship between the requirements at service and geo-object levels is obtained and, finally, the RAIM parameters are derived.

5.2. Examples of ETC requirements and performance

The Ducth ABvM project specified the ETC requirements at service level, indicating that *"the requirement set for the registration unit is that the amount, corresponding to the distances recorded over a one-month period, may not deviate by more than 1% from a 'perfect' measurement in 99% of cases"* [ARS, 2006].

A similar requirement type is proposed by Expert Group 9 supporting the European Commission on the work of the Directive 2004/52/EC when specifies that the measurement device *"should be certified to provide distance measurement accurate to within 2%"* [EG9, 2006].

The Expert Group 9 report also expresses requirements for ETC tests directly at the geo-object level, indicating that *"it is necessary to define a specific set of test conditions in which test geo-objects are guaranteed to be successfully recognized with a success rate of at least 99.99 %. False recognition of a geo-object should be less than 1 in 10^6 "* [EG9, 2006].

The operators of current GPS-based ETC systems offer performance statistics. For instance, Toll Collect, operator of the ETC deployed in German highways, affirms that the overall toll detection rate remains at 99.75 % [Toll Collect, 2011 (a)]. Sky Toll, operator of the ETC deployed in Slovak highways and certain national roads, confirms a toll collection efficiency of 98.99% [SkyToll, 2011 (b)]. These detection rates include undercharging cases because of different causes, not only due to GNSS positioning failures or unavailability (for example, vehicles that circulate through the network without the OBU, etc.).

The number of claims is an important parameter which is also monitored by ETC operators. For instance, Sky Toll affirms that the claim rate (not necessarily due to an incorrect toll computation) of users with at least one toll transaction during June of 2011 was 0.25%, and 0.05% considering only claims judged as justified by the company [SkyToll, 2011 (a)].

5.3. Geo-object recognition requirements

A missed road segment (or geo-object) recognition occurs whenever the toll system does not charge a user the price of a road segment he has actually used.

A false road segment (or geo-object) recognition occurs whenever the toll system charges a user a the price of a road segment he has not used.

The geo-object requirements are the maximum allowable rates of missed geo-object recognition (P_{MGoR}) and false geo-object recognition (P_{FGoR}). Before selecting an appropriate value of these parameters, the relationship between them and the accuracy of the invoice periodically calculated by the toll system operator is presented.

5.3.1. Relationship between invoice accuracy and geo-object requirements

The requirements expressed as invoice accuracy or as false and missed geo-object recognition probabilities are interrelated. Indeed, the invoice error depends on the price of the incorrectly recognized segments (missed or false recognitions) during the invoice period.

Let us consider a service level specification that requires a minimum percentage 1 % of the total invoices processed by the toll system to have an error equal to or lower than $M_e\%$ of the real charge. Assuming that each segment has the same price and considering the worst case in which no missed recognitions compensate the false ones or vice versa, the invoice error can be expressed as the number of incorrect geo-object recognitions present in the invoice. Although the invoice error of real systems will depend on the price of each road segment, this approach allows to obtain a good analytical approximation.

5.3.1.1. Undercharging

The undercharging requirement at geo-object level is given by the maximum allowable probability of missed geo-object recognition (P_{MGoR}). If missed segment recognitions are independent events that occur with a constant probability equal to P_{MGoR} , the probability that there are n missed geo-object recognitions (N_{MGoR}) during the invoice period is:

$$p\{N_{\text{MGoR}} = n\} = \binom{N_{\text{Go}}}{n} \cdot (P_{\text{MGoR}})^n \cdot (1 - P_{\text{MGoR}})^{N_{\text{Go}}-n} \quad (5.1)$$

where N_{Go} is the real number of road segments the user has driven through during the invoice period.

Assuming all road segments have the same fee, an invoice has an undercharging error equal to or lower than M_e % of the correct bill if the number of missed geo-object recognitions in the invoice computation does not exceed $N_{\text{MGoR,max}}$:

$$N_{\text{MGoR,max}} = \lfloor M_e/100 \cdot N_{\text{Go}} \rfloor \quad (5.2)$$

where the operator $\lfloor x \rfloor$ is the highest integer lower than x .

At least I % of the invoices must meet the accuracy requirement. That is, the undercharging error of any invoice must not exceed M_e % with a probability equal to or higher than I %:

$$p\{N_{\text{MGoR}} \leq N_{\text{MGoR,max}}\} = \sum_{n=0}^{N_{\text{MGoR,max}}} p\{N_{\text{MGoR}} = n\} \geq \frac{I}{100} \quad (5.3)$$

where $p\{N_{\text{MGoR}} = n\}$ is given in eq.(5.1).

Introducing the expressions (5.1) and (5.2) in equation (5.3), the maximum allowable probability of missed geo-object recognition P_{MGoR} can be related to the ETC high-level requirements (I, M_e) and the real number of geo-objects the user has driven through during the invoice period (N_{Go}).

$$\sum_{n=0}^{\lfloor M_e/100 \cdot N_{\text{Go}} \rfloor} \left\{ \binom{N_{\text{Go}}}{n} \cdot (P_{\text{MGoR}})^n \cdot (1 - P_{\text{MGoR}})^{N_{\text{Go}}-n} \right\} \geq \frac{I}{100} \quad (5.4)$$

The required P_{MGoR} is a function of N_{Go} and the invoice accuracy specifications (Figure 5.1). The required P_{MGoR} decreases as the number of used geo-objects N_{Go} augments, until N_{Go} is sufficiently high to increase the number of allowed missed geo-object recognitions $N_{\text{MGoR,max}}$ in one. At that point the required P_{MGoR} is significantly relaxed (increased) with respect to lower N_{Go} .

Given the invoice accuracy specifications (I, M_e), the worst case, i.e. the lowest P_{MGoR} , occurs when the user has driven through $N_{\text{Go}} = \lfloor 100/M_e \rfloor - 1$ geo-objects during the period for which the invoice is computed. This is the maximum number of geo-objects for which a single missed recognition would cause an undercharging error higher than M_e %, so in this case $N_{\text{MGoR,max}} = 0$. The P_{MGoR} that still meets the invoice accuracy specifications in the worst case is obtained setting $N_{\text{Go}} = \lfloor 100/M_e \rfloor - 1$, and therefore $N_{\text{MGoR,max}} = \lfloor M_e/100 \cdot N_{\text{Go}} \rfloor = 0$, in eq.(5.4):

$$P_{\text{MGoR}} \leq 1 - \left(\frac{I}{100} \right)^{\frac{1}{\lfloor 100/M_e \rfloor - 1}} \quad (5.5)$$

Table 5.1 contains the worst case values of P_{MGoR} for various invoice high-level requirements. These values correspond to the most demanding cases; a different N_{Go} would result in less restrictive (higher) P_{MGoR} for the same invoice accuracy specifications.

Table 5.1. Maximum probability of missed geo-object recognition (P_{MGoR}) for different invoice requirements in the worst case.

		Maximum invoice error (M_e %)		
		1 % ($N_{Go} = 99$)	0.1 % ($N_{Go} = 999$)	0.01 % ($N_{Go} = 9999$)
Percentage of invoices meeting the maximum error requirement (I %)	99 %	10^{-4}	10^{-5}	10^{-6}
	99.9 %	10^{-5}	10^{-6}	10^{-7}
	99.9 %	10^{-6}	10^{-7}	10^{-8}

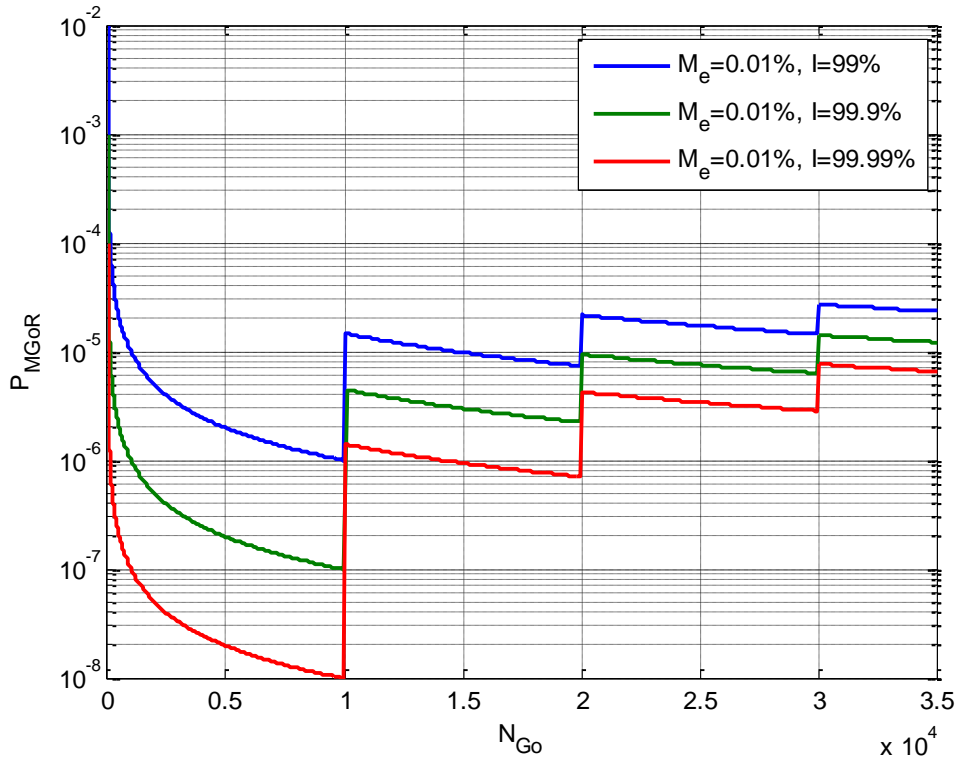


Figure 5.1. Probability of missed geo-object recognition needed for different invoice requirements.

5.3.1.2. Overcharging

The overcharging requirement at geo-object level is given by the maximum allowable probability of false geo-object recognition (P_{FGoR}). If false segment recognitions are independent events that occur with a constant probability equal to P_{FGoR} , the probability of making n false geo-object recognitions (N_{MGoR}) during the invoice period is:

$$p\{N_{FGoR} = n\} = \binom{N_{PFGoR}}{n} \cdot (P_{FGoR})^n \cdot (1 - P_{FGoR})^{N_{PFGoR} - n} \quad (5.6)$$

where N_{PFGoR} is the number of potentially false geo-object recognitions during the invoice period, that is, the number of road segments that, although the user has not driven through them, are susceptible to be incorrectly recognized with a probability P_{FGoR} .

Assuming all road segments have the same charge, an invoice has an overcharging error equal to or lower than M_e % of the correct bill if the number of false geo-object recognitions in the invoice computation does not exceed $N_{\text{FGoR,max}}$:

$$N_{\text{FGoR,max}} = \lfloor M_e/100 \cdot N_{\text{Go}} \rfloor \quad (5.7)$$

where N_{Go} is the total number of geo-objects driven by the user during the invoice period.

Since the overcharging error of any invoice must be below M_e % with a probability equal to or higher than I %:

$$p\{N_{\text{FGoR}} \leq N_{\text{FGoR,max}}\} = \sum_{n=0}^{N_{\text{FGoR,max}}} p\{N_{\text{FGoR}} = n\} \geq \frac{I}{100} \quad (5.8)$$

where $p\{N_{\text{FGoR}} = n\}$ is given in eq.(5.6).

Introducing the expressions (5.6) and (5.7) in eq.(5.8), the maximum allowable probability of false geo-object recognition (P_{FGoR}) that meets the invoice requirements (I, M_e) can be related to the number potential false geo-object recognitions (N_{PFGoR}) and the number of geo-objects really used (N_{Go}) during the invoice period:

$$\sum_{n=0}^{\lfloor M_e/100 \cdot N_{\text{Go}} \rfloor} \left\{ \binom{N_{\text{PFGoR}}}{n} \cdot (P_{\text{FGoR}})^n \cdot (1 - P_{\text{FGoR}})^{N_{\text{PFGoR}}-n} \right\} \geq \frac{I}{100} \quad (5.9)$$

Figure 5.2 shows the required P_{FGoR} as a function of N_{PFGoR} , I % and $N_{\text{FGoR,max}}$ (note that $N_{\text{FGoR,max}}$ is a function of N_{Go} and the invoice percentage error M_e %, given in eq. (5.7)). Being I % and $N_{\text{FGoR,max}}$ fixed, the required P_{FGoR} becomes more stringent (decreases) as the number of geo-objects susceptible to be false recognized (N_{PFGoR}) increases.

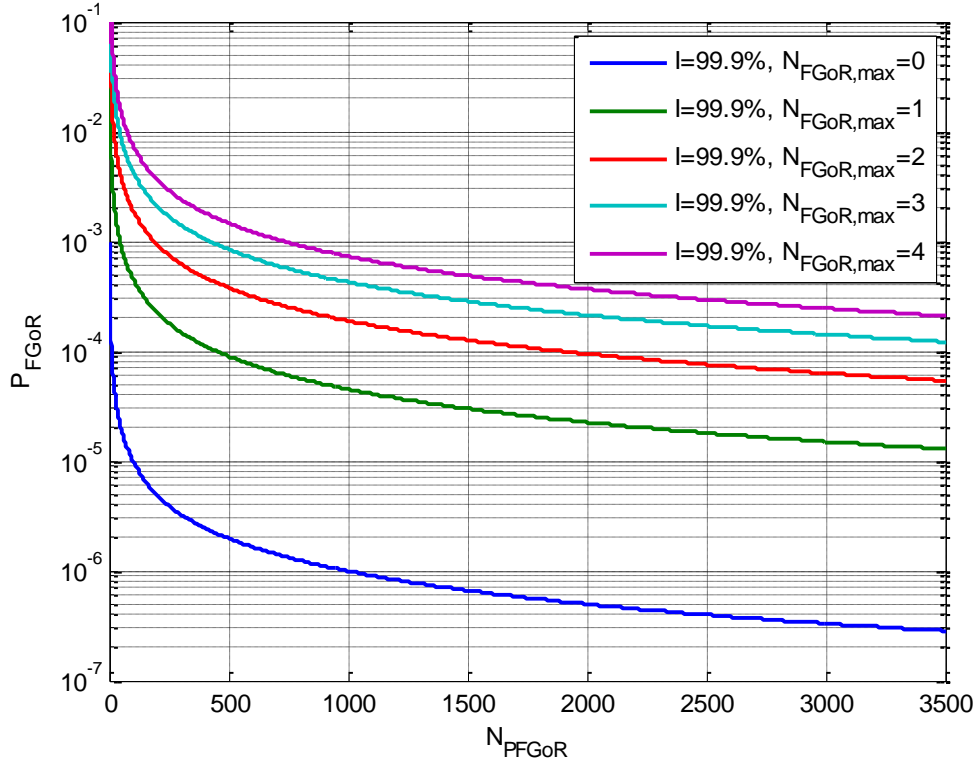


Figure 5.2. Probability of false geo-object recognition needed for different invoice requirements.

Given the invoice accuracy specifications I and M_e , the worst case, i.e. the lowest P_{FGoR} , for any N_{PFGoR} occurs when $N_{FGoR,max} = 0$. This happens when the number of geo-objects really used (N_{GO}) is so low that a single false geo-object recognition would cause an overcharging error greater than M_e % of the real invoice for that user. Introducing $N_{FGoR,max} = \lfloor M_e/100 \cdot N_{GO} \rfloor = 0$ into eq.(5.9), the worst case P_{FGoR} results:

$$P_{FGoR} \leq 1 - \left(\frac{I}{100} \right)^{\frac{1}{N_{PFGoR}}} \quad (5.10)$$

As opposed to the undercharging case, there is no lower bound in the required P_{FGoR} , which is a monotonically decreasing function of N_{PFGoR} .

The reason is that in the undercharging case, the maximum allowed number of missed segments ($N_{MGoR,max}$) and the probability of having a certain number of missed segments in the invoice ($p\{N_{MGoR}\}$) depend on the total number of route segments used (N_{GO}). The higher N_{GO} , the higher the probability of having more missed segments. Nevertheless, the fee that should be really charged to a vehicle for using the road infrastructure during a given period increases with the number of geo-objects he has used, N_{GO} . Consequently, the number of allowed missed geo-objects $N_{MGoR,max}$ that reaches a specific undercharging percentage of the real invoice charge also increases with N_{GO} . Both effects compensate each other, providing the P_{MGoR} lower bound of eq.(5.5).

In the overcharging case, the probability of having a certain number of false segment recognitions in the invoice ($p\{N_{FGoR}\}$) increases with the number of segments susceptible to be overcharged

(N_{PFGoR}), while the maximum allowed number of false segment recognitions ($N_{\text{FGoR,max}}$) depends on the total number of used segments (N_{Go}). Therefore, $p\{N_{\text{FGoR}}\}$ and $N_{\text{FGoR,max}}$ are independent from each other. For example, in the case of a user that has not driven through the tolled road network at all, a single false geo-object recognition would exceed the allowable invoice error, regardless the number of segments susceptible to be overcharged. And clearly, the higher is this number, the lower is the P_{FGoR} needed to avoid false recognitions.

Consequently, if an invoice percentage error must be assured, the number of segments likely to be overcharged must be limited. Another option is to express the overcharging requirement as the probability of false geo-object recognition, knowing that its performance depends on the number of potentially false geo-object recognitions (N_{PFGoR}).

5.3.2. Conclusions and proposition of geo-object level requirements

The maximum allowable probabilities of missed and false geo-object recognition have been derived assuming that all geo-objects in the road network have the same fee and the same probability of being missed or false recognized. Furthermore, the fact of missing or false detecting a geo-object is assumed to be an independent event. ETC systems need to be adapted to the road network characteristics and therefore these assumptions may not be exactly held. For example, a GPS satellite may be affected by a major service failure during several hours before it is repaired or warned, introducing some correlation in the probability of erroneous geo-object recognition to users employing the signals from that satellite during the failure period. Nevertheless, the methodology presented in section 5.3.1 to relate the invoice accuracy specifications with the geo-object requirements can be adapted to any particular road topology, and equations (5.5) and (5.10) still provide a good analytical approximation of the geo-object requirements of real systems.

In this work a missed geo-object recognition probability of 10^{-4} is proposed:

$$P_{\text{MGoR}} = 10^{-4} \quad (5.11)$$

It corresponds to the value given in [EG9, 2006]. The requirement is more severe than the toll collection efficiency rates reported by operating GPS-based ETC systems, which are between 98.99% and 99.75% [Toll Collect, 2011 (a)], [SkyToll, 2011 (b)], although these rates also include road segments missed due to non-technical reasons. Moreover, under the conditions of equation (5.5), a missed geo-object probability of 10^{-4} assures that the undercharging error of at least $I = 99\%$ of all invoices processed by the toll system do not exceed $M_e = 1\%$ of the real charge, regardless the number of road segments crossed by the user. The same invoice accuracy specification $I = 99\%$ and $M_e = 1\%$ is given in [ARS, 2006].

As in [EG9, 2006], the proposed false geo-object recognition rate is 10^{-6} :

$$P_{\text{FGoR}} = 10^{-6} \quad (5.12)$$

For example, under the assumptions of equation (5.10), a false geo-object probability of 10^{-6} assures that $I = 99\%$ of all the invoices processed by the toll system will not have a single false geo-object detection, if the number of geo-objects likely to be false recognized of a user during the invoice period does not exceed $N_{\text{PFGoR}} = 10050$.

5.4. GNSS integrity requirements

A snapshot RAIM algorithm performing only Fault Detection (FD) functions is assumed (no fault identification and exclusion capabilities are taken into account). The alert is raised when there is a fault detection because the RAIM is a snapshot algorithm. The general diagram of FDE events of Figure 2.3 is simplified for this type of RAIM as depicted in Figure 5.3. The probability of missed alert is equal to the probability of missed detection and will be denoted P_{MD} , and the probability of false alarm is equal to the probability of false detection and will be denoted P_{FA} .

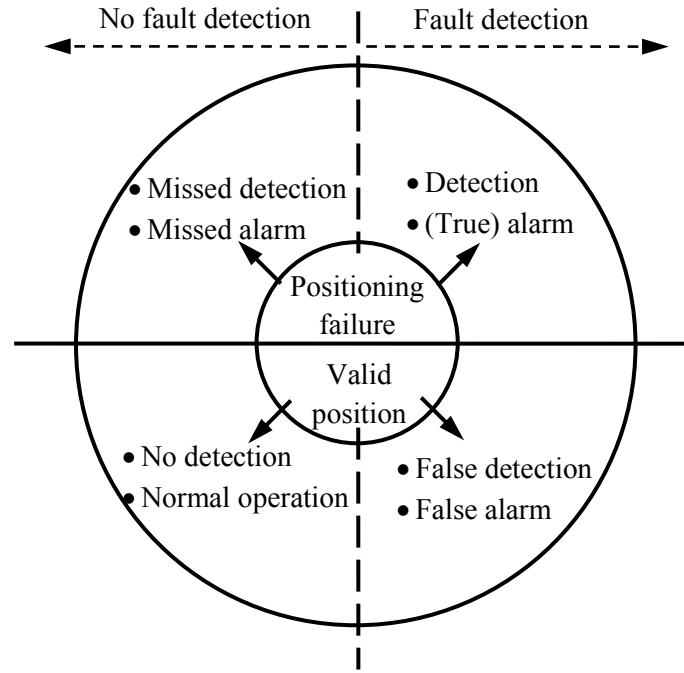


Figure 5.3. Diagram of events for snapshot fault detection RAIM algorithms.

This section derives the GNSS integrity requirements needed to meet the geo-object requirements, that is, the values of the P_{MD} and P_{FA} that meet the missed and false geo-object recognition specifications. The RAIM is assumed to monitor integrity with constant values of P_{MD} and P_{FA} , as it does in civil aviation.

The relationship between geo-object (P_{MGoR} , P_{FGoR}) and RAIM (P_{MD} , P_{FA}) requirements depends on the geo-object recognition algorithm. The recognition rule of eq.(3.6) is followed: a road segment is charged to a user if the number of independent valid positions inside the geo-object is equal to or higher than a threshold:

$$\text{road segment is charged} \Leftrightarrow N_{\text{valid,in}} \geq N_{Th}$$

The GNSS integrity specifications depend therefore on the minimum number of positions required to decide the user has been inside the geo-object (N_{Th}), the number of independent positions estimated during the user trajectory through the road segment (or nearby in the overcharging case), and on how many of them are affected by a positioning error exceeding the alert limit.

The number of independent estimated positions per segment depends on several factors such as the segment length, the time spent by the user inside it (or nearby in the overcharging case) and the correlation time of position errors.

5.4.1. Definitions

This subsection presents the main concepts and events involved in the relationship between the RAIM parameters (P_{MD} and P_{FA}) and the geo-object missed and false recognition specifications (P_{MGoR} and P_{FGoR}).

Geo-object Recognition Process: it is the process followed to decide whether a user has been or not inside a road segment. It comprises the selection of the valid estimated positions for ETC and the geo-object recognition algorithm.

Detectable Failure (F_D): detectable failures are the failures the RAIM has been designed to detect. For example, Weighted Least Squares Residuals (WLSR) RAIM algorithms are designed to detect pseudorange failures, and not other failures like receiver hardware or software errors that may cause as well the a positioning error.

Undetectable Failure (F_U): failures the RAIM has not been designed to detect but contribute to an erroneous geo-object recognition. Nevertheless, a RAIM may detect a failure it has not been designed to detect, without guaranteeing the P_{MD} is respected.

Pseudorange Failure (F_{PSR}): pseudorange failures are pseudorange measurement errors not considered in the nominal case, and consequently not included in the nominal measurement model. In this work, pseudorange failures are assumed to be caused only by major service failures.

Positioning Failure (PF): a PF occurs whenever the difference between the estimated and the true positions exceeds the alert limit. Since this work focuses in road applications, only the horizontal positioning failure will be studied:

$$PF \Leftrightarrow |e_H| = |x_H - \hat{x}_H| > HAL \quad (5.13)$$

Valid Position ($\hat{x}_{H,valid}$): an estimated horizontal position \hat{x}_H is declared valid for ETC purposes whenever the RAIM is available and has not detected a failure:

$$\hat{x}_{H,valid} \Leftrightarrow (HPL \leq HAL) \& \text{ (no alert)} \quad (5.14)$$

An estimated position may not be declared valid because of different reasons: it is not possible to monitor its integrity (due to insufficient number of visible satellites, for instance), RAIM unavailability (i. e. $HPL > HAL$), or a failure detected by the RAIM.

Undetected Positioning Failure (UPF): undetected positioning failures are those estimated positions that contain a positioning failure but are declared valid by the RAIM:

$$UPF \Leftrightarrow (|e_H| > HAL) \& \text{ (no alert)} \quad (5.15)$$

Geo-object Misleading Position (GoMP): geo-object misleading positions are those estimated positions, declared valid by the RAIM, that are in a different side of the geo-object boundaries than the true position (that is, a valid estimated position outside the geo-object when the user is inside it, and vice versa):

$$\hat{x}_H \text{ is GoMP} \Leftrightarrow \begin{cases} (\hat{x}_H \text{ inside the geo object}) \& (x_H \text{ outside the geo object}) \& \text{(no alert)} \\ (\hat{x}_H \text{ outside the geo object}) \& (x_H \text{ inside the geo object}) \& \text{(no alert)} \end{cases} \quad (5.16)$$

As opposed to the civil aviation case, not all Undetected Positioning Failures (UPF) occurred in GNSS-based toll systems have negative consequences. Only those UPF constituting a Geo-object Misleading Position (GoMP) may cause a geo-object recognition error (Figure 5.4).

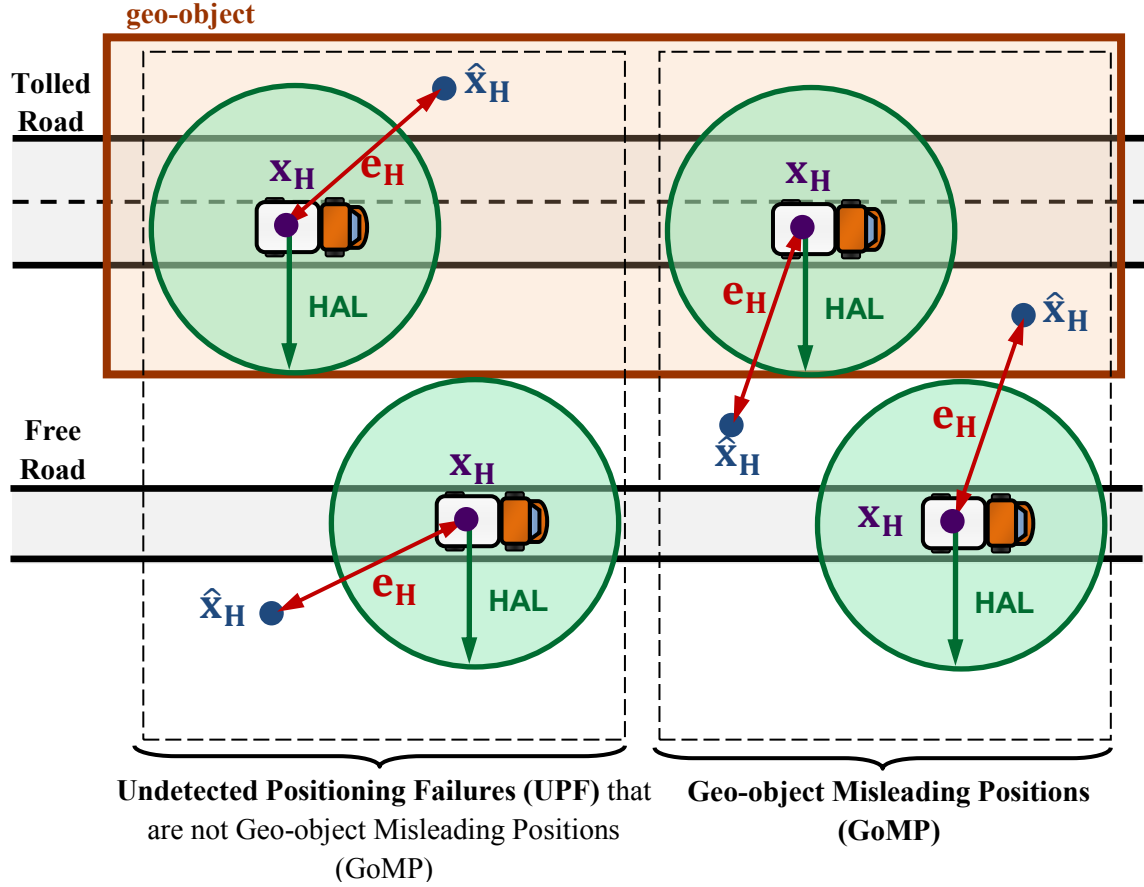


Figure 5.4. Examples of Undetected Positioning Failures (UPF) and Geo-object Misleading Positions (GoMP).

5.4.2. Failure tree of geo-object misleading positions (GoMP)

Geo-object Misleading Positions (GoMP) are those estimated positions, declared valid for its use in ETC by the RAIM, that contain positioning failures which contribute to geo-object recognition errors. Various failures at different stages and components of the geo-object recognition process can lead to a GoMP (Figure 5.6). They can be divided in three groups:

- 1) Pseudorange failures (F_{PSR}). In this thesis they are caused by major service failures.
- 2) Positioning failures not caused by a pseudorange failure ($PF_{non-PSR}$). For example, positioning failures caused by receiver hardware or processing errors.
- 3) Failures that generate a GoMP, but not a positioning failure ($GoMP_{non-PF}$). For example, an error in the geo-object boundaries database can make the segment detection algorithm to consider an estimated position to be outside the geo-object when the user is inside, or vice versa, even if the positioning error does not exceed the alert limit.

The probability of occurrence of each of these failures is known or can be set as a specification the GNSS receiver and the associated algorithm implementations must meet. A failure tree is used to derive, from these known probabilities, the probability of occurrence of Geo-object Misleading Positions (GoMP).

a) Undetected Positioning Failures caused by a Pseudorange Failure

Integrity monitoring techniques like WLSR RAIM algorithms are designed to protect only against pseudorange failures. Assuming pseudorange failures (F_{PSR}) are caused by major service failures, they are sufficiently large to cause a positioning error exceeding the alert limit (HAL). Therefore, in this work pseudorange failures always generate a positioning failure:

$$p\{PF_{PSR} | F_{PSR}\} = 1 \quad (5.17)$$

where PF_{PSR} stands for Positioning Failure caused by a Pseudorange Failure.

Whenever a Positioning Failure caused by a Pseudorange Failure (PF_{PSR}) occurs, the RAIM algorithm does not detect it with a probability lower than the probability of missed detection (P_{MD}):

$$p\{UPF_{PSR} | PF_{PSR}\} < P_{MD} \quad (5.18)$$

where UPF_{PSR} stands for Undetected Positioning Failure caused by a Pseudorange Failure.

Introducing eq.(5.17) into (5.18):

$$p\{UPF_{PSR} | F_{PSR}\} < P_{MD} \quad (5.19)$$

b) Undetected Positioning Failures not caused by a Pseudorange Failure ($PF_{non-PSR}$)

GNSS receivers and RAIM implementations may suffer from other failures different than pseudorange ones, like hardware or software errors, that lead to positioning failures ($PF_{non-PSR}$). RAIM algorithms are not designed to detect these failures because their origin is not a pseudorange failure. Consequently, neglecting the effect of RAIM false alerts, whenever these failures occur, they become undetected positioning errors:

$$p\{UPF_{non-PSR} | PF_{non-PSR}\} = 1 \quad (5.20)$$

where UPF_{PSR} stands for Undetected Positioning Failure caused by any Failure different than a Pseudorange Failure.

c) Geo-object Misleading Positions (GoMP) caused by Positioning Failures

As explained in section 5.4.1 and Figure 5.4, only those Undetected Positioning Failures (UPF), originated by a pseudorange failure or not, in which the estimated position is outside the geo-object when the user is inside it, or vice versa, are Geo-object Misleading Positions (GoMP) and contribute to road segment recognition errors.

The probability that an UPF becomes a GoMP depends on the magnitude and direction of the positioning error, and on the user position with respect to the geo-object boundaries. The worst case is taken, in which every undetected positioning failure, caused by a pseudorange failure or not, generates a GoMP:

$$p\{GoMP | UPF\} = 1 \quad (5.21)$$

The probability of a geo-object misleading position given a pseudorange failure is obtained combining equations (5.19) and (5.21):

$$p\{ \text{GoMP} \mid F_{\text{PSR}} \} < P_{\text{MD}} \quad (5.22)$$

The probability of a geo-object misleading position given a positioning failure not originated by a pseudorange failure is obtained combining equations (5.20) and (5.21):

$$p\{ \text{GoMP} \mid PF_{\text{non-PSR}} \} = 1 \quad (5.23)$$

d) Geo-object Misleading Position not caused by a Positioning Failure ($\text{GoMP}_{\text{non-PF}}$)

Some failures, like erroneous geo-object boundaries, may generate a GoMP without causing a positioning failure ($F_{\text{non-PF}}$). The occurrence of these failures cannot be detected with RAIM algorithms:

$$p\{ \text{GoMP} \mid F_{\text{non-PF}} \} = 1 \quad (5.24)$$

e) Summary

RAIM algorithms are designed to detect positioning failures caused by pseudorange failures. Taking the worst case in which any undetected positioning failure is a geo-object misleading position (GoMP), the probability that a pseudorange failure (F_{PSR}) generates a GoMP is lower than the RAIM's probability of missed detection (P_{MD}), as given in eq.(5.22). In this thesis, the probability of a pseudorange failure is the probability of a major service failure, which is given in [DoD, 2008].

The two remaining failure categories, i.e. positioning failures not caused by pseudorange failures ($PF_{\text{non-PSR}}$) and failures that generate a GoMP without causing a positioning failure ($F_{\text{non-PF}}$), are not detectable by RAIM algorithms. Therefore, these failures always generate a GoMP, as shown in equations (5.23) and (5.24). These failures can be described jointly as failures undetectable by the RAIM (F_U):

$$p\{ \text{GoMP} \mid F_U \} = 1 \quad (5.25)$$

The probability of the failures causing GoMP are known or set as requirements. Particularly, pseudorange failures are assumed to occur with the known probability of major service failures, and the maximum allowable probability of failures undetectable by the RAIM are set as an specification of the ETC system equipment.

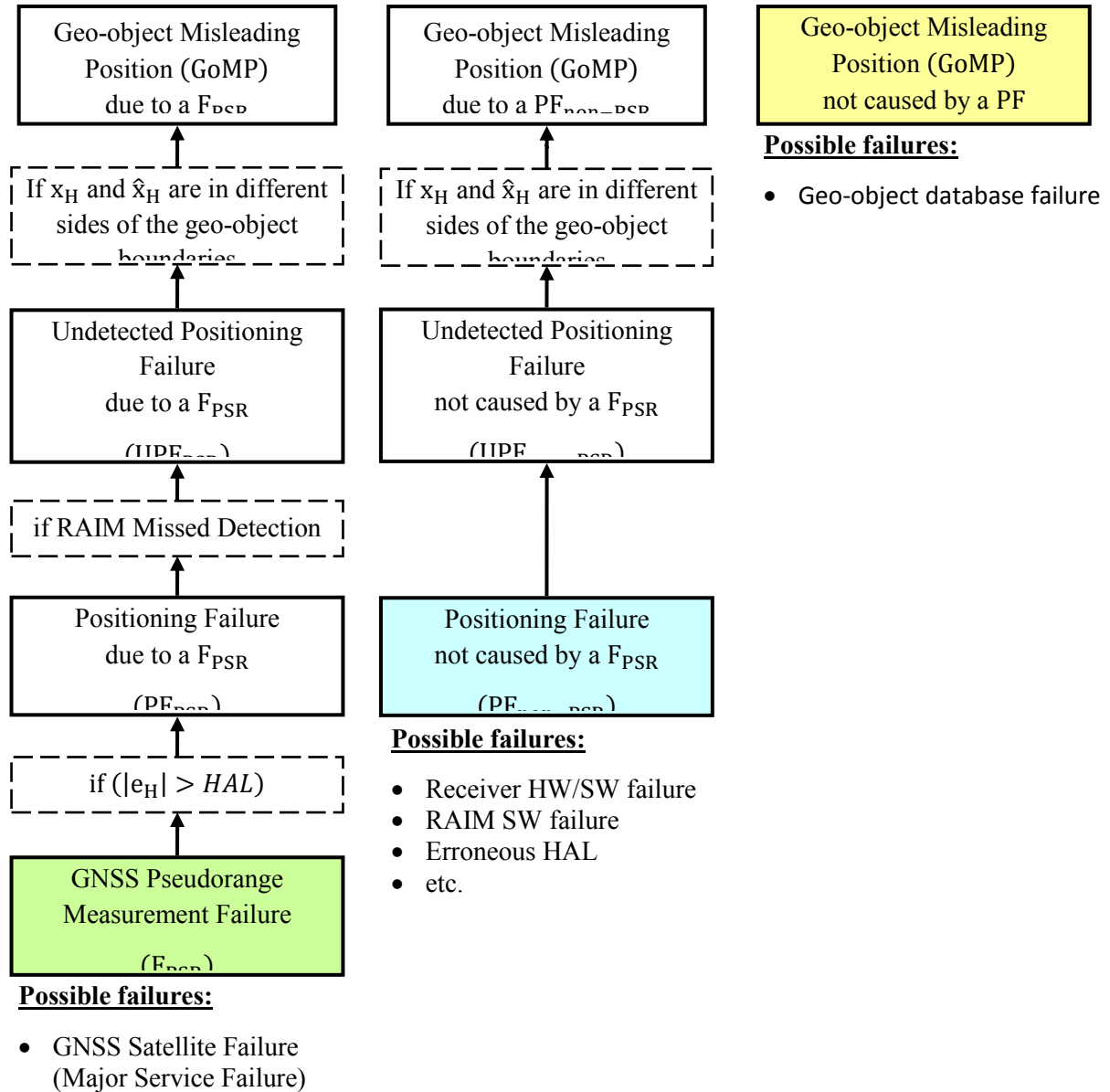


Figure 5.5. Failures that lead to a Geo-object Misleading Position (GoMP).

5.4.3. Scenario description

The probability of missing or incorrectly charging a geo-object depends on the number of geo-object misleading positions (GoMP) present in the geo-object recognition process. This section characterizes the presence of GoMP caused by pseudorange failures, the only ones the RAIM is designed to detect.

As described in the fault model used in this thesis (section 4.4), pseudorange failures are assumed to be caused by Major Service Failures (MSF). Major service failures only appear at specific instants but, once they occur, they remain during a period of time until the GNSS broadcasts the corresponding warning flag. Although this period can last up to six hours [DoD, 2008], a period of one hour is taken, which is a reasonable assumption for modernized GPS and Galileo. The probability of simultaneous major service failures is neglected.

For this reason, two scenarios are considered:

- **Nominal scenario: nominal pseudorange measurements.**

In this case, any of the satellites used to estimate the user trajectory along the road segment is affected by a major service failure. However, there may be Geo-object Misleading Positions (GoMP) caused by other failures the RAIM is not designed to detect.

- **Faulty scenario: faulty pseudorange measurement.**

In this case, all positions involved in the geo-object recognition process have been estimated with one faulty pseudorange due to a major service failure present during the whole user trajectory along the road segment. Consequently, any RAIM missed detection results in a Geo-object Misleading Position (GoMP).

A possible third scenario would occur whenever a major service failure appears or disappears while the user is crossing the road segment. In this case, only a portion of the estimated positions involved in the geo-object recognition process are affected by a pseudorange failure. This scenario will be simplified to the worst case as the faulty pseudorange measurement scenario.

The probability of the faulty scenario ($P_{\text{Faulty Scenario}}$), that is, the probability that all positions used in the geo-object recognition process are affected by a major service failure, is bounded by the probability that a major service failure is set in the period of time beginning one hour before the moment the user enters the geo-object, and finishing at the instant the user leaves it. Neglecting simultaneous failures and following a similar method as in eq.(4.78):

$$P_{\text{Faulty Scenario}} < N_{\text{sat}} \cdot (1 + t_{\text{Go}}) \cdot p_{\text{MSF,h}} = N_{\text{sat}} \cdot (1 + t_{\text{Go}}) \cdot 10^{-5} \quad (5.26)$$

where:

- t_{Go} is the duration of the user trajectory along the geo-object (in hours)
- $p_{\text{MSF,h}} = 10^{-5}/\text{satellite/h}$ is the probability of major service failure per satellite per hour [DoD, 2008]

Equation (5.26) is an upper bound of the faulty scenario probability that also includes the case in which a major service failure appears or disappears while the user moves along the road segment.

In order to set a value of $P_{\text{Faulty Scenario}}$, a 6-minute trajectory is proposed. This is the trajectory duration corresponding to a user moving at a constant speed of 50 km/h through a 5 km-long geo-object. Note that this is a pessimistic approximation because road segments in urban environments are expected to be shorter. The average number of visible satellites in urban environment using jointly GPS and Galileo constellations, obtained via simulations, is $N_{\text{sat}} = 12$. The satellite visibility simulation is completely described and analyzed in section 7.3. Introducing $t_{\text{Go}} = 6 \text{ min} = 0.1 \text{ h}$ and $N_{\text{sat}} = 12$ in eq.(5.26), the faulty scenario probability used hereafter is:

$$P_{\text{Faulty Scenario}} < 12 \cdot (1 + 0.1) \cdot 10^{-5} = 1.32 \cdot 10^{-4} \quad (5.27)$$

The probability of the nominal scenario is:

$$P_{\text{Nominal Scenario}} = 1 - P_{\text{Faulty Scenario}} = 1 - 1.32 \cdot 10^{-4} \quad (5.28)$$

The calculated $P_{\text{Faulty Scenario}}$ is the rate of segment recognition processes affected by a major service from the total number of processes managed by the toll system. Nevertheless, it is important to remark that for a specific user that travels through or near several consecutive segments, the probability that the recognition process of a given segment is disturbed by a major service failure is correlated with the fact that the failure was already present in previous segments or not, since they may remain up to one hour.

5.4.4. Probability of missed detection (P_{MD}) and probability of false alarm (P_{FA})

This section presents the method followed to derive the RAIM specifications (P_{MD} and P_{FA}) that meet the high level toll requirements, i.e. the maximum rate of missed geo-object recognition $P_{\text{MGoR}} = 10^{-4}$ and the maximum rate of false geo-object recognition $P_{\text{FGoR}} = 10^{-6}$.

With this purpose, the road segment overcharging (false geo-object recognition) and undercharging (missed geo-object) cases are analyzed in the nominal and faulty scenarios.

5.4.4.1. False geo-object recognition (Road segment overcharging)

This section analyzes the case of a user moving outside a road segment, but close enough to it so faulty estimated positions may be inside the geo-object. These positioning failures lying inside the geo-object become geo-object misleading positions (GoMP) if the RAIM does not detect them, contributing in that case to the false geo-object recognition, i.e. incorrectly charging the road segment.

Two events result in a false geo-object recognition. The first one is a number of GoMP (N_{GoMP}) equal to or higher than N_{Th} , the minimum number of positions inside the geo-object required to decide the user has been inside the road segment, defined in the geo-object recognition algorithm of eq.(3.6). If the number of valid positions is lower than N_{Th} , the geo-object recognition algorithm is not available and the probability of false segment recognition due to misleading positions is zero. The second event are those failures that directly overcharge a segment ($F_{\text{overcharge}}$), regardless the positioning information. Examples of these failures are implementation errors in the geo-object recognition algorithm.

The maximum allowed probability of false geo-object recognition (P_{FGoR}) must be divided between the two events that originate it (Figure 5.6):

$$P_{\text{FGoR}} = 10^{-6} = P_{\text{FGoR (failure)}} + P_{\text{FGoR (GoMP)}} \quad (5.29)$$

where:

- $P_{\text{FGoR (failure)}}$ is the maximum allowed probability that the geo-object recognition process suffers a failure that directly causes the segment overcharging ($F_{\text{overcharge}}$)
- $P_{\text{FGoR (GoMP)}}$ is the maximum allowed probability that a segment is overcharged due to an excessive number of GoMP:

$$p\{N_{\text{GoMP}} \geq N_{\text{Th}}\} \leq P_{\text{FGoR (GoMP)}} \quad (5.30)$$

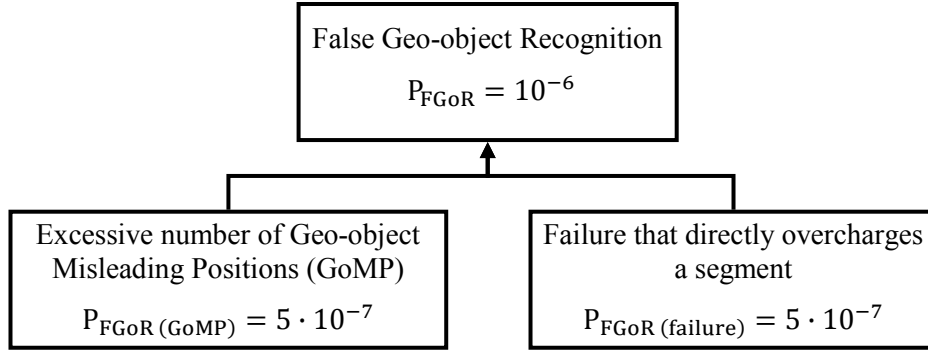


Figure 5.6. Events that lead to a false geo-object recognition.

The following allocation of P_{FGoR} between $P_{\text{FGoR}}(\text{failure})$ and $P_{\text{FGoR}}(\text{GoMP})$ is proposed:

$$P_{\text{FGoR}}(\text{failure}) = 5 \cdot 10^{-7} \quad (5.31)$$

$$P_{\text{FGoR}}(\text{GoMP}) = 5 \cdot 10^{-7} \quad (5.32)$$

The probability $P_{\text{FGoR}}(\text{failure}) = 5 \cdot 10^{-7}$ is set as a toll system equipment specification.

The probability $P_{\text{FGoR}}(\text{GoMP})$ depends on the RAIM performance and on the occurrence of the different failures leading to a GoMP. The following subsections apply the required $P_{\text{FGoR}}(\text{GoMP}) = 5 \cdot 10^{-7}$ to the segment recognition case in the nominal and faulty case.

5.4.4.1.1. Nominal scenario (no pseudorange failures)

In this scenario, a user moves outside a road segment in the absence of a major service failure. All estimated positions that may be used in the geo-object recognition algorithm are free of pseudorange failures, although they can be affected by other failures undetectable by the RAIM (Figure 5.7). Whenever a user moves outside a road segment, this scenario occurs with a probability $P_{\text{Nominal Scenario}} = 1 - 1.32 \cdot 10^{-4}$.

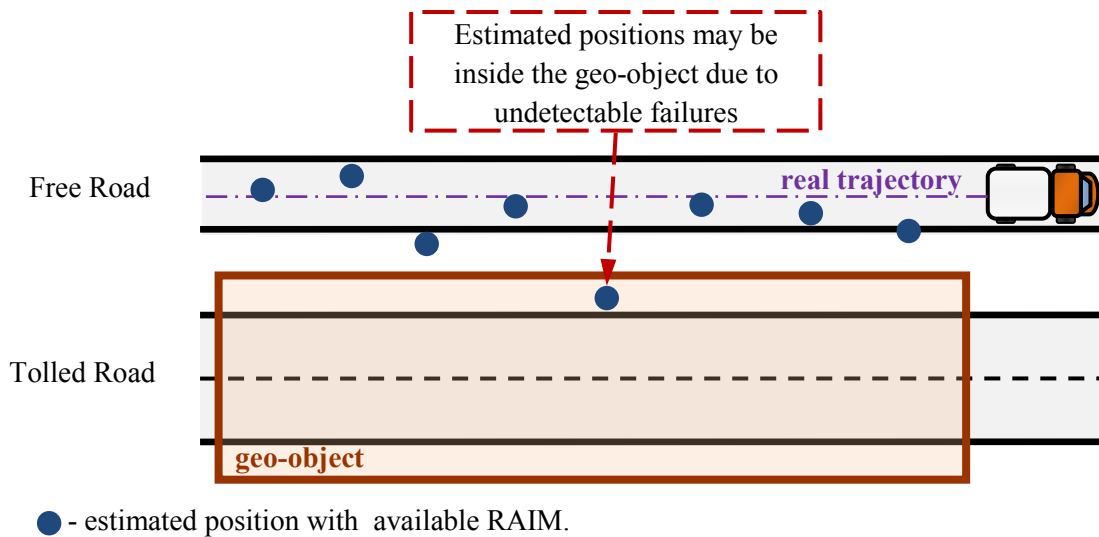


Figure 5.7. Example of scenario susceptible to false geo-object recognition without pseudorange failures.

All Geo-object Misleading Positions (GoMP) are caused by failures not detectable by the RAIM. Neglecting the probability of RAIM false detections, any undetectable failure automatically becomes a GoMP. This results in the following requirement on the number of GoMP caused by undetectable failures ($N_{\text{GoMP (Undetectable)}}$) in the nominal scenario, i.e. with no major service failure:

$$p\{N_{\text{GoMP (Undetectable)}} \geq N_{\text{Th}} \mid \text{Nominal Scenario}\} \leq \frac{P_{\text{FGoR (GoMP)}}}{P_{\text{Nominal Scenario}}} \leq P_{\text{FGoR (GoMP)}} \quad (5.33)$$

The worst case of eq.(5.25) is taken, in which undetectable failures always generate a GoMP. Moreover, the presence of undetectable failures is independent from the scenario type, nominal or faulty:

$$p\{N_{\text{GoMP (Undetectable)}} \geq N_{\text{Th}} \mid \text{Nominal Scenario}\} = p\{N_{\text{Undetectable Failure}} \geq N_{\text{Th}}\} \quad (5.34)$$

Hence, the toll system equipment must meet the following specification in order to fulfill the false geo-object recognition requirement in the nominal scenario:

$$p\{N_{\text{Undetectable Failure}} \geq N_{\text{Th}}\} \leq P_{\text{FGoR (GoMP)}} = 5 \cdot 10^{-7} \quad (5.35)$$

where $N_{\text{Undetectable Failure}}$ is the number of independent estimated positions affected by a failure not detectable by the RAIM while the user moves close to a road segment.

Let us remark that e overcharging requirement in the nominal scenario does not set any constraint to the RAIM parameters P_{MD} and P_{FA} .

5.4.4.1.2. Faulty scenario (major service failure)

In this scenario, a user moves outside a road segment in the presence of a major service failure. All estimated positions that may be used by the segment recognition algorithm are inside the geo-object due to pseudorange failures, so any RAIM missed detection results in a geo-object misleading position (Figure 5.8). Undetectable failures are not considered because all estimated positions are already faulty. Whenever a user moves outside a road segment, this scenario occurs with a probability $P_{\text{Faulty Scenario}} = 1.32 \cdot 10^{-4}$.

The RAIM is able to detect a pseudorange failure with a probability $(1 - P_{\text{MD}})$. As shown in eq.(5.22), any undetected failure becomes a Geo-object Misleading Position (GoMP). Therefore, with a constant probability of missed detection (P_{MD}), the number of GoMP ($N_{\text{GoMP (PSR)}}$), caused in this case by pseudorange failures, in the faulty scenario must meet:

$$p\{N_{\text{GoMP (PSR)}} = n \mid \text{Faulty Scenario}\} = \binom{N_{\text{F,PSR}}}{n} \cdot P_{\text{MD}}^n \cdot (1 - P_{\text{MD}})^{N_{\text{F,PSR}} - n} \quad (5.36)$$

where $N_{\text{F,PSR}}$ is the number of independent positions with available RAIM that are inside the geo-object due to a pseudorange failure. In the faulty scenario, $N_{\text{F,PSR}}$ is equal to the total number of independent positions estimated with available RAIM while the user moves close the road segment.

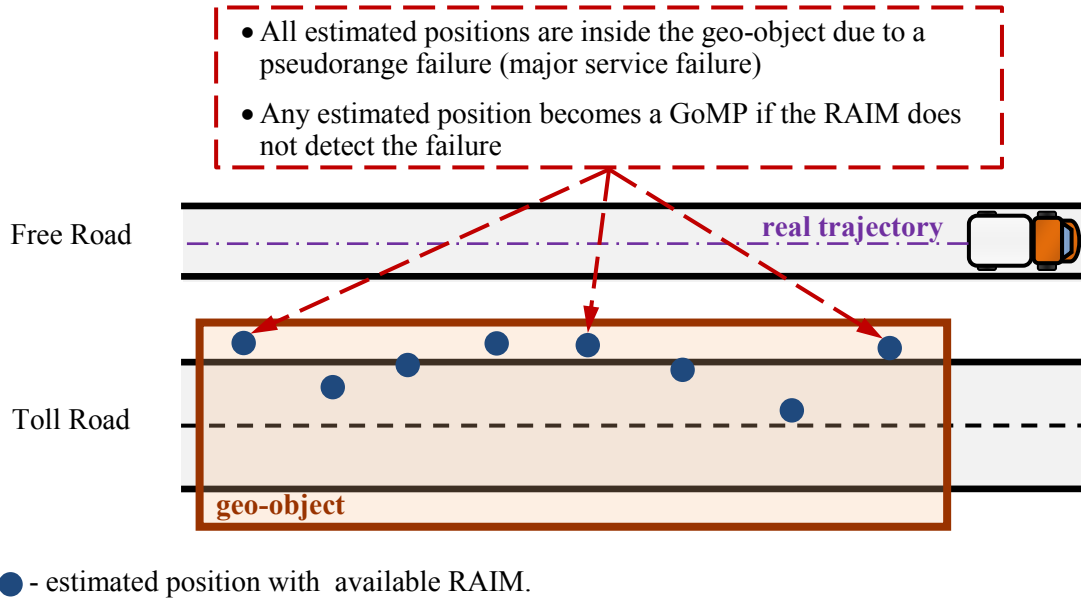


Figure 5.8. Example of scenario susceptible to false geo-object recognition affected by a major service failure.

The probability that the number of geo-object misleading positions ($N_{\text{GoMP (PSR)}}$) is equal to or higher than the threshold N_{th} , consequently overcharging the road segment, is:

$$\begin{aligned}
 & p\{N_{\text{GoMP (PSR)}} \geq N_{\text{Th}} \mid \text{Faulty Scenario}\} = \\
 & = 1 - \sum_{n=0}^{N_{\text{Th}}-1} p\{N_{\text{GoMP (PSR)}} = n \mid \text{Faulty Scenario}\} \quad (5.37)
 \end{aligned}$$

Figure 5.9 shows the probability of false geo-object recognition due to GoMP in the faulty scenario of eq.(5.37) with $P_{\text{MD}} = 10^{-3}$ as a function of the number of pseudorange failures ($N_{\text{F,PSR}}$) for various values of N_{Th} . The error probability increases with $N_{\text{F,PSR}}$ and decreases with higher N_{th} or lower P_{MD} .

Expression (5.37) must meet the required probability of false geo-object recognition $P_{\text{FGoR (GoMP)}}$:

$$p\{N_{\text{GoMP (PSR)}} \geq N_{\text{Th}} \mid \text{Faulty Scenario}\} \leq \frac{P_{\text{FGoR (GoMP)}}}{P_{\text{Faulty scenario}}} = \frac{5 \cdot 10^{-7}}{1.32 \cdot 10^{-4}} = 3.8 \cdot 10^{-3} \quad (5.38)$$

The P_{MD} is derived from eq.(5.38) as a function of N_{th} and the number of pseudorange failures ($N_{\text{F,PSR}}$), which in this case is the total number of independent positions (Figure 5.10). The P_{MD} becomes more stringent (lower) as $N_{\text{F,PSR}}$, the number of positions estimated along the road segment, grows. Increasing N_{th} relaxes (increments) P_{MD} .

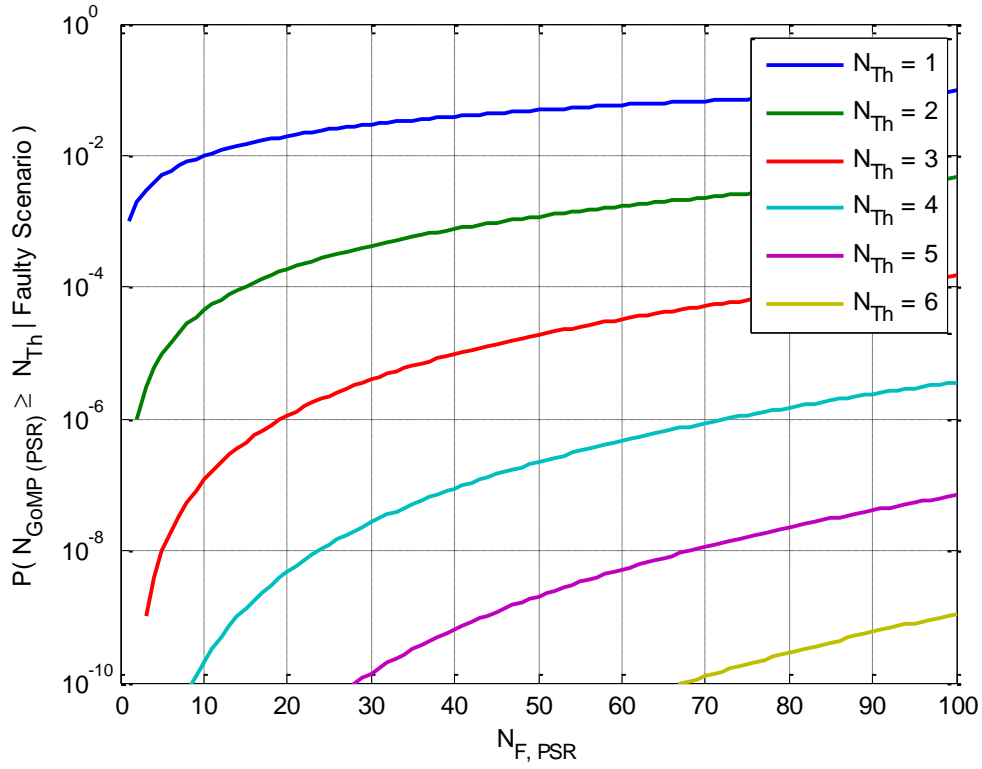


Figure 5.9. Probability of false recognized geo-object due to positioning failures caused by pseudorange failures with $P_{MD}=10^{-3}$ in the presence of a major service failure.

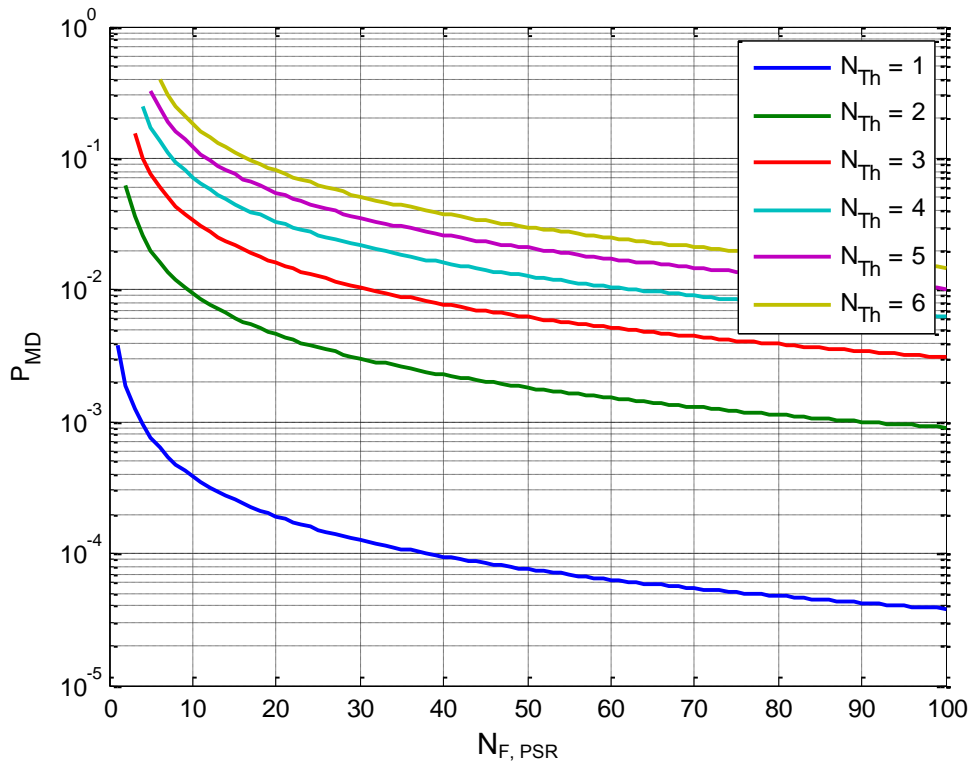


Figure 5.10. Maximum allowable probability of missed detection P_{MD} that meets the false geo-object recognition requirement $p\{N_{GoMP}(PSR) \geq N_{Th} | \text{Faulty Scenario}\} \leq 3.8 \cdot 10^{-3}$.

The threshold N_{th} is a design parameter of the recognition algorithm, but $N_{F,PSR}$ depends on the duration of the user trajectory near the road segment and on the RAIM availability, which in turn is a function of the geometry between the satellites and the user. In this work the worst case is taken, in which RAIM is always available so $N_{F,PSR}$ counts for each independent position.

Let us take 5 km as the maximum road segment length expected in rural or urban environments; the trajectory duration of a user moving at a constant speed of $v = 50$ km/h parallel to the geo-object is $t_{Go} = 5\text{km}/50\text{ km per hour} = 360$ seconds. Assuming two positions are independent when the time elapsed between them is at least $T_c = 5$ seconds, and that the RAIM always available, the maximum number of independent positions per segment is $N_{F,PSR} = 360/5 = 72$.

Table 5.2 shows the maximum allowable probability of missed detection P_{MD} required to meet the probability of false geo-object recognition ($P_{FGoR} = 10^{-6}$) with various thresholds of the geo-object recognition algorithm (N_{th}) and $N_{F,PSR} = 72$ independent position samples involved in the geo-object recognition process.

Table 5.2. Probability of missed detection P_{MD} that meets the overcharging requirement in the worst-case scenario.

N_{th}	1	2	3	4	5
P_{MD}	$5.3 \cdot 10^{-5}$	$1.3 \cdot 10^{-3}$	$4.4 \cdot 10^{-3}$	$8.7 \cdot 10^{-3}$	$1.4 \cdot 10^{-2}$

Let us remark that the decision of the RAIM fault detection algorithm with two different position estimates contaminated by the same a major service failure is likely to be highly correlated. Nevertheless, it can be uncorrelated by variations of the nominal errors and the satellite/user geometry. Since the number of independent positions estimated with the same faulty satellite ($N_{F,PSR}$) is likely to be low, the P_{MD} of Table 5.2 calculated with $N_{F,PSR} = 72$ can be taken as a worst case.

It is observed that the overcharging requirement in the faulty scenario is a constraint for the P_{MD} , but not for the P_{FA} .

5.4.4.2. Missed geo-object recognition (road segment undercharging)

This section analyzes the case of a user moving inside a road segment. Those independent positions lying outside the geo-object become Geo-object Misleading Positions (GoMP) if the RAIM does not detect the positioning failure, contributing to the missed geo-object recognition, i.e. not charging the road segment.

Two events result in a missed geo-object recognition. The first one is a number of positions, independent and declared valid by the RAIM, inside the geo-object ($N_{valid\ pos\ IN}$) lower than the threshold N_{Th} defined in the geo-object recognition algorithm of eq.(3.6). The second event are those failures that directly miss a segment ($F_{undercharge}$), regardless the positioning information. Examples of these failures are implementation errors in the geo-object recognition algorithm.

The maximum allowed probability of missed geo-object recognition (P_{MGoR}) must be divided between the two events that lead to a segment undercharging (Figure 5.11):

$$P_{\text{MGoR}} = P_{\text{MGoR (failure)}} + P_{\text{MGoR (valid pos IN)}} \quad (5.39)$$

where:

- $P_{\text{MGoR (failure)}}$ is the maximum allowed probability that the geo-object recognition process suffers a failure that directly causes the segment undercharging ($F_{\text{undercharge}}$)
- $P_{\text{MGoR (positions IN)}}$ is the maximum allowed probability that a geo-object is missed due to an insufficient number of independent and valid positions inside it:

$$p\{N_{\text{valid pos IN}} < N_{\text{Th}}\} \leq P_{\text{MGoR (valid pos IN)}} \quad (5.40)$$

The following allocation of P_{MGoR} between $P_{\text{MGoR (failure)}}$ and $P_{\text{MGoR (positions IN)}}$ is proposed (Figure 5.11):

$$P_{\text{MGoR (failure)}} = 5 \cdot 10^{-5} \quad (5.41)$$

$$P_{\text{MGoR (valid pos IN)}} = 5 \cdot 10^{-5} \quad (5.42)$$

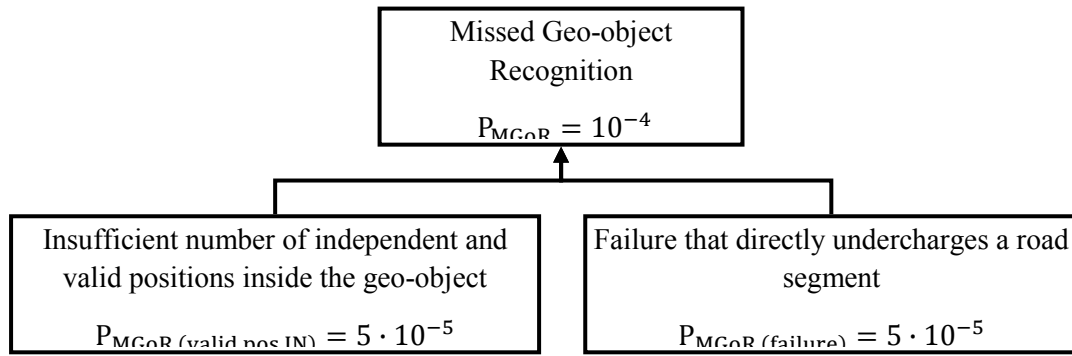


Figure 5.11. Failure tree that leads to a missed geo-object recognition.

The probability $P_{\text{MGoR (failure)}} = 5 \cdot 10^{-5}$ is set as a toll system equipment specification.

Several reasons may lead to a missed road segment due to an insufficient number of independent and valid positions inside the geo-object ($N_{\text{valid pos IN}} < N_{\text{Th}}$). These causes include RAIM fault detections, periods of RAIM unavailability, and the difficulty of estimating multiple independent positions in the case of insufficient satellite visibility, short road segments or long error correlation times. The following subsections apply the required $P_{\text{MGoR (valid pos IN)}} = 5 \cdot 10^{-5}$ in the nominal and faulty scenarios.

5.4.4.2.1. Nominal scenario (no pseudorange failure)

In this scenario, a user moves inside a road segment in the absence of a major service failure. All estimated positions that may be used in the geo-object recognition algorithm are free of pseudorange failures, although they can be affected by other failures undetectable by the RAIM (Figure 5.12).

Whenever a user moves inside a road segment, this scenario occurs with a probability $P_{\text{Nominal Scenario}} = 1 - 1.32 \cdot 10^{-4}$.

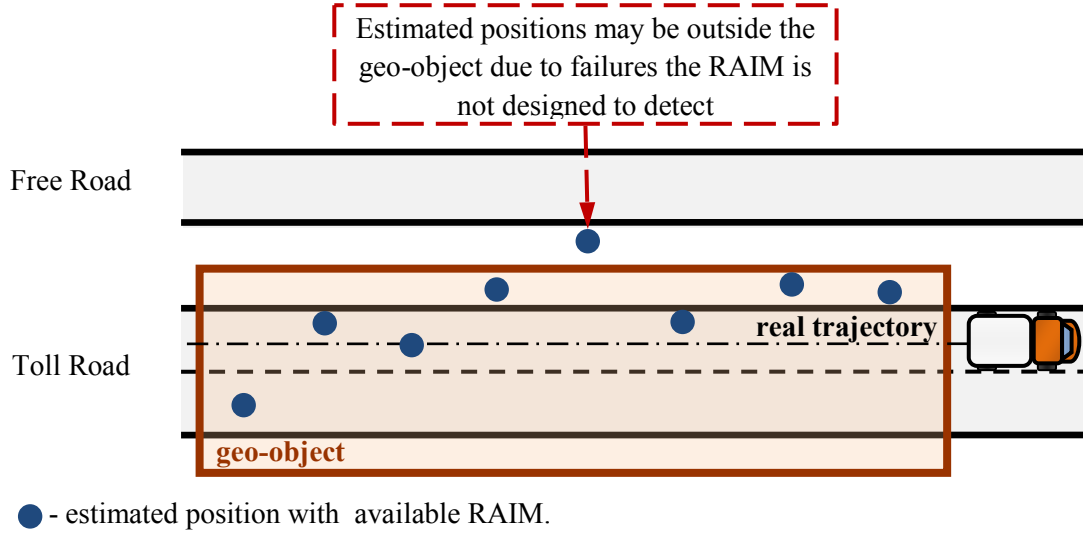


Figure 5.12. Example of scenario susceptible to missed geo-object recognition without pseudorange failures.

The total number of independent positions with available RAIM can be divided in faulty and fault free positions:

$$N_{IP} = N_{UF} + N_{FF} \quad (5.43)$$

where:

- N_{IP} is the total number of positions, independent and with available RAIM, estimated during the user trajectory along the road segment.
- N_{UF} is the number of positions affected by a failure. In the nominal scenario, failures are not detectable by the RAIM because they are not pseudorange failures. All of these estimated positions are outside the geo-object.
- N_{FF} is the number of fault-free positions, disturbed only by nominal errors. All of these estimated positions are inside the geo-object.

Faulty positions do not contribute to a correct segment recognition because they are outside the geo-object boundaries. The number of independent and valid positions inside the geo-object ($N_{\text{valid pos IN}}$) is the number of fault-free positions for which the RAIM has not detected a failure (i.e. false detection). Assuming a constant probability of false alarm P_{FA} :

$$p\{N_{\text{valid pos IN}} = n \mid \text{Nominal Scenario}\} = \binom{N_{FF}}{n} \cdot P_{FA}^{N_{FF}-n} \cdot (1 - P_{FA})^n \quad (5.44)$$

The probability that $N_{\text{valid pos IN}}$ is lower than the minimum threshold N_{th} to charge the road segment is:

$$p\{N_{\text{valid pos IN}} < N_{Th} \mid \text{Nominal Scenario}\} = \sum_{n=0}^{N_{Th}-1} p\{N_{\text{valid pos IN}} = n \mid \text{Nominal Scenario}\}$$

(5.45)

Figure 5.13 shows the probability of missing a road segment in the nominal scenario as a function of the number of fault-free positions (N_{FF}) for $P_{FA} = 10^{-3}$ and various thresholds N_{Th} . This probability decreases quickly as N_{FF} increases. For the same N_{FF} and P_{FA} , a higher threshold provides a higher probability of missing the segment.

The expression (5.45) must meet the required probability of missed geo-object recognition $P_{MGoR}(\text{valid pos IN})$:

The P_{FA} requirement is obtained from which derive the P_{FA} is:

$$p\{N_{\text{valid pos IN}} < N_{Th} \mid \text{Nominal Scenario}\} \leq \frac{P_{MGoR}(\text{valid pos IN})}{P_{\text{Nominal Scenario}}} = 5 \cdot 10^{-5} \quad (5.46)$$

The P_{FA} that meets the requirement (5.46) is a function of the number of fault-free positions (N_{FF}) and the threshold (N_{th}) (Figure 5.14). The requirement on the P_{FA} is considerably relaxed as N_{FF} augments, and becomes more stringent when N_{th} is increased.

From the two parameters affecting the P_{FA} , only the geo-object recognition algorithm threshold N_{th} is parameter under the control of the toll system designer. The threshold N_{th} also have effects in the required P_{MD} (see Figure 5.10).

The second parameter, the number of independent and fault-free positions estimated during the user trajectory (N_{FF}) is not fully under control. It depends on the total number of independent positions with available RAIM (N_{IP}) and on the probability of positioning failures. In fact, N_{IP} depends of the duration of the user trajectory through the road segment, the error correlation time and the RAIM availability, which in turn is a function of the geometry between the visible satellites and the user. Therefore, N_{FF} depends on the environment. This is one of the reasons why chapter 7 analyzes the performance of toll systems and RAIM algorithms via simulations in different scenarios.

If the total number N_{IP} of independent positions with available RAIM is known, the following requirement can be set to the number N_{UF} of undetectable failures:

$$\begin{aligned} \sum_{n=0}^{N_{IP}-1} p\{N_{UF} = n\} \cdot p\{N_{\text{valid pos IN}} < N_{Th} \mid \text{Nominal Scenario} \& N_{FF} = N_{IP} - n\} \leq \\ & \leq \frac{P_{MGoR}(\text{valid pos IN})}{P_{\text{Nominal Scenario}}} = 5 \cdot 10^{-5} \end{aligned} \quad (5.47)$$

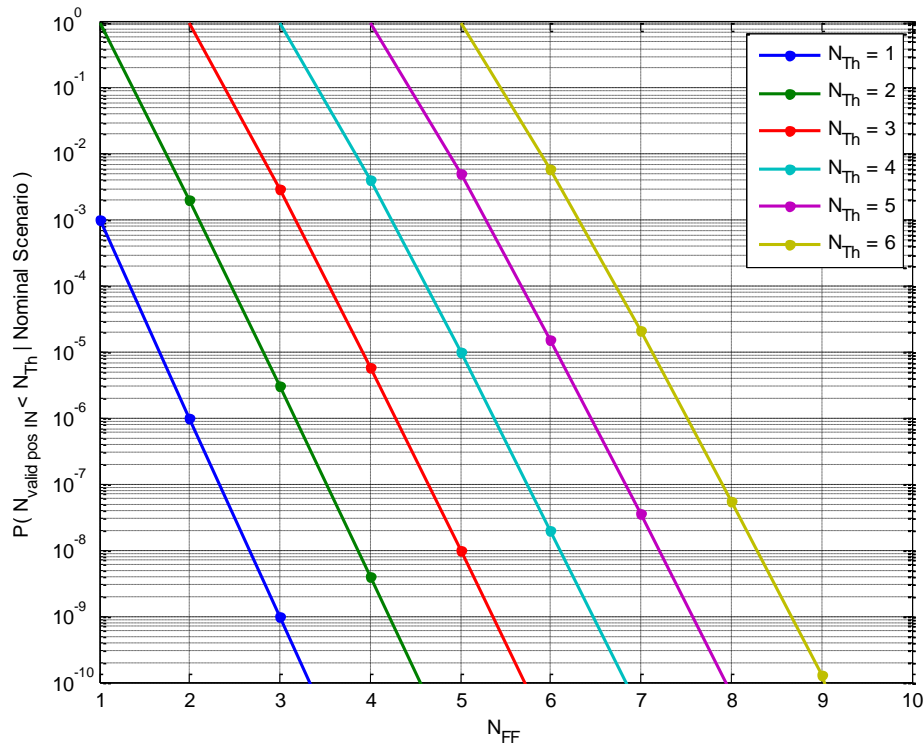


Figure 5.13. Probability of missed geo-object recognition due to false detections with $P_{\text{FA}} = 10^{-3}$.

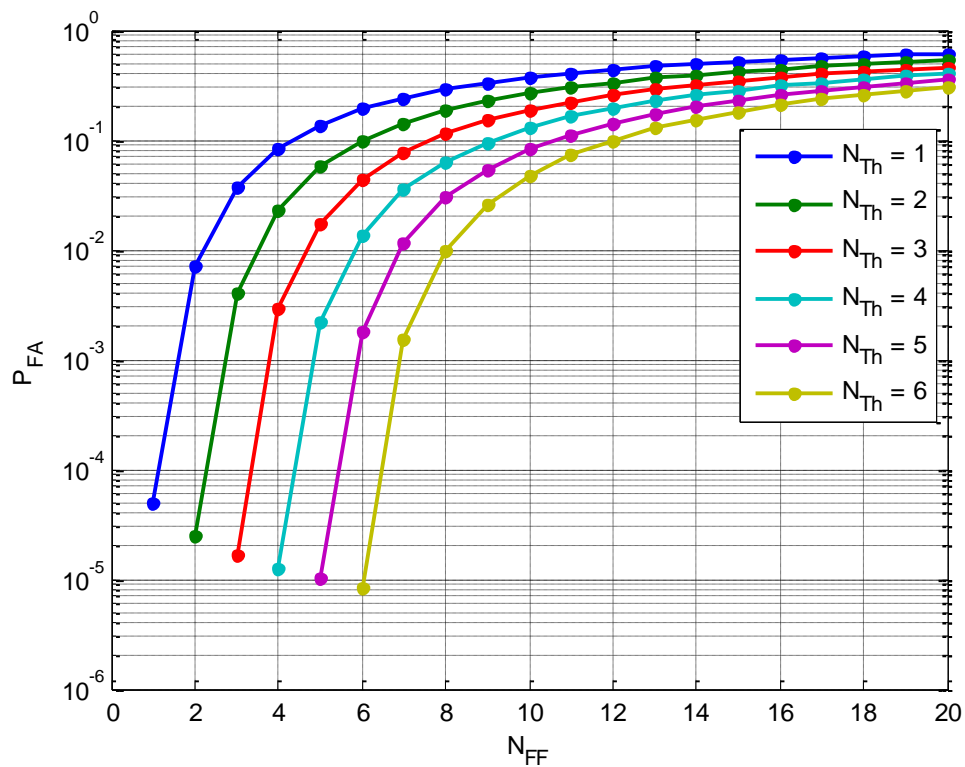


Figure 5.14. Maximum allowable probability of false alarm P_{FA} that meets the missed geo-object recognition requirement $p\{N_{\text{valid pos IN}} < N_{\text{Th}} | \text{Nominal Scenario}\} \leq 5 \cdot 10^{-5}$.

5.4.4.2.2. Faulty scenario (major service failure)

In this scenario, a user moves inside a road segment in the presence of a major service failure that makes all estimated positions to be outside the geo-object (Figure 5.15). Undetectable failures are not considered because all estimated positions are already faulty. Whenever a user moves inside a road segment, this scenario occurs with a probability $P_{\text{Faulty Scenario}} = 1.32 \cdot 10^{-4}$.

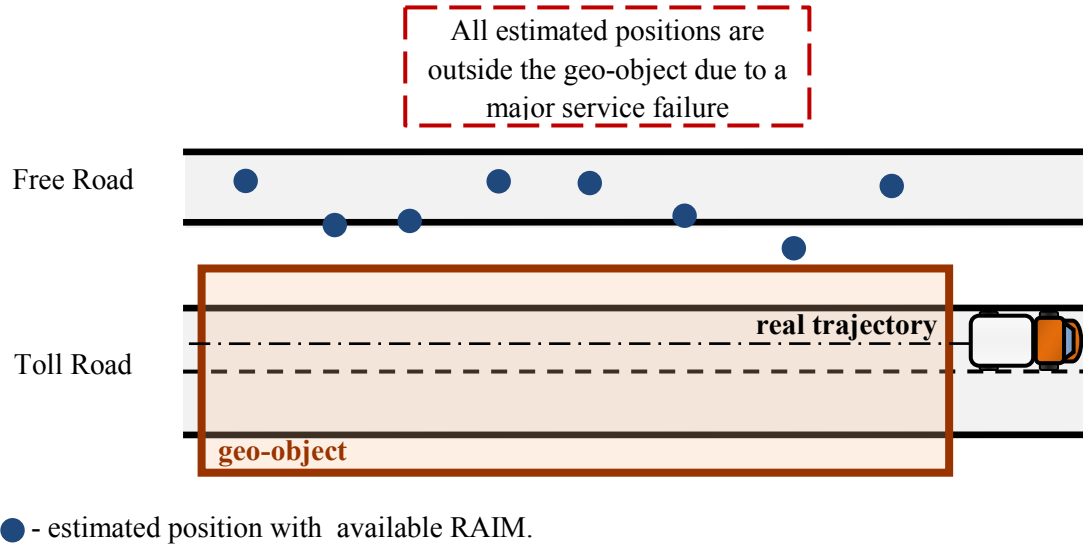


Figure 5.15. Example of missed geo-object recognition in the faulty scenario (major service failure).

This work derives the P_{MD} and P_{FA} of a RAIM with Fault Detection (FD) capabilities (see the introduction of section 5.4). In this case, an alert is raised whenever the RAIM detects a failure, but the position estimate is not corrected. As a consequence, the road segment is missed whenever a major service failure is present. Nevertheless, the faulty scenario occurs with a higher probability than the required missed geo-object recognition rate:

$$P_{\text{Faulty Scenario}} = 1.32 \cdot 10^{-4} \not\leq P_{\text{MGoR (valid pos IN)}} = 5 \cdot 10^{-5} \quad (5.48)$$

It is important to remark that this is a worst case result in which all estimated positions are affected by the major service failure and lie outside the geo-object.

Using a Fault Detection and Exclusion (FDE) technique capable of correcting positioning failures would increase the number of valid positions inside the geo-object. In this case, the required probability that the number of valid positions is lower than the geo-object recognition threshold is:

$$p\{N_{\text{valid pos IN (with FDE)}} < N_{\text{Th}} \mid \text{Faulty Scenario}\} \leq \frac{P_{\text{MGoR (valid pos IN)}}}{P_{\text{Faulty Scenario}}} \approx 0.38 \quad (5.49)$$

The GNSS integrity requirements derived for FD capabilities are applicable to FDE if the probability of false exclusion is negligible.

5.4.4.3. Performance for a particular user trajectory throughout successive road segments

The P_{MD} and P_{FA} constraints derived in sections 5.4.4.1 and 5.4.4.2 have been calculated to achieve a global rate of false and missed geo-object recognitions of $P_{FGoR} = 10^{-6}$ and $P_{MGoR} = 10^{-4}$ over the total number of segment recognition processes managed by the toll system during a given period of time.

However, the analysis of the number of overcharged or undercharged road segments during the trajectory of a particular user instead of the average global rate over a given period must take into account the fact that a major service failure may remain up to one hour and disturb the recognition of several consecutive road segments.

The P_{MD} and P_{FA} constraints plotted in Figure 5.10 and Figure 5.14, valid to meet the average false and missed geo-object rates over all road segments processed by the toll system, will be used in this thesis. Nevertheless, the performance analysis for a particular trajectory throughout multiple successive road segments will be outlined in this section.

The problem could be simplified in two possible scenarios, faulty and nominal. In the faulty case a major service failure disturbs all the positions estimated along the user trajectory, while in the nominal case user positioning is affected only by nominal errors and failures not detectable by the RAIM. The probability of each scenario can be calculated as in section 5.4.3.

Let us consider first the case of a user trajectory inside various road segments. In the nominal scenario, position estimates may lie outside the geo-object only due to failures not detectable by the RAIM. Provided a short temporal correlation of these failures, the decision of charging each road segment is independent as described in section 5.4.4.2.1. In the faulty scenario, all position estimated are outside the geo-object and each road segment is missed unless fault detection and exclusion algorithms are used.

The second case consists in a user moving outside and parallel to various road segments. In the nominal scenario, position estimates may lie inside the geo-object only due to failures not detectable by the RAIM. Provided a short temporal correlation of these failures, the decision of overcharging each road segment is independent as described in section 5.4.4.1.1. In the faulty scenario, all position estimated are inside the geo-object. The probability of overcharging a road segment depends on the P_{MD} and the number of independent position estimates with a pseudorange failure ($N_{F,PSR}$) inside the geo-object. Note that positions estimated at different road segments may not be independent.

5.5. Conclusions

Electronic Toll Collection (ETC) systems specify the maximum allowable impact of over- and undercharging errors. These requirements are usually defined either at service level (e.g. invoice accuracy), or at geo-object level as the maximum allowable rate of missed geo-object recognitions (P_{MGoR}) and false geo-object recognitions (P_{FGoR}). The relationship between the invoice accuracy and P_{MGoR} and P_{FGoR} has been obtained.

A missed geo-object recognition probability of $P_{MGoR} = 10^{-4}$ has been proposed for road toll applications because existing ETC systems report similar efficiency rates in non-urban environments and it is the value proposed in [EG9, 2006]. A false geo-object recognition rate of $P_{FGoR} = 10^{-6}$ is proposed, which agrees with the value stated in [EG9, 2006].

The geo-object specifications have been translated into the requirements of a snapshot RAIM algorithm with Fault Detection capabilities, i.e. the probabilities of missed detection (P_{MD}) and of false alarm (P_{FA}). The relationship between the requirements at geo-object recognition level (P_{MGoR} , P_{FGoR}) and at positioning failure detection level (P_{MD} , P_{FA}) has been obtained. The geo-object recognition algorithm of (3.6) has been used, in which a road segment is charged if the number of valid positions estimated inside it exceeds a threshold. Additionally, faulty positions are assumed to be caused only by major service failures, which requires the GNSS receiver to employ robust mechanisms against other failure sources.

The P_{MD} is derived from the maximum probability of false geo-object recognition (overcharging), and it is a function of the segment recognition threshold N_{Th} and of the number N_{DF} of detectable faulty positions inside the geo-object (Figure 5.10). The P_{FA} is derived from the maximum probability of missed geo-object recognition (undercharging), and it is a function of the segment recognition threshold N_{Th} and of the number N_{IP} of fault-free positions with available RAIM inside the geo-object (Figure 5.14). Since N_{IP} depends on the RAIM availability, which in turn depends on the user/satellite geometry (the environment), RAIM performance has to be tested with simulations.

Chapter 6

RAIM Algorithms

6.1. Introduction

Receiver Autonomous Integrity Monitoring (RAIM) are GNSS integrity monitoring algorithms based on the redundancy of GNSS measurements and optionally other sensors, that are run autonomously by the receiver. They can provide Fault Detection (FD) and Fault Detection and Exclusion (FDE) capabilities.

To achieve the required level of redundancy, at least an additional range measurement than the minimum needed to compute the navigation solution is needed for the failure detection function, and at least two additional measurements are necessary for fault exclusion.

RAIM algorithms can be designed to protect against horizontal and vertical positioning errors. Only the integrity monitoring in the horizontal plane will be considered for road toll applications.

This section presents the design and characteristics of the two RAIM techniques under study. First, the Weighted Least Squares Residuals (WLSR) RAIM used in civil aviation is analyzed and afterwards a novel version of the algorithm, suitable for road toll systems and specially adapted to environments with reduced satellite visibility is proposed.

6.2. WLSR RAIM

Least Squares Residuals (LSR) RAIM and the solution separation RAIM are ones of the most used RAIM algorithms in civil aviation. LSR RAIM usually outperforms solution separation methods and is usually taken as reference to check the performance of other RAIM algorithms [van Graas, 1993].

The LSR RAIM algorithm was published in 1988 [Parkinson et. al, 1988] and has been proven to be equivalent to the parity matrix method [Sturza, 1988] and the range comparison method [Lee, 1986] in [Brown, 1992].

LSR RAIM was originally developed under the assumption that pseudorange nominal errors are described by independent Gaussian distributions with equal variance, which was a good supposition when the selective availability (SA) dominated the pseudorange error. Nowadays, with SA switched off, each pseudorange error is best characterized with its own variance, which usually depends on the satellite elevation angle. This case requires the Weighted Least Squares Residuals (WLSR) RAIM [Walter and Enge, 1995].

The main elements of the WLSR RAIM are the availability check, the fault detection and, optionally, the fault isolation and exclusion modules. First, the Horizontal Protection Level (HPL) is calculated and compared against the Horizontal Alert Level (HAL) to check the RAIM availability. The RAIM

assures to detect a positioning failure that exceeds the HAL with the probabilities of missed detection (P_{MD}) and false alarm (P_{FA}) only when the HPL does not exceed the HAL. Afterwards, a test statistic (t) characterized by chi-squared statistics is computed. A positioning failure is detected whenever t exceeds a detection threshold (Th). Both HPL and Th are functions of the desired P_{MD} and P_{FA} . The fault exclusion algorithm can be optionally run after a fault detection in order to eliminate the faulty pseudorange measurement from the position estimation.

6.2.1. Algorithm design

The following subsections provide the rationale of the computation of the test statistic, the detection threshold and the HPL of the WLSR RAIM. The equivalent RAIM obtained with the parity matrix method is presented in Appendix D.

6.2.1.1. Navigation solution and pseudorange measurement models

The WLSR RAIM provides integrity for navigation solutions obtained applying the Weighted Least Squares Estimator (WLSE) to the linear pseudorange measurement model:

$$\Delta y = H \cdot \Delta x + E \quad (6.1)$$

$$\Delta \hat{x} = A \cdot \Delta y \quad (6.2)$$

where:

- the observation matrix H depends on the navigation state vector to be estimated and on the receiver type (appendix A). For example, when the position is to be estimated in the North-East-Up coordinates in the user local frame with a single constellation receiver:

$$H = \begin{pmatrix} \cos(\theta_1)\cos(\psi_1) & \cos(\theta_1)\sin(\psi_1) & \sin(\theta_1) & 1 \\ \vdots & \vdots & \vdots & \vdots \\ \cos(\theta_N)\cos(\psi_N) & \cos(\theta_N)\sin(\psi_N) & \sin(\theta_N) & 1 \end{pmatrix} \quad (6.3)$$

- θ_i : elevation of i^{th} satellite relative to the user position
- ψ_i : azimuth of i^{th} satellite relative to the user position

- the matrix A is a function of the observation matrix H and the nominal pseudorange error correlation matrix :

$$A = (H^T \Sigma^{-1} H)^{-1} H^T \Sigma^{-1} \quad (6.4)$$

A detailed analysis of the WLSE applied to the navigation solution estimation is done in Appendix C.

Pseudorange measurement errors are divided in nominal errors and faults:

$$E = \varepsilon + b \quad (6.5)$$

where:

- nominal errors are assumed to have independent, zero-mean and normal distributions:

$$\varepsilon \sim N(0, \Sigma) \quad (6.6)$$

$$\Sigma = \begin{pmatrix} \sigma_1^2 & 0 & \cdots & 0 \\ 0 & \sigma_2^2 & & \vdots \\ \vdots & & \ddots & 0 \\ 0 & \cdots & 0 & \sigma_N^2 \end{pmatrix} \quad (6.7)$$

- faults are biased pseudorange measurement. In this work, only one simultaneous bias is assumed (the probability of multiple simultaneous failures is neglected):

$$\mathbf{b} = [0, \dots, 0, b_i, 0, \dots, 0]^T \quad (6.8)$$

Some fault models also include the effect of nominal biases [Martineau, 2008].

6.2.1.2. Test Statistic

Since positioning errors are not directly measurable, the WLSR RAIM calculates a measurable scalar parameter that provides information about pseudorange measurement errors. This measurable parameter, called test statistic (t), is a random variable with a known distribution.

WLSR RAIM computes the test statistic processing the pseudorange residual vector (\mathbf{r}), defined as the difference between the measured pseudorange vector and the pseudorange vector derived from the estimated navigation solution:

$$\mathbf{r} = \Delta \mathbf{y} - \mathbf{H} \cdot \Delta \hat{\mathbf{x}} \quad (6.9)$$

The pseudorange residual vector has two important properties:

- 1) each element of the vector \mathbf{r} can be expressed as a known linear combination of the elements of $\Delta \mathbf{y}$ or \mathbf{E} (demonstration in appendix C):

$$\mathbf{r} = (\mathbf{I} - \mathbf{B}) \cdot \Delta \mathbf{y} = (\mathbf{I} - \mathbf{B}) \cdot \mathbf{E} \quad (6.10)$$

where the matrix \mathbf{B} is a function of the observation matrix and the nominal error covariance:

$$\mathbf{B} = \mathbf{H}(\mathbf{H}^T \Sigma^{-1} \mathbf{H})^{-1} \mathbf{H}^T \Sigma^{-1} \quad (6.11)$$

- 2) if pseudorange nominal measurement errors follow independent and normal distributions with variance unity, i.e. $\varepsilon \sim \mathcal{N}(0, \mathbf{I})$, the squared magnitude of the residual vector $\|\mathbf{r}\|^2$, also known as the sum of squared residual errors (SSE), is a chi-squared random variable in the fault free case, and a non-central chi-squared one in the faulty case:

$$\text{SSE} = \|\mathbf{r}\|^2 = \mathbf{r}^T \mathbf{r} \sim \begin{cases} \chi_k^2 & \text{if } \mathbf{E} \sim \mathcal{N}(0, \mathbf{I}) \\ \chi_{k,\lambda}^2 & \text{if } \mathbf{E} \sim \mathcal{N}(\mathbf{b}, \mathbf{I}) \end{cases} \quad (6.12)$$

where k is the number of degrees of freedom and λ is the non-centrality parameter of the chi-squared distribution.

The SSE does not follow any known statistical law when pseudorange nominal errors do not have equal variance, i.e. $\varepsilon \sim \mathcal{N}(0, \Sigma)$. This case can be transformed dividing each line of the equation system (6.1) by the corresponding nominal error standard deviation, resulting in an equivalent system with normalized nominal error covariance matrix equal to the identity, $\varepsilon_n \sim \mathcal{N}(0, \mathbf{I})$. The SSE of the

normalized equation system is equivalent to a weighted SSE (WSSE) and is a suitable test statistic that follows a known chi-squared distribution:

$$SSE_n = r_n^T r_n = r^T \Sigma^{-1} r = WSSE \quad (6.13)$$

$$r_n = \Sigma^{-1/2} \cdot r \quad (6.14)$$

where the subscript n stands for normalized.

Hence, the test statistic is calculated as follows:

$$t = WSSE = r^T \Sigma^{-1} r = \Delta y^T \Sigma^{-1} (I - B) \Delta y \quad (6.15)$$

$$t \sim \begin{cases} \chi_k^2 & \text{if } E \sim N(0, \Sigma) \\ \chi_{k,\lambda}^2 & \text{if } E \sim N(b, \Sigma) \end{cases} \quad (6.16)$$

The number of degrees of freedom of the chi-squared distribution is the number of redundant pseudorange measurements:

$$k = N - N_u \quad (6.17)$$

where N_u is the number of unknowns to be estimated as in Table 3.10, and N is the total number of used range measurements.

The non-centrality parameter of the non-central chi-squared distribution due to a faulty pseudorange is a function of the matrix B , the nominal error covariance and the bias vector (appendix D):

$$\lambda = b^T \Sigma^{-1} (I - B) b \quad (6.18)$$

Since only the i^{th} satellite contains a bias, eq.(6.18) results:

$$\lambda = \frac{(I - B)_{ii}}{\sigma_i^2} \cdot b_i^2 \quad (6.19)$$

The test statistic contains information about pseudorange errors via the following relationship (appendix D):

$$t = E^T \Sigma^{-1} (I - B) E \quad (6.20)$$

6.2.1.3. Detection Threshold

Failure detection is achieved comparing the test statistic against the detection threshold:

$$t \leq Th \Leftrightarrow \text{no failure detection}$$

$$t > Th \Leftrightarrow \text{failure detection} \quad (6.21)$$

The value of the detection threshold is set in order to obtain a Neyman-Pearson test with a constant false detection rate under fault free conditions. Although other alternative algorithms are possible, a

constant false alarm rate is chosen in civil aviation because false alarm is not a safety matter. This way, the RAIM is set to provide a fixed false alert rate that is always equal to the required P_{FA} , and a variable probability that undetected positioning failures exceed the HAL equal to or lower than P_{MD} [Brown, 1992].

Neglecting the probability that a positioning failure is caused by nominal errors, any fault detection with fault-free measurements is a false detection. The detection threshold is set to achieve a detection rate equal to P_{FA} under fault free conditions (Figure 6.1):

$$P_{FA} = p\{\text{detection} \mid \text{fault free}\} = p\{t > Th \mid t \sim \chi_k^2\} = 1 - \text{cdf}_{\chi_k^2}\{Th\} \quad (6.22)$$

Thus, Th is a function of the P_{FA} and the number of degrees of freedom, k .

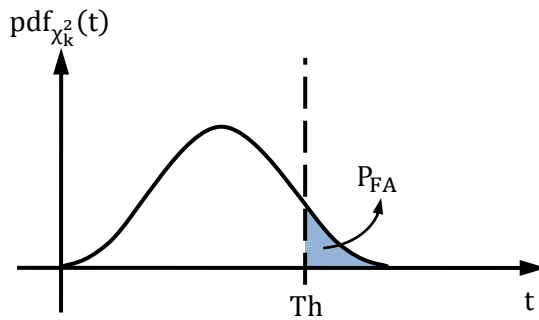


Figure 6.1. Derivation of the detection threshold (Th).

It is important to point out the assumption that the fault-free horizontal positioning error due to pseudorange nominal errors does not exceed the HPL:

$$p\{|e_H| > HPL \mid \text{fault free}\} = 0 \quad (6.23)$$

6.2.1.4. Minimum detectable failures

Let us define λ_{det} as the non-centrality parameter of the test distribution in the faulty case that results in a missed detection rate of P_{MD} (Figure 6.2):

$$P_{MD} = p\{\text{no detection} \mid \text{faulty case}\} = p\{t \leq Th \mid t \sim \chi_{k,\lambda_{det}}^2\} = \text{cdf}_{\chi_{k,\lambda_{det}}^2}\{Th\} \quad (6.24)$$

Thus, λ_{det} is a function of the P_{MD} , the number of degrees of freedom k and Th , which in turn depends on the P_{FA} .

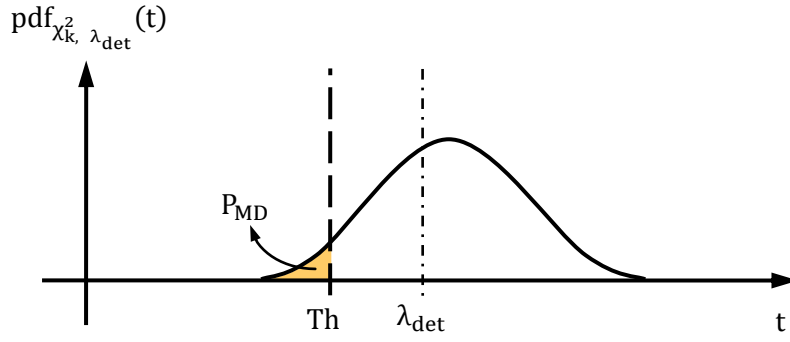


Figure 6.2. Derivation of the minimum detectable non-centrality parameter (λ_{det}).

Given fixed values of T_h and k , the missed detection rate decreases as λ increases. Thus, λ_{det} is the minimum non-centrality parameter the RAIM is able to detect with a probability equal to or lower than P_{MD} :

$$p\{\text{no detection} \mid \text{faulty case}\} = p\{t \leq T_h \mid t \sim \chi_{k, \lambda_{\text{det}}}^2\} \begin{cases} > P_{\text{MD}} & \text{if } \lambda < \lambda_{\text{det}} \\ = P_{\text{MD}} & \text{if } \lambda = \lambda_{\text{det}} \\ < P_{\text{MD}} & \text{if } \lambda > \lambda_{\text{det}} \end{cases} \quad (6.25)$$

According to eq.(6.19), λ is proportional to the squared magnitude of the bias. Therefore, the minimum pseudorange bias in the i^{th} satellite the WLSR RAIM is capable to detect with a probability of missed detection equal to or lower than P_{MD} is:

$$b_{\text{det},i} = \sqrt{\frac{\sigma_i^2}{(I - B)_{ii}}} \cdot \sqrt{\lambda_{\text{det}}} \quad (6.26)$$

Thus:

$$p\{\text{no detection} \mid \text{faulty case}\} \begin{cases} > P_{\text{MD}} & \text{if } b_i < b_{\text{det},i} \\ = P_{\text{MD}} & \text{if } b_i = b_{\text{det},i} \\ < P_{\text{MD}} & \text{if } b_i > b_{\text{det},i} \end{cases} \quad (6.27)$$

Each satellite has their own minimum detectable bias magnitude $b_{\text{det},i}$.

6.2.1.5. Relationship between test statistic and position errors

The aim of the WLSR RAIM algorithm is to protect against horizontal positioning errors, raising an alert whenever $|e_H|$ exceeds the HPL within the required P_{MD} and P_{FA} . Nevertheless, fault detection is performed via the test statistic. The relationship between the measurable test statistic t and what the RAIM protects, i.e. the horizontal position errors $|e_H|$, is the key information used to derive the HPL from parameters used in the fault detection process with the test statistic.

Pseudorange errors have a statistic component - the nominal errors, $\varepsilon \sim N(0, \Sigma)$ - and a deterministic component - the bias of faulty measurements. Since the test statistic t and the horizontal position error

$|e_H|$ are derived from the pseudorange errors, they also have a statistic component due to the nominal errors, and a deterministic component due to the pseudorange bias.

6.2.1.5.1. Deterministic component (Slope)

The deterministic component of $|e_H|$ is the projection of the pseudorange bias present in the i^{th} satellite into the horizontal position error domain. Considering the horizontal position is estimated in the north and east directions of the user's local plane:

$$|b_H| = \sqrt{b_N^2 + b_E^2} = \sqrt{A_{N,i}^2 + A_{E,i}^2} \cdot b_i \quad (6.28)$$

where b_N and b_E are the projection of the bias in the north and east directions, and A_N and A_E are the lines of the matrix A that correspond to the north and east position components:

$$\begin{bmatrix} b_N \\ b_E \\ \vdots \end{bmatrix} = A \cdot b = \begin{bmatrix} A_N \\ A_E \\ \vdots \end{bmatrix} b = \begin{bmatrix} A_{N,i} \\ A_{E,i} \\ \vdots \end{bmatrix} b_i \quad (6.29)$$

Note that $|b_H|$ is the bias projection in the horizontal error and not the mean of the horizontal positioning error.

The deterministic component introduced by a pseudorange bias in the test statistic is the non-centrality parameter. Combining equations (6.19) and (6.28), the following relationship between λ and $|b_H|$ is found:

$$|b_H| = \text{slope}_i \cdot \sqrt{\lambda} \quad (6.30)$$

where:

$$\text{slope}_i = \sigma_i \cdot \sqrt{\frac{A_{N,i}^2 + A_{E,i}^2}{(I - B)_{ii}}} \quad (6.31)$$

The slope is a measure of the coupling between the effect of a pseudorange bias in the observable parameter, i.e. the test statistic's $\sqrt{\lambda}$, and what the RAIM wishes to protect, the horizontal position error (Figure 6.3). Each satellite has its own slope. The satellite with the highest slope is the most difficult to detect, in the sense that a given $|b_H|$ has the lowest $\sqrt{\lambda}$ among all satellites, that is, the lowest detection probability.

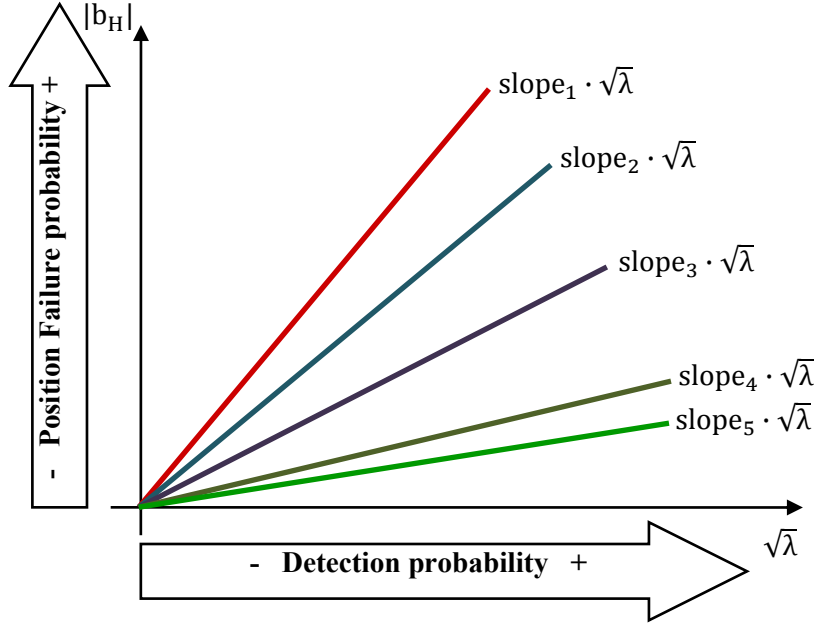


Figure 6.3. Examples of the slope as the relationship between the test statistic non-centrality (λ) and the bias projection $|b_H|$.

6.2.1.5.2. Statistic component

The statistic components of the test statistic and the navigation solution errors are uncorrelated [Ober, 1997] (see appendix D):

$$\text{cov}(t, e) = 0 \quad (6.32)$$

Thus, the pdf of the joint distribution of t and $|e_H|$ is the product of their individual pdf:

$$\text{pdf}(\sqrt{t}, |e_H|) = \text{pdf}(\sqrt{t}) \cdot \text{pdf}(|e_H|) \quad (6.33)$$

The test statistic follows a chi-squared distribution as in eq.(6.16).

The horizontal positioning error follows a bivariate Gaussian distribution. Describing it as two independent monodimensional Gaussian distributions in the direction of the major and minor semiaxes of the equidensity ellipses:

$$e_H = e_{\text{major}} + e_{\text{minor}} \quad (6.34)$$

Its magnitude results:

$$|e_H| = \sqrt{e_{\text{major}}^2 + e_{\text{minor}}^2} \quad (6.35)$$

In general, the error components e_{major} and e_{minor} have different variances and $|e_H|$ does not follow a known distribution. Alternatively, $|e_H|$ can be expressed as the sum of the monodimensional Gaussian distributions of the error in the north and east directions, which in general are correlated (appendix C).

Hence, the joint distribution of t and $|e_H|$ follows a chi-squared law in the t axis, non-central or central depending on the presence of a faulty measurement, and the root of the sum of two squared Gaussians in the $|e_H|$ axis (Figure 6.4). The joint distribution is usually represented in the plane \sqrt{t} vs. $|e_H|$ in order to represent linearly the relationship provided by the slope in eq.(6.30).

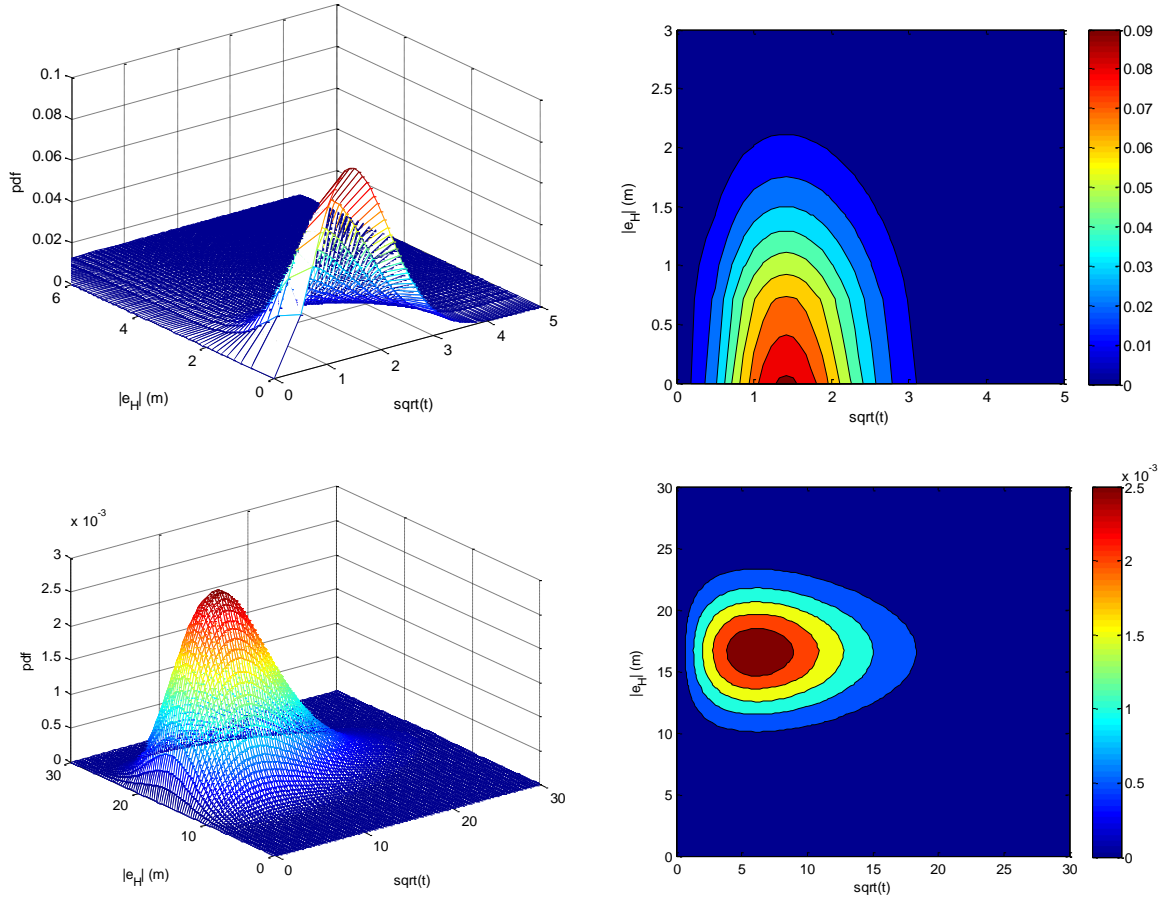


Figure 6.4. Examples of bidimensional pdf in the plane square root(t) vs. $|e_H|$ in the a) fault free case, b) faulty case.

6.2.1.6. Horizontal protection level

The WLSR RAIM calculates the HPL as:

$$\text{HPL} = \text{slope}_{\text{MAX}} \cdot \sqrt{\lambda_{\text{det}}} \quad (6.36)$$

where:

$$\text{slope}_{\text{MAX}} = \max_i(\text{slope}_i) \quad (6.37)$$

Equation (6.36) does not depend on current measurements, so the HPL can be predicted according to the expected satellite/user geometry and nominal error covariance.

Figure 6.5 illustrates the joint distribution of \sqrt{t} and $|e_H|$ in different stages of the WLSR RAIM design. It is a visual analysis of the relationship between the measurable domain in which the fault detection is performed (i.e. the test statistic \sqrt{t}), and the positioning error $|e_H|$ against which the RAIM tries to protect. Figure 6.5 is useful to understand the interpretation of the HPL equation (6.36) explained in the next paragraphs.

The HPL is calculated as the projection in the position domain of the pseudorange bias in the most-difficult-to-detect satellite, i.e. the satellite with the highest slope, that generates a test statistic with a non-centrality parameter equal to λ_{det} . Let us denote the magnitude of this bias $b_{\text{det,MAX}}$. By definition, the RAIM detects the presence of this bias with a missed detection probability equal to P_{MD} , regardless the positioning error.

Hereafter, pseudorange biases are assumed to be in the maximum slope satellite. This is a worst case scenario because pseudorange biases that generate a non-centrality parameter equal to λ_{det} in other satellites with lower slopes provide lower $|b_H|$, meaning that the RAIM is able to detect them within the required P_{MD} when they cause smaller positioning errors (Figure 6.3).

When the pseudorange bias projection in the position domain $|b_H|$ is sufficiently larger than the statistical error component, the distribution of $|e_H|$ is approximately centered around $|b_H|$. Consequently, the probability that a pseudorange bias b_{det} causes an undetected positioning error larger than HPL is approximately $P_{\text{MD}}/2$; in any case it is always lower than P_{MD} (Figure 6.5-c).

Pseudorange biases larger than b_{det} generate a non-centrality parameter larger than λ_{det} , which is explained graphically as a displacement of the joint $\text{pdf}(\sqrt{t}, |e_H|)$ upwards along the slope in Figure 6.5-c. Despite their projection in the position domain larger than the HPL, and consequently a higher probability that $|e_H|$ exceeds it, the integrity requirements are met because the RAIM detects them with a missed detection probability lower than P_{MD} , regardless the positioning error.

Pseudorange biases smaller than b_{det} generate a non-centrality parameter smaller than λ_{det} , which is explained graphically as a displacement of the joint $\text{pdf}(\sqrt{t}, |e_H|)$ downwards along the slope in Figure 6.5-c. Therefore, the rate of missed detection increases and exceeds P_{MD} , while the probability of positioning failure decreases because of the lower $|b_H|$. Thus, the HPL equation (6.36) is valid if the lower positioning failure probability compensates the higher missed detection rate, so that the probability of undetected positioning failures is below P_{MD} . Unfortunately it has been proven that for certain satellite/user geometries, principally when the maximum slope has a low value, the HPL should be higher [Brown and Chin, 1997]. However, the HPL computed as in eq.(6.36) is judged to be practical in most of the cases and it is in use.

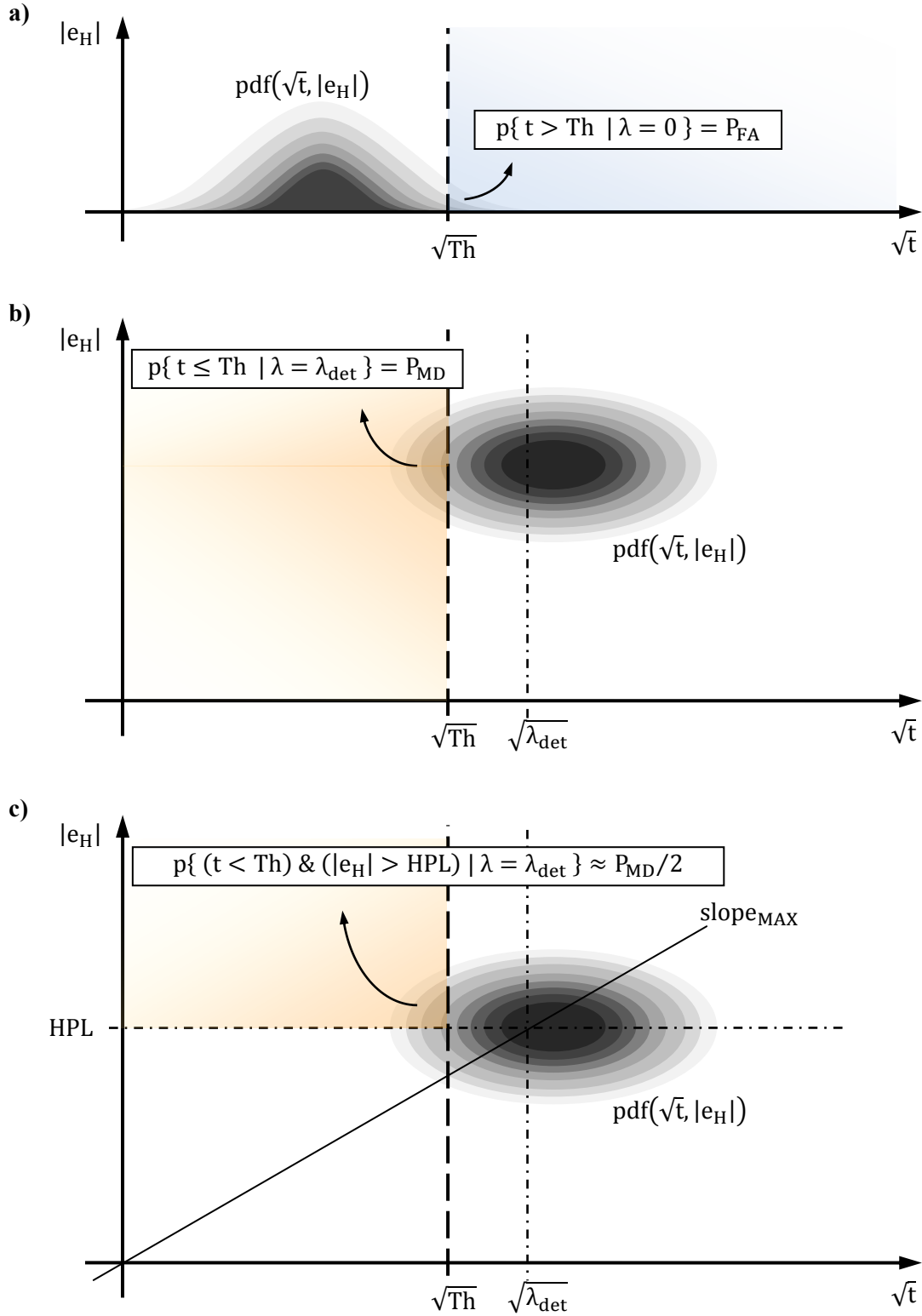


Figure 6.5. Relationship between the test statistic and the position error in different stages of the WLSR RAIM design. a) Derivation of the detection threshold. b) Computation of the minimum detectable non-centrality parameter. c) Estimation of the HAL.

6.2.2. Implementation

The GNSS receiver will carry out at least the availability check and the fault detection tasks. Fault exclusion can be optionally implemented.

6.2.2.1. Availability check and fault detection

The availability check and fault detection modules run within the receiver are depicted in Figure 6.6. The inputs are the observation matrix H and the nominal error covariance Σ for the RAIM availability check, plus the current pseudorange measurements Δy for the fault detection module.

The values of λ_{det} and Th are functions of P_{MD} , P_{FA} and the number of redundant range measurements k . Since they do not depend on current measurements, they can be computed offline and stored in the receiver as look-up tables. For given P_{MD} and P_{FA} , the stored data are the vectors $\sqrt{\lambda_{\text{det}}(k)}$ and $Th(k)$.

The RAIM availability check do not employ current measurements, so the HPL can be predicted with the expected satellite/user geometry and nominal error covariance.

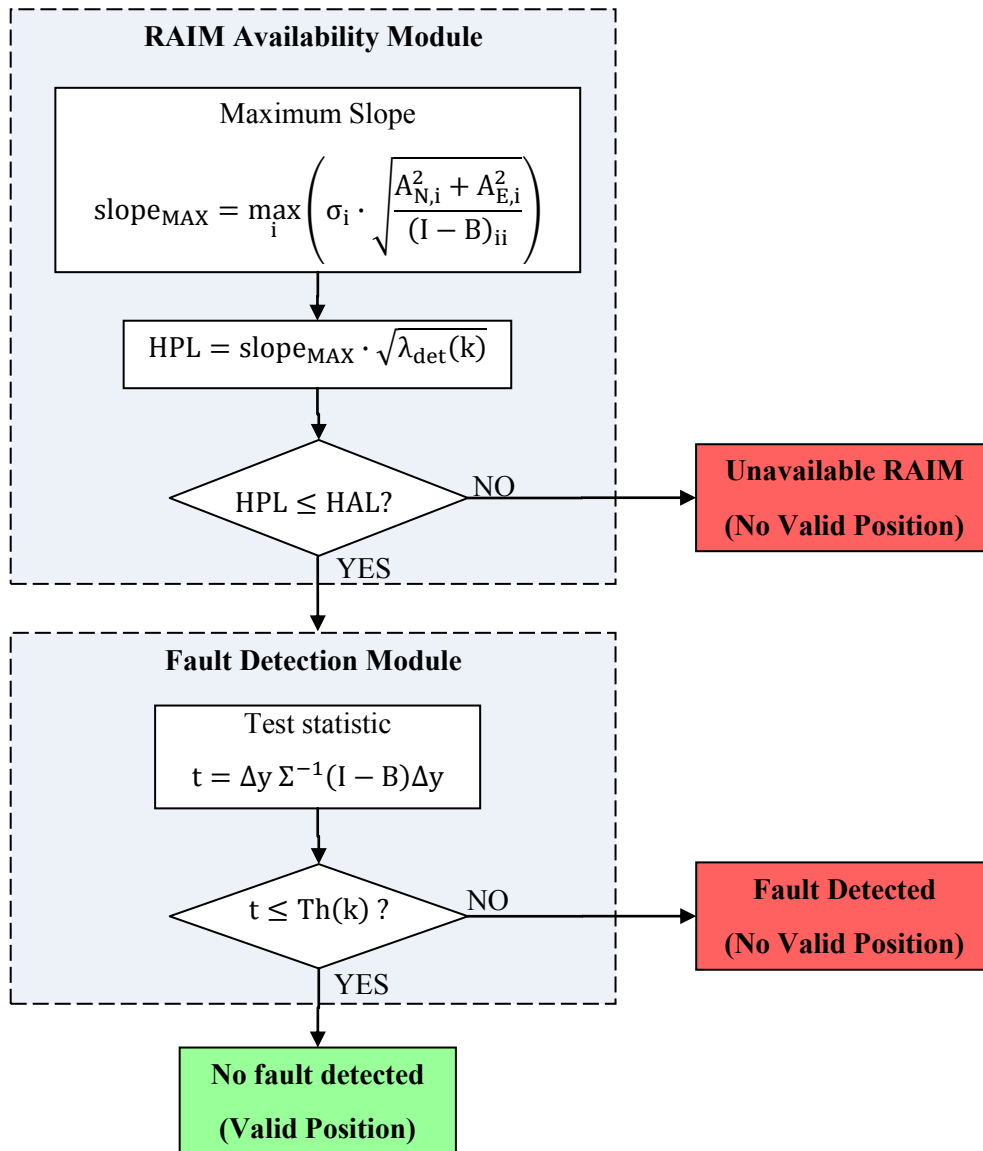


Figure 6.6. WLSR RAIM algorithm.

6.2.2.2. Fault exclusion

The RAIM can optionally perform fault exclusion, which in case of a fault detection eliminates the faulty pseudorange measurement from the position estimation, providing integrity information without service interruption.

A possible fault exclusion technique consists in creating N subgroups of $N - 1$ range measurements each, excluding one range measurement at each subgroup. Since there is only one faulty satellite, applying the fault detection module to each subgroup will detect a fault in all of them except in the one excluding the faulty measurement.

Fault exclusion needs at least two redundant range measurements and it is available when fault detection is available for each subgroup.

6.2.3. Limitations

6.2.3.1. Assumptions made during the algorithm design

WLSR RAIM algorithms are limited by the following assumptions made during their design:

- the navigation state vector must be calculated with the Weighted Least Squared Estimator (WLSE)
- pseudorange nominal errors must be characterized as zero-mean Gaussian variables
- the faulty case consists in a single pseudorange failure at a given instant (there are no simultaneous failures)
- the probability that nominal errors cause a positioning failure must be negligible

Additionally, the probability that undetected horizontal positioning errors exceed the HPL should be equal to or lower than P_{MD} , although this cannot be assured in specific cases, particularly with low values of the maximum slopes (see section 6.2.1.6).

6.2.3.2. Pseudorange detection and probability of false detection

Although the aim of integrity monitoring is to detect horizontal positioning failures, i.e. $|e_H| > HAL$, the WLSR RAIM fault detection module is actually designed to decide whether at a given instant there is a biased pseudorange measurement or not. It is afterwards when the RAIM translates the effect of the bias plus noise to the positioning error domain via the HPL.

A probability of false detection equal to P_{FA} is assured only in the fault free case. Any pseudorange bias, regardless its size and the positioning error, generates a certain chi-squared non-centrality parameter λ that increases the detection probability over P_{FA} .

Only pseudorange biases that generate a chi-squared non-centrality parameter equal to or greater than λ_{det} are assured to be detected with a probability of missed detection equal to or lower than the required P_{MD} . These are the minimum detectable biases, which magnitude b_{det} varies from one satellite to another.

The HPL is calculated to assure that the probability of undetected positioning errors exceeding it meets the required P_{MD} under the effect of a pseudorange bias equal to or larger than b_{det} in the maximum slope satellite.

Consequently, the probability of false detections under the presence of pseudorange biases that generate $\lambda \in (0, \lambda_{\text{det}})$ exceeds the P_{FA} .

6.2.3.3. Minimum allowable HAL

The WLSR RAIM assumes that positions estimated with fault free range measurements do not contain positioning failures. Nevertheless, positioning errors due to pseudorange nominal errors may exceed the HAL with a non-negligible probability depending on the user/satellite geometry, the nominal error model and the required alert limit. Thus, the assumption of a negligible probability of positioning failures in the fault free case only holds for sufficiently large HAL.

The HAL exceeded with a given probability P by nominal positioning errors could be computed numerically for each error distribution $(\sigma_{\text{major}}^2, \sigma_{\text{minor}}^2)$. For the sake of simplicity analytical upper and lower bounds will be computed as a function of σ_{major}^2 .

The worst case occurs when $\sigma_{\text{minor}} = \sigma_{\text{major}}$. In this case, the squared fault-free horizontal error scaled by the variance follows a chi-squared distribution of 2 degrees of freedom:

$$\sigma_{\text{major}}^2 \cdot |e_H|^2 \sim \chi_2^2 \quad (6.38)$$

Hence, the upper bound of the HAL that $|e_H|$ exceeds with a probability P is:

$$\text{HAL} \leq \sigma_{\text{major}} \cdot \sqrt{\text{cdf}_{\chi_2^2}^{-1}(1 - P)} \quad (6.39)$$

where $\text{cdf}_{\chi_2^2}^{-1}$ is the inverse cdf of a χ_2^2 distribution.

The lower bound is found with $\sigma_{\text{minor}} = 0$. In this case, the horizontal error follows a unidimensional normal distribution of variance σ_{major}^2 . Thus, the lower bound of the HAL that $|e_H|$ exceeds with a probability P is:

$$\text{HAL} \geq \sigma_{\text{major}} \cdot \text{cdf}_{N(0,1)}^{-1}(P/2) \quad (6.40)$$

where $\text{cdf}_{N(0,1)}^{-1}$ is the inverse cdf of a zero-mean normal distribution of variance unity.

The minimum allowable HAL is a function of the horizontal positioning error distribution and the maximum allowable probability of positioning failures in the fault-free case, which are actually undetectable by the RAIM (Figure 6.7).

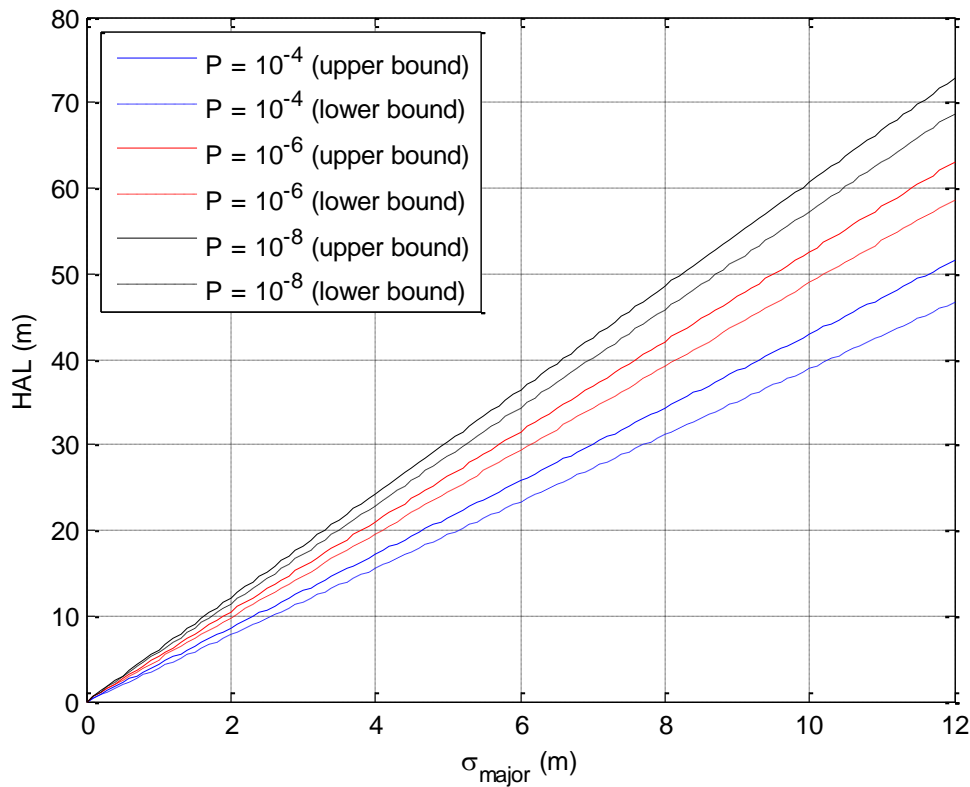


Figure 6.7. HAL exceeded by nominal horizontal positioning errors with a probability P .

6.3. WLSR RAIM with a variable P_{FA}

Scenarios with limited satellite visibility like urban environments are likely to provide bad user/satellite geometries that result in a high unavailability rate of the WLSR RAIM introduced in section 6.2. Every time the RAIM is unavailable, the estimated position must be rejected because it is not supported by integrity information.

The aim of this section is to present a novel WLSR RAIM algorithm adapted to the characteristics of road toll systems with the objective of increasing the number of valid positions in urban environments.

6.3.1. Motivation and rationale

WLSR RAIM algorithms for civil aviation are designed with the values of P_{MD} and P_{FA} that assure agreement with the integrity risk and continuity levels standardized by the ICAO [ICAO, 2006]. Positions estimated with a missed detection probability higher than P_{MD} or a false alert rate higher than P_{FA} are unacceptable in civil aviation because they do not guarantee the integrity and the continuity risks; consequently, the RAIM is declared unavailable whenever the user/satellite geometry and the nominal errors make impossible to monitor integrity with the required P_{MD} and P_{FA} . RAIM availability rates in typical aviation environments generally fulfill the ICAO requirements.

Urban environments can be more challenging than civil aviation ones in terms of RAIM availability. In GNSS-based Electronic Toll Collection (ETC) systems in urban environments, RAIM unavailability decreases the number of positions valid to be used by the segment recognition algorithm and raises the undercharging rate. Fortunately, road toll requirements differ from those of civil

aviation, which allows to redesign the WLSR RAIM in order to increase the number of valid positions in environments with reduced visibility.

The toll algorithm proposed in equation (3.6) charges a road segment to a user if the number of valid positions inside the geo-object is at least equal to a threshold N_{Th} , being valid positions those with available RAIM for which no fault has been detected:

$$\text{road segment is charged} \Leftrightarrow N_{\text{valid,in}} \geq N_{Th}$$

Then, the desired goal of the RAIM is to reject enough faulty positions to meet the overcharging requirement while attaining the number of valid positions that reaches the undercharging requirement in the fault free case.

The P_{MD} calculated in chapter 5 (Figure 5.10) is the maximum allowable probability of missed detection that meets the overcharging requirements. For fixed values of P_{FA} and k , the HPL decreases when the P_{MD} increases, so RAIM availability could be improved at the expense of the missed detection probability. This option is not chosen because the overcharging requirement would not be met; thus, the proposed RAIM will be designed to provide a maximum allowable probability of missed detection equal to P_{MD} .

The P_{FA} calculated in chapter 5 (Figure 5.14) has been derived to meet the undercharging requirement. It is the maximum allowable probability of false alarm that assures the maximum allowed probability that the number of fault-free valid positions in the road segment is lower than N_{Th} , given a minimum number of independent positions with available RAIM (N_{IP}). However, the P_{FA} does not fulfil the undercharging requirement if N_{IP} is lower than its required minimum value, which may happen due to positioning or RAIM unavailability.

For fixed values of P_{MD} and k , the HPL increases as the P_{FA} decreases (Figure 6.8). Hence, the probability that a fault-free position is declared valid (available RAIM and no fault detected) results from a trade-off between the false alarm and the RAIM unavailability rates: the more stringent is P_{FA} , the lower is the number of fault-free positions rejected due to false alarms but the higher due to RAIM unavailability, and vice versa.

When the number of estimated positions, independent and with available RAIM, is not sufficiently high, the WLSR RAIM of section 6.2 could be designed with a maximum allowable probability of false detection higher than the required P_{FA} , which would increase the RAIM availability, and consequently the average N_{IP} per road segment, at the expense of a false alarm rate augmentation. Although this solution does not meet the undercharging requirements, it may improve the obtained undercharging rate in scenarios with severe RAIM unavailability rates. However, another strategy will be adopted in order to provide a better undercharging rate.

The new WLSR RAIM design relies on the fact that road toll systems do not have a GNSS continuity requirement as defined in civil aviation, that is, they do not need all positions of a user trajectory along a road segment to be valid uninterruptedly; instead, the geo-object recognition algorithm requires a minimum number of valid positions per road segment, regardless they are consecutive or not. Therefore, RAIM for GNSS-ETC systems do not require imperatively a fixed P_{FA} , but rather the best trade-off between false alarm and RAIM availability that results in the highest probability that a fault-free position is declared valid.

Estimated positions are automatically rejected whenever the RAIM is unavailable because they are not supported by integrity information; that is, the probability of providing a valid position is zero.

The proposed algorithm has a constant HPL equal to the HAL, so the RAIM is always available and fault-free positions are rejected only due to false detections. The constant maximum missed detection probability equal to P_{MD} makes the resulting false detection probability to vary in time as a function of the user/satellite geometry and the pseudorange nominal error covariance.

The algorithm design is the following (Figure 6.9):

- 1) The minimum detectable chi-squared non-centrality parameter that corresponds to an HPL equal to HAL is obtained from eq. (6.36):

$$\lambda_{det} = \left(\frac{HAL}{slope_{MAX}} \right)^2 \quad (6.42)$$

- 2) The detection threshold is derived from P_{MD} and λ_{det} using eq.(6.24):

$$Th = cdf_{\chi_k^2, \lambda_{det}}^{-1} \{P_{MD}\} \quad (6.43)$$

- 3) The fault detection process only needs the detection threshold, so the RAIM implemented in the receiver could finish in step 2). For performance analysis, the probability of false alarm can be obtained as in eq.(6.22):

$$P_{FA} = 1 - cdf_{\chi_k^2} \{Th\} \quad (6.44)$$

The resulting algorithm is a Constant-Probability-of-Detection (CPOD) RAIM [Sturza and Brown, 1990] with the particularity of having no maximum allowed P_{FA} . The probability that a fault-free position is declared valid is:

$$P_{valid} = 1 - P_{FA} = cdf_{\chi_k^2} \{Th\} \quad (6.45)$$

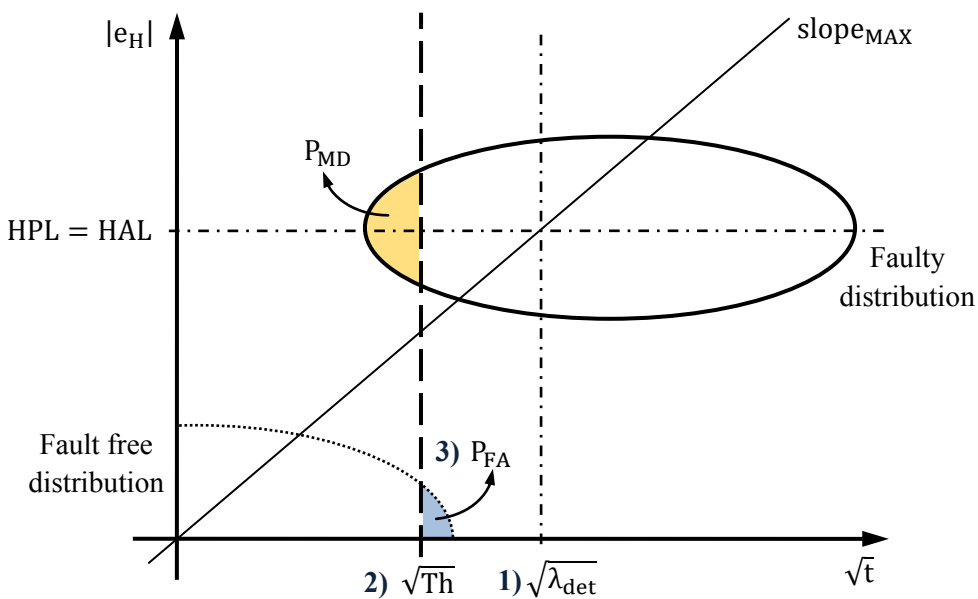


Figure 6.9. Design of the WLSR RAIM that maximizes the number of valid positions.

6.3.3. Implementation

The fault detection module run at the receiver is depicted in Figure 6.10. There is no availability check module because the RAIM is always available (positions are rejected only by fault detections and bad user/satellite geometries are translated into high probabilities of false alarm, not into RAIM unavailability). The inputs are the observation matrix H , the nominal error covariance Σ and the current pseudorange measurements Δy . Note that the probability of false detection does not depend on Δy and can be predicted with eq.(6.44).

To reduced the computational burden of the calculation at each instant of the detection threshold with the inverse CDF of a chi-squared distribution, look-up tables can be calculated offline for discrete values of λ_{det} .

Fault exclusion can be optionally implemented applying the fault detection module to the N subgroups resulting from excluding one range measurement at each subgroup; the only subgroup for which no fault has been detected is the one excluding the faulty measurement. Fault exclusion needs at least two redundant range measurements.

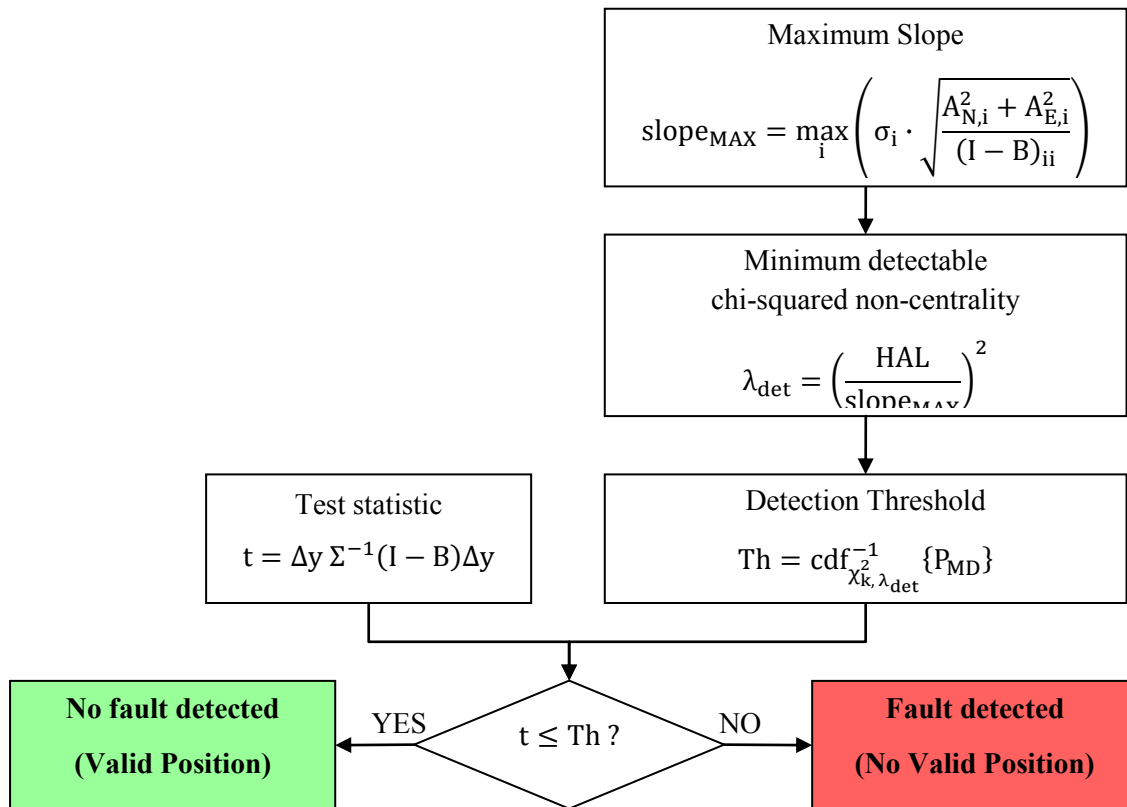


Figure 6.10. WLSR RAIM fault detection that maximizes the number of valid positions.

6.3.4. Comparison against the WLSR RAIM used in civil aviation

Both RAIM algorithms presented in sections 6.2 and 6.3 rely on the same WLSR test statistic and their main difference resides in the rule used to set the detection threshold.

The classic WLSR RAIM used in civil aviation provides a constant false detection rate under fault free conditions equal to P_{FA} , and assures that undetected positioning errors exceed the HPL with a

probability equal to or lower than P_{MD} . That is, the RAIM detects positioning errors greater than the HPL as if they were positioning failures (Figure 6.11). The HPL varies in time as a function of the user/satellite geometry and the nominal pseudorange covariance matrix. Therefore, when the RAIM is available, the actual maximum probability that an undetected error exceeds the HAL evolves together with the HPL, and it is lower than the probability that it exceeds the HPL.

The novel WLSR RAIM provides a constant HPL equal to the HAL. Consequently it detects positioning errors larger than the HAL with a constant probability of missed detection equal to P_{MD} (Figure 6.11). The probability of false detection in the fault-free case varies in time as a function of the user/satellite geometry and the pseudorange nominal error covariance matrix.

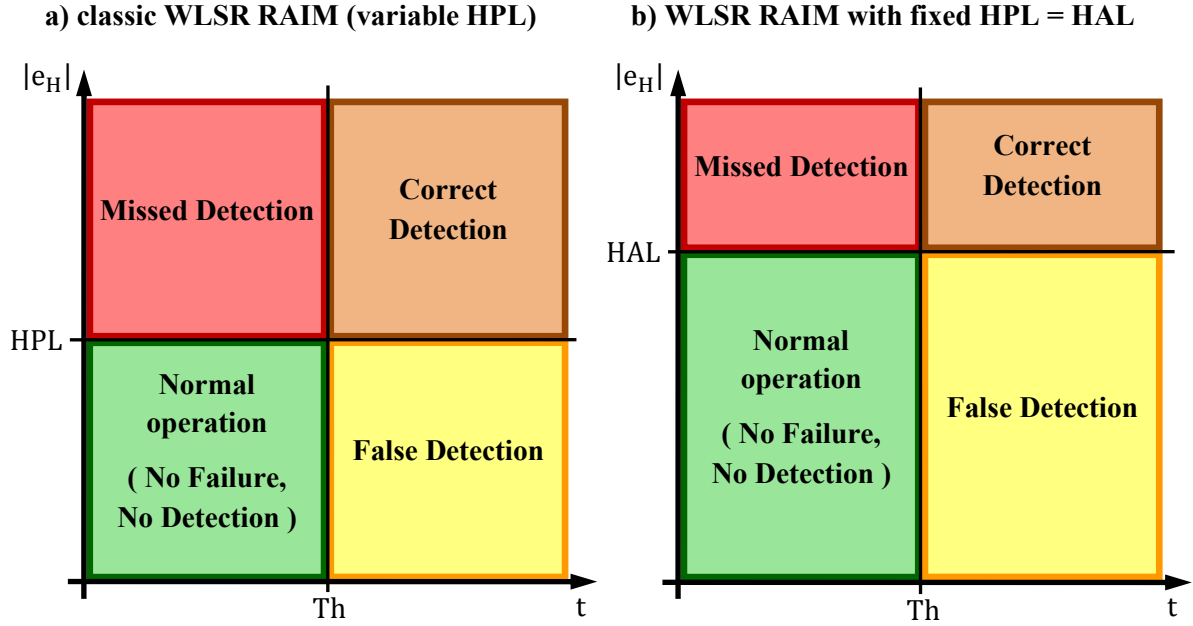


Figure 6.11. Comparison of fault detection events in the classic and novel WLSR RAIM algorithms.

Both algorithms assure that the maximum probability of missed detection of positioning failures ($e_H > HAL$) is equal to P_{MD} at any instant. The difference is that, while the classic RAIM is pushed to obtain the lowest possible HPL, and hence the lowest probability of an undetected positioning failure, at the cost of providing continuously the maximum allowable P_{FA} , the novel algorithm is set to obtain the lowest possible probability of false alarm for a given HAL, at the expense of providing continuously the maximum allowable P_{MD} .

The motivation of the novel algorithm is to improve the rate of valid positions in environments with degraded visibility. The probability of not declaring valid a fault-free position with the novel algorithm is given by the probability of false alarm of eq.(6.44), whereas with the classic WLSR RAIM it is the required P_{FA} when the RAIM is available, and one if it is not (Figure 6.12). The classic WLSR RAIM is available when the $\sqrt{\lambda_{det}}$ calculated as in eq.(6.24) is greater than the ratio $HAL/slope_{MAX}$. The novel algorithm always provides a probability of rejecting a fault-free position lower than the classic WLSR RAIM, especially when the latter is unavailable due to high slopes frequent in scenarios with degraded satellite visibility.

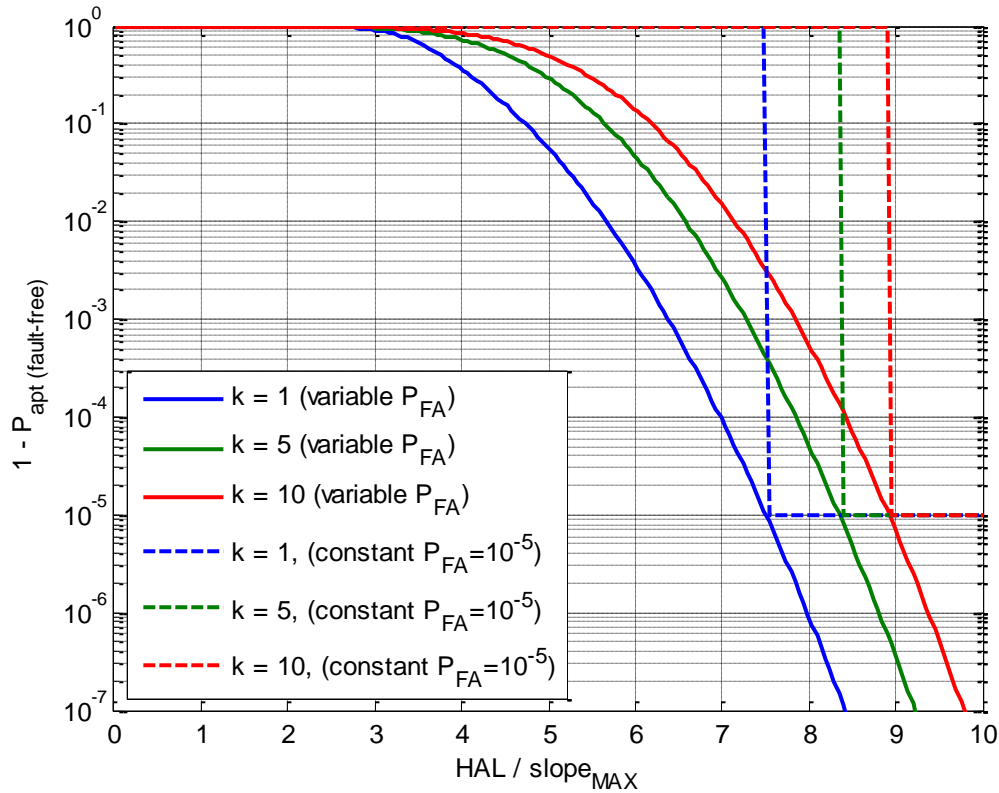


Figure 6.12. Probability of not declaring valid a fault free position as a function of the ratio $HAL/slope_{MAX}$ and the number of chi-squared degrees of freedom k . Example with $P_{MD}=10^{-3}$ and $P_{FA}=10^{-5}$.

Applications like civil aviation specify a maximum allowable P_{FA} . In these applications, the RAIM with variable probability of false alarm should be declared unavailable whenever the probability of false detection exceeds the required P_{FA} , as the algorithm proposed for civil aviation in [Feng et al, 2006]. In this case, both WLSR RAIM have equivalent availability, although the new algorithm still provides a higher probability of valid positions due to the probability of false alarm lower than the maximum allowable P_{FA} .

6.3.5. Limitations

Since the WLSR RAIM with variable P_{FA} is based on the WLSR test statistic, it has the same limitations as the civil aviation WLSR RAIM presented in section 6.2.3.

6.4. Conclusions

Two RAIM algorithms have been selected as candidates to be employed in urban road toll applications. The first one is the WLSR RAIM because it is an algorithm widely used in civil aviation and it is usually set as a reference, against which other RAIM techniques are compared. The second one is a novel algorithm based on the WLSR RAIM, adapted to the needs of road toll systems with the aim of increasing the rate of valid positions in scenarios with degraded satellite visibility.

The rationale of the WLSR RAIM design has been presented, including the derivation of the test statistic, the detection threshold and the HPL. Afterwards, the availability check, the fault detection

and the fault exclusion modules run at the receiver have been depicted. Finally, the limitations of the RAIM have been identified. These include the assumptions of Gaussian nominal pseudorange errors and no simultaneous failures, the fact that the probability of false alarm only applies to the fault-free case, and the minimum HAL derived from the nominal positioning errors.

The novel RAIM is obtained modifying the rule to set the detection threshold of the WLSR RAIM used in civil aviation. The objective is to develop a RAIM for GNSS-ETC systems that provide a trade-off between false alarm and RAIM availability in order to get the highest rate of valid positions with fault-free measurements. Whereas the classic WLSR RAIM is designed to obtain the lowest possible HPL providing continuously the maximum allowable P_{FA} , the novel algorithm is set to obtain the lowest possible probability of false alarm for a given HAL, providing continuously the maximum allowable P_{MD} . The novel RAIM has been proved to increase the probability of valid positions under fault-free conditions with respect to the classic WLSR RAIM.

Chapter 7

Simulation results of GNSS-based ETC Systems

7.1. Introduction

The performance of GNSS-based road toll systems strongly depends on the environment where they operate. Whereas the RAIM P_{MD} has been set to always meet the false road segment recognition requirement in the worst case, the actual missed segment recognition rate varies with the number of independent positions with available RAIM per geo-object, which directly depends on the GNSS receiver, the RAIM algorithm, the user's trajectory duration and the environment (section 5.4.4). For this reason, various simulations have been run in order to obtain the performance of road toll systems for different configurations and scenarios. First, the different configurations of the simulations are described. Later, the satellite visibility and positioning error statistics are shown in rural and urban environments. Afterwards, the performance of the WLSR RAIM algorithms introduced in Chapter 6 is studied. Finally, the GNSS-based ETC performance is analyzed.

7.2. Description and configuration of the simulations

7.2.1. Scenario

The simulated scenario consists of a user circulating at 50 km/h along the axis of a straight street of 20 metres of width. Buildings are generated statistically at both sides of the street, being separated by a gap with a probability $P_G = 0.1$. Two different environments, which represent typical urban and a rural scenarios, are simulated following the building generation pattern of Table 7.1.

Data is output at a 1-Hz sampling frequency in order to follow the variations on the user/satellite geometry due to satellite masking.

Table 7.1. Building generation pattern of urban and rural environments.

Scenario	Building height (H_B)	Building width (W_B)	Width of the gaps between buildings (W_G)
Urban	$H_B \sim N(15 \text{ m.}, 3 \text{ m.})$ $4 \text{ m.} \leq H_B \leq 25 \text{ m}$	$W_B \sim N(20 \text{ m.}, 25 \text{ m.})$ $W_B \geq 10 \text{ m}$	$W_G \sim N(15 \text{ m.}, 25 \text{ m.})$ $W_G \geq 10 \text{ m}$
Rural	$H_B \sim N(6 \text{ m.}, 1.5 \text{ m.})$ $4 \text{ m.} \leq H_B \leq 20 \text{ m}$	$W_B \sim N(20 \text{ m.}, 25 \text{ m.})$ $W_B \geq 10 \text{ m}$	$W_G \sim N(15 \text{ m.}, 25 \text{ m.})$ $W_G \geq 10 \text{ m}$

7.2.2. GNSS receiver configuration

The receiver configurations described in Table 3.4 - Table 3.9 are studied. These include single and dual constellation GPS and Galileo single-frequency receivers operating standalone or augmented by SBAS corrections, as well as dual frequency L1/E1-L5/E5a receivers. For each receiver configuration, the four different navigation solutions summarized in Table 3.10 are considered: 2D and 3D positioning with and without the knowledge of inter-system time shift in dual constellation receivers. Additionally, receivers providing 3D positioning hybridized with external altitude information are also analyzed.

Dual constellation receivers that track BOC(1,1) signals and estimate a navigation solution consisting of 3D positioning plus the receiver/GNSS time shift have been identified as the baseline study case. The baseline case includes SBAS corrections and iono-free measurements with L5/E5a BPSK(10). The joint use of GPS and Galileo satellites has been chosen to face the limited visibility of urban environments (Figure 7.1), while the BOC(1,1) modulation is GPS/Galileo interoperable and requires a minimum bandwidth of 4 MHz, narrower than those of TMBOC or CBOC. The selected navigation solution is the most common one in current receivers and allows a direct performance comparison between dual- and single constellation users. For the sake of clarity, only the performance of baseline receivers will be presented in detail, relegating the analysis in depth of other receiver types to Appendix E and F.

7.2.3. Nominal pseudorange error model and user location

The nominal pseudorange error model depends on the GNSS receiver. The model described in section 4.3.7 is used, that is, tracking loops with a 1-Hz bandwidth DLL, a correlator with a 20-ms integration time and a DP discriminator. The signal to noise ratio is fixed to $C/N_0 = 30$ dB.

Single frequency ionospheric residual delay is the only error source which model depends on the user location; limiting the real position within continental France, the GPS nominal error is simplified to an elevation angle function independent from the user's position (Figure 4.4), while the Galileo error increases as the geomagnetic latitude decreases (Figure 4.7). In order to deal with a scenario close to the worst case, the user is set to be located in the city of Perpignan [42°41', 2°53'], in southern France.

The same tropospheric residual error model as in civil aviation is used (Figure 4.9).

The GNSS modernization level is presumed to assure a nominal error due to ephemeris and satellite clock inaccuracies with a standard deviation of 85 cm (eq. (4.18)).

7.2.4. Satellite constellations

The nominal 24-satellite GPS and 27-satellite Galileo constellations are used. A 72-hour simulation is run to obtain approximately all possible ground track combinations of GPS and Galileo satellites. The user is assumed to track only satellites directly visible from its position, with a minimum elevation angle of 5°.

7.2.5. RAIM algorithms

The chosen RAIM algorithms are the constant- P_{FA} and the variable- P_{FA} WLSR RAIMs presented in Chapter 6.

7.2.6. Positioning error correlation time

The positioning error correlation time T_c depends on the pseudorange correlation and on the variations of the user/satellite geometry. Two cases are studied:

- 1) Only one independent sample per segment. This case corresponds to receivers with pseudorange errors mainly driven by the ionospheric delay, with typically long correlation times.
- 2) Correlation time of $T_c = 5$ seconds. This case corresponds to receivers with pseudorange errors dominated by thermal noise, with short correlation times.

Two positions can be taken as independent, i.e. they produce independent fault detection outputs, when the difference between their estimation instants is at least T_c .

7.2.7. Geo-object detection algorithm

The geo-object recognition algorithm of eq.(3.6) is followed, in which a road segment is charged to a user if the number of independent valid positions inside the geo-object is equal to or higher than a threshold:

$$\text{charge road segment} \Leftrightarrow N_{\text{valid pos IN}} \geq N_{\text{Th}}$$

In order to contain only independent positions, the set of valid positions used to recognize a geo-object is obtained as depicted in Figure 3.11: every estimated position (sampled at 1 Hz) is checked until an valid position is found, and once it happens, a period of time equal to the positioning error correlation time T_c is waited before searching for the next valid position.

7.2.8. HAL

The HAL for road toll applications depends on the road network topology as described in section 3.4. Given the RAIM availability results obtained in the urban scenario (section 7.5) and the advice of experts, two different values of HAL are studied, 25 and 50 meters.

7.2.9. Trajectory duration

The objective of the simulations is to analyze the rate of missed road segments, so shorter segments represent worse cases. According to the statistics of existing GNSS-ETC systems in non-urban environments (Figure 3.6, Figure 3.7), the percentage of road segments with a length smaller than 500 meters in the Slovak system (which mainly covers national roads, which usually have shorter segments than highways) is lower than 30%, decreasing below to 20% and 5% for lengths of 250 and 70 meters respectively. Thus, a user's trajectory duration up to 40 seconds is taken, which corresponds to a geo-object length up to 555 meters for a user's speed of 50 km/h.

7.3. Satellite visibility

The positioning error and the RAIM performance depend on the user/satellite geometry, i.e. the number and position of the satellites used to estimate the navigation solution.

The statistics of the number of visible satellites obtained from the simulation results in urban and rural environments are illustrated in Figure 7.1, and the percentage of epochs in which a user is capable to perform fault detection and fault exclusion according to its required minimum number of satellites

(Table 3.10) are compiled in Table 7.2 - Table 7.4. These results are compared with those of an open air scenario in which any satellite with an elevation angle over 5° is visible. The higher visibility rates with Galileo than with GPS are due to the fact that the number of satellites is 27 for the Galileo nominal constellation, per 24 for the GPS one.

Dual constellation receivers provide a significant improvement in terms of satellite visibility with respect to single GPS or Galileo ones. Let us consider the example of a user that needs 5 satellites to perform fault detection, which is always attained in the open air scenario but in only 22.99 % and 42.41 % of the epochs in urban environments if it process only GPS or Galileo satellites respectively. Using both GPS and Galileo satellites increases the instants with $N_{\text{sat}} \geq 5$ up to 96.22% of the total time.

Table 7.2. Percentage of epochs with a number of visible GPS satellites enough for running a RAIM algorithm.

GPS				
Environment	$N_{\text{sat}} \geq 4$	$N_{\text{sat}} \geq 5$	$N_{\text{sat}} \geq 6$	$N_{\text{sat}} \geq 7$
Open air	100 %	100 %	100 %	94.57 %
Rural	98.95 %	85.96 %	49.50 %	14.85 %
Urban	53.62 %	22.99 %	7.01 %	1.5 %

Table 7.3. Percentage of epochs with a number of visible Galileo satellites enough for running a RAIM algorithm.

Galileo				
Environment	$N_{\text{sat}} \geq 4$	$N_{\text{sat}} \geq 5$	$N_{\text{sat}} \geq 6$	$N_{\text{sat}} \geq 7$
Open air	100 %	100 %	100 %	97.66 %
Rural	99.99 %	99.02 %	81.20 %	45.62 %
Urban	73.59 %	42.41 %	17.51 %	5.96 %

Table 7.4. Percentage of epochs with a number of visible GPS & Galileo satellites enough for running a RAIM algorithm.

GPS & Galileo				
Environment	$N_{\text{sat}} \geq 4$	$N_{\text{sat}} \geq 5$	$N_{\text{sat}} \geq 6$	$N_{\text{sat}} \geq 7$
Open air	100 %	100 %	100 %	100 %
Rural	100 %	100 %	100 %	99.996 %
Urban	99.26 %	96.22 %	89.01 %	75.84 %

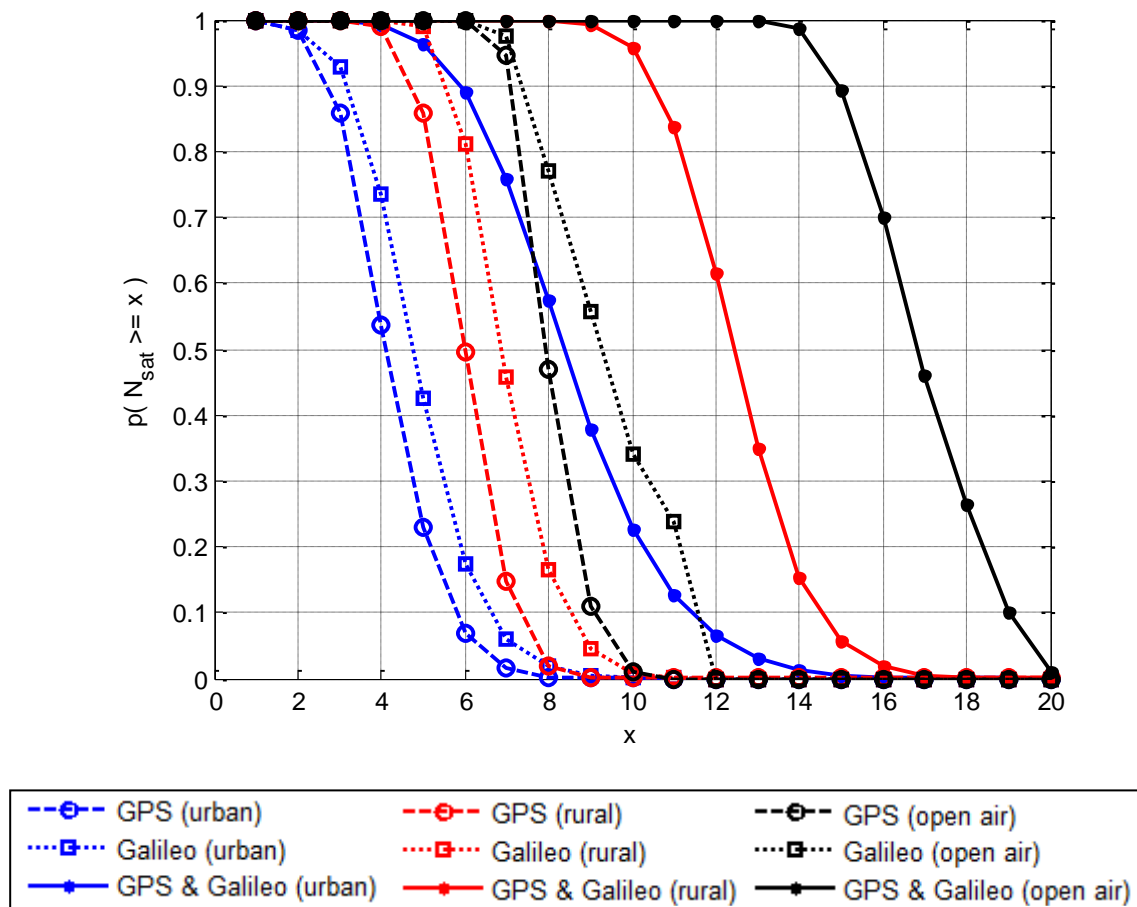


Figure 7.1. Measured probability that at a given epoch there is a minimum number of visible satellites (x).

In an open air scenario, the distribution of the GNSS satellites seen over the horizon from the user's location is an approximately decreasing function of the elevation angle (Figure 7.2). Obstacles in rural and urban environments mask more frequently satellites with low elevation angles, redistributing the probability from low towards higher elevation angles. There are no relevant differences between the distribution in elevation of GPS and Galileo satellites.

In the absence of obstacles, the azimuth of visible satellites is approximately uniformly distributed between -180° and 180° . The shape of the distribution becomes elliptical in the simulated rural and urban scenarios, with an increased probability of azimuth angles aligned with the street axis (Figure 7.3, where the street axis has been set in the line defined by the angles 0° - 180°). There are no relevant differences between the distribution in azimuth of GPS and Galileo satellites.

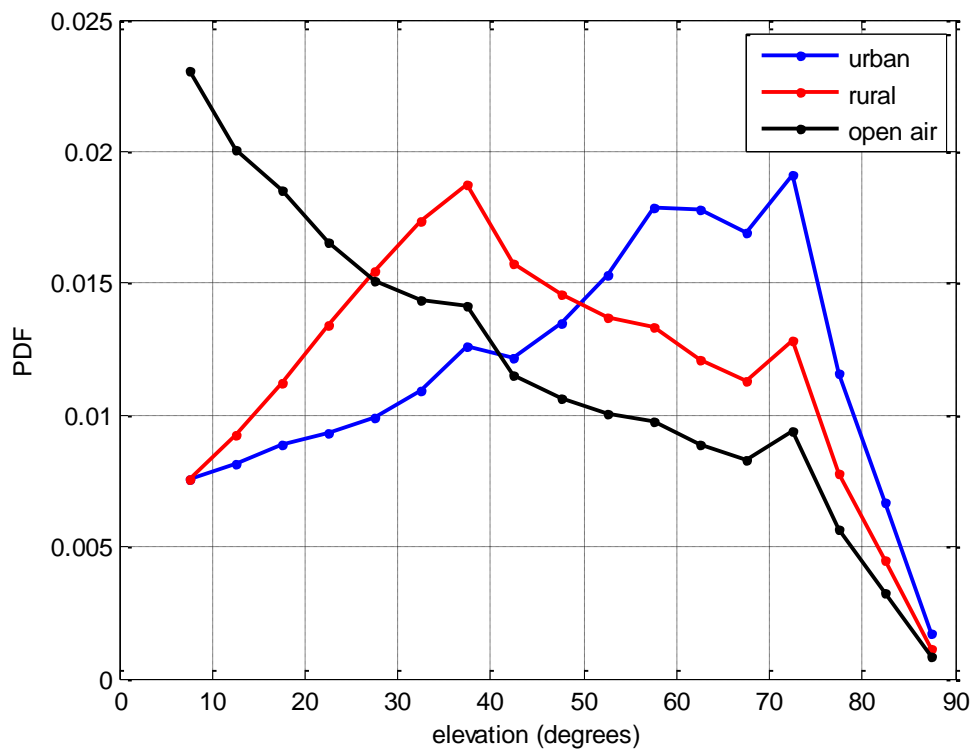


Figure 7.2. Measured distribution of visible GPS and Galileo satellites according to their elevation angle.

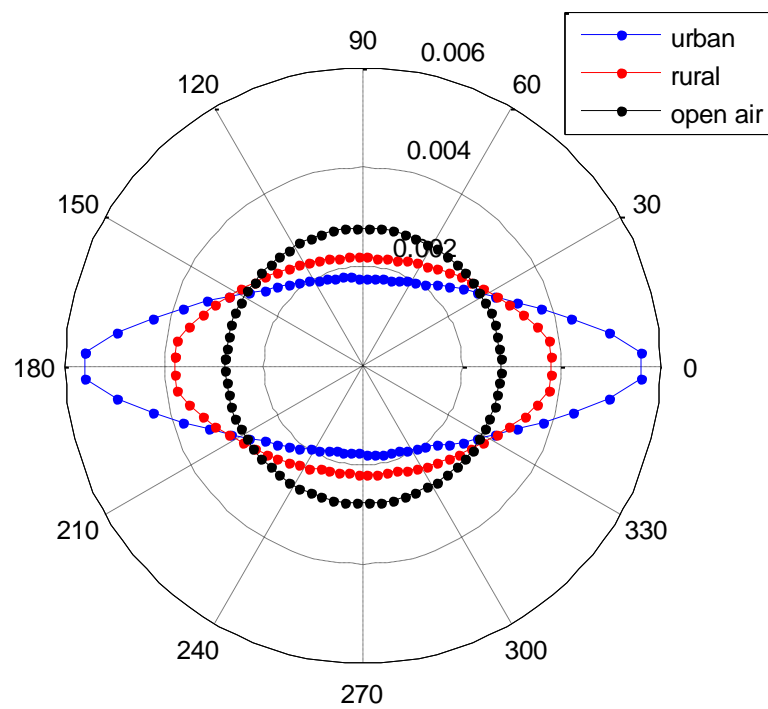


Figure 7.3. Measured distribution of visible GPS and Galileo satellites according to their azimuth with respect to the street axis (set in the line 0° - 180°).

As example, Figure 7.4 shows the observed distribution of visible satellites in the urban environment as a function of both their elevation and azimuth angle with respect to the street axis.

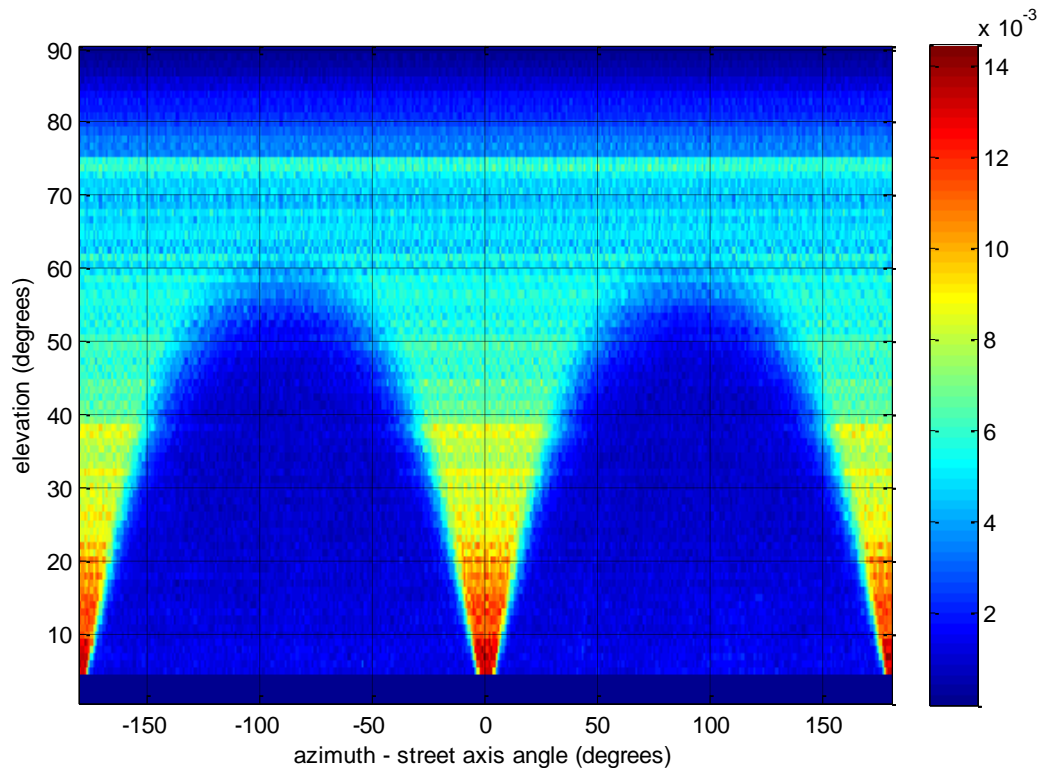


Figure 7.4. Distribution of the visible satellites in the urban environment.

7.4. Horizontal positioning error

The horizontal positioning error is a bivariate Gaussian distribution, so it that can be described as the joint distribution of two independent Gaussian random variables in the axis of the equidensity ellipses, which directions and variances depend on the user/satellite geometry and the pseudorange nominal error (Appendix C).

The difference of the standard deviation of the positioning error components in the major and minor semiaxes, σ_{major} and σ_{minor} , can reach several meters (Figure 7.5). The horizontal positioning error magnitude, as well as the importance of the major axis component over the minor axis one, increases as the number of visible satellites decreases (Figure 7.6).

In general, the error ellipse is likely to be oriented with its major axis perpendicular to the street axis, so that the positioning errors tend to situate the estimated position outside the street boundaries (Figure 7.7).

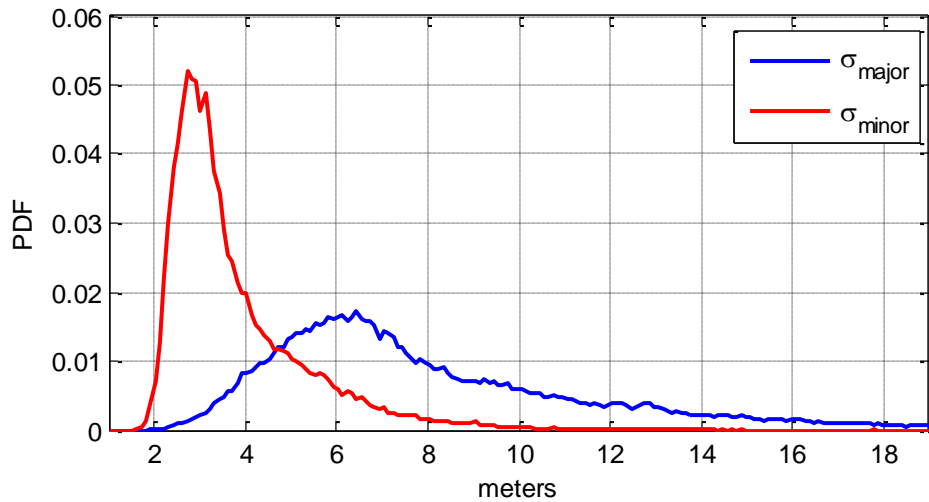


Figure 7.5. Measured PDF of σ_{major} and σ_{minor} in the urban scenario. Receiver: dual constellation, dual frequency receiver L1/E1 BOC(1,1) - L5/E5a BPSK(10). Navigation solution: 3D position and receiver/GNSS time shift.

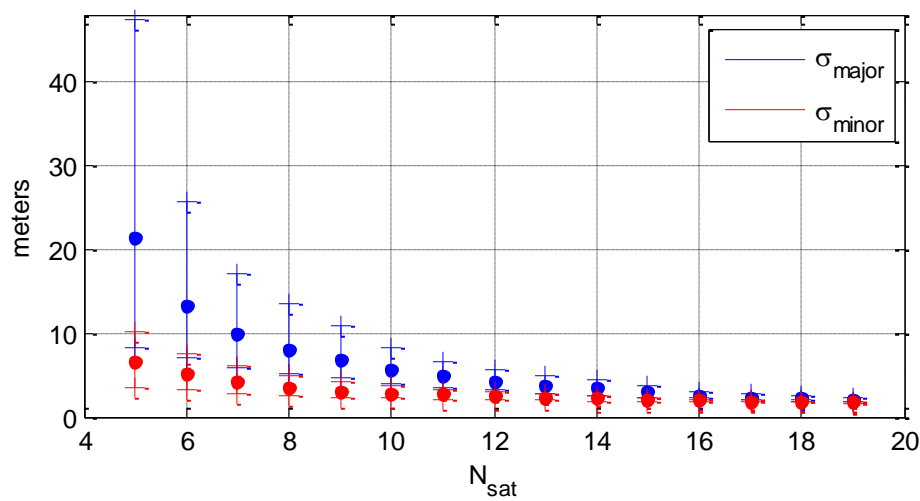


Figure 7.6. Mean, 5% and 95% percentiles of the measured σ_{major} and σ_{minor} as a function of the number of visible satellites. Receiver: dual constellation, dual frequency receiver L1/E1 BOC(1,1) - L5/E5a BPSK(10). Navigation solution: 3D position and receiver/GNSS time shift.

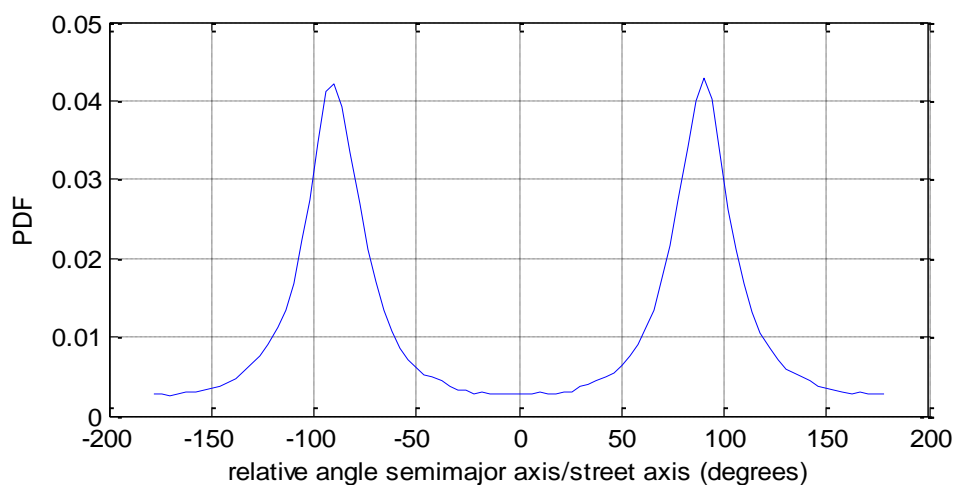


Figure 7.7. Measured distribution of the relative angle between the positioning error major axis and the street axis. Receiver: dual constellation, dual frequency receiver L1/E1 BOC(1,1) - L5/E5a BPSK(10). Navigation solution: 3D position and receiver/GNSS time shift.

7.5. RAIM performance

RAIM performance can be measured by the probability of not detecting a positioning failure and by the probability of missing an valid position (because of a false alarm or RAIM unavailability). For a given user/satellite geometry and pseudorange nominal errors, the RAIM performance depends on the combination of P_{MD} , P_{FA} and its availability, that is, the comparison between HPL and HAL. Since both analyzed RAIM have been designed with a fixed P_{MD} , they always attain the missed alarm rate they have been conceived to meet, and it is the probability of providing an valid position in the fault-free case which varies in time. The civil aviation WLSR RAIM has constant P_{MD} and P_{FA} with a time-variant HPL, whereas the novel WLSR RAIM is designed to provide fixed P_{MD} and HPL with a time-variant P_{FA} . Therefore the RAIM performance at a given instant is characterized by the HPL in the first algorithm and by the P_{FA} in the second one. Both variable parameters are directly related with the $slope_{MAX}$ and depend on the user/satellite geometry, the nominal pseudorange error and the other integrity monitoring requirements (P_{MD} and P_{FA} for the variable HPL, P_{MD} and HAL for the variable P_{FA}).

In the studied case, single-frequency SBAS users have the lowest nominal errors, followed by dual-frequency and finally, with the highest errors, non-augmented single-frequency ones (section 4.3.7). Dual-frequency SBAS users are not studied because their nominal errors are approximately equal to those of the non-augmented case. Therefore, for the same RAIM configuration and geometry, SBAS users provide the best performance, followed by dual-frequency ones.

The user/satellite geometry depends on the number of visible satellites and on how these are introduced in the observation matrix. In general, at a given instant and for the same RAIM and pseudorange errors, dual constellation receivers outperform single-constellation ones. The different navigation solutions modify the observation matrix and also play an important role in the user/geometry; in decreasing order of performance:

- 1) 2D position and receiver/GNSS delay,
- 2) 2D position, receiver/GPS delay and inter-GNSS delay,
- 3) 3D position and receiver/GNSS delay
- 4) 3D position, receiver/GPS delay and inter-GNSS delay.

This section presents a statistical analysis of the $slope_{MAX}$, the HPL of the standard WLSR RAIM and the P_{FA} of the novel RAIM for the baseline receiver (dual frequency receivers with BOC(1,1) modulation in L1/E1 and navigation solution consisting of 3D position plus user/GNSS delay), in urban and rural scenarios, in the fault-free case (no major service failure). Afterwards, the behavior of other receivers is overviewed and finally, the performance of the fault exclusion module is analyzed.

7.5.1. Maximum slope

The maximum slope is a function of the nominal error covariance matrix and the user/satellite geometry, independent from the WLSR RAIM algorithm and its configuration. It is an indicator of the performance the WLSR RAIM is able to attain at a given instant: the smaller it is, the lower is the HPL in the classic WLSR RAIM, as well as the P_{FA} in the variable- P_{FA} WLSR RAIM.

Figure 7.8 compares the maximum slope CDF obtained with the baseline receiver in the urban and rural scenarios. In order to obtain comparable functions for different users and environments, the CDF has been computed over the whole simulation length, setting $slope_{MAX}$ to infinity when the number of satellites does not reach the minimum necessary to perform integrity monitoring. That is, the obtained

curves represent the probability that at a given instant the user is able to run the integrity monitoring function with a $\text{slope}_{\text{MAX}}$ equal to or lower than a given value.

The environment has a significant impact on the maximum slope: the values of $\text{slope}_{\text{MAX}}$ are much lower in the rural scenario than in the urban one, which is additionally limited by the fact that only 96% of the epochs have 5 or more visible satellites. As expected, SBAS receivers have the best performance, followed by dual frequency ones.

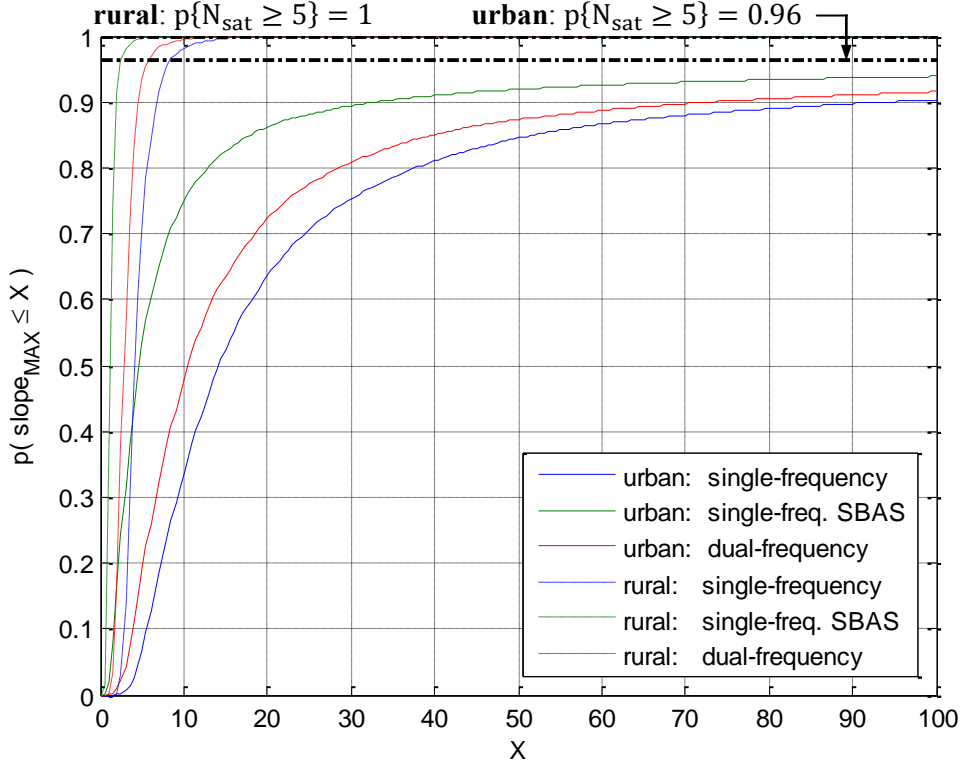
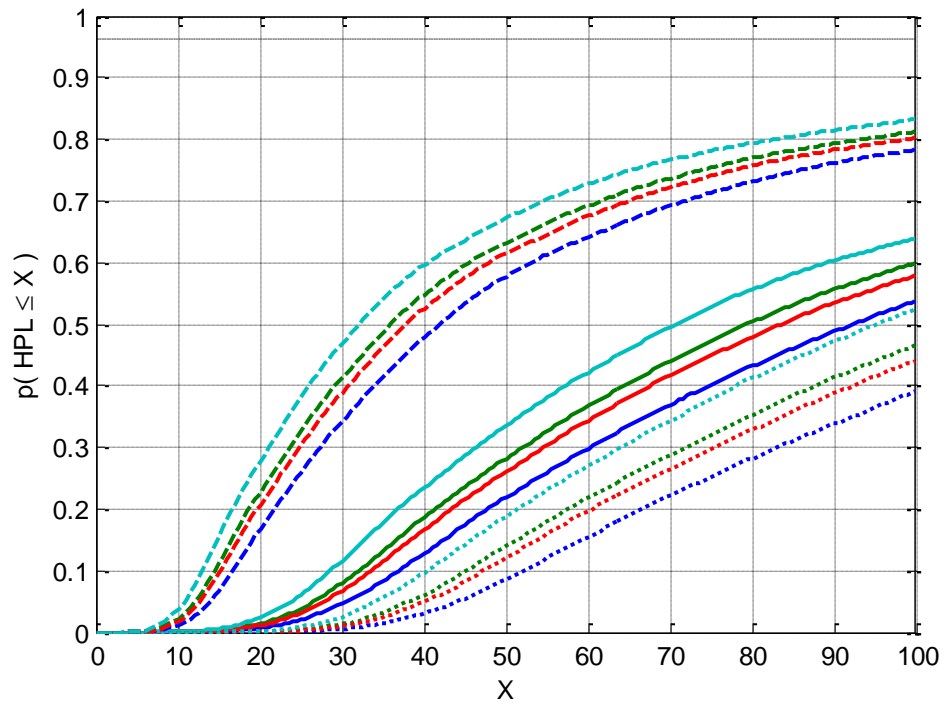


Figure 7.8. Measured CDF of the $\text{slope}_{\text{MAX}}$ in the fault detection RAIM (fault-free case). Receiver: dual constellation L1/E1 BOC(1,1); dual frequency with L5/E5a BPSK(10). Navigation solution: 3D position and receiver/GNSS time shift.

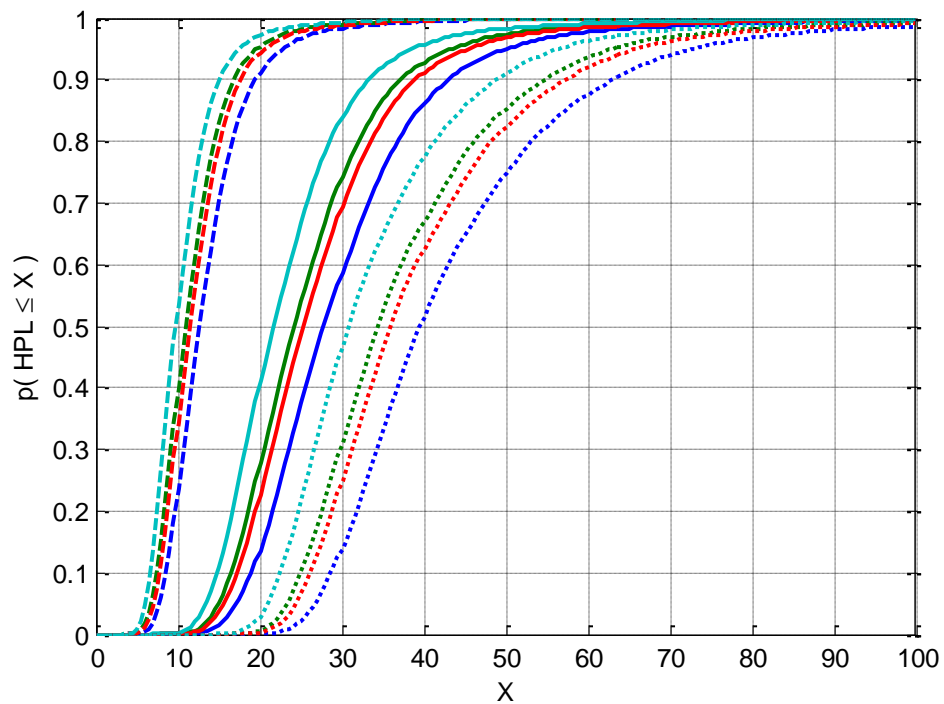
7.5.2. Variable HPL (WLSR RAIM with constant P_{FA})

The HPL of the classic WLSR RAIM of eq.(6.36) is a function of $\text{slope}_{\text{MAX}}$, which varies with the user/satellite geometry and the nominal pseudorange error, and λ_{det} , which depends on the P_{MD} and P_{FA} . Figure 7.9 depicts the probability that the RAIM is available at a given instant as a function of the HAL. In general, the availability rate in urban environments for HAL below 100 meters is low; with HAL=50 m., it spans between 9% and 19% for single frequency receivers, 22% and 34% for dual frequency ones, and between 58% and 68% for L1/E1 SBAS users. Despite the improvement in rural environments, the RAIM availability remains low, specially for single frequency receivers. For the same P_{MD} , higher P_{FA} give smaller HPL (better availability).

Hybridized GNSS receivers with external altitude information increase the RAIM availability according to the altitude nominal noise σ_{alt} , being able to reach a performance level up to that of 2D receivers that do not estimate the altitude (Figure 7.10). For instance, an external altitude with $\sigma_{\text{alt}} = 5$ meters increases the availability rate of baseline dual-frequency receivers with $P_{\text{MD}} = 5 \cdot 10^{-5}$, $P_{\text{FA}} = 10^{-3}$ and HAL = 50 meters in urban environments from 28% to 44%.



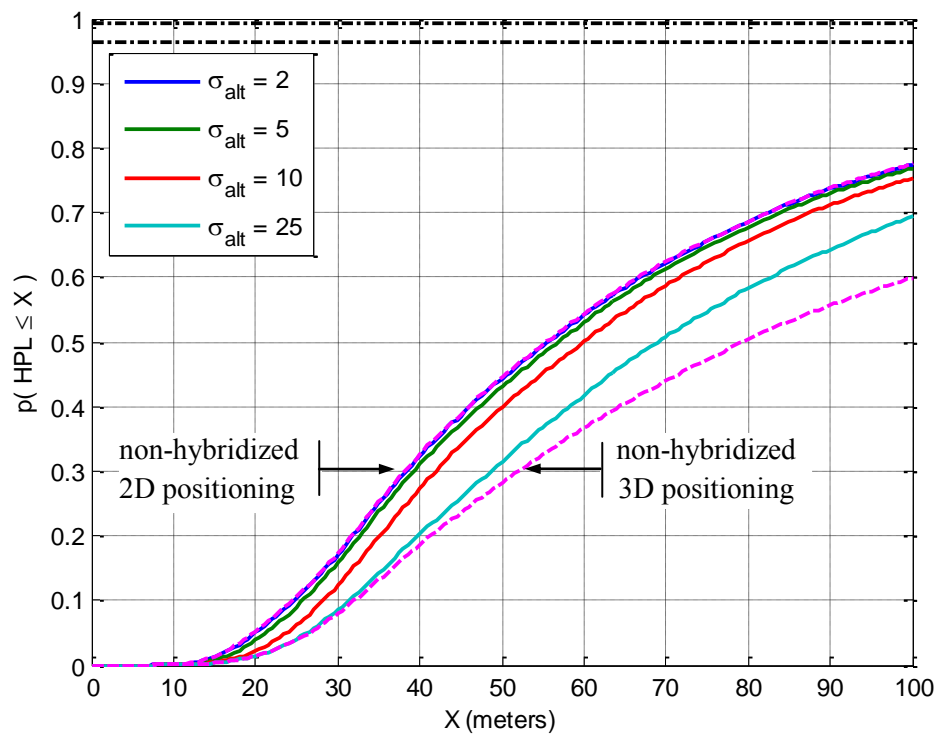
a) Urban environment



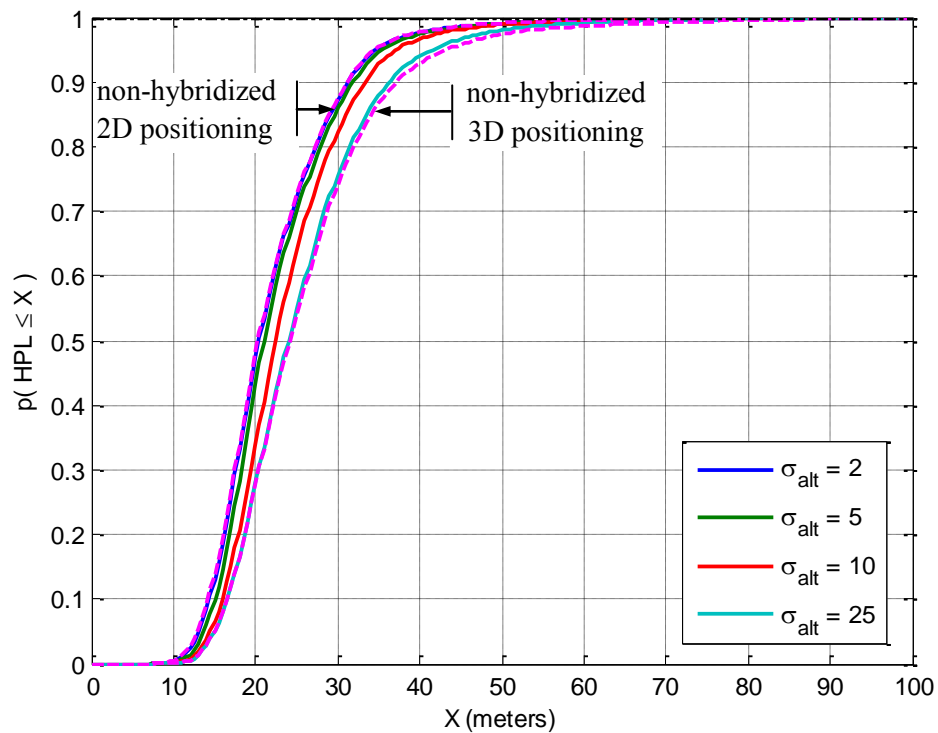
b) Rural environment

$P_{MD} = 5 \cdot 10^{-5}, P_{FA} = 5 \cdot 10^{-5}$	Dotted line: L1/E1
$P_{MD} = 5 \cdot 10^{-5}, P_{FA} = 5 \cdot 10^{-3}$	Dashed line: L1/E1 + SBAS corrections
$P_{MD} = 10^{-3}, P_{FA} = 5 \cdot 10^{-5}$	Solid line: iono-free L1/E1 - L5/E5a
$P_{MD} = 10^{-3}, P_{FA} = 5 \cdot 10^{-3}$	

Figure 7.9. CDF of the HPL obtained in the fault detection civil aviation WLSR RAIM (fault-free case). Receiver: dual constellation L1/E1 BOC(1,1); dual frequency with L5/E5a BPSK(10). Navigation solution: 3D position and receiver/GNSS time shift.



a) Urban environment



b) Rural environment

Figure 7.10. CDF of the HPL obtained in the fault detection module of the civil aviation WLSR RAIM for hybrid receivers with external altitude with an error model σ_{alt} . Receiver: dual constellation, dual frequency L1/E1 BOC(1,1) - L5/E5a BPSK(10). Navigation solution: 3D position and receiver/GNSS time shift. RAIM configuration: $P_{MD} = 5 \cdot 10^{-5}$, $P_{FA} = 5 \cdot 10^{-3}$.

7.5.3. Variable P_{FA} (WLSR RAIM with constant HPL)

The variable P_{FA} - eq.(6.44) - depends on the P_{MD} , the HAL, the user/satellite geometry and the nominal pseudorange error.

Figure 7.11 illustrates the CDF of the probability of false alert with the HAL set to 25 and 50 meters. The HAL has a significant effect on the P_{FA} ; for example, a iono-free baseline user with $P_{MD} = 5 \cdot 10^{-5}$ has $P_{FA} \leq 10^{-3}$ the 63% of the epochs if HAL = 50 m, and 32% if HAL = 25 m.

The CDF of the P_{FA} is equivalent to the RAIM availability in the civil aviation WLSR RAIM. For instance, the probability that baseline users have $P_{FA} \leq 10^{-3}$ in an urban environment with $P_{MD} = 5 \cdot 10^{-5}$ and HAL = 50 is the same that $HPL \leq 50$ with $P_{MD} = 5 \cdot 10^{-5}$ and $P_{FA} = 10^{-3}$. This probability is 14% for L1/E1 receivers, 28% for dual frequency and 63% for SBAS users (Figure 7.9, Figure 7.11)

Hybridized GNSS receivers with external altitude information decrease the P_{FA} up to the levels of 2D receivers that do not estimate the altitude (Figure 7.12).

7.5.4. Alternative receivers

Appendix E contains the classic WLSR RAIM unavailability rate, i.e. $p\{HPL > HAL\}$, in the fault-free case, obtained from the simulations for all the combinations of GNSS signals and navigation solutions under study in the urban and rural environment, with HAL equal to 25 and 50 meters. The RAIM has been configured with the values selected in section 7.6, that is, $P_{MD} = 5 \cdot 10^{-5}$, $P_{MD} = 10^{-3}$ and $P_{FA} = 5 \cdot 10^{-3}$. The shown RAIM unavailability is equivalent to the probability that the P_{FA} of the variable- P_{FA} WLSR RAIM exceeds $5 \cdot 10^{-3}$.

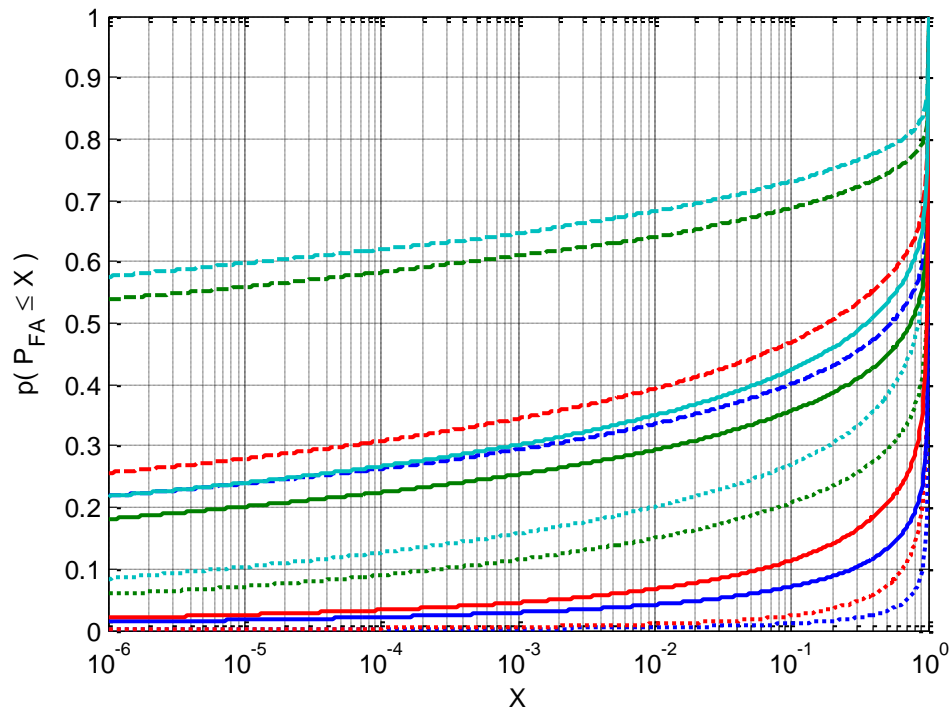
In general, the best performance is obtained for users computing 2D positioning with SBAS corrections.

In the dual constellation case, SBAS 2D users reach, with a 50-m HAL in urban environment, an unavailability rate of 6.9% for L1 TMBOC(6,1,4/33) & E1 CBOC(6,1,1/11,-) users, and of 5.5% for L5/E5a BPSK(10) users. Three-dimensional positioning receivers that integrate external altitude data with $\sigma_{alt} = 5$ m attain unavailability rates close to those of 2D users: 7.4% for L1 TMBOC(6,1,4/33) & E1 CBOC(6,1,1/11,-) users, and 6% for L5/E5a BPSK(10) users.

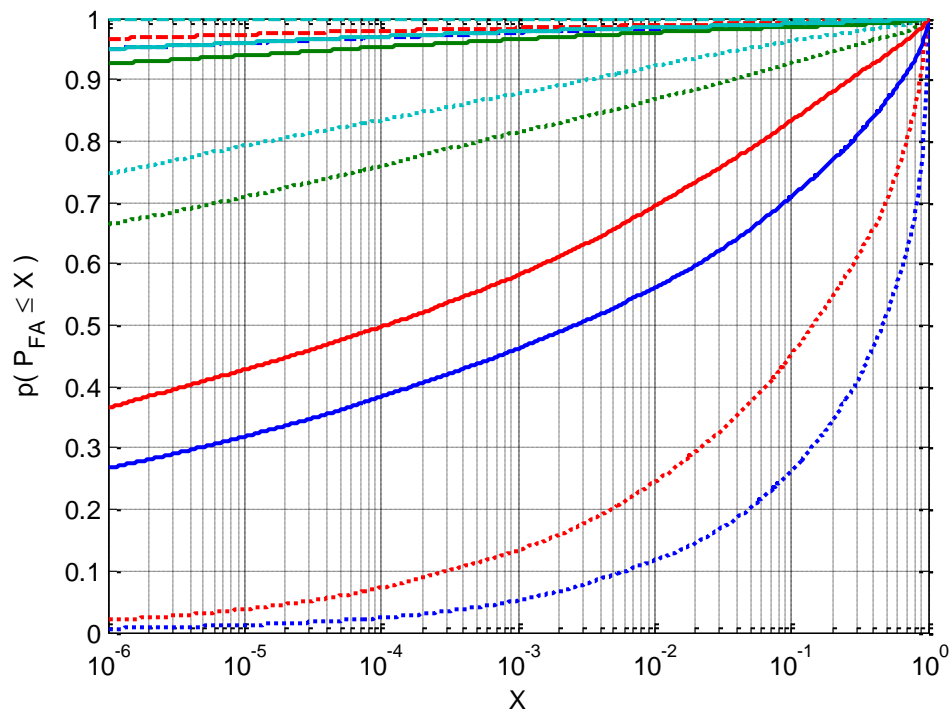
Using E1 CBOC(6,1,1/11,+) or E1 CBOC(6,1,1/11,-) do not provide important differences; for example, the unavailability for 3D positioning with both signals combined with L1 TMBOC(6,1,4/33) varies from 18.8% to 17.8%.

RAIM unavailability is considerably smaller in the rural scenario, attaining values around 10^{-5} or even lower for 2D SBAS users. Nevertheless, some receiver configurations, specially single frequency ones with HAL=25 m, provide unacceptably large unavailability rates.

Users using only one constellation, GPS or Galileo, have a very high unavailability in urban environment. For instance, a dual-frequency, 2D-positioning GPS user with TMBOC, has the RAIM unavailable 80.5% of the time for $P_{MD} = 5 \cdot 10^{-5}$ and a HAL of 50 meters; in the same conditions, a dual constellation user that additionally process E1 CBOC- signals decreases the unavailability rate to 18%. The high unavailability rate of single constellation users in the urban scenario make them suitable for road toll only in rural environments.



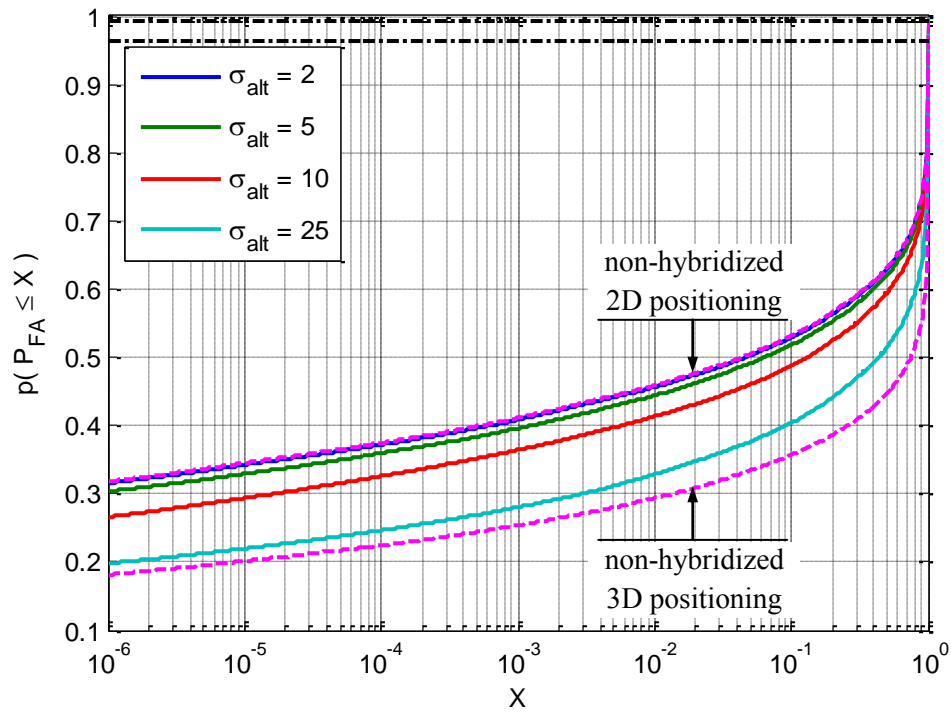
a) Urban environment



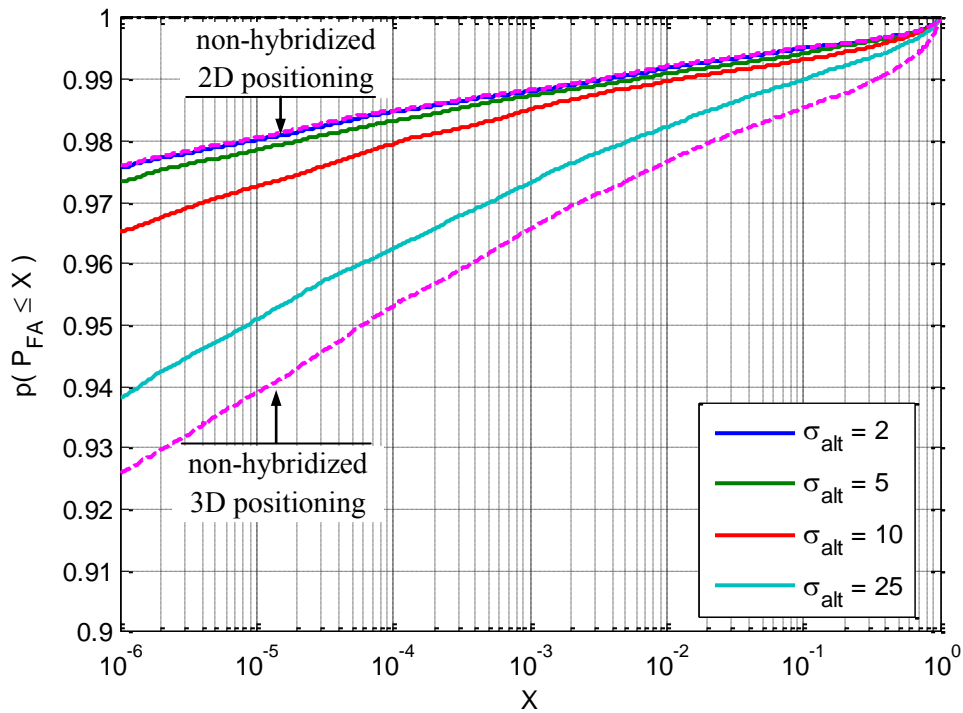
b) Rural environment

— $P_{MD} = 5 \cdot 10^{-5}$, HAL = 25 m.	Dotted line: L1/E1
— $P_{MD} = 5 \cdot 10^{-5}$, HAL = 50 m.	Dashed line: L1/E1 + SBAS corrections
— $P_{MD} = 10^{-3}$, HAL = 25 m.	Solid line: iono-free L1/E1 - L5/E5a
— $P_{MD} = 10^{-3}$, HAL = 50 m.	

Figure 7.11. CDF of the P_{FA} obtained in the fault detection module of the variable- P_{FA} WLSR RAIM (fault-free case). Receiver: dual constellation L1/E1 BOC(1,1); dual frequency with L5/E5a BPSK(10). Navigation solution: 3D position and receiver/GNSS time shift.



a) Urban environment



b) Rural environment

Figure 7.12. CDF of the P_{FA} obtained in the fault detection module of the variable- P_{FA} WLSR RAIM for hybrid receivers with external altitude with an error model σ_{alt} . HAL=50 meters. Receiver: dual constellation, dual frequency L1/E1 BOC(1,1) - L5/E5a BPSK(10). Navigation solution: 3D position and receiver/GNSS time shift.

7.5.5. Fault exclusion module

Although this work focuses in the RAIM fault detection capability, Appendix E contains the unavailability rate of the WLSR RAIM fault exclusion module, obtained from the simulations for all the combinations of GNSS signals and navigation solutions under study in the urban and rural environment, with HAL equal to 25 and 50 meters. These data are equivalently the probability that the P_{FA} of the variable- P_{FA} WLSR RAIM exceeds $5 \cdot 10^{-3}$. The unavailability of the fault exclusion module has been calculated as the worst-case value computed in the N subgroups of $N-1$ range measurements at each instant. The RAIM has been configured as in fault-free case, that is, $P_{MD} = 5 \cdot 10^{-5}$, $P_{MD} = 10^{-3}$ and $P_{FA} = 5 \cdot 10^{-3}$.

The satellite removal process, which deteriorates the user/satellite geometry, and the fact of selecting the worst-case subgroup, results in a poorer performance than in the fault detection case. As in the fault detection case, the best performance is obtained for users computing 2D positioning with SBAS corrections, and the integration of external altitude information improve the performance up to a maximum equal to that of users that only estimate the bidimensional horizontal position.

7.6. Road toll performance

WLSR RAIM algorithms are designed with a fixed P_{MD} , so they always attain the false segment recognition rate (overcharging) they have been conceived to meet in section 5.4.4.1, independently from the environment. Therefore, the analysis of the GNSS-ETC performance focuses in the missed geo-object recognition rate (undercharging).

The probability of missed segment recognition, i.e. $p\{N_{\text{valid pos IN}} < N_{Th}\}$, has been computed for any user trajectory beginning every $T_s = 1$ second and duration ranging from 1 to 40 seconds. The presented results are the average probability obtained along the 72 hours of simulation.

First, the best parameters of the geo-object recognition algorithm are found. Afterwards the probability of missed road segment detection in the fault-free case is calculated, first with baseline receivers and finally for the rest of users.

7.6.1. Segment recognition algorithm and RAIM configuration

A road segment is correctly recognized and charged to the user when the number of valid positions inside the geo-object is equal to or greater than the threshold N_{Th} of the segment recognition algorithm. A higher threshold requires the RAIM to be designed with a less restrictive P_{MD} in order to meet the overcharging constraint (Table 5.2).

The probability of missed segment recognition has been analyzed for different N_{Th} and their corresponding P_{MD} , proving that the best results are obtained with $N_{Th} = 1$ (Figure 7.13). In all different combinations of GNSS signals, RAIM algorithms and trajectory durations under study, the increased P_{MD} allowed by a higher N_{Th} does not compensate the increment in the required number of valid positions per segment.

For this reason, the geo-object recognition algorithm threshold is set to $N_{Th} = 1$, that is, only one valid position inside the geo-object is necessary to charge the road segment.

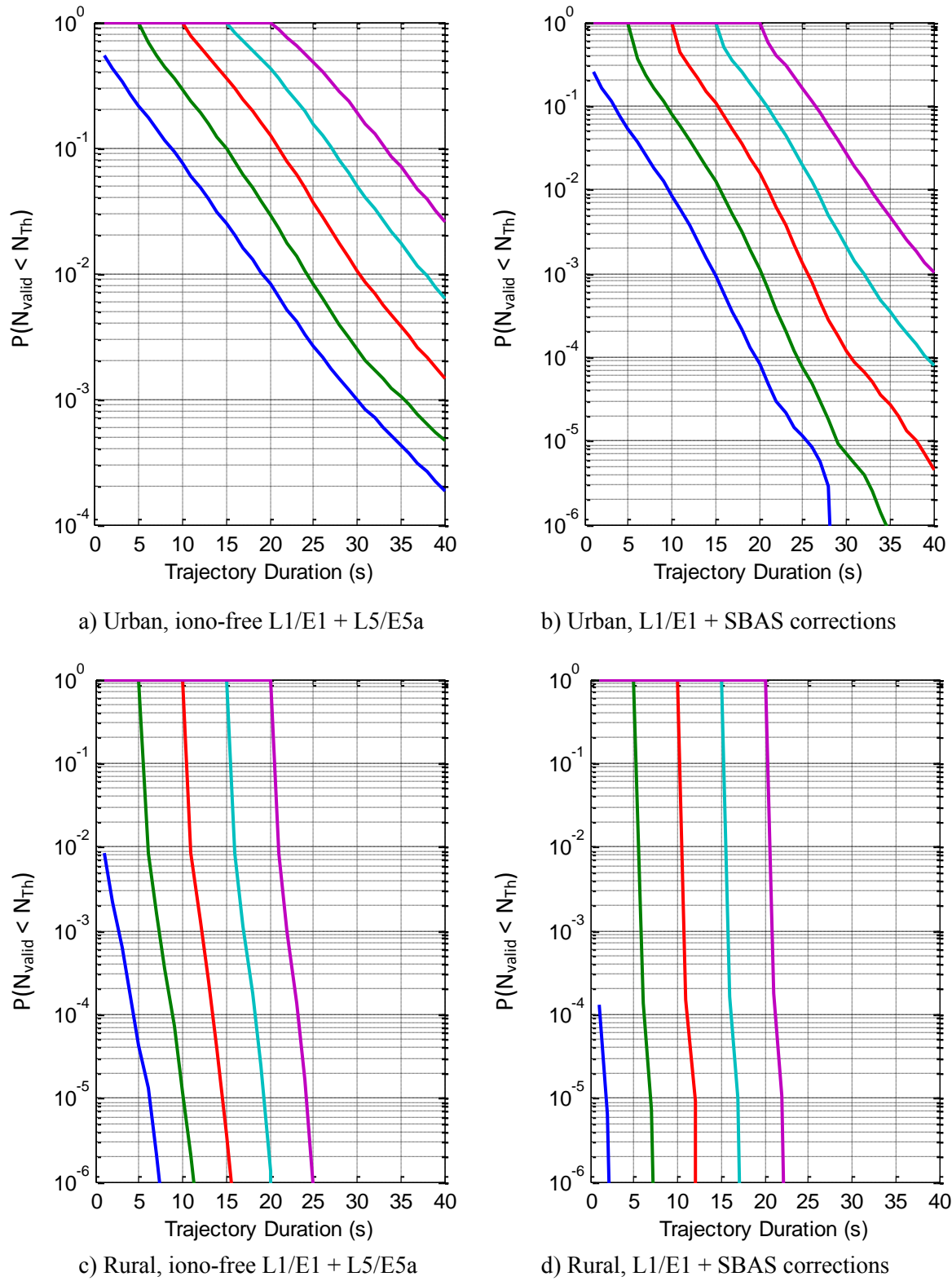


Figure 7.13. Probability that, in the fault-free case, the number of valid positions inside the geo-object is lower than the segment recognition threshold for different N_{Th} and P_{MD} . HAL=50 meters. Variable- P_{FA} WLSR RAIM. Receiver: dual constellation L1/E1 BOC(1,1); dual frequency with L5/E5a BPSK(10). Navigation solution: 3D position and receiver/GNSS time shift.

The P_{MD} is obtained from the curve $N_{Th} = 1$ of Figure 5.10 (or Table 5.2). Two values of P_{MD} will be studied:

- $P_{MD} = 5 \cdot 10^{-5}$, which meets the overcharging requirement in the worst-case with a positioning error correlation of $T_c = 5$ seconds (it meets the maximum allowed probability of false geo-object recognition for up to 72 independent geo-object misleading positions, which corresponds to a user trajectory of 360 seconds -5 km at 50 km/h- outside the geo-object and all its positions incorrectly estimated inside it).
- $P_{MD} = 10^{-3}$, which meets the overcharging requirement when there is only one independent position per segment.

The P_{FA} is obtained from the curve $N_{Th} = 1$ of Figure 5.14. Two values of P_{FA} are studied:

- $P_{FA} = 5 \cdot 10^{-5}$, which meets the undercharging requirement if there is always one independent position with available RAIM in the geo-object.
- $P_{FA} = 5 \cdot 10^{-3}$, which meets the undercharging requirement if there is always two independent positions with available RAIM in the geo-object.

7.6.2. Probability of missed geo-object recognition

The toll system performance with baseline receivers is analyzed in the fault-free scenario described in section 5.4.4.2.1, in which a user circulates through a road segment and all estimated positions that may be used by the segment recognition algorithm are free of pseudorange failures because there is no major service failure (Figure 5.12). The undercharging requirement $P_{MGoR} = 10^{-4}$ is met when the probability of an insufficient number of valid positions inside the geo-object in the fault-free case is $p\{N_{valid\ pos\ IN} = 0\} \leq 5 \cdot 10^{-5}$ - eq.(5.46) -.

The average probability of missed segment recognition has been calculated for the baseline receiver for trajectory durations up to 40 seconds and the configurations set in the previous subsection, that is, $N_{Th} = 1$, $P_{MD} = 5 \cdot 10^{-5}$, $P_{MD} = 10^{-3}$, and for the civil aviation RAIM, $P_{FA} = 5 \cdot 10^{-5}$ and $P_{FA} = 5 \cdot 10^{-3}$.

In general, the WLSR RAIM with variable P_{FA} outperforms the classic one, which in turn provides better results with $P_{FA} = 5 \cdot 10^{-3}$ than with $P_{FA} = 5 \cdot 10^{-5}$ (Figure 7.14); this behavior is found in all studied cases, so only the case with $P_{FA} = 5 \cdot 10^{-3}$ will be analyzed hereafter (Figure 7.15 - Figure 7.16).

The probability of missed geo-object recognition decreases as the user trajectory along it gets longer. Table 7.5 and Table 7.6 contain the minimum user trajectory duration (T_{min}) from which the required probability of missed road segment recognition with $N_{Th} = 1$ is met, i.e. $p\{N_{valid\ pos\ IN} = 0 \mid T \geq T_{min}\} \leq 5 \cdot 10^{-5}$, where T is the total trajectory duration.

In the urban environment, users with the classic WLSR RAIM are able to meet the undercharging requirement only if they apply SBAS corrections and the HAL is 50 meters. The RAIM with variable P_{FA} reduces the trajectory duration needed to attain the requirement with those configurations, and adds two more valid cases with $P_{MD} = 10^{-3}$: HAL=25 m. for SBAS users and HAL=50 m. for iono-free receivers. The integration of external altitude information with an error model $\sigma_{alt} = 5$ m. decreases T_{min} for all valid cases with non-hybridized receivers, and includes the case of HAL=25 m. with $P_{MD} = 5 \cdot 10^{-5}$ and the variable- P_{FA} WLSR RAIM.

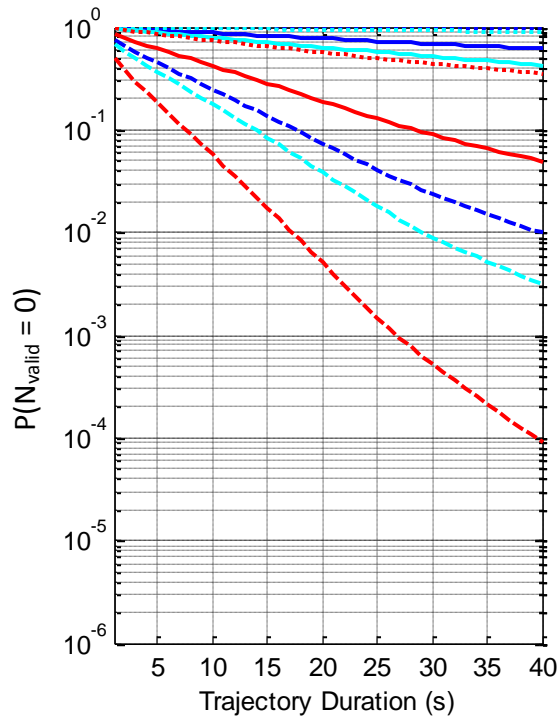
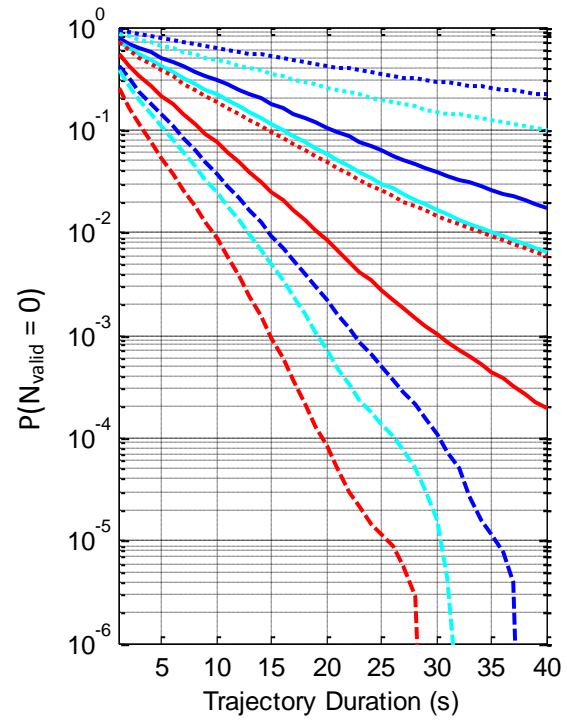
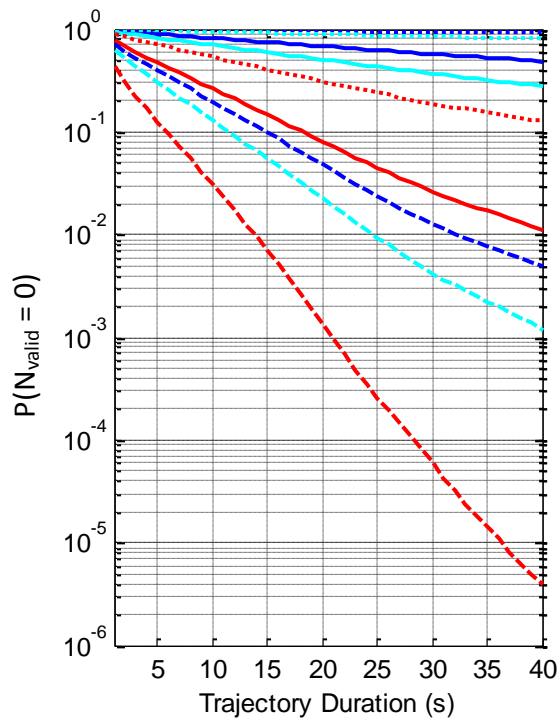
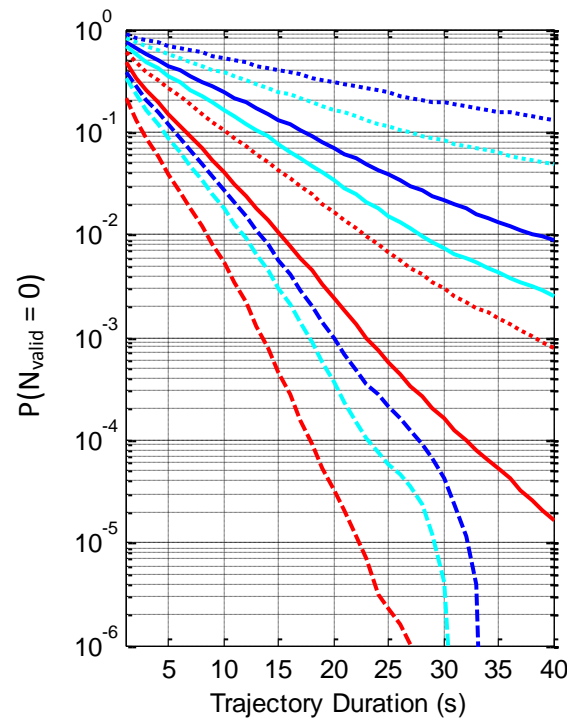
In the rural environment, the classic WLSR RAIM attains the requirement in all cases except for single-frequency receivers without SBAS corrections with an HAL of 25 m. If the variable- P_{FA} RAIM is used, the only case that does not meet the maximum allowed undercharging ratio is for $HAL=25$ m. and $P_{MD} = 5 \cdot 10^{-5}$.

Table 7.5. Minimum user trajectory that meets the undercharging requirement. Urban environment. Receiver: GPS & Galileo L1/E1 BOC(1,1); iono-free with L5/E5a BPSK(10). Navigation solution: 3D position and receiver/GNSS time shift.

External altitude hibridization	Pseudorange nominal error model	Environment							
		Urban							
		WLSR RAIM							
		Classic ($P_{FA} = 5 \cdot 10^{-3}$)				Variable P_{FA} (HPL = HAL)			
		P_{MD}							
		$5 \cdot 10^{-5}$		10^{-3}		$5 \cdot 10^{-5}$		10^{-3}	
		HAL							
		25	50	25	50	25	50	25	50
No hibridization	L1/E1	x	x	x	x	x	x	x	x
	L1/E1 + SBAS	x	29	x	26	x	22	31	20
	L1/E1 + L5/E5a	x	x	x	x	x	x	x	36
$\sigma_{alt} = 5$ m.	L1/E1	x	x	x	x	x	x	x	x
	L1/E1 + SBAS	x	20	x	17	29	15	21	13
	L1/E1 + L5/E5a	x	x	x	x	x	30	x	21

Table 7.6. Minimum user trajectory that meets the undercharging requirement. Rural environment. Receiver: GPS & Galileo L1/E1 BOC(1,1); iono-free with L5/E5a BPSK(10). Navigation solution: 3D position and receiver/GNSS time shift.

External altitude hibridization	Pseudorange nominal error model	Environment							
		Rural							
		WLSR RAIM							
		Classic ($P_{FA} = 5 \cdot 10^{-3}$)				Variable P_{FA} (HPL = HAL)			
		P_{MD}							
		$5 \cdot 10^{-5}$		10^{-3}		$5 \cdot 10^{-5}$		10^{-3}	
		HAL							
		25	50	25	50	25	50	25	50
No hibridization	L1/E1	✗	20	✗	17	✗	10	23	7
	L1/E1 + SBAS	9	3	8	3	5	2	4	2
	L1/E1 + L5/E5a	✗	10	28	8	15	5	12	4
$\sigma_{alt} = 5$ m.	L1/E1	✗	17	✗	14	26	8	18	6
	L1/E1 + SBAS	8	3	6	2	5	1	4	1
	L1/E1 + L5/E5a	25	8	20	6	12	5	9	4

a) $P_{MD} = 5 \cdot 10^{-5}$, HAL = 25 mb) $P_{MD} = 5 \cdot 10^{-5}$, HAL = 50 mc) $P_{MD} = 10^{-3}$, HAL = 25 md) $P_{MD} = 10^{-3}$, HAL = 50 m

— Constant- P_{FA} WLSR RAIM ($P_{FA} = 5 \cdot 10^{-5}$)	Dotted line: L1/E1
— Constant- P_{FA} WLSR RAIM ($P_{FA} = 5 \cdot 10^{-3}$)	Dashed line: L1/E1 + SBAS corrections
— Variable- P_{FA} WLSR RAIM	Solid line: iono-free L1/E1 - L5/E5a

Figure 7.14. Probability of zero valid positions during a user trajectory through a geo-object in the fault-free case. Environment: urban. Receiver: dual constellation L1/E1 BOC(1,1); dual frequency with L5/E5a BPSK(10). Navigation solution: 3D position and receiver/GNSS time shift.

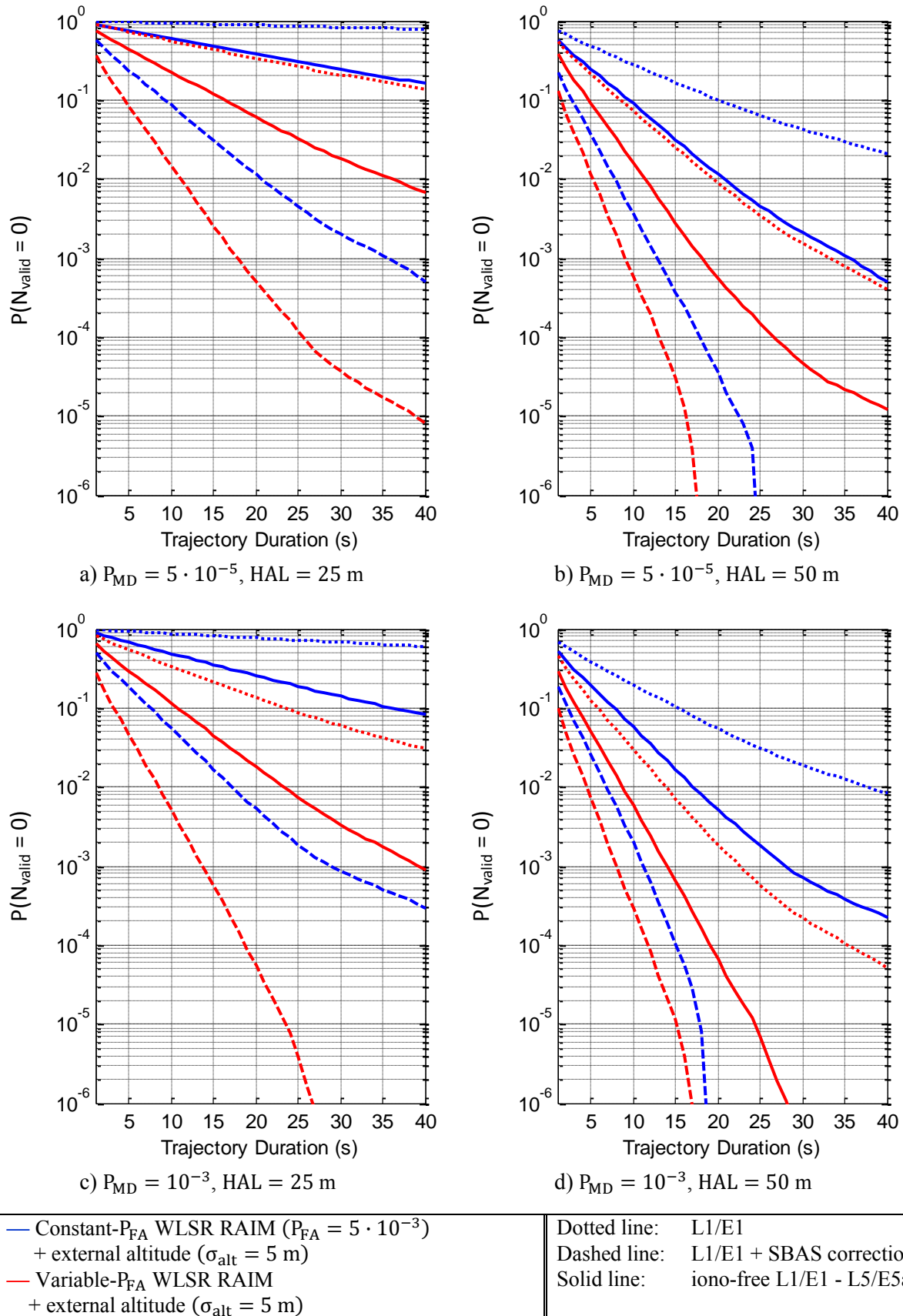
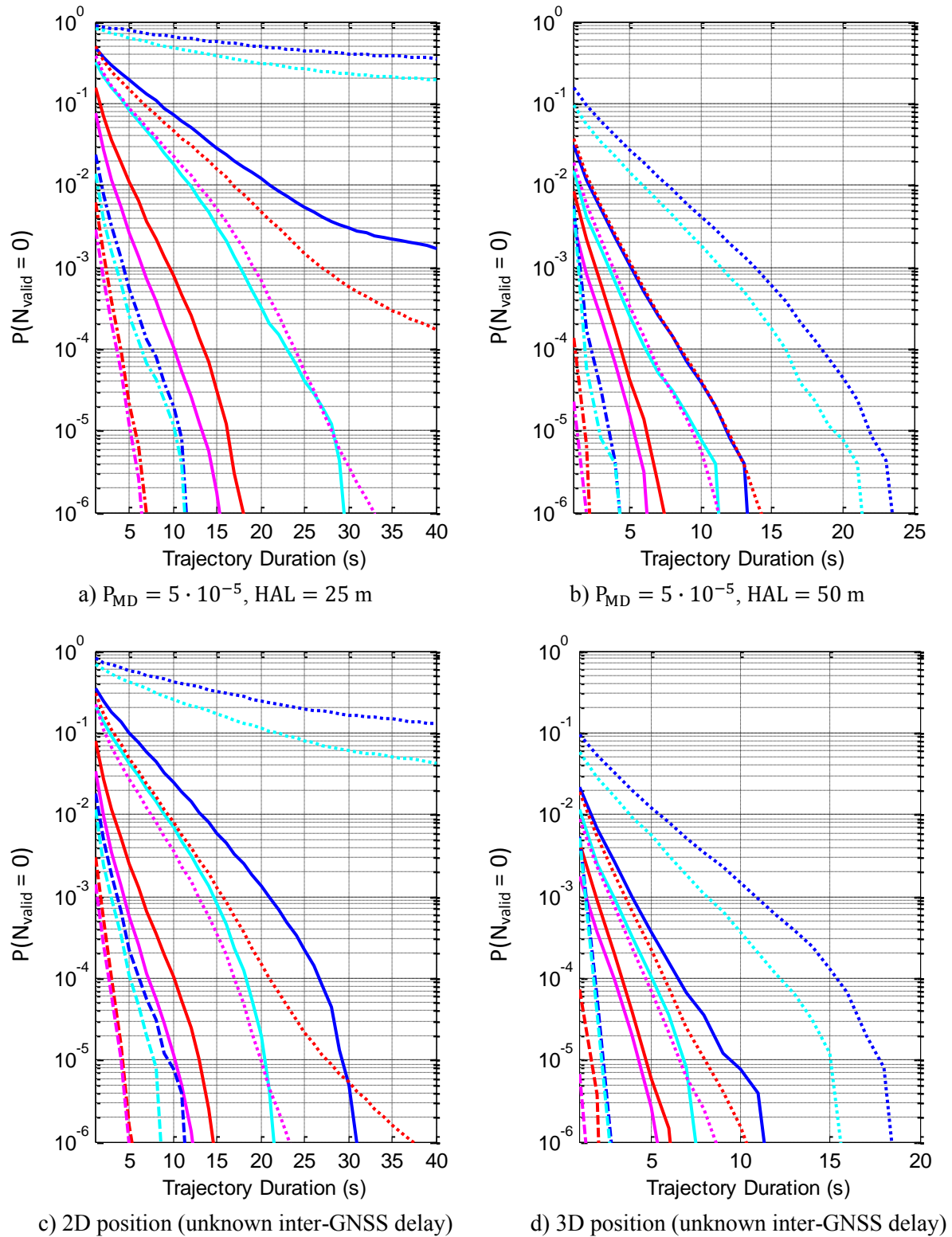


Figure 7.15. Probability of zero valid positions during a user's trajectory trough a geo-object in the fault-free case. Environment: urban. Receiver: dual constellation L1/E1 BOC(1,1); dual frequency with L5/E5a BPSK(10); hybridization with external altitude $\sigma_{\text{alt}} = 5$ m. Navigation solution: 3D position and receiver/GNSS time shift.



— constant- P_{FA} WLSR RAIM ($P_{FA} = 5 \cdot 10^{-3}$)	⋯ Dotted line: L1/E1
— constant- P_{FA} WLSR RAIM + external altitude $\sigma_{alt} = 5$ m.	- - - Dashed line: L1/E1 + SBAS corrections
— variable- P_{FA} WLSR RAIM	— Solid line: iono-free L1/E1 - L5/E5a
— variable- P_{FA} WLSR RAIM + external altitude $\sigma_{alt} = 5$ m.	

Figure 7.16. Probability of zero valid positions during a user's trajectory trough a geo-object in the fault-free case. Environment: rural. Receiver: dual constellation L1/E1 BOC(1,1); dual frequency with L5/E5a BPSK(10). Navigation solution: 3D position and receiver/GNSS time shift.

7.6.3. Alternative receivers

Appendix F contains, for all the studied combinations of GNSS receivers, RAIM algorithms and HAL, the average minimum user trajectory duration (T_{\min}) from which the required probability of missed road segment recognition is met in the fault-free case.

As expected, the performance with 2D positioning are better than with 3D solutions, and TMBOC or CBOC signals provide better results than BOC. In general, the variable- P_{FA} RAIM outperforms the classic one.

Single constellation users only attain the required undercharging level in the rural environment in certain cases.

7.6.4. A note on the performance in the faulty case

Let us consider the faulty scenario described in section 5.4.4.2.2, in which a user circulates through a road segment and all positions that may be used by the segment recognition algorithm have been estimated with a biased pseudorange due to a major service failure. In this case, the undercharging requirement $P_{MGoR} = 10^{-4}$ is met when the probability of an insufficient number of valid positions inside the geo-object after the fault exclusion process is $p\{N_{\text{valid pos IN}}(\text{with FDE}) = 0\} \leq 0.38$ - eq.(5.49)-.

A first approximation of the toll system performance in the faulty case has been obtained as the probability of missed geo-object recognition in the fault-free case with the worst-case subgroup created in the fault exclusion algorithm; it has been proved that, whenever the undercharging requirement is met in the fault-free case, it is also met in the faulty one.

7.7. Conclusions

Simulations have been run in order to obtain the probability of missed geo-object recognition in urban and rural environments. Different satellite visibility and positioning error statistics have been shown, proving the performance decrement in the urban environment with respect to the rural one.

The evolution of the maximum slope, the HPL of the standard WLSR RAIM and the P_{FA} of the novel RAIM has been analyzed to study the performance of the different integrity monitoring techniques. In the studied case, for the same RAIM configuration and geometry, SBAS users provide the best performance, followed by dual-frequency ones. In addition, the different navigation solutions also play an important role in the RAIM performance, resulting the following order of decreasing performance: 1) 2D position and receiver/GNSS delay, 2) 2D position, receiver/GPS delay and inter-GNSS delay, 3) 3D position and receiver/GNSS delay, 4) 3D position, receiver/GPS delay and inter-GNSS delay.

Hybridized GNSS 3D-positioning receivers with external altitude information increase the RAIM availability according to the altitude nominal noise σ_{alt} , being able to reach a performance level up to that of users that only need 2D positioning.

WLSR RAIM algorithms designed with a fixed P_{MD} always meet the false segment recognition rate they have been conceived to attain, so the analysis of the toll system performance focuses in the missed geo-object recognition rate.

The geo-object recognition algorithm gives best results with a threshold $N_{Th} = 1$, that is, only one valid position inside the geo-object is necessary to charge the road segment. The reason is that the

increased P_{MD} allowed by a higher N_{Th} does not compensate, in terms of the final probability of missed geo-object recognition, the increment in the required of number of valid positions per segment.

The final RAIM configuration, dependent on N_{Th} , is $P_{MD} = 5 \cdot 10^{-5}$ when there are multiple independent positions per geo-object, and $P_{MD} = 10^{-3}$ when only one independent position per geo-object is assumed. For the civil aviation RAIM, $P_{FA} = 5 \cdot 10^{-3}$. The value $P_{FA} = 5 \cdot 10^{-5}$ has also been studied and discarded because it always provided worse results.

The probability of missed geo-object recognition decreases as the user trajectory duration increases, so the toll performance is shown as the minimum user trajectory duration that meets the required probability of missed road segment recognition. Two values of HAL are studied, 25 and 50 meters. All combinations of GNSS receivers and RAIM algorithms previously identified as potentially suitable for road toll applications have been studied. For example, baseline receivers (dual constellation, BOC(1,1) signals, 3D positioning) with the civil aviation WLSR RAIM are capable to meet the undercharging requirement within a maximum trajectory duration of 40 seconds only augmented with SBAS corrections and if HAL is 50 meters; the RAIM with variable P_{FA} reduces the necessary trajectory duration and includes new cases that meet the undercharging requirement, like HAL of 25 meters with a hybrid SBAS receiver. Single constellation users do not attain the required undercharging level in urban environments, and in rural ones only in certain cases.

Chapter 8

Conclusions and Future Work

8.1. Conclusions

The aim of the present work is to study GNSS integrity monitoring techniques applied to GNSS-based electronic toll collection systems in rural and urban environments. Satellite navigation provides flexible, free-flow toll systems with a reduced quantity of roadside infrastructure, and it is one of the recommended technologies for the European Electronic Toll Service [EU, 2004]. Electronic toll is a liability critical application that needs GNSS integrity monitoring in order to control erroneous invoicing, often described in terms of undercharging and overcharging.

GNSS integrity has been originally developed in the civil aviation framework; currently GPS integrity monitoring relies on different augmentation systems (GBAS, SBAS, ABAS) that have been conceived to meet the ICAO requirements. For this reason, the GNSS integrity requirements for civil aviation applications have been first presented in order to understand the design objectives and constraints of the different integrity monitoring systems.

Current GNSS-based e-toll systems have been presented and geo-fencing has been identified as the most suitable technique for developing a GNSS-based ETC over a given area or road network, so the tolled region is divided in geo-objects which are the basic pricing sections. Thus, the application's objective is the geo-object recognition process, that is, to detect whether a user has been or not in a pricing section. The relationship between the road topology and the HAL has been obtained. The use of the different augmentation systems inherited from civil aviation to urban toll applications has been analyzed; autonomous integrity monitoring algorithms (RAIM) have been selected because they do not require additional equipment, are easily extended to the multi-constellation case at any frequency band, can be tuned to a given performance level, and are able to deal with all pseudorange errors. SBAS is optionally used to correct pseudorange measurement errors. A modernized SBAS capable to augment future GPS and Galileo signals is assumed.

Snapshot positioning and integrity monitoring techniques are used in order to avoid feedback loops and have full control of the integrity at each instant. Integration of external altitude information is considered. The most suitable GNSS receiver configurations have been identified, with special interest in dual constellation GPS & Galileo users.

A geo-object recognition algorithm based on the number of independent positions inside the geo-object has been proposed. In this context, two positions are defined to be independent when they provide independent outputs of the integrity monitoring algorithm.

A nominal pseudorange measurement model suitable for integrity-driven applications in urban environments has been presented. The pseudorange nominal error model is a zero-mean Gaussian function, which assures consistency with the assumptions of integrity monitoring systems used in civil

aviation. The nominal model has been obtained dividing the total pseudorange error into five independent error sources which can be modelled independently: broadcasted satellite clock corrections and ephemeris errors, ionospheric delay, tropospheric delay, receiver thermal noise (plus interferences) and multipath. Some of these errors have been characterized with existing and tested models, others like the multipath one have been specifically modelled for the targeted application.

The fault model considers only pseudorange failures due to major service failures. This choice allows to know its probability of occurrence but requires GNSS receivers to have robust protection mechanisms against other failures.

The top level requirements of toll applications have been defined in terms of probability of missed and false geo-object recognition. The GNSS integrity requirements needed to design the RAIM algorithms have been derived afterwards from the top level requirements, assuming a RAIM with fault detection capabilities and a major service failure as the faulty case. A failure tree for toll systems has been also proposed. The resulting RAIM's P_{MD} is a function of the probability of false geo-object recognition, the road segment recognition threshold (N_{Th}), and the number of geo-object misleading positions, which in this work are set to a worst case value of 72 (that corresponds to the case of a 5-km length geo-object, a user speed of 50 km/h and T_c of 5 s.). The resulting RAIM's P_{FA} is a function of the probability of missed geo-object recognition, N_{Th} , and the number of positions with available RAIM.

Two RAIM algorithms have been selected as candidates to be employed in urban road toll applications. First, the Weighted Least Squares Residual (WLSR) RAIM, widely used in civil aviation and usually set as the reference against which compare other RAIM techniques, has been presented. One of the main challenges of RAIM in urban environments is the bad user/geometry geometry, which usually results in a high RAIM unavailability rate. With the aim to cope with this problem, a novel RAIM has been designed with the objective of providing a trade-off between false alarm and RAIM availability, in order to get the highest rate of valid positions within the integrity requirements.

The novel RAIM employs the same WLSR test statistic used in civil aviation. While the classic WLSR RAIM is designed to provide fixed P_{FA} and P_{MD} and the lowest possible HPL at each instant, the novel algorithm is set to obtain constant HPL and P_{MD} , and the lowest possible P_{FA} at each instant. Thus, setting the HPL equal to the HAL, the new algorithm is always available (provided at least 5 satellites are visible) and valid positions are discarded only because of false detections, which increases the probability that a position is declared valid by the RAIM. Since the P_{MD} is fixed, the maximum allowed probability of missed detection is always met.

Electronic toll systems using any of both considered WLSR RAIM algorithms meet the probability of false geo-object recognition (overcharging constraint) assured by the P_{MD} in the worst case, independently from the environment. On the other hand, the undercharging rate depends on the number of valid positions in the geo-object, which not only depends on the GNSS receiver and RAIM configuration, but also on the user/satellite geometry. For this reason, simulations in MATLAB have been run analyze the viability of toll systems using different on-board units in urban and rural environments.

Satellite visibility and positioning error statistics have been shown, proving the performance decrement in the urban environment with respect to the rural one.

The evolution of the HPL of the standard WLSR RAIM and the P_{FA} of the novel RAIM have been analyzed to study the performance of the different integrity monitoring techniques. In the studied case, for the same RAIM configuration and geometry, SBAS users provide the best performance, followed by dual-frequency ones. In addition, the different navigation solutions also play an important role in the RAIM performance, resulting the following order of decreasing performance: 1) 2D position and

receiver/GNSS delay, 2) 2D position, receiver/GPS delay and inter-GNSS delay, 3) 3D position and receiver/GNSS delay, 4) 3D position, receiver/GPS delay and inter-GNSS delay.

Hybridized GNSS 3D-positioning receivers with external altitude information increase the RAIM availability according to the altitude nominal noise σ_{alt} , being able to reach a performance level up to that of users that only need 2D positioning.

WLSR RAIM algorithms designed with a fixed P_{MD} always meet the false segment recognition rate they have been conceived to attain, so the analysis of the toll system performance focuses in the missed geo-object recognition rate.

The geo-object recognition algorithm gives best results with a threshold $N_{Th} = 1$, that is, only one valid position inside the geo-object is necessary to charge the road segment. The reason is that the increased P_{MD} allowed by a higher N_{Th} does not compensate, in terms of the final probability of missed geo-object recognition, the increment in the required number of valid positions per segment.

The final selected RAIM configuration, that meets the overcharging requirement for $N_{Th} = 1$, is $P_{MD} = 5 \cdot 10^{-5}$ in the case of multiple independent positions per geo-object, and $P_{MD} = 10^{-3}$ in the case of only one independent position per geo-object is assumed. For the classic WLSR RAIM, $P_{FA} = 5 \cdot 10^{-3}$. The value $P_{FA} = 5 \cdot 10^{-5}$ has also been studied and discarded because it always provided worse results.

The probability of missed geo-object recognition decreases as the user trajectory duration increases, so the toll performance has been shown as the minimum user trajectory duration that meets the required probability of missed road segment recognition. Two values of HAL are studied, 25 and 50 meters. All combinations of GNSS receivers and RAIM algorithms previously identified as potentially suitable for road toll applications have been studied. The novel WLSR RAIM with variable P_{FA} outperforms the original one in terms of missed geo-object recognition in all studied scenarios.

The feasibility of electronic toll systems by means of GNSS with integrity in urban and rural environments has been proven for certain GNSS receivers and RAIM algorithms. In particular, dual constellation receivers are needed for a satisfactory performance in urban environments. Single constellation users only attain the desired undercharging level in rural environments in certain cases. For example, baseline receivers (dual constellation, BOC(1,1) signals, 3D positioning) using the civil aviation WLSR RAIM are capable to meet the undercharging requirement within a maximum trajectory duration of 40 seconds only augmented with SBAS corrections and if the HAL is 50 meters, while the RAIM with variable P_{FA} reduces the necessary trajectory duration and includes new cases that meet the undercharging requirement, like HAL of 25 meters with a hybrid SBAS receiver.

8.2. Original contributions

The main contributions presented in this thesis are the following:

- Detailed analysis of GNSS-based road toll collection applications with geo-fencing: relationship between the HAL and the road topology for geo-object recognition with integrity (section 3.4)
- Pseudorange nominal error model due to ionospheric delay in Galileo single-frequency receivers, based on a VTEC database and suitable for applications with GNSS integrity (section 2)
- Pseudorange nominal error model due to multipath in urban environments, suitable for applications with GNSS integrity (section 2)
- Failure tree that leads to geo-object misleading positions (5.4.2)

- Derivation of the P_{MD} and P_{FA} of fault detection RAIM algorithms for GNSS-based electronic toll systems from the required probabilities of missed and false geo-object recognition, in the case of a threat model consisting on major service failures (section 5.4.4)
- Design of a novel WLSR RAIM with variable probability of false alarm and constant HPL that maximizes the number of valid positions within the integrity requirements in the fault-free case (section 6.3). It consists in an algorithm with a constant probability of missed detection, without restriction in the maximum allowable P_{FA} .

8.3. Perspectives for future work

The joint use of GPS & Galileo has been proved to considerably improve the RAIM performance with respect to the single constellation case. It would be interesting to extend the analysis to a multi-constellation case that includes more systems, such as Glonass or Compass. This task is not problematic from a RAIM point of view, since it can easily integrate signals from different systems and frequency bands, requiring mainly the pseudorange nominal measurement model of each signal.

The threat model addressed in this work consists in pseudorange failures caused by major service failures, which requires the user to be equipped with mechanisms that protect against other failures like NLOS multipath. A more complete threat model could be considered, including other pseudorange failure types. This work would need the identification of the possible failure sources and a reliable characterization of each of them, including their probability of occurrence and their duration. The GNSS integrity requirements should be recalculated to take into account the new pseudorange failure types.

One of the main limitations of the studied WLSR RAIM algorithms is the assumption that the occurrence of multiple simultaneous failures is negligible, that is, the probability of positioning failure missed detections is assured to be within the required P_{MD} only if they are caused by a single pseudorange bias. This is a common assumption in civil aviation RAIM, which is valid for single constellation users and a threat model composed only of major service failures. However, simultaneous failures may occur with a non-negligible probability if multi-constellation GNSS receivers and additional failure sources such as NLOS multipath in urban environments are considered. The use of RAIM able to deal with simultaneous pseudorange failures should be addressed in this case.

Another limitation of the WLSR RAIM is the assumption that the probability of positioning failures in the fault-free case is negligible. Nevertheless, nominal positioning errors can exceed the HAL with a probability that depends on the HAL, the pseudorange nominal errors and the user/satellite geometry, which has been shown to be specially degraded in urban environments. A study could be carried out to characterize the missed detections in nominal conditions.

The present work has focused on GNSS positioning and RAIM monitoring based on the least squares estimator, where the integration of external altitude information has resulted to significantly improve the RAIM performance. Hybridization of GNSS and external sensors like IMU with a Kalman filter are commonly used to improve navigation accuracy and availability in urban environments, and moreover, integrity monitoring with Kalman filters has been investigated. Therefore, the use of GNSS receivers based on Kalman filter could be studied for electronic toll systems, paying special attention to the effect of the feedback loops in the temporal evolution of the integrity monitoring algorithm.

Although WLSR RAIM has been selected for this first study, it would be interesting to compare its performance in urban environments against other RAIM algorithms. The design of a variable P_{FA} and a fixed HPL can be extended to other existing RAIM.

The pseudorange nominal error model used to compute the RAIM and the toll system performance represents the worst case. An analysis with the actual ionospheric residual errors or the actual C/N_0 would improve the obtained results, specially of non-SBAS users.

The funding entities of the thesis preferred an overall theoretical analysis of the toll collection problem, leaving the measurement of real data and its comparison with simulation results as future work. Since the RAIM performance has been shown to strongly depend on the environment, more different scenarios could be tested.

Thus, further studies should be conducted to conclude on the use of GNSS integrity monitoring techniques in urban environments for different applications.

References

- [AFIFT, 2011] Agence de financement des infrastructures de transport de France (AFITF), "Communiqué de presse", 8 septembre 2011 (in French)
- [Arbesser, 2006] B. Arbesser-Rastburg, "The GALILEO single frequency ionospheric correction algorithm", 3rd European Space Weather Week, Brussels, 2006.
- [ARINC, 2005] ARINC Engineering Services, LLC, "GPS Space Segment/Navigation User L5C Interfaces"; Interface Specification IS-GPS-705, 2005
- [ARINC, 2006] ARINC Engineering Services, LLC, "GPS Space Segment/Navigation User Interfaces"; Interface Specification, IS-GPS-200, Revision D, 7 March 2006
- [ARS, 2006] ARS Traffic & Transport Technology bv, "Accuracy and reliability of distance and position measurements by GNSS systems", September 2006
- [Betz and Kolodziejewski, 2000] Betz J., Kolodziejewski K., "Extended Theory of Early-Late Code Tracking for a Band limited GPS Receiver", Journal of the Institute of Navigation, Vol.47, No.3, Fall 2003
- [Brown, 1992] R. G. Grover Brown, 'A Baseline GPS RAIM Scheme and a Note on the Equivalence of Three RAIM Methods'. Navigation: Journal of the Institute of Navigation, Vol. 39, No. 3, Fall 1992.
- [Brown and Chin, 1997] R. G. Grover Brown, G. Y. Chin, 'GPS RAIM: Calculation of threshold and protection radius using chi-square methods – a geometric approach'. GPS Papers published in NAVIGATION (Red Book Series), Institute of Navigation, vol. V, pp. 155–178, 1998.
- [Collins, 1999] Collins, J. P., "Assessment and Development of a Tropospheric Delay Model for Aircraft Users of the Global Positioning System"; M.Sc.E. thesis, Department of Geodesy and Geomatics Engineering Technical Report No. 203, University of New Brunswick
- [Collins and Langley, 1999] Collins, J. P., and R. B. Langley, "Nominal and Extreme Error Performance of the UNB3 Tropospheric Delay Model"; Final contract report for Nav Canada Satellite Navigation Program Office, Department of Geodesy and Geomatics Engineering Technical Report No. 204, University of New Brunswick.
- [Dautermann et al., 2011] T. Dautermann, M. Felux, A. Grosch, "Approach service type D evaluation of the DLR GBAS testbed", GPS Solutions vol. 16, no. 3, pp. 375-387, 2011
- [De Cleene, 2000] B. De Cleene, "Defining Pseudorange Integrity - Overbounding", ION GPS 2000, 19-22 September 2000
- [De Cleene, 2007] B. De Cleene, "Proposed Revision to GNSS Performance Requirements for Precision Approach", Navigation Systems Panel (NSP) Working Groups 1 and 2 Meeting, March 5-17 2007

- [DoD, 2001] Department of Defense USA, "Global Positioning Service Standard Positioning Service Performance Standard", Oct. 2001.
- [DoD, 2008] Department of Defense USA, "Global Positioning Service Standard Positioning Service Performance Standard", 4th Edition, Sept. 2008.
- [EG9, 2006] Expert Group 9, "Report of Expert Group 9 Working to support the European Commission on the work on Directive 2004/52/EC: Specification of the EFC application based on satellite technologies", version 3.2, 20 February 2006
- [EU, 2004] European Parliament, "Directive 2004/52/EC of the European Parliament and of the Council of 29 April 2004 on the interoperability of electronic road toll systems in the Community", Official Journal of the European Union, 29 April 2004.
- [EU, 2010] European Union, "European GNSS (Galileo) Open Service. Signal In Space Interface Control Document", OD SIS ICD, Issue 1, February 2010
- [EU-UE CSN, 2010] EU-US Cooperation on Satellite Navigation, Working Group C, "Combined Performance for SBAS Receivers Using WAAS and EGNOS", Final version, July 19, 2010
- [Eurocontrol, 2011] Eurocontrol, "Press Release - EGNOS operational for aviation", 3 March 2011
- [FDF, 2011] Swiss Federal Department of Finance (FDF), Swiss Federal Customs Administration (FCA), "Performance-Related Heavy Vehicle Fee HVF - Overview. 2011 Edition", January 2011.
- [Feng et al, 2006] S. Feng, W.Y. Ochieng, D. Walsh, R. Ioannides, "A measurement domain receiver autonomous integrity monitoring algorithm", *GPS Solutions*, 2006, vol.10, no.2, pp.85-96.
- [Fouque et al., 2008] C. Fouque, Ph. Bonnifait, "Tightly-coupled GIS data in GNSS fix computations with integrity testing", *International Journal of Intelligent Information and Database Systems* 2, pp. 167-186, 2008.
- [Gutierrez-Lanza et al., 2011] L. Gutierrez-Lanza, K. Diamandouros, "Meet GINA. Road user pricing using GNSS and EGNOS", *Inside GNSS*, March/April 2011, pp.26-38.
- [Have, 2003] Have D., "Reference set of parameters for RAIM availability simulations" Working paper Sofréavia, 8-9 April, Madrid Spain, 2003.
- [Hernández-Pajares et al., 2008] Hernández-Pajares, M. Hernández-Pajares, J. M. Juan, J. Sanz, R. Orus, A. Garcia-Rigo, J. Feltens, A. Komjathy, S. C. Schaer, A. Krankowski, "The IGS VTEC maps: a reliable source of ionospheric information since 1998", *Journal of Geodesy*, 2009, Volume 83, pp. 263-275
- [ICAO, 2001] International Civil Aviation Organization, "International Standards and Recommended Practices, Annex 6 to Convention on International Civil aviation, Operation of aircraft", 8th Edition, July 2001.
- [ICAO, 2002] International Civil Aviation Organization, "Global Air Navigation Plan for CNS/ATM Systems", 2nd Edition, Doc 9750 AN/963, 2002

- [ICAO, 2006] International Civil Aviation Organization, "International Standards and Recommended Practices - Annex 10 to the Convention on International Civil Aviation - Aeronautical Telecommunications - Volume I, Radio Navigation Aids", 6th Edition (with amendment 85), July 2006.
- [Jabbour et al., 2008] M. Jabbour, P. Bonnifait, V. Cherfaoui, "Map-Matching Integrity using Multi-Sensor Fusion and Multi-Hypothesis Road Tracking", *Journal of Intelligent Transportation Systems, Technology, Planning and Operations*, vol. 12, no. 4 pp. 189-201, 2008
- [Julien, 2005] O. Julien, "Design of Galileo L1F tracking loops", PhD thesis, University of Calgary, Department of Geomatics Engineering, 2005
- [Julien et al., 2007] O. Julien, C. Macabiau, J.L. Issler, L. Ries, "Two for One. Tracking Galileo CBOC Signal with TMBOC", *Inside GNSS*, Spring 2007
- [Klobuchar, 1987] Klobuchar J.A., "Ionospheric Time-Dealy Algorithm for Single-Frequency GPS Users"; *IEEE Transactions on Aerospace and Electronic Systems*, vol AES-23, no.3, 1987
- [Kovach, 2008] K. Kovach, J. Dobyne, M. Crews, C. Miles, "GPS III Integrity Concept"; *ION GNSS 2008*
- [Lee and McLaughlin, 2007] Lee Y.C., McLaughlin M.C., "Feasibility Analysis of RAIM to Provide LPV-200 Approaches with Future GPS"; *ION GNSS 2007*
- [Lee, 1986] Y.C. Lee, "Analysis of range and position comparison methods as a means to provide GPS integrity in the user receiver"; *Proceedings of the Annual Meeting of The Institute of Navigation*, June, 1986
- [Lehner and Steingass, 2005] Alexander Steingass, Andreas Lehner, "A Novel Channel Model for Land Mobile Satellite Navigation"; *ION GNSS 18th International Technical Meeting of the Satellite Division*, 13-16 Sept. 2005, Long Beach, California
- [Mainul-Hoque et al., 2007] Mainul Hoque, M. and N. Jakowski, "Higher order ionospheric effects in precise GNSS positioning"; *Journal of Geodesy* Vol. 81, pp 259-268.
- [Martineau, 2008] A. Martineau, "Performance of Receiver Autonomous Integrity Monitoring (RAIM) for Vertically Guided Approaches", PhD thesis Institut National Polytechnique de Toulouse, 2008
- [MEEDAT, 2009] Ministry of Ecology, Energy, Sustainable development and Regional development of France (MEEDAT), "Partnership contract concerning the national HGV eco-tax and the Alsace experimental tax. Project presentation note", 31 March 2009 (English version 2 Nov. 2009)
- [NDSAS, 2010] Motorways and Express roads in Slovakia (NDSAS), "Multi-lane Free-flow Electronic Tolling in the Slovak Republic", February 2010
- [Ober, 1997] P.B. Ober, "Ways to Improve RAIM/AAIM Availability Using Position Domain Performance Computations," *Proceedings of the 1997 National Technical Meeting of The Institute of Navigation*, Santa Monica, CA, January 1997, pp. 485-497.

- [Oehler et al, 2004] V. Oehler, F. Luongo, J.P. Boyero, R. Stanford, H.L. Trautenberg, J. Krueger, J. Hahn, F. Amarillo, M. Crisci, B. Schlarmann, J.F. Flamand "The Galileo Integrity Concept"; ION GNSS 2004
- [Parkinson et al., 1996] Parkinson B.W., Spilker J.J., Axelrad P., Enge P., "Global Positioning System: Theory and Applications. Volume I", Progress in Astronautics and Aeronautics Volume 163, American Institute of Aeronautics and Astronautics (AIAA) Inc., 1996.
- [Parkinson et. al, 1988] B.W. Parkinson, P. Axelrad, "Autonomous GPS Integrity Monitoring using the Pseudorange Residual", *NAVIGATION*, Vol. 35, No. 2, Summer 1988, pp. 255-274.
- [Pérez-Fontán et al., 2001] F.Perez-Fontan, M. Vazquez-Castro, C.E. Cabado, J.P. Garcia, E. Kubista, "Statistical modeling of the LMS channel," *Vehicular Technology, IEEE Transactions on* , vol.50, no.6, pp.1549-1567, Nov 2001.
- [Quddus et al., 2006] M.A. Quddus, W.Y. Ochieng, R.B. Noland, "Integrity of map-matching algorithms", *Transportation Research Part C*, vol. 14, no. 4, pp. 283–302, 2006.
- [Quddus et al., 2007] M.A. Quddus, W.Y. Ochieng, R.B. Noland, "Current map-matching algorithms for transport applications: State-of-the art and future research directions", *Transportation research Part C*, vol. 15, no. 5, pp. 312-328, 2007.
- [RacalTracs, 2000] Racal Tracs Ltd., "Galileo Overall Architecture Definition (GALA). Definition and Sizing For The Safety of Life Market", 6 October 2000
- [Rogers et al., 2005] Rogers N.C., Field J.E.N., Griffin C., Cannon P.S., Angling M.J., Hollreiser M., "An assessment of the Galileo single frequency correction model"; Second European Space Weather Week, ESA-ESTEC, Noordwijk, The Netherlands, 14 - 18 November 2005
- [Roturier, 2001] Roturier B., Chatre E., and Ventura-Traveset J., " The SBAS Integrity Concept Standardised by ICAO. Application to EGNOS ", GNSS 2001, May 2001
- [RTCA, 2003] RTCA Inc., "Minimum Aviation System Performance Standards: Required Navigation Performance for Area Navigation", RTCA DO-236B, 2003
- [RTCA, 2006] RTCA Inc., "Minimum Operational Performance Standards for Global Positioning System/Wide Area Augmentation System Airborne Equipment", RTCA DO-229D, Dec. 13, 2006
- [RTCA, 2008] "Minimum Operational Performance standards for GPS Local Area Augmentation System Airborne Equipment", DO-253C, RTCA SC-159, Dec 2008
- [SAIC, 2008] Science Applications International Corporation, "GPS Space Segment/Navigation User L1C Interfaces"; Interface Specification IS-GPS-200, 4 Sept. 2008.
- [SkyToll, 2010] SkyToll, "Press Note", 7 Dec. 2010
- [SkyToll, 2011 (a)] SkyToll, "Press Note", 15 April 2011
- [SkyToll, 2011 (b)] SkyToll, "Press Note", 14 July 2011

- [Steingass and Lehner, 2004] Alexander Steingass, Andreas Lehner, "Measuring the Navigation Multipath Channel – A Statistical Analysis", ION GNSS 17th International Technical Meeting of the Satellite Division, 21-24 September 2004, Long Beach, California
- [Sturza, 1988] M.A. Sturza, "Navigation System Integrity Monitoring Using Redundant Measurements"; NAVIGATION: Journal of The Institute of Navigation, Vol. 35, No. 4, Winter 1988-89.
- [Sturza and Brown, 1990] M.A. Sturza, A.K. Brown, "Comparison of Fixed and Variable Threshold RAIM Algorithms," *Proceedings of the 3rd International Technical Meeting of the Satellite Division of The Institute of Navigation (ION GPS 1990)*, Colorado Spring, CO, September 1990, pp. 437-443.
- [Tierolf, 2010] J.W. Tierolf, "Large-scale implementation of satellite-based systems. Nation-wide kilometre pricing in the Netherlands", Galileo application days, 5 March 2010
- [TollCollect, 2008] Toll Collect, "Mobility for Tomorrow. Opportunities for transport, business and the environment", Oct. 2008
- [TollCollect, 2011 (a)] Toll Collect, "Press Statement", 25 Feb. 2011
- [TollCollect, 2011 (b)] Toll Collect, ASFINAG, "Press Statement", 23 Aug. 2011.
- [van Graas, 1993] F. van Graas, J. L. Farrell, "Baseline Fault Detection and Exclusion Algorithm," *Proceedings of the 49th Annual Meeting of The Institute of Navigation*, Cambridge, MA, June 1993, pp. 413-420.
- [Velaga et al., 2012] N.R. Velaga, M.A. Quddus, A.L. Bristow, Yuheng Zheng, "Map-Aided Integrity Monitoring of a Land Vehicle Navigation System," *Intelligent Transportation Systems, IEEE Transactions on*, vol.13, no.2, pp.848-858, June 2012.
- [Walter and Enge, 1995] T. Walter and P. Enge, "Weighted RAIM for precision approach", *Proceedings ION Global Positioning System (GPS'95)*, Jan. 1995

Acronyms

AAIM	Aircraft Autonomous Integrity Monitoring
ABAS	Aircraft Based Augmentation System
AGPS	Assisted GPS
APV	Approach with Vertical Guidance
ARNS	Aeronautical Radio Navigation System
BOC	Binary Offset Carrier
CBOC	Composite Binary Offset Carrier
CNES	<i>Centre National d'Etudes Spaciales</i>
CNS/ATM	Communications, Navigation, and Surveillance / Air Traffic Management
DLL	Delay Lock Loop
DSRC	Dedicated Short Range Communications
EETS	European Electronic Toll Service
EFC	Electronic Fee Collection
EGNOS	European Geostationary Navigation Overlay Service
ENAC	<i>Ecole Nationale de l'Aviation Civile</i>
ETC	Electronic Toll Collection
FD	Fault Detection
FDE	Fault Detection and Exclusion
FLL	Frequency Lock Loop
GBAS	Ground Based Augmentation System
GIVE	Grid Ionosphere Vertical Error
GNSS	Global Navigation Satellite System
GPRS	General Packet Radio Service
GPS	Global Positioning System
GSM	Global System for Mobile Communications (<i>Groupe Spécial Mobile</i>)
HAL	Horizontal Alert Level
HPL	Horizontal Protection Level
HVF	Performance-Related Heavy Vehicle Fee
ICAO	International Civil Aviation Organisation
ILS	Instrument Landing System
IMU	Inertial Measurement Unit

INS	Inertial Navigation System
LAAS	Local Area Augmentation System
LNAV	Lateral Navigation
LOS	Line Of Sight
LP	Localizer Performance
LPV	Localizer Performance with Vertical guidance
LS	Least Squares
LSR	Least Squares Residuals
LSVA	<i>Leistungsabhängige Schwerverkehrsabgabe</i> (German acronym of HVF)
MBOC	Multiplex Binary Offset Carrier
MSAS	Multi-functional Satellite Augmentation System
NLOS	Non-Line-Of-Sight
NPA	Non-Precision Approach
NTE	Not To Exceed (tolerance)
OBU	On-board Unit
OS	Open Service
PLL	Phase Lock Loop
PPS	Precise Positioning Service
PRN	Pseudo-Random Noise
RAIM	Receiver Autonomous Integrity Monitoring
RAMS	Reliability, Availability, Maintainability, and Safety
RTCA	Radio Technical Commission for Aeronautics
RUC	Road User Charging
SBAS	Satellite Based Augmentation System
SIS	Signal In Space
SISA	Signal In Space Accuracy
SISE	Signal In Space Error
SISNeT	Signal in Space through the Internet
SoL	Safety of Life
SPS	Standard Positioning Service
STEC	Slant Total Electron Content
SV	Space Vehicle
TEC	Total Electron Content
TMBOC	Time Multiplexed Binary Offset Carrier

TTA	Time To Alert
UDRE	User Differential Range Error
UNB3	University of New Brunswick (Tropospheric delay correction algorithm)
URA	User Range Accuracy
URE	User Range Error
VAL	Vertical Alert Level
VNAV	Vertical Navigation
VPL	Vertical Protection Level
VHF	Very High Frequency
VPL	Vertical Protection Level
VTEC	Vertical Total Electron Content
WAAS	Wide Area Augmentation System
WLS	Weighted Least Squares
WSS	Wide Sense Stationary

Appendix A

Derivation of the Linear Pseudorange Measurement Equation

A.1. Linearization

Let us consider a navigation system in which the solution consists of the user 3D position and the bias due to the time shift between the receiver clock and the GNSS reference time. This model corresponds to a single-constellation receiver or a multi-constellation receiver that knows the inter-system time shift. The navigation solution vector has four unknowns:

$$\mathbf{x} = [x_u, y_u, z_u, b_u]^T \quad (\text{A.1})$$

where:

- $[x_u, y_u, z_u]^T$: user's 3D position expressed in WGS-84 coordinates
- b_u : pseudorange bias due to GNSS/receiver time delay

The exact relationship between pseudorange measurements and the navigation solution is non-linear:

$$\mathbf{y} = \mathbf{h}(\mathbf{x}) + \mathbf{E} \quad (\text{A.2})$$

with N range measurements:

- $\mathbf{y} = [y_1, y_2, \dots, y_N]^T$: pseudorange measurement vector
- $\mathbf{x} = [x_u, y_u, z_u, b_u]^T$: user's true navigation solution vector
- $\mathbf{E} = [E_1, E_2, \dots, E_N]^T$: pseudorange measurement error vector
- $\mathbf{h}(\mathbf{x}) = [h_1(\mathbf{x}), h_2(\mathbf{x}), \dots, h_N(\mathbf{x})]^T$: non-linear relationship between \mathbf{x} and \mathbf{y}

$$h_i(\mathbf{x}) = \sqrt{(x_u - x_{\text{sat},i})^2 + (y_u - y_{\text{sat},i})^2 + (z_u - z_{\text{sat},i})^2} + b_u \quad (\text{A.3})$$

where:

- $[x_{\text{sat},i}, y_{\text{sat},i}, z_{\text{sat},i}]^T$: i^{th} satellite's true position in WGS-84 coordinates
- N: number of pseudorange measurements

The Taylor series of \mathbf{y} around an initial estimate $\hat{\mathbf{x}}_0$ is:

$$y = \sum_{n_x=0}^{\infty} \sum_{n_y=0}^{\infty} \sum_{n_z=0}^{\infty} \sum_{n_b=0}^{\infty} \frac{\Delta x_u^{n_x}}{n_x!} \frac{\Delta y_u^{n_y}}{n_y!} \frac{\Delta z_u^{n_z}}{n_z!} \frac{\Delta b_u^{n_b}}{n_b!} \cdot \left(\frac{\partial^{n_x+n_y+n_z+n_b}}{\partial x_u^{n_x} \partial y_u^{n_y} \partial z_u^{n_z} \partial b_u^{n_b}} h(x) \right)_{x=\hat{x}_0} \quad (A.4)$$

where:

$$\Delta x = x - \hat{x}_0 = [\Delta x_u, \Delta y_u, \Delta z_u, \Delta b_u]^T \quad (A.5)$$

The first-order Taylor series about \hat{x}_0 gives a linear approximation of y :

$$y \cong h(\hat{x}_0) + \nabla h(\hat{x}_0) \cdot \Delta x + E \quad (A.6)$$

with:

$$\nabla h(\hat{x}_0) = H = \begin{pmatrix} \frac{\partial h_1}{\partial x_u} & \frac{\partial h_1}{\partial y_u} & \frac{\partial h_1}{\partial z_u} & \frac{\partial h_1}{\partial b_u} \\ \frac{\partial h_2}{\partial x_u} & \frac{\partial h_2}{\partial y_u} & \frac{\partial h_2}{\partial z_u} & \frac{\partial h_2}{\partial b_u} \\ \vdots & \vdots & \vdots & \vdots \\ \frac{\partial h_N}{\partial x_u} & \frac{\partial h_N}{\partial y_u} & \frac{\partial h_N}{\partial z_u} & \frac{\partial h_N}{\partial b_u} \end{pmatrix}_{x=\hat{x}_0} \quad (A.7)$$

Finally, the following linear equation system is obtained :

$$\Delta y = H \cdot \Delta x + \varepsilon \quad (A.8)$$

where:

- $\Delta y = y_i - h(\hat{x}_0)$: pseudorange measurement vector after linearization [Nx1]
- $\Delta x = x - \hat{x}_0$: navigation solution vector after linearization [4x1]
- $H = \nabla h(\hat{x}_0)$: observation matrix [Nx4]
- $\varepsilon = [\varepsilon_1, \varepsilon_2, \dots, \varepsilon_N]^T$: pseudorange measurement error vector [Nx1]

A.2. Positioning in the User Geographic Frame

The observation matrix (A.7) provides the user position in WGS-84 coordinates. If the user position is to be estimated in the North-East-Height coordinates in the user local geographic frame, the navigation solution vector after linearization results:

$$\Delta x = [\Delta x_N, \Delta x_E, \Delta x_h, \Delta x_b]^T \quad (A.9)$$

The observation matrix H has to be adapted to the desired navigation solution:

$$H = \begin{pmatrix} \cos(\theta_1)\cos(\psi_1) & \cos(\theta_1)\sin(\psi_1) & \sin(\theta_1) & 1 \\ \vdots & \vdots & \vdots & \vdots \\ \cos(\theta_N)\cos(\psi_N) & \cos(\theta_N)\sin(\psi_N) & \sin(\theta_N) & 1 \end{pmatrix} \quad (A.10)$$

- θ_i : elevation of i^{th} satellite relative to the user's position

- ψ_i : azimuth of i^{th} satellite relative to the user's position

A.3. Bidimensional positioning

If only 2D positioning in the North-East coordinates in the user local geographic frame is needed, the navigation solution vector and the observation matrix are:

$$\Delta \mathbf{x} = [\Delta x_N, \Delta x_E, \Delta x_b]^T \quad (\text{A.11})$$

$$\mathbf{H} = \begin{pmatrix} \cos(\theta_1)\cos(\psi_1) & \cos(\theta_1)\sin(\psi_1) & 1 \\ \vdots & \vdots & \vdots \\ \cos(\theta_N)\cos(\psi_N) & \cos(\theta_N)\sin(\psi_N) & 1 \end{pmatrix} \quad (\text{A.12})$$

A.4. Dual-constellation receivers

Let us consider a dual-constellation GPS/Galileo receiver in which the inter-system time shift is not known. The navigation solution vector has five variables:

$$\mathbf{x} = [x_u, y_u, z_u, b_{\text{GPS}}, b_{\text{Gal}}]^T \quad (\text{A.13})$$

where:

- $[x_u, y_u, z_u]^T$: user's tridimensional position expressed in the WGS 84 coordinates
- b_{GPS} : bias in GPS pseudorange measurements due to the receiver/GPS time delay
- b_{Gal} : bias in Galileo pseudorange measurements due to the receiver/Galileo time delay

The number of satellites used to estimate the navigation solution vector is $N = N_{\text{GPS}} + N_{\text{Gal}}$, where N_{GPS} and N_{Gal} are the number of GPS and Galileo satellites respectively. A linear equation system similar to eq.(A.8) can be built where the first N_{GPS} lines correspond to GPS measurements and the last N_{Gal} to Galileo ones, with the following observation matrix:

$$\mathbf{H} = \begin{pmatrix} \frac{\partial h_1}{\partial x_u} & \frac{\partial h_1}{\partial y_u} & \frac{\partial h_1}{\partial z_u} & 1 & 0 \\ \vdots & \vdots & \vdots & \vdots & \vdots \\ \frac{\partial h_{N_{\text{GPS}}}}{\partial x_u} & \frac{\partial h_{N_{\text{GPS}}}}{\partial y_u} & \frac{\partial h_{N_{\text{GPS}}}}{\partial z_u} & 1 & 0 \\ \frac{\partial h_{N_{\text{GPS}}+1}}{\partial x_u} & \frac{\partial h_{N_{\text{GPS}}+1}}{\partial y_u} & \frac{\partial h_{N_{\text{GPS}}+1}}{\partial z_u} & 0 & 1 \\ \vdots & \vdots & \vdots & \vdots & \vdots \\ \frac{\partial h_N}{\partial x_u} & \frac{\partial h_N}{\partial y_u} & \frac{\partial h_N}{\partial z_u} & 0 & 1 \end{pmatrix}_{\mathbf{x}=\hat{\mathbf{x}}_0} \quad (\text{A.14})$$

Expressing the position in North-East-Height coordinates at the user's local geographic plane:

$$\Delta \mathbf{x} = [\Delta x_N, \Delta x_E, \Delta x_h, \Delta x_{b,\text{GPS}}, \Delta x_{b,\text{Gal}}]^T \quad (\text{A.15})$$

$$H = \begin{pmatrix} \cos(\theta_1)\cos(\psi_1) & \cos(\theta_1)\sin(\psi_1) & \sin(\theta_1) & 1 & 0 \\ \vdots & \vdots & \vdots & \vdots & \vdots \\ \cos(\theta_{N_{GPS}})\cos(\psi_{N_{GPS}}) & \cos(\theta_{N_{GPS}})\sin(\psi_{N_{GPS}}) & \sin(\theta_{N_{GPS}}) & 1 & 0 \\ \cos(\theta_{N_{GPS}+1})\cos(\psi_{N_{GPS}+1}) & \cos(\theta_{N_{GPS}+1})\sin(\psi_{N_{GPS}+1}) & \sin(\theta_{N_{GPS}+1}) & 0 & 1 \\ \vdots & \vdots & \vdots & \vdots & \vdots \\ \cos(\theta_N)\cos(\psi_N) & \cos(\theta_N)\sin(\psi_N) & \sin(\theta_N) & 0 & 1 \end{pmatrix} \quad (A.16)$$

If only 2D positioning is needed:

$$\Delta X = [\Delta x_N, \Delta x_E, \Delta x_{b,GPS}, \Delta x_{b,Gal}]^T \quad (A.17)$$

$$H = \begin{pmatrix} \cos(\theta_1)\cos(\psi_1) & \cos(\theta_1)\sin(\psi_1) & 1 & 0 \\ \vdots & \vdots & \vdots & \vdots \\ \cos(\theta_{N_{GPS}})\cos(\psi_{N_{GPS}}) & \cos(\theta_{N_{GPS}})\sin(\psi_{N_{GPS}}) & 1 & 0 \\ \cos(\theta_{N_{GPS}+1})\cos(\psi_{N_{GPS}+1}) & \cos(\theta_{N_{GPS}+1})\sin(\psi_{N_{GPS}+1}) & 0 & 1 \\ \vdots & \vdots & \vdots & \vdots \\ \cos(\theta_N)\cos(\psi_N) & \cos(\theta_N)\sin(\psi_N) & 0 & 1 \end{pmatrix} \quad (A.18)$$

A.5. External altitude information

Three-dimensional positioning can be aided by external sensors that provide altitude information, like barometers or digital terrain maps. This external information can be included in the pseudorange linear measurement equation as an additional range measured at an elevation angle $\theta = 90^\circ$:

$$\Delta y = [\Delta y_1, \Delta y_2, \dots, \Delta y_N, \Delta y_{h,ext}]^T \quad (A.19)$$

where:

- Δy_i : is the i^{th} pseudorange measurement after linearization
- $\Delta y_{h,ext}$: is the external altitude information

In the case where only one receiver/GNSS time shift must be estimated:

$$H = \begin{pmatrix} \cos(\theta_1)\cos(\psi_1) & \cos(\theta_1)\sin(\psi_1) & \sin(\theta_1) & 1 \\ \vdots & \vdots & \vdots & \vdots \\ \cos(\theta_N)\cos(\psi_N) & \cos(\theta_N)\sin(\psi_N) & \sin(\theta_N) & 1 \\ 0 & 0 & 1 & 0 \end{pmatrix} \quad (A.20)$$

In the dual constellation case with unknown inter-system time delay:

$$\mathbf{H} = \begin{pmatrix} \cos(\theta_1)\cos(\psi_1) & \cos(\theta_1)\sin(\psi_1) & \sin(\theta_1) & 1 & 0 \\ \vdots & \vdots & \vdots & \vdots & \vdots \\ \cos(\theta_{N_{GPS}})\cos(\psi_{N_{GPS}}) & \cos(\theta_{N_{GPS}})\sin(\psi_{N_{GPS}}) & \sin(\theta_{N_{GPS}}) & 1 & 0 \\ \cos(\theta_{N_{GPS}+1})\cos(\psi_{N_{GPS}+1}) & \cos(\theta_{N_{GPS}+1})\sin(\psi_{N_{GPS}+1}) & \sin(\theta_{N_{GPS}+1}) & 0 & 1 \\ \vdots & \vdots & \vdots & \vdots & \vdots \\ \cos(\theta_N)\cos(\psi_N) & \cos(\theta_N)\sin(\psi_N) & \sin(\theta_N) & 0 & 1 \\ 0 & 0 & 1 & 0 & 0 \end{pmatrix}$$

(A.21)

Appendix B

Overbounding Gaussian of a Uniform Distribution

B.1. CDF Overbounding of a Uniform Distribution

Let us consider a random variable uniformly distributed between $\pm x_{\text{MAX}}$:

$$X \sim U(-x_{\text{MAX}}, x_{\text{MAX}}) \quad (\text{B.1})$$

According to the CDF overbounding technique [DeCleene, 2000], X is overbounded by a zero-mean Gaussian, $X_o \sim N(0, \sigma_o)$, if:

$$\begin{aligned} \text{cdf}_{X_o}(x) &\geq \text{cdf}_X(x) & \forall x \leq 0 \\ \text{cdf}_{X_o}(x) &\leq \text{cdf}_X(x) & \forall x \geq 0 \end{aligned} \quad (\text{B.2})$$

The CDF of the uniform distribution is:

$$\text{cdf}_X(x) = \begin{cases} 0 & \text{for } x < -x_{\text{MAX}} \\ \frac{1}{2} \left(1 + \frac{x}{x_{\text{MAX}}} \right) & \text{for } -x_{\text{MAX}} \leq x \leq x_{\text{MAX}} \\ 1 & \text{for } x > x_{\text{MAX}} \end{cases} \quad (\text{B.3})$$

The CDF of the overbounding Gaussian is:

$$\text{cdf}_{X_o}(x) = \frac{1}{2} \left[1 + \text{erf} \left(\frac{x}{\sqrt{2}\sigma_o} \right) \right], \quad \forall x \quad (\text{B.4})$$

where erf is the error function.

The Gaussian standard deviation that meets the overbounding requirements is obtained introducing equations (B.3) and (B.4) in (B.1):

$$\sigma_o \begin{cases} \leq \frac{x}{\sqrt{2} \operatorname{erf}^{-1}\left(\frac{x}{x_{\text{MAX}}}\right)}, & x \in [-x_{\text{MAX}}, 0] \\ \geq \frac{x}{\sqrt{2} \operatorname{erf}^{-1}\left(\frac{x}{x_{\text{MAX}}}\right)}, & x \in [0, x_{\text{MAX}}] \\ = \text{any value}, & |x| > |x_{\text{MAX}}| \end{cases} \quad (\text{B.5})$$

where erf^{-1} is the inverse error function.

The erf^{-1} is an odd function, so the restrictions on σ_o for $x \in [-x_{\text{MAX}}, 0]$ and $x \in [0, x_{\text{MAX}}]$ are equivalent. Thus:

$$\sigma_o \geq \frac{x}{\sqrt{2} \operatorname{erf}^{-1}\left(\frac{x}{x_{\text{MAX}}}\right)}, \quad x \in [0, x_{\text{MAX}}] \quad (\text{B.6})$$

Requirement (B.6) is a monotonically decreasing function of x . Since σ_o must meet the overbounding requirements for any value of x , it is obtained for $x = 0$:

$$\sigma_o = \lim_{x \rightarrow 0} \frac{x}{\sqrt{2} \operatorname{erf}^{-1}\left(\frac{x}{x_{\text{MAX}}}\right)} \quad (\text{B.7})$$

Substituting erf^{-1} by its Taylor series and truncating it in the first term:

$$\sigma_o = \lim_{x \rightarrow 0} \frac{x}{\sqrt{2} \cdot \frac{\sqrt{\pi}}{2} \left(\frac{x}{x_{\text{MAX}}}\right)} \quad (\text{B.8})$$

Hence:

$$\sigma_o = \sqrt{2/\pi} \cdot x_{\text{MAX}} \quad (\text{B.9})$$

Appendix C

Weighted Least Squares Estimator (WLSE)

C.1. Measurement equation

The present appendix analyzes the WLSE applied to obtain the navigation solution from a linear pseudorange measurement equation system like that of eq.(A.8):

$$\Delta y = H \cdot \Delta x + E \quad (C.1)$$

with pseudorange errors described by:

$$E = \varepsilon + b \quad (C.2)$$

$$\varepsilon \sim N(0, \Sigma) \quad (C.3)$$

$$b = [b_1, b_2, \dots, b_N]^T \quad (C.4)$$

C.2. WLS Navigation Solution Estimation

The WLSE minimizes the squared Mahalanobis distance (squared norm of the estimation residual vector weighted by the corresponding standard deviation):

$$\Delta \hat{x} \text{ that minimizes } (\Delta y - H \cdot \Delta \hat{x}) \Sigma^{-1} (\Delta y - H \cdot \Delta \hat{x}) \quad (C.5)$$

Solving eq.(C.5) the WLS estimation of Δx results:

$$\Delta \hat{x} = A \cdot \Delta y \quad (C.6)$$

$$A = (H^T \Sigma^{-1} H)^{-1} H^T \Sigma^{-1} \quad (C.7)$$

C.3. WLS Estimation Error vector

The estimation error vector is defined as:

$$\mathbf{e} = \Delta \hat{\mathbf{x}} - \Delta \mathbf{x} \quad (\text{C.8})$$

The relation between the estimation error vector (\mathbf{e}) and the pseudorange error vector (\mathbf{E}) is obtained introducing (C.6) in (C.8):

$$\mathbf{e} = \mathbf{A} \cdot \Delta \mathbf{y} - \Delta \mathbf{x} = (\mathbf{H}^T \Sigma^{-1} \mathbf{H})^{-1} \mathbf{H}^T \Sigma^{-1} \cdot (\mathbf{H} \cdot \Delta \mathbf{x} + \mathbf{E}) - \Delta \mathbf{x} = (\mathbf{H}^T \Sigma^{-1} \mathbf{H})^{-1} \mathbf{H}^T \Sigma^{-1} \cdot \mathbf{E}$$

$$\mathbf{e} = \mathbf{A} \cdot \mathbf{E} = \mathbf{A}(\boldsymbol{\varepsilon} + \mathbf{b}) \quad (\text{C.9})$$

Therefore, each estimation error component is a Gaussian random variable (because $\mathbf{E} \sim \mathcal{N}(\mathbf{b}, \Sigma)$).

C.4. Estimation Error Covariance Matrix

By definition, the estimation error covariance matrix is:

$$\text{cov}\{\mathbf{e}\} = \mathbf{E}\{\mathbf{e} \cdot \mathbf{e}^T\} - \mathbf{E}\{\mathbf{e}\}\mathbf{E}\{\mathbf{e}\}^T \quad (\text{C.10})$$

Introducing (C.9) in (C.10):

$$\text{cov}\{\mathbf{e}\} = \mathbf{E}\{(\mathbf{A}\boldsymbol{\varepsilon} + \mathbf{A}\mathbf{b}) \cdot (\mathbf{A}\boldsymbol{\varepsilon} + \mathbf{A}\mathbf{b})^T\} - \mathbf{E}\{\mathbf{A}\boldsymbol{\varepsilon} + \mathbf{A}\mathbf{b}\} \cdot \mathbf{E}\{\mathbf{A}\boldsymbol{\varepsilon} + \mathbf{A}\mathbf{b}\}^T$$

- Operating the first term:

$$\begin{aligned} \mathbf{E}\{(\mathbf{A}\boldsymbol{\varepsilon} + \mathbf{A}\mathbf{b}) \cdot (\mathbf{A}\boldsymbol{\varepsilon} + \mathbf{A}\mathbf{b})^T\} &= \\ &= \mathbf{E}\{\mathbf{A}\boldsymbol{\varepsilon} \cdot \boldsymbol{\varepsilon}^T \mathbf{A}^T\} + \underbrace{\mathbf{E}\{\mathbf{A}\boldsymbol{\varepsilon} \cdot \mathbf{b}^T \mathbf{A}^T\}}_0 + \underbrace{\mathbf{E}\{\mathbf{A}\mathbf{b} \cdot \boldsymbol{\varepsilon}^T \mathbf{A}^T\}}_0 + \mathbf{E}\{\mathbf{A}\mathbf{b} \cdot \mathbf{b}^T \mathbf{A}^T\} \\ &= \mathbf{A}\Sigma\mathbf{A}^T + \mathbf{A}\mathbf{b} \cdot \mathbf{b}^T \mathbf{A}^T \end{aligned}$$

- Operating the second term:

$$\mathbf{E}\{\mathbf{A}\boldsymbol{\varepsilon} + \mathbf{A}\mathbf{b}\} \cdot \mathbf{E}\{\mathbf{A}\boldsymbol{\varepsilon} + \mathbf{A}\mathbf{b}\}^T = \left[\underbrace{\mathbf{E}\{\mathbf{A}\boldsymbol{\varepsilon}\}}_0 + \mathbf{E}\{\mathbf{A}\mathbf{b}\} \right] \cdot \left[\underbrace{\mathbf{E}\{\mathbf{A}\boldsymbol{\varepsilon}\}^T}_0 + \mathbf{E}\{\mathbf{A}\mathbf{b}\}^T \right] = \mathbf{A}\mathbf{b} \cdot \mathbf{b}^T \mathbf{A}^T$$

Hence:

$$\text{cov}\{\mathbf{e}\} = \mathbf{A}\Sigma\mathbf{A}^T = (\mathbf{H}^T \Sigma^{-1} \mathbf{H})^{-1} \quad (\text{C.11})$$

C.5. Horizontal positioning Estimation Error

The horizontal positioning error (e_H) is a bivariate normal distribution, so its PDF describes equidensity ellipses. It can be expressed as the joint distribution of the estimation error components in the north and east directions of (e_N, e_E) , which follow correlated normal distributions as given in eq.(C.11). Alternatively, e_H can be represented in a rotated basis aligned with the major and minor equidensity ellipse semiaxes, so it can be expressed as the joint distribution of the estimation error components in the ellipse axes $(e_{\text{major}}, e_{\text{minor}})$, which follow uncorrelated normal distributions (Figure C.1). The directions of the ellipse axes are those of the eigenvectors of the horizontal observation submatrix ($H_H = H_{1:2,1:2}$), and the estimation error variances ($\sigma_{\text{major}}^2, \sigma_{\text{minor}}^2$) are their corresponding eigenvalues.

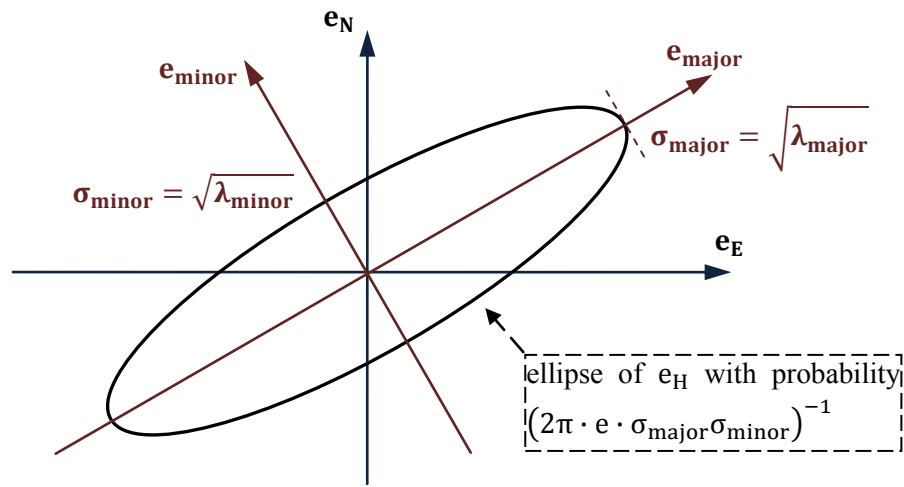


Figure C.1. Horizontal positioning error distribution.

The horizontal positioning error magnitude is:

$$|e_H| = \sqrt{e_N^2 + e_E^2} = \sqrt{e_{\text{major}}^2 + e_{\text{minor}}^2} \quad (\text{C.12})$$

Therefore, e_H^2 can be expressed as the sum of two squared uncorrelated normal distributions, which does not follow any known statistical law.

(Note: e_H^2 does not follow a chi squared distribution unless $\sigma_{\text{major}} = \sigma_{\text{minor}}$).

C.6. Pseudorange Residuals

The pseudorange residual vector (r) is defined as the difference between the measured pseudorange vector and the pseudorange vector estimated from the estimated navigation solution:

$$r = \Delta y - H \cdot \Delta \hat{x} \quad (\text{C.13})$$

Introducing (C.6) eq. in (C.13), each element of r can be expressed as a linear combination of the elements of Δy :

$$r = (I - HA) \cdot \Delta y = (I - B) \cdot \Delta y \quad (C.14)$$

where:

$$B = HA = H(H^T \Sigma^{-1} H)^{-1} H^T \Sigma^{-1} \quad (C.15)$$

The relationship between the pseudorange residuals and the pseudorange measurement error is obtained introducing eq.(A.8) in (C.14):

$$r = (I - B) \cdot (H \cdot \Delta x + E) = (I - B) \cdot E = (I - B) \cdot (\varepsilon + b) \quad (C.16)$$

Summarizing, the pseudorange residual vector is a parameter calculated from the pseudorange measurements that contains information about pseudorange measurement errors, which are not directly measurable:

$$r = (I - B) \cdot \Delta y = (I - B) \cdot E \quad (C.17)$$

C.7. Uncorrelation between residual and position error vectors

The covariance between r and e is zero:

$$\text{cov}(r, e) = E\{r \cdot e^T\} - E\{r\} \cdot E\{e\}^T = 0 \quad (C.18)$$

Introducing the expressions (C.9) and (C.16):

$$\text{cov}(r, e) = E\{(I - B)(\varepsilon + b) \cdot [A \cdot (\varepsilon + b)]^T\} - E\{(I - B)(\varepsilon + b)\} \cdot E\{A \cdot (\varepsilon + b)\}^T \quad (C.19)$$

- Operating the first term:

$$\begin{aligned} E\{r \cdot e^T\} &= E\{(I - B)(\varepsilon + b) \cdot [A \cdot (\varepsilon + b)]^T\} = \\ &= E\{(I - B)\varepsilon \cdot \varepsilon^T A^T\} + \underbrace{E\{(I - B)\varepsilon \cdot b^T A^T\}}_0 + \\ &+ \underbrace{E\{(I - B)b \cdot \varepsilon^T A^T\}}_0 + E\{(I - B)b \cdot b^T A^T\} \\ &= (I - B)E\{\varepsilon \cdot \varepsilon^T\}A^T + (I - B)b \cdot b^T A^T = \underbrace{(I - B) \cdot \Sigma \cdot A^T}_0 + (I - B)b \cdot b^T A^T \\ &= (I - B)b \cdot b^T A^T \end{aligned}$$

- Operating the second term:

$$\begin{aligned}
 E\{r\} \cdot E\{e\}^T &= E\{ (I - B)(\varepsilon + b) \} \cdot E\{A \cdot (\varepsilon + b)\}^T = \\
 &= \left[\underbrace{E\{ (I - B)\varepsilon \}}_0 + E\{ (I - B)b \} \right] \cdot \left[\underbrace{E\{A \cdot \varepsilon\}^T}_0 + E\{A \cdot b\}^T \right] = (I - B)b \cdot b^T A^T \\
 &= (I - B)b \cdot b^T A^T
 \end{aligned}$$

Hence:

$$\text{cov}(r, e) = 0 \quad (\text{C.20})$$

- Demonstration of $(I - B) \cdot \Sigma \cdot A^T = 0$

$$\begin{aligned}
 (I - B) \cdot \Sigma \cdot A^T &= \left(I - \underbrace{H(H^T \Sigma^{-1} H)^{-1} H^T \Sigma^{-1}}_B \right) \cdot \Sigma \cdot \underbrace{\Sigma^{-1} H(H^T \Sigma^{-1} H)^{-1}}_{A^T} = \\
 &= H(H^T \Sigma^{-1} H)^{-1} - H(H^T \Sigma^{-1} H)^{-1} \underbrace{H^T \Sigma^{-1} H(H^T \Sigma^{-1} H)^{-1}}_I = \\
 &= H(H^T \Sigma^{-1} H)^{-1} - H(H^T \Sigma^{-1} H)^{-1} = 0
 \end{aligned}$$

C.8. WLSE as the LSE of a Normalized System

First RAIM algorithms were designed under the assumption of independent pseudorange measurement errors with identical variance. Consequently, their algorithms are based in the non-weighted least squares estimator (LSE). This appendix describes the transformation of pseudorange measurement equations with a general nominal error covariance matrix into an equivalent normalized system with a unitary nominal error covariance matrix, in which the original RAIM algorithms could be applied.

C.8.1. Normalized pseudorange measurement equation system

The objective is find an equivalent equation system to that one described in (C.1) - (C.4), with a nominal error correlation matrix equal to the identity matrix. An equivalent normalized pseudorange measurement equation system can be obtained dividing each equation of eq.(C.1) by the inverse of its corresponding nominal noise standard deviation:

$$\Delta y_n = H_n \cdot \Delta x + E_n \quad (\text{C.21})$$

where:

- $\Delta y_n = W \cdot \Delta y$
- $H_n = W \cdot H$
- $E_n = \varepsilon_n + b_n = W \cdot (\varepsilon + b) = W \cdot E$
 - $\varepsilon_n = W \cdot \varepsilon$
 - $b_n = W \cdot b$

The normalizing matrix is the squared root inverse of the noise covariance matrix:

$$W = \Sigma^{-1/2} = \begin{pmatrix} 1/\sigma_1 & 0 & \cdots & 0 \\ 0 & 1/\sigma_2 & & \vdots \\ \vdots & & \ddots & 0 \\ 0 & \cdots & 0 & 1/\sigma_N \end{pmatrix} \quad (C.22)$$

Indeed, the measurement nominal error covariance matrix is the unity:

$$\text{var}(\epsilon_n) = \text{var}(W\epsilon) = \underbrace{E\{W\epsilon \cdot \epsilon^T W^T\}}_I - \underbrace{E\{W\epsilon\}}_0 \underbrace{E\{W\epsilon\}^T}_0 = I \quad (C.23)$$

C.8.2. LSE Properties

The LS solution estimation ($\Delta\hat{x}_n$) is the same as in the non-normalized system:

$$\Delta\hat{x}_n = A_n \cdot \Delta y_n = A \cdot \Delta y = \Delta\hat{x} \quad (C.24)$$

$$A_n = (H_n^T H_n)^{-1} H_n^T \quad (C.25)$$

The estimation error (e_n) is the same as in the non-normalized system:

$$e_n = A_n \cdot E_n = A \cdot E = e \quad (C.26)$$

$$\text{cov}\{e_n\} = A_n A_n^T = (H^T \Sigma^{-1} H)^{-1} = \Sigma A^T = \text{cov}\{e\} \quad (C.27)$$

The normalized residual vector is the non-normalized one scaled by the matrix W :

$$r_n = (I - B_n) \cdot \Delta y_n = W \cdot (I - B) \cdot \Delta y = W \cdot r \quad (C.28)$$

$$r_n = (I - B_n) \cdot E_n = W \cdot (I - B) \cdot E = W \cdot r \quad (C.29)$$

$$B_n = H_n (H_n^T H_n)^{-1} H_n^T \quad (C.30)$$

The normalized residual vector and the normalized estimation error are uncorrelated:

$$\text{cov}(r_n, e_n) = 0 \quad (C.31)$$

Appendix D

WLSR RAIM related subjects

D.1. Derivation of the non-centrality parameter

Let us recall the WLSR RAIM test statistic formula:

$$t = r^T \Sigma^{-1} r \quad (D.1)$$

Introducing eq.(C.17) gives the following relationship between t and the pseudorange errors:

$$t = E^T \underbrace{(I - B)^T \Sigma^{-1} (I - B)}_{\Sigma^{-1}(I-B)} E = E^T \Sigma^{-1} (I - B) E \quad (D.2)$$

where $(I - B)^T \Sigma^{-1} (I - B) = \Sigma^{-1} (I - B)$ is demonstrated in Appendix D.3.

The test statistic with fault-free measurements ($E = \varepsilon$) is:

$$t_{FF} = \varepsilon^T \Sigma^{-1} (I - B) \varepsilon \quad (D.3)$$

The test statistic t_{FF} has a chi-squared distribution ($t_{FF} \sim \chi_k^2$), which is known to have a mean value equal to the number of degrees of freedom (k):

$$E\{t_{FF}\} = E\{\varepsilon^T \Sigma^{-1} (I - B) \varepsilon\} = k \quad (D.4)$$

The test statistic with faulty measurements ($E = \varepsilon + b$) is:

$$t_F = (\varepsilon + b)^T \Sigma^{-1} (I - B) (\varepsilon + b) \quad (D.5)$$

The test statistic t_F has a non-central chi-squared distribution ($t_F \sim \chi_{k,\lambda}^2$), which is known to have a mean value equal to the sum of the number of degrees of freedom (k) plus the non-centrality parameter (λ):

$$E\{t_F\} = E\{(\varepsilon + b)^T \Sigma^{-1} (I - B) (\varepsilon + b)\} = k + \lambda \quad (D.6)$$

Developing eq.(D.6):

$$E\{t_F\} = \underbrace{E\{\varepsilon^T \Sigma^{-1} (I - B) \varepsilon\}}_{E\{t_{FF}\} = k} + \underbrace{E\{\varepsilon^T \Sigma^{-1} (I - B) b\}}_0 + \dots$$

$$\dots + \underbrace{E\{b^T \Sigma^{-1}(I - B)\varepsilon\}}_0 + E\{b^T \Sigma^{-1}(I - B)b\} = k + \lambda$$

Hence:

$$\lambda = b^T \Sigma^{-1}(I - B)b \quad (D.7)$$

D.2. Uncorrelation between the test statistic and the estimation error vector

The covariance between the test statistic t and any component of the navigation solution error vector e is zero:

$$\text{cov}(t, e) = E\{t \cdot e^T\} - E\{t\} \cdot E\{e\}^T = 0 \quad (D.8)$$

Expression (D.8) is demonstrated calculating the covariance in the faulty case, $E = \varepsilon + b$. The fault free case is the specific case with $b = 0$.

1) First term of the covariance (D.8), $E\{t \cdot e^T\}$:

Introducing equations (D.2) and (C.9), operating and rearranging the resulting terms:

$$\begin{aligned} E\{t \cdot e^T\} = & \quad (D.9) \\ = & \underbrace{E\{b^T \Sigma^{-1}(I - B)bb^T A^T\}}_a + \underbrace{E\{\varepsilon^T \Sigma^{-1}(I - B)bb^T A^T\}}_b + \\ & + \underbrace{E\{b^T \Sigma^{-1}(I - B)\varepsilon b^T A^T\}}_b + \underbrace{E\{b^T \Sigma^{-1}(I - B)b\varepsilon^T A^T\}}_b + \\ & + \underbrace{E\{\varepsilon^T \Sigma^{-1}(I - B)b\varepsilon^T A^T\}}_c + \underbrace{E\{b^T \Sigma^{-1}(I - B)\varepsilon \varepsilon^T A^T\}}_d + \\ & + \underbrace{E\{\varepsilon^T \Sigma^{-1}(I - B)b\varepsilon^T A^T\}}_e + \underbrace{E\{\varepsilon^T \Sigma^{-1}(I - B)\varepsilon \varepsilon^T A^T\}}_f \end{aligned}$$

The different terms of eq.(D.9) have been labelled from a) to f) and developed as follows:

a) The term without ε is deterministic:

$$E\{b^T \Sigma^{-1}(I - B)bb^T A^T\} = b^T \Sigma^{-1}(I - B)bb^T A^T$$

b) The expected values of terms in which ε appears only once is zero:

$$E\{\varepsilon^T \Sigma^{-1}(I - B)bb^T A^T\} = E\{b^T \Sigma^{-1}(I - B)\varepsilon b^T A^T\} = E\{b^T \Sigma^{-1}(I - B)b\varepsilon^T A^T\} = 0$$

c) Using the eq.(D.4):

$$E\{ \varepsilon^T \Sigma^{-1} (I - B) \varepsilon b^T A^T \} = \underbrace{E\{ \varepsilon^T \Sigma^{-1} (I - B) \varepsilon \}}_k \cdot b^T A^T = k \cdot b^T A^T$$

d) Introducing the noise covariance matrix $\Sigma = E\{ \varepsilon \varepsilon^T \}$:

$$E\{ b^T \Sigma^{-1} (I - B) \varepsilon \varepsilon^T A^T \} = b^T \Sigma^{-1} (I - B) \cdot E\{ \varepsilon \varepsilon^T \} \cdot A^T = b^T \underbrace{\Sigma^{-1} (I - B) \Sigma A^T}_0 = 0$$

where the proof of $\Sigma^{-1} (I - B) \Sigma A^T = 0$ can be found in Appendix D.3.

e) When the faulty case consists of a single pseudorange bias, the result of the product of the 4 first matrices of e) is a scalar, so it is equal to its transpose:

$$\varepsilon^T \Sigma^{-1} (I - B) b = [\varepsilon^T \Sigma^{-1} (I - B) b]^T = b^T [\Sigma^{-1} (I - B)]^T \varepsilon$$

Substituting $\varepsilon^T \Sigma^{-1} (I - B) b$ by its transpose in e) gives the same term as in d):

$$E\{ \varepsilon^T \Sigma^{-1} (I - B) b \varepsilon^T A^T \} = E\{ b^T [\Sigma^{-1} (I - B)]^T \varepsilon \varepsilon^T A^T \} = 0$$

f) Pseudorange nominal errors are modeled as zero mean, uncorrelated Gaussian variables. Therefore, they have null skewness and the expected value of the term with a triple product of noise is zero:

$$E\{ \varepsilon^T \Sigma^{-1} (I - B) \varepsilon \varepsilon^T A^T \} = 0$$

Then, the expression (D.9) results:

$$E\{ t \cdot e^T \} = k \cdot b^T A^T + b^T \Sigma^{-1} (I - B) b b^T A^T = (k + \lambda) b^T A^T \quad (D.10)$$

2) Second term of the covariance (D.8), $E\{t\} \cdot E\{e\}^T$:

The expectation of the test statistic in the faulty case is given in eq.(D.6):

$$E\{t\} = k + b^T \Sigma^{-1} (I - B) b = k + \lambda$$

The mean of the navigation solution error is:

$$E\{e\}^T = E\{ A(\varepsilon + b) \}^T = E\{ A\varepsilon \}^T + E\{ Ab \}^T = b^T A^T \quad (D.11)$$

Combining (D.6) and (D.11):

$$E\{t\} \cdot E\{e\}^T = (k + \lambda) b^T A^T \quad (D.12)$$

Finally, introducing equations (D.10) and (D.13) in the covariance expression (D.8):

$$\text{cov}(\mathbf{t}, \mathbf{e}) = (\mathbf{k} + \lambda)\mathbf{b}^T \mathbf{A}^T - (\mathbf{k} + \lambda)\mathbf{b}^T \mathbf{A}^T = 0 \quad (\text{D.13})$$

D.3. Demonstration of matrix expressions

D.3.1. Demonstration 1

The objective is to demonstrate:

$$(\mathbf{I} - \mathbf{B})^T \Sigma^{-1} (\mathbf{I} - \mathbf{B}) = \Sigma^{-1} (\mathbf{I} - \mathbf{B}) = (\mathbf{I} - \mathbf{B})^T \Sigma^{-1} \quad (\text{D.14})$$

Developing the products:

$$(\mathbf{I} - \mathbf{B})^T \Sigma^{-1} (\mathbf{I} - \mathbf{B}) = \Sigma^{-1} - \Sigma^{-1} \mathbf{B} - \mathbf{B}^T \Sigma^{-1} + \mathbf{B}^T \Sigma^{-1} \mathbf{B} \quad (\text{D.15})$$

Introducing the definition of the matrix \mathbf{B} in each term:

- 1st term: Σ^{-1}
- 2nd term: $\Sigma^{-1} \mathbf{B} = \Sigma^{-1} \underbrace{\mathbf{H}(\mathbf{H}^T \Sigma^{-1} \mathbf{H})^{-1} \mathbf{H}^T}_{\mathbf{B}} \Sigma^{-1}$
- 3rd term: $\mathbf{B}^T \Sigma^{-1} = \underbrace{\Sigma^{-1} \mathbf{H}(\mathbf{H}^T \Sigma^{-1} \mathbf{H})^{-1} \mathbf{H}^T}_{\mathbf{B}^T} \Sigma^{-1}$
- 4th term: $\mathbf{B}^T \Sigma^{-1} \mathbf{B} = \underbrace{\Sigma^{-1} \mathbf{H}(\mathbf{H}^T \Sigma^{-1} \mathbf{H})^{-1} \mathbf{H}^T}_{\mathbf{B}^T} \cdot \Sigma^{-1} \cdot \underbrace{\mathbf{H}(\mathbf{H}^T \Sigma^{-1} \mathbf{H})^{-1} \mathbf{H}^T}_{\mathbf{B}} =$
 $= \Sigma^{-1} \mathbf{H}(\mathbf{H}^T \Sigma^{-1} \mathbf{H})^{-1} \mathbf{H}^T \Sigma^{-1}$

The last three terms are equal:

$$\Sigma^{-1} \mathbf{B} = \mathbf{B}^T \Sigma^{-1} = \mathbf{B}^T \Sigma^{-1} \mathbf{B} = \Sigma^{-1} \mathbf{H}(\mathbf{H}^T \Sigma^{-1} \mathbf{H})^{-1} \mathbf{H}^T \Sigma^{-1} \quad (\text{D.16})$$

The first equality of (D.14) is demonstrated substituting $\mathbf{B}^T \Sigma^{-1}$ and $\mathbf{B}^T \Sigma^{-1} \mathbf{B}$ by $\Sigma^{-1} \mathbf{B}$ in (D.15):

$$(\mathbf{I} - \mathbf{B})^T \Sigma^{-1} (\mathbf{I} - \mathbf{B}) = \Sigma^{-1} (\mathbf{I} - \mathbf{B}) \quad (\text{D.17})$$

The second equality of (D.14) is demonstrated substituting $\Sigma^{-1} \mathbf{B}$ and $\mathbf{B}^T \Sigma^{-1} \mathbf{B}$ by $\mathbf{B}^T \Sigma^{-1}$ in (D.15):

$$(\mathbf{I} - \mathbf{B})^T \Sigma^{-1} (\mathbf{I} - \mathbf{B}) = (\mathbf{I} - \mathbf{B})^T \Sigma^{-1} \quad (\text{D.18})$$

D.3.2. Demonstration 2

The objective is to demonstrate:

$$\Sigma^{-1}(I - B)\Sigma A^T = 0 \quad (D.19)$$

Developing the products:

$$\Sigma^{-1}(I - B)\Sigma A^T = \underbrace{\Sigma^{-1}\Sigma}_I A^T - \Sigma^{-1}B\Sigma A^T$$

Introducing the definition the matrices A and B:

$$\Sigma^{-1}(I - B)\Sigma A^T = A^T - \Sigma^{-1} \underbrace{H(H^T \Sigma^{-1} H)^{-1} H^T \Sigma^{-1}}_B \cdot \underbrace{\Sigma \cdot \Sigma^{-1} H(H^T \Sigma^{-1} H)^{-1}}_{A^T}$$

Regrouping the terms:

$$\Sigma^{-1}(I - B)\Sigma A^T = A^T - \underbrace{\Sigma^{-1} H(H^T \Sigma^{-1} H)^{-1}}_{A^T} \cdot \underbrace{H^T \Sigma^{-1} H(H^T \Sigma^{-1} H)^{-1}}_I = 0$$

D.4. LSR RAIM design with the Parity Matrix method

WLSR RAIM can be designed with the parity matrix method, resulting an algorithm equivalent to the one obtained with the least squares residuals [Sturza, 1988].

Given an observation matrix H, it is always possible to find a parity matrix P that spans the null space (parity space) of H:

$$P \cdot H = 0 \quad (D.20)$$

The rows of P are an orthogonal basis of the null space:

$$P \cdot P^T = I_k \quad (D.21)$$

For an observation matrix size of $[N \times M]$, the resulting parity matrix size is $[k \times N]$, with $k = N - M$. Parity matrices can be obtained with different methods. For instance, the lower k rows of the Q matrix transpose derived from a QR factorization of H gives a suitable P [Brown, 1997].

The parity vector p, of size $[k, 1]$, is the result of multiplying any side of the pseudorange measurement equation system by the parity matrix, so it provides information about the pseudorange measurement errors:

$$p = P \cdot \Delta y = P \cdot E \quad (D.22)$$

If pseudorange nominal measurement errors have independent and normal distributions with variance unity, i.e. $\varepsilon \sim N(0, I)$, the squared magnitude of the parity vector is a valid test statistic that has a chi-squared distribution in the fault free case, and non-central chi-squared one in the faulty case:

$$t = \|p_n\|^2 = p_n^T p_n \sim \begin{cases} \chi_k^2 & \text{if } E = E_n \sim N(0, I) \\ \chi_{k,\lambda}^2 & \text{if } E = E_n \sim N(b_n, I) \end{cases} \quad (D.23)$$

In normalized case $\varepsilon \sim N(0, I)$, the test statistic is the same as the computed with the least squares residual [Sturza, 1988]:

$$t = \|p_n\|^2 = \|r_n\|^2 \quad (D.24)$$

In the general case $\varepsilon \sim N(0, \Sigma)$, the squared magnitude of the parity vector does not have the properties of eq.(D.23), so the test statistic is computed as the squared magnitude of the parity vector of the normalized measurement equation system described in eq.(C.21):

$$P_n \cdot H_n = P_n \cdot \Sigma^{-1/2} H = 0 \quad (D.25)$$

$$P_n \cdot P_n^T = I_k \quad (D.26)$$

$$p_n = P_n \cdot \Delta y_n = P_n \cdot \Sigma^{-1/2} \Delta y_n = P_n \cdot \Sigma^{-1/2} E \quad (D.27)$$

$$t = \|p_n\|^2 = (\Delta y_n)^T P_n^T \cdot P_n \Delta y_n \quad (D.28)$$

where subscript n indicates normalized parameters.

Considering the i^{th} pseudorange measurement contains a bias b_i , the relationship between λ and b_i in terms of the parity matrix is:

$$\lambda = b_n^T P_n^T P_n b_n = (P_n^T P_n)_{ii} \cdot b_{n,i}^2 = \frac{(P_n^T P_n)_{ii}}{\sigma_i^2} \cdot b_i^2 \quad (D.29)$$

The minimum detectable bias in the i^{th} pseudorange measurement, corresponding to a minimum detectable non-centrality parameter λ_{det} is:

$$b_{\text{det},i} = \sqrt{\frac{\sigma_i^2}{(P_n^T P_n)_{ii}} \cdot \lambda_{\text{det}}} \quad (D.30)$$

The comparison of previous equations with those of residuals yields:

$$(I - B)_{ii} = (P_n^T P_n)_{ii} \quad (D.31)$$

Appendix E

Simulation Results (I): RAIM Performance

E.1. WLSR RAIM unavailability

This appendix compiles the WLSR RAIM unavailability rate obtained from the simulations in urban and rural environments for all combination of GNSS receivers under study and HAL equal to 50 and 25 meters. Two values of probability of missed detection are studied, $P_{MD} = 5 \cdot 10^{-5}$ and $P_{MD} = 10^{-3}$, and one of false detection, $P_{FA} = 5 \cdot 10^{-3}$.

Equivalently, the unavailability rates correspond to the probability that the false detection of the variable- P_{FA} WLSR RAIM exceeds the limit of $5 \cdot 10^{-3}$.

The following tables contain the fault detection unavailability probabilities:

- Table E.1. - Unavailability of the WLSR RAIM fault detection capability in dual constellation GPS & Galileo users.
- Table E.2. - Unavailability of the WLSR RAIM fault detection capability in GPS users.
- Table E.3. - Unavailability of the WLSR RAIM fault detection capability in Galileo users.

The unavailability probability of the WLSR RAIM fault exclusion capability has been computed as the highest fault detection unavailability probability among all subgroups of N-1 range measurements at each instant. The following tables contain the fault exclusion unavailability rates:

- Table E.4. - Unavailability of the WLSR RAIM fault exclusion capability in dual constellation GPS & Galileo users.
- Table E.5. - Unavailability of the WLSR RAIM fault exclusion capability in GPS users.
- Table E.6. - Unavailability of the WLSR RAIM fault exclusion capability in Galileo users.

Table E.1 (a). Unavailability ratio of the WLSR RAIM with a constant $P_{FA} = 5 \cdot 10^{-3}$ ($p\{HPL > HAL\}$). Equivalently, probability that the WLSR RAIM variable P_{FA} exceeds $5 \cdot 10^{-3}$ ($p\{P_{FA} > 5 \cdot 10^{-3}\}$). Dual constellation GPS & Galileo receivers. RAIM: Fault detection.

Navigation solution (observation matrix)	GNSS signals	Pseudorange nominal error model	Environment							
			Urban				Rural			
			P _{MD}							
			5 · 10 ⁻⁵		10 ⁻³		5 · 10 ⁻⁵		10 ⁻³	
			HAL (m)							
			25	50	25	50	25	50	25	50
3 variables: • 2D position • T _{Rcx} /GNSS	L1 BOC(1,1) E1 BOC(1,1)	L1/E1	0.987	0.745	0.973	0.681	0.795	0.083	0.643	0.048
		L1/E1 + SBAS	0.505	0.196	0.441	0.164	0.007	1.2e-4	0.004	6.2e-5
		L1/E1 + L5/E5a	0.894	0.554	0.855	0.493	0.274	0.009	0.178	0.006
	L1 TMBOC(6,1,4/33) E1 CBOC(6,1,1/11,+)	L1/E1	0.984	0.721	0.968	0.656	0.746	0.072	0.589	0.038
		L1/E1 + SBAS	0.199	0.074	0.166	0.062	1.1e-4	0	6.2e-5	0
		L1/E1 + L5/E5a	0.504	0.200	0.442	0.168	0.005	1.1e-4	0.004	7.7e-5
	L1 TMBOC(6,1,4/33) E1 CBOC(6,1,1/11,-)	L1/E1	0.984	0.720	0.967	0.655	0.744	0.072	0.587	0.038
		L1/E1 + SBAS	0.183	0.069	0.153	0.058	8.1e-5	0	3.1e-5	0
		L1/E1 + L5/E5a	0.473	0.180	0.409	0.150	0.005	8.1e-5	0.004	5.4e-5
	L5 BPSK(10) E5a BPSK(10)	L5/E5a	1	0.966	1	0.941	1	0.575	1	0.426
		L5/E5a + SBAS	0.144	0.055	0.120	0.047	1.9e-5	0	1.5e-5	0
	4 variables: • 2D position • T _{Rcx} /GPS • T _{Rcx} /Galileo	L1 BOC(1,1) E1 BOC(1,1)	L1/E1	0.994	0.821	0.986	0.760	0.899	0.114	0.788
L1/E1 + SBAS			0.589	0.324	0.536	0.285	0.011	0.001	0.007	0.001
L1/E1 + L5/E5a			0.914	0.631	0.884	0.576	0.338	0.014	0.239	0.010
L1 TMBOC(6,1,4/33) E1 CBOC(6,1,1/11,+)		L1/E1	0.992	0.801	0.983	0.738	0.872	0.095	0.742	0.051
		L1/E1 + SBAS	0.332	0.158	0.293	0.139	0.001	3.1e-5	0.001	1.9e-5
		L1/E1 + L5/E5a	0.583	0.329	0.534	0.289	0.009	0.001	0.006	3.7e-4
L1 TMBOC(6,1,4/33) E1 CBOC(6,1,1/11,-)		L1/E1	0.992	0.801	0.983	0.738	0.871	0.094	0.740	0.051
		L1/E1 + SBAS	0.314	0.149	0.276	0.132	0.001	2.3e-5	4.8e-4	1.9e-5
		L1/E1 + L5/E5a	0.561	0.304	0.510	0.266	0.009	0.001	0.006	2.7e-4
L5 BPSK(10) E5a BPSK(10)		L5/E5a	1	0.982	1	0.965	1	0.731	1	0.563
		L5/E5a + SBAS	0.266	0.128	0.233	0.114	4.5e-4	1.5e-5	1.8e-4	7.7e-6

Table E.1 (b). Unavailability ratio of the WLSR RAIM with a constant $P_{FA} = 5 \cdot 10^{-3}$ ($p\{HPL > HAL\}$). Equivalently, probability that the WLSR RAIM variable P_{FA} exceeds $5 \cdot 10^{-3}$ ($p\{P_{FA} > 5 \cdot 10^{-3}\}$). Dual constellation GPS & Galileo receivers. RAIM: Fault detection.

Navigation solution (observation matrix)	GNSS signals	Pseudorange nominal error model	Environment							
			Urban				Rural			
			P_{MD}							
			$5 \cdot 10^{-5}$		10^{-3}		$5 \cdot 10^{-5}$		10^{-3}	
			HAL (m)							
			25	50	25	50	25	50	25	50
4 variables: • 3D position • $T_{rcx}/GNSS$	L1 BOC(1,1) E1 BOC(1,1)	L1/E1	0.996	0.860	0.991	0.812	0.899	0.147	0.785	0.090
		L1/E1 + SBAS	0.674	0.368	0.619	0.328	0.018	0.001	0.013	2.9e-4
		L1/E1 + L5/E5a	0.962	0.718	0.939	0.664	0.460	0.026	0.333	0.017
	L1 TMBOC(6,1,4/33) E1 CBOC(6,1,1/11,+)	L1/E1	0.995	0.843	0.989	0.792	0.865	0.125	0.733	0.074
		L1/E1 + SBAS	0.370	0.188	0.328	0.168	0.001	4.6e-5	2.9e-4	3.1e-5
		L1/E1 + L5/E5a	0.676	0.375	0.623	0.335	0.018	0.001	0.013	3.7e-4
	L1 TMBOC(6,1,4/33) E1 CBOC(6,1,1/11,-)	L1/E1	0.995	0.842	0.989	0.791	0.864	0.125	0.731	0.074
		L1/E1 + SBAS	0.348	0.178	0.309	0.159	3.7e-4	3.9e-5	2.3e-4	3.1e-5
		L1/E1 + L5/E5a	0.646	0.350	0.592	0.311	0.015	4.9e-4	0.010	2.4e-4
	L5 BPSK(10) E5a BPSK(10)	L5/E5a	1	0.988	1	0.978	1	0.719	1	0.564
		L5/E5a + SBAS	0.295	0.152	0.262	0.137	1.9e-4	2.7e-5	1.1e-4	1.5e-5
4 variables: • 3D position • $T_{rcx}/GNSS$ Hybridization external altitude $\sigma_{alt} = 5$ m.	L1 BOC(1,1) E1 BOC(1,1)	L1/E1	0.988	0.746	0.974	0.682	0.798	0.084	0.647	0.048
		L1/E1 + SBAS	0.516	0.201	0.451	0.168	0.008	1.2e-4	0.005	6.6e-5
		L1/E1 + L5/E5a	0.896	0.557	0.858	0.496	0.278	0.009	0.182	0.006
	L1 TMBOC(6,1,4/33) E1 CBOC(6,1,1/11,+)	L1/E1	0.984	0.722	0.969	0.657	0.750	0.073	0.593	0.039
		L1/E1 + SBAS	0.215	0.079	0.180	0.067	1.3e-4	0	7.3e-5	0
		L1/E1 + L5/E5a	0.515	0.204	0.453	0.172	0.006	1.1e-4	0.004	7.7e-5
	L1 TMBOC(6,1,4/33) E1 CBOC(6,1,1/11,-)	L1/E1	0.984	0.721	0.968	0.657	0.747	0.072	0.591	0.039
		L1/E1 + SBAS	0.199	0.074	0.166	0.062	9.3e-5	0	4.2e-5	0
		L1/E1 + L5/E5a	0.485	0.185	0.420	0.153	0.006	8.1e-5	0.004	5.4e-5
	L5 BPSK(10) E5a BPSK(10)	L5/E5a	1	0.966	1	0.942	1	0.576	1	0.427
		L5/E5a + SBAS	0.159	0.060	0.132	0.051	3.1e-5	0	1.9e-5	0

Table E.1 (c). Unavailability ratio of the WLSR RAIM with a constant $P_{FA} = 5 \cdot 10^{-3}$ ($p\{HPL > HAL\}$). Equivalently, probability that the WLSR RAIM variable P_{FA} exceeds $5 \cdot 10^{-3}$ ($p\{P_{FA} > 5 \cdot 10^{-3}\}$). Dual constellation GPS & Galileo receivers. RAIM: Fault detection.

Navigation solution (observation matrix)	GNSS signals	Pseudorange nominal error model	Environment							
			Urban				Rural			
			P _{MD}							
			5 · 10 ⁻⁵		10 ⁻³		5 · 10 ⁻⁵		10 ⁻³	
			HAL (m)							
			25	50	25	50	25	50	25	50
5 variables: • 3D position • T _{rcx} /GPS • T _{rcx} /Galileo	L1 BOC(1,1) E1 BOC(1,1)	L1/E1	0.998	0.907	0.995	0.867	0.954	0.200	0.882	0.121
		L1/E1 + SBAS	0.742	0.499	0.698	0.462	0.032	0.003	0.023	0.002
		L1/E1 + L5/E5a	0.970	0.775	0.953	0.733	0.518	0.042	0.389	0.029
	L1 TMBOC(6,1,4/33) E1 CBOC(6,1,1/11,+)	L1/E1	0.997	0.894	0.994	0.852	0.936	0.171	0.852	0.102
		L1/E1 + SBAS	0.505	0.321	0.467	0.298	0.004	0.001	0.002	4.1e-4
		L1/E1 + L5/E5a	0.742	0.505	0.699	0.468	0.031	0.004	0.022	0.002
	L1 TMBOC(6,1,4/33) E1 CBOC(6,1,1/11,-)	L1/E1	0.997	0.893	0.994	0.851	0.935	0.170	0.850	0.101
		L1/E1 + SBAS	0.486	0.309	0.448	0.288	0.003	4.6e-4	0.002	3.6e-4
		L1/E1 + L5/E5a	0.719	0.481	0.674	0.445	0.026	0.003	0.019	0.002
	L5 BPSK(10) E5a BPSK(10)	L5/E5a	1	0.994	1	0.988	1	0.844	1	0.708
		L5/E5a + SBAS	0.436	0.282	0.402	0.264	0.002	3.4e-4	0.001	2.7e-4
	5 variables: • 3D position • T _{rcx} /GPS • T _{rcx} /Galileo Hybridization external altitude σ _{alt} = 5 m.	L1 BOC(1,1) E1 BOC(1,1)	L1/E1	0.994	0.822	0.986	0.761	0.900	0.114	0.790
L1/E1 + SBAS			0.597	0.331	0.545	0.292	0.012	0.001	0.008	0.001
L1/E1 + L5/E5a			0.916	0.633	0.886	0.578	0.342	0.014	0.242	0.010
L1 TMBOC(6,1,4/33) E1 CBOC(6,1,1/11,+)		L1/E1	0.993	0.802	0.983	0.740	0.874	0.096	0.745	0.052
		L1/E1 + SBAS	0.350	0.168	0.311	0.149	0.001	5e-5	0.001	3.1e-5
		L1/E1 + L5/E5a	0.592	0.336	0.543	0.295	0.010	0.001	0.007	3.9e-4
L1 TMBOC(6,1,4/33) E1 CBOC(6,1,1/11,-)		L1/E1	0.993	0.802	0.983	0.739	0.872	0.095	0.743	0.051
		L1/E1 + SBAS	0.332	0.160	0.295	0.142	0.001	3.9e-5	0.001	1.9e-5
		L1/E1 + L5/E5a	0.571	0.312	0.520	0.273	0.010	0.001	0.006	3.3e-4
L5 BPSK(10) E5a BPSK(10)		L5/E5a	1	0.982	1	0.966	1	0.732	1	0.564
		L5/E5a + SBAS	0.288	0.141	0.255	0.125	0.001	1.9e-5	3.0e-4	1.5e-5

Table E.2 (a). Unavailability ratio of the WLSR RAIM with a constant $P_{FA} = 5 \cdot 10^{-3}$ ($p\{HPL > HAL\}$). Equivalently, probability that the WLSR RAIM variable P_{FA} exceeds $5 \cdot 10^{-3}$ ($p\{P_{FA} > 5 \cdot 10^{-3}\}$). GPS receivers. RAIM: Fault detection.

Navigation solution (observation matrix)	GNSS signals	Pseudorange nominal error model	Environment							
			Urban				Rural			
			P_{MD}							
			$5 \cdot 10^{-5}$		10^{-3}		$5 \cdot 10^{-5}$		10^{-3}	
			HAL (m)							
			25	50	25	50	25	50	25	50
3 variables: • 2D position • T_{rcx}/GPS	L1 BPSK(1) (2-sided BW=2 MHz)	L1	1	0.998	1	0.996	1	0.983	1	0.957
		L1 + SBAS	0.999	0.968	0.998	0.952	0.994	0.737	0.985	0.635
		L1 + L5	1	1	1	0.999	1	0.998	1	0.994
	L1 BPSK(1) (2-sided BW=20 MHz)	L1	1	0.994	1	0.988	1	0.927	1	0.874
		L1 + SBAS	0.933	0.802	0.911	0.781	0.534	0.222	0.449	0.194
		L1 + L5	0.997	0.943	0.994	0.923	0.973	0.583	0.943	0.501
	L1 BOC(1,1)	L1	1	0.995	1	0.989	1	0.931	1	0.879
		L1 + SBAS	0.944	0.815	0.926	0.796	0.584	0.242	0.504	0.213
		L1 + L5	0.998	0.954	0.997	0.938	0.986	0.648	0.967	0.561
	L1 TMBOC(6,1,4/33)	L1	1	0.993	1	0.986	1	0.913	1	0.855
		L1 + SBAS	0.816	0.697	0.795	0.676	0.239	0.114	0.208	0.102
		L1 + L5	0.934	0.805	0.912	0.784	0.546	0.226	0.457	0.199
	L5 BPSK(10)	L5	1	1	1	1	1	1	1	1
		L5 + SBAS	0.792	0.673	0.767	0.655	0.202	0.100	0.168	0.091

Table E.2 (b). Unavailability ratio of the WLSR RAIM with a constant $P_{FA} = 5 \cdot 10^{-3}$ ($p\{HPL > HAL\}$). Equivalently, probability that the WLSR RAIM variable P_{FA} exceeds $5 \cdot 10^{-3}$ ($p\{P_{FA} > 5 \cdot 10^{-3}\}$). GPS receivers. RAIM: Fault detection.

Navigation solution (observation matrix)	GNSS signals	Pseudorange nominal error model	Environment							
			Urban				Rural			
			P _{MD}							
			5 · 10 ⁻⁵		10 ⁻³		5 · 10 ⁻⁵		10 ⁻³	
			HAL (m)							
			25	50	25	50	25	50	25	50
4 variables: • 3D position • T _{rcx} /GPS	L1 BPSK(1) (2-sided BW=2 MHz)	L1	1	1	1	0.999	1	0.995	1	0.990
		L1 + SBAS	1	0.993	1	0.990	0.999	0.904	0.998	0.868
		L1 + L5	1	1	1	1	1	1	1	0.999
	L1 BPSK(1) (2-sided BW=20 MHz)	L1	1	0.999	1	0.998	1	0.980	1	0.960
		L1 + SBAS	0.984	0.932	0.977	0.923	0.806	0.491	0.741	0.463
		L1 + L5	1	0.987	0.999	0.981	0.996	0.835	0.989	0.787
	L1 BOC(1,1)	L1	1	0.999	1	0.998	1	0.981	1	0.962
		L1 + SBAS	0.988	0.938	0.982	0.929	0.839	0.510	0.790	0.481
		L1 + L5	1	0.991	1	0.986	0.999	0.875	0.995	0.823
	L1 TMBOC(6,1,4/33)	L1	1	0.999	1	0.997	1	0.975	1	0.953
		L1 + SBAS	0.940	0.880	0.930	0.870	0.512	0.345	0.479	0.326
		L1 + L5	0.985	0.933	0.977	0.924	0.813	0.495	0.753	0.467
L5 BPSK(10)	L5	1	1	1	1	1	1	1	1	
	L5 + SBAS	0.929	0.869	0.917	0.861	0.475	0.324	0.436	0.306	

Table E.2 (c). Unavailability ratio of the WLSR RAIM with a constant $P_{FA} = 5 \cdot 10^{-3}$ ($p\{HPL > HAL\}$). Equivalently, probability that the WLSR RAIM variable P_{FA} exceeds $5 \cdot 10^{-3}$ ($p\{P_{FA} > 5 \cdot 10^{-3}\}$). GPS receivers. RAIM: Fault detection.

Navigation solution (observation matrix)	GNSS signals	Pseudorange nominal error model	Environment							
			Urban				Rural			
			P_{MD}							
			$5 \cdot 10^{-5}$		10^{-3}		$5 \cdot 10^{-5}$		10^{-3}	
			HAL (m)							
			25	50	25	50	25	50	25	50
4 variables: • 3D position • T_{rcx}/GPS Hybridization external altitude $\sigma_{alt} = 5$ m.	L1 BPSK(1) (2-sided BW=2 MHz)	L1	1	0.999	1	0.996	1	0.983	1	0.958
		L1 + SBAS	0.999	0.969	0.998	0.952	0.995	0.740	0.986	0.638
		L1 + L5	1	1	1	0.999	1	0.998	1	0.994
	L1 BPSK(1) (2-sided BW=20 MHz)	L1	1	0.995	1	0.988	1	0.929	1	0.875
		L1 + SBAS	0.938	0.808	0.917	0.788	0.552	0.232	0.468	0.202
		L1 + L5	0.997	0.944	0.995	0.924	0.975	0.588	0.946	0.507
	L1 BOC(1,1)	L1	1	0.995	1	0.989	1	0.932	1	0.880
		L1 + SBAS	0.948	0.820	0.930	0.801	0.604	0.250	0.522	0.222
		L1 + L5	0.999	0.955	0.997	0.939	0.987	0.651	0.968	0.564
	L1 TMBOC(6,1,4/33)	L1	1	0.993	1	0.986	1	0.914	1	0.856
		L1 + SBAS	0.832	0.713	0.812	0.693	0.266	0.123	0.233	0.110
		L1 + L5	0.938	0.810	0.918	0.791	0.558	0.237	0.476	0.208
	L5 BPSK(10)	L5	1	1	1	1	1	1	1	1
		L5 + SBAS	0.814	0.695	0.792	0.677	0.233	0.109	0.196	0.100

Table E.3 (a). Unavailability ratio of the WLSR RAIM with a constant $P_{FA} = 5 \cdot 10^{-3}$ ($p\{HPL > HAL\}$). Equivalently, probability that the WLSR RAIM variable P_{FA} exceeds $5 \cdot 10^{-3}$ ($p\{P_{FA} > 5 \cdot 10^{-3}\}$). Galileo receivers. RAIM: Fault detection.

Navigation solution (observation matrix)	GNSS signals	Pseudorange nominal error model	Environment							
			Urban				Rural			
			P_{MD}							
			$5 \cdot 10^{-5}$		10^{-3}		$5 \cdot 10^{-5}$		10^{-3}	
			HAL (m)							
			25	50	25	50	25	50	25	50
3 variables: • 2D position • $T_{rcx}/Galileo$	E1 BOC(1,1)	E1	1	0.990	1	0.984	1	0.932	1	0.893
		E1 + SBAS	0.908	0.784	0.890	0.760	0.382	0.210	0.332	0.181
		E1 + E5a	0.992	0.918	0.988	0.896	0.937	0.489	0.913	0.343
	E1 CBOC(6,1,1/11,+)	E1	1	0.989	1	0.982	1	0.926	1	0.868
		E1 + SBAS	0.799	0.662	0.777	0.629	0.226	0.085	0.199	0.065
		E1 + E5a	0.913	0.795	0.893	0.771	0.439	0.223	0.335	0.194
	E1 CBOC(6,1,1/11,-)	E1	1	0.989	1	0.982	1	0.926	1	0.866
		E1 + SBAS	0.782	0.637	0.761	0.604	0.205	0.069	0.179	0.051
		E1 + E5a	0.893	0.771	0.876	0.747	0.334	0.193	0.314	0.164
	E5a BPSK(10)	E5a	1	1	1	1	1	1	1	0.999
E5a + SBAS		0.757	0.597	0.734	0.568	0.173	0.047	0.148	0.034	
4 variables: • 3D position • $T_{rcx}/Galileo$	E1 BOC(1,1)	E1	1	0.998	1	0.996	1	0.980	1	0.948
		E1 + SBAS	0.970	0.881	0.956	0.867	0.617	0.295	0.494	0.280
		E1 + E5a	0.999	0.977	0.998	0.965	0.991	0.699	0.980	0.586
	E1 CBOC(6,1,1/11,+)	E1	1	0.997	1	0.995	1	0.974	1	0.940
		E1 + SBAS	0.893	0.810	0.879	0.795	0.305	0.207	0.289	0.189
		E1 + E5a	0.974	0.886	0.962	0.873	0.669	0.301	0.559	0.287
	E1 CBOC(6,1,1/11,-)	E1	1	0.997	1	0.995	1	0.974	1	0.939
		E1 + SBAS	0.883	0.798	0.868	0.785	0.293	0.192	0.277	0.176
		E1 + E5a	0.961	0.873	0.946	0.859	0.555	0.287	0.429	0.271
	E5a BPSK(10)	E5a	1	1	1	1	1	1	1	1
E5a + SBAS		0.867	0.782	0.853	0.767	0.274	0.171	0.257	0.156	

Table E.3 (b). Unavailability ratio of the WLSR RAIM with a constant $P_{FA} = 5 \cdot 10^{-3}$ ($p\{HPL > HAL\}$). Equivalently, probability that the WLSR RAIM variable P_{FA} exceeds $5 \cdot 10^{-3}$ ($p\{P_{FA} > 5 \cdot 10^{-3}\}$). Galileo receivers. RAIM: Fault detection.

Navigation solution (observation matrix)	GNSS signals	Pseudorange nominal error model	Environment							
			Urban				Rural			
			P_{MD}							
			$5 \cdot 10^{-5}$		10^{-3}		$5 \cdot 10^{-5}$		10^{-3}	
			HAL (m)							
			25	50	25	50	25	50	25	50
4 variables: • 3D position • $T_{rcx}/Galileo$ Hybridization external altitude $\sigma_{alt} = 5\text{ m}$	E1 BOC(1,1)	E1	1	0.990	1	0.984	1	0.932	1	0.893
		E1 + SBAS	0.914	0.788	0.895	0.765	0.400	0.214	0.339	0.188
		E1 + E5a	0.992	0.919	0.988	0.898	0.938	0.494	0.915	0.348
	E1 CBOC(6,1,1/11,+)	E1	1	0.989	1	0.983	1	0.926	1	0.869
		E1 + SBAS	0.810	0.677	0.785	0.646	0.234	0.102	0.209	0.083
		E1 + E5a	0.919	0.799	0.898	0.775	0.461	0.227	0.346	0.201
	E1 CBOC(6,1,1/11,-)	E1	1	0.989	1	0.982	1	0.926	1	0.867
		E1 + SBAS	0.792	0.655	0.770	0.625	0.215	0.089	0.190	0.070
		E1 + E5a	0.899	0.776	0.883	0.753	0.347	0.201	0.319	0.174
E5a BPSK(10)	E5a	1	1	1	1	1	1	1	0.999	
	E5a + SBAS	0.768	0.622	0.747	0.592	0.185	0.070	0.162	0.054	

Table E.4 (a). Unavailability ratio of the WLSR RAIM with a constant $P_{FA} = 5 \cdot 10^{-3}$ ($p\{HPL > HAL\}$). Equivalently, probability that the WLSR RAIM variable P_{FA} exceeds $5 \cdot 10^{-3}$ ($p\{P_{FA} > 5 \cdot 10^{-3}\}$). Dual constellation GPS & Galileo receivers. RAIM: Fault exclusion (Fault detection in the worst subgroup).

Navigation solution (observation matrix)	GNSS signals	Pseudorange nominal error model	Environment							
			Urban				Rural			
			P_{MD}							
			$5 \cdot 10^{-5}$		10^{-3}		$5 \cdot 10^{-5}$		10^{-3}	
			HAL (m)							
			25	50	25	50	25	50	25	50
3 variables: • 2D position • $T_{rcx}/GNSS$	L1 BOC(1,1) E1 BOC(1,1)	L1/E1	0.999	0.945	0.998	0.922	0.994	0.447	0.974	0.341
		L1/E1 + SBAS	0.800	0.507	0.756	0.458	0.082	0.006	0.055	0.004
		L1/E1 + L5/E5a	0.974	0.827	0.961	0.789	0.746	0.113	0.638	0.073
	L1 TMBOC(6,1,4/33) E1 CBOC(6,1,1/11,+)	L1/E1	0.999	0.939	0.998	0.914	0.991	0.411	0.965	0.307
		L1/E1 + SBAS	0.515	0.275	0.466	0.246	0.006	3.5e-4	0.004	1.9e-4
		L1/E1 + L5/E5a	0.797	0.510	0.754	0.463	0.079	0.006	0.052	0.004
	L1 TMBOC(6,1,4/33) E1 CBOC(6,1,1/11,-)	L1/E1	0.999	0.938	0.998	0.914	0.991	0.409	0.964	0.306
		L1/E1 + SBAS	0.492	0.261	0.443	0.232	0.005	2.7e-4	0.003	1.5e-4
		L1/E1 + L5/E5a	0.775	0.482	0.729	0.433	0.064	0.005	0.043	0.003
	L5 BPSK(10) E5a BPSK(10)	L5/E5a	1	0.997	1	0.994	1	0.962	1	0.906
		L5/E5a + SBAS	0.428	0.225	0.382	0.201	0.003	1.4e-4	0.002	1.0e-4
4 variables: • 2D position • T_{rcx}/GPS • $T_{rcx}/Galileo$	L1 BOC(1,1) E1 BOC(1,1)	L1/E1	1	0.962	0.999	0.944	0.998	0.553	0.988	0.436
		L1/E1 + SBAS	0.843	0.646	0.815	0.610	0.130	0.018	0.096	0.013
		L1/E1 + L5/E5a	0.980	0.861	0.969	0.834	0.794	0.164	0.695	0.118
	L1 TMBOC(6,1,4/33) E1 CBOC(6,1,1/11,+)	L1/E1	1	0.957	0.999	0.940	0.997	0.518	0.984	0.401
		L1/E1 + SBAS	0.656	0.452	0.621	0.420	0.020	0.002	0.014	0.001
		L1/E1 + L5/E5a	0.840	0.649	0.812	0.613	0.124	0.017	0.090	0.012
	L1 TMBOC(6,1,4/33) E1 CBOC(6,1,1/11,-)	L1/E1	1	0.957	0.999	0.939	0.997	0.516	0.984	0.400
		L1/E1 + SBAS	0.640	0.436	0.604	0.405	0.017	0.001	0.012	0.001
		L1/E1 + L5/E5a	0.826	0.627	0.796	0.591	0.106	0.015	0.079	0.010
	L5 BPSK(10) E5a BPSK(10)	L5/E5a	1	0.999	1	0.997	1	0.983	1	0.947
		L5/E5a + SBAS	0.596	0.398	0.559	0.369	0.011	0.001	0.007	0.001

Table E.4 (b). Unavailability ratio of the WLSR RAIM with a constant $P_{FA} = 5 \cdot 10^{-3}$ ($p\{HPL > HAL\}$). Equivalently, probability that the WLSR RAIM variable P_{FA} exceeds $5 \cdot 10^{-3}$ ($p\{P_{FA} > 5 \cdot 10^{-3}\}$). Dual constellation GPS & Galileo receivers. RAIM: Fault exclusion (Fault detection in the worst subgroup).

Navigation solution (observation matrix)	GNSS signals	Pseudorange nominal error model	Environment							
			Urban				Rural			
			P_{MD}							
			$5 \cdot 10^{-5}$		10^{-3}		$5 \cdot 10^{-5}$		10^{-3}	
			HAL (m)							
			25	50	25	50	25	50	25	50
4 variables: • 3D position • $T_{rcx}/GNSS$	L1 BOC(1,1) E1 BOC(1,1)	L1/E1	1	0.982	0.999	0.972	0.999	0.654	0.994	0.522
		L1/E1 + SBAS	0.904	0.691	0.874	0.651	0.193	0.020	0.140	0.014
		L1/E1 + L5/E5a	0.995	0.923	0.991	0.897	0.906	0.256	0.834	0.182
	L1 TMBOC(6,1,4/33) E1 CBOC(6,1,1/11,+)	L1/E1	1	0.979	0.999	0.967	0.998	0.608	0.991	0.475
		L1/E1 + SBAS	0.698	0.471	0.655	0.437	0.021	0.002	0.014	0.002
		L1/E1 + L5/E5a	0.904	0.696	0.875	0.656	0.196	0.022	0.142	0.015
	L1 TMBOC(6,1,4/33) E1 CBOC(6,1,1/11,-)	L1/E1	1	0.979	0.999	0.967	0.998	0.606	0.991	0.473
		L1/E1 + SBAS	0.677	0.454	0.634	0.422	0.017	0.002	0.012	0.002
		L1/E1 + L5/E5a	0.887	0.672	0.856	0.631	0.161	0.017	0.116	0.012
	L5 BPSK(10) E5a BPSK(10)	L5/E5a	1	0.999	1	0.998	1	0.990	1	0.968
		L5/E5a + SBAS	0.620	0.413	0.580	0.387	0.010	0.001	0.007	0.001
	4 variables: • 3D position • $T_{rcx}/GNSS$ Hybridization external altitude $\sigma_{alt} = 5$ m.	L1 BOC(1,1) E1 BOC(1,1)	L1/E1	0.999	0.948	0.998	0.927	0.995	0.465	0.978
L1/E1 + SBAS			0.814	0.524	0.773	0.476	0.093	0.007	0.063	0.004
L1/E1 + L5/E5a			0.977	0.834	0.964	0.798	0.764	0.123	0.660	0.079
L1 TMBOC(6,1,4/33) E1 CBOC(6,1,1/11,+)		L1/E1	0.999	0.942	0.998	0.919	0.993	0.427	0.970	0.322
		L1/E1 + SBAS	0.545	0.296	0.498	0.266	0.008	4.2e-4	0.005	2.6e-4
		L1/E1 + L5/E5a	0.812	0.527	0.772	0.480	0.090	0.006	0.060	0.004
L1 TMBOC(6,1,4/33) E1 CBOC(6,1,1/11,-)		L1/E1	0.999	0.942	0.998	0.919	0.993	0.425	0.970	0.321
		L1/E1 + SBAS	0.524	0.283	0.477	0.254	0.006	3.3e-4	0.004	2.2e-4
		L1/E1 + L5/E5a	0.793	0.499	0.748	0.452	0.073	0.005	0.049	0.003
L5 BPSK(10) E5a BPSK(10)		L5/E5a	1	0.998	1	0.994	1	0.966	1	0.916
		L5/E5a + SBAS	0.466	0.248	0.419	0.222	0.004	2.1e-4	0.002	1.2e-4

Table E.4 (c). Unavailability ratio of the WLSR RAIM with a constant $P_{FA} = 5 \cdot 10^{-3}$ ($p\{HPL > HAL\}$). Equivalently, probability that the WLSR RAIM variable P_{FA} exceeds $5 \cdot 10^{-3}$ ($p\{P_{FA} > 5 \cdot 10^{-3}\}$). Dual constellation GPS & Galileo receivers. RAIM: Fault exclusion (Fault detection in the worst subgroup).

Navigation solution (observation matrix)	GNSS signals	Pseudorange nominal error model	Environment							
			Urban				Rural			
			P_{MD}							
			$5 \cdot 10^{-5}$		10^{-3}		$5 \cdot 10^{-5}$		10^{-3}	
			HAL (m)							
			25	50	25	50	25	50	25	50
5 variables: • 3D position • T_{rcx}/GPS • $T_{rcx}/Galileo$	L1 BOC(1,1) E1 BOC(1,1)	L1/E1	1	0.989	1	0.982	1	0.759	0.998	0.643
		L1/E1 + SBAS	0.932	0.789	0.911	0.762	0.283	0.054	0.221	0.040
		L1/E1 + L5/E5a	0.996	0.945	0.993	0.927	0.933	0.345	0.873	0.268
	L1 TMBOC(6,1,4/33) E1 CBOC(6,1,1/11,+)	L1/E1	1	0.987	1	0.980	0.999	0.722	0.997	0.603
		L1/E1 + SBAS	0.798	0.639	0.771	0.614	0.057	0.011	0.042	0.009
		L1/E1 + L5/E5a	0.932	0.792	0.912	0.766	0.286	0.055	0.223	0.041
	L1 TMBOC(6,1,4/33) E1 CBOC(6,1,1/11,-)	L1/E1	1	0.987	1	0.980	0.999	0.721	0.997	0.602
		L1/E1 + SBAS	0.784	0.627	0.757	0.602	0.050	0.010	0.037	0.008
		L1/E1 + L5/E5a	0.920	0.775	0.898	0.748	0.247	0.046	0.190	0.034
	L5 BPSK(10) E5a BPSK(10)	L5/E5a	1	1	1	0.999	1	0.997	1	0.987
		L5/E5a + SBAS	0.750	0.595	0.723	0.573	0.034	0.008	0.024	0.006
	5 variables: • 3D position • T_{rcx}/GPS • $T_{rcx}/Galileo$ Hybridization external altitude $\sigma_{alt} = 5$ m.	L1 BOC(1,1) E1 BOC(1,1)	L1/E1	1	0.964	0.999	0.948	0.998	0.571	0.990
L1/E1 + SBAS			0.854	0.660	0.827	0.625	0.144	0.020	0.107	0.014
L1/E1 + L5/E5a			0.982	0.867	0.972	0.840	0.809	0.176	0.714	0.126
L1 TMBOC(6,1,4/33) E1 CBOC(6,1,1/11,+)		L1/E1	1	0.960	0.999	0.943	0.998	0.536	0.987	0.419
		L1/E1 + SBAS	0.681	0.477	0.647	0.447	0.024	0.003	0.018	0.002
		L1/E1 + L5/E5a	0.852	0.662	0.824	0.628	0.139	0.020	0.101	0.014
L1 TMBOC(6,1,4/33) E1 CBOC(6,1,1/11,-)		L1/E1	1	0.960	0.999	0.943	0.998	0.534	0.987	0.418
		L1/E1 + SBAS	0.665	0.463	0.632	0.433	0.021	0.002	0.015	0.001
		L1/E1 + L5/E5a	0.838	0.642	0.810	0.607	0.119	0.017	0.089	0.012
L5 BPSK(10) E5a BPSK(10)		L5/E5a	1	0.999	1	0.997	1	0.986	1	0.954
		L5/E5a + SBAS	0.627	0.431	0.593	0.402	0.014	0.001	0.010	0.001

Table E.5 (a). Unavailability ratio of the WLSR RAIM with a constant $P_{FA} = 5 \cdot 10^{-3}$ ($p\{HPL > HAL\}$). Equivalently, probability that the WLSR RAIM variable P_{FA} exceeds $5 \cdot 10^{-3}$ ($p\{P_{FA} > 5 \cdot 10^{-3}\}$). GPS receivers. RAIM: Fault exclusion (Fault detection in the worst subgroup).

Navigation solution (observation matrix)	GNSS signals	Pseudorange nominal error model	Environment							
			Urban				Rural			
			P_{MD}							
			$5 \cdot 10^{-5}$		10^{-3}		$5 \cdot 10^{-5}$		10^{-3}	
			HAL (m)							
			25	50	25	50	25	50	25	50
3 variables: • 2D position • T_{rcx}/GPS	L1 BPSK(1) (2-sided BW=2 MHz)	L1	1	1	1	1	1	1	1	1
		L1 + SBAS	1	0.998	1	0.997	1	0.988	1	0.976
		L1 + L5	1	1	1	1	1	1	1	1
	L1 BPSK(1) (2-sided BW=20 MHz)	L1	1	1	1	1	1	1	1	1
		L1 + SBAS	0.996	0.968	0.993	0.963	0.955	0.728	0.930	0.695
		L1 + L5	1	0.996	1	0.994	1	0.963	1	0.943
	L1 BOC(1,1)	L1	1	1	1	1	1	1	1	1
		L1 + SBAS	0.997	0.971	0.995	0.967	0.967	0.751	0.947	0.717
		L1 + L5	1	0.997	1	0.996	1	0.977	1	0.957
	L1 TMBOC(6,1,4/33)	L1	1	1	1	1	1	1	1	0.999
		L1 + SBAS	0.974	0.937	0.969	0.930	0.760	0.561	0.722	0.532
		L1 + L5	0.995	0.968	0.992	0.964	0.954	0.730	0.930	0.699
	L5 BPSK(10)	L5	1	1	1	1	1	1	1	1
		L5 + SBAS	0.969	0.929	0.963	0.921	0.718	0.526	0.673	0.500

Table E.5 (b). Unavailability ratio of the WLSR RAIM with a constant $P_{FA} = 5 \cdot 10^{-3}$ ($p\{HPL > HAL\}$). Equivalently, probability that the WLSR RAIM variable P_{FA} exceeds $5 \cdot 10^{-3}$ ($p\{P_{FA} > 5 \cdot 10^{-3}\}$). GPS receivers. RAIM: Fault exclusion (Fault detection in the worst subgroup).

Navigation solution (observation matrix)	GNSS signals	Pseudorange nominal error model	Environment							
			Urban				Rural			
			P_{MD}							
			$5 \cdot 10^{-5}$		10^{-3}		$5 \cdot 10^{-5}$		10^{-3}	
			HAL (m)							
			25	50	25	50	25	50	25	50
4 variables: • 3D position • T_{rcx}/GPS	L1 BPSK(1) (2-sided BW=2 MHz)	L1	1	1	1	1	1	1	1	1
		L1 + SBAS	1	1	1	1	1	0.999	1	0.998
		L1 + L5	1	1	1	1	1	1	1	1
	L1 BPSK(1) (2-sided BW=20 MHz)	L1	1	1	1	1	1	1	1	1
		L1 + SBAS	0.999	0.994	0.999	0.993	0.995	0.917	0.989	0.897
		L1 + L5	1	1	1	0.999	1	0.997	1	0.992
	L1 BOC(1,1)	L1	1	1	1	1	1	1	1	1
		L1 + SBAS	1	0.995	0.999	0.993	0.997	0.928	0.993	0.911
		L1 + L5	1	1	1	0.999	1	0.998	1	0.996
	L1 TMBOC(6,1,4/33)	L1	1	1	1	1	1	1	1	1
		L1 + SBAS	0.995	0.988	0.994	0.986	0.931	0.848	0.913	0.832
		L1 + L5	0.999	0.994	0.999	0.992	0.995	0.917	0.989	0.898
	L5 BPSK(10)	L5	1	1	1	1	1	1	1	1
		L5 + SBAS	0.994	0.987	0.993	0.985	0.912	0.831	0.899	0.815

Table E.5 (c). Unavailability ratio of the WLSR RAIM with a constant $P_{FA} = 5 \cdot 10^{-3}$ ($p\{HPL > HAL\}$). Equivalently, probability that the WLSR RAIM variable P_{FA} exceeds $5 \cdot 10^{-3}$ ($p\{P_{FA} > 5 \cdot 10^{-3}\}$). GPS receivers. RAIM: Fault exclusion (Fault detection in the worst subgroup).

Navigation solution (observation matrix)	GNSS signals	Pseudorange nominal error model	Environment							
			Urban				Rural			
			P_{MD}							
			$5 \cdot 10^{-5}$		10^{-3}		$5 \cdot 10^{-5}$		10^{-3}	
			HAL (m)							
			25	50	25	50	25	50	25	50
4 variables: • 3D position • T_{rcx}/GPS Hybridization external altitude $\sigma_{alt} = 5$ m.	L1 BPSK(1) (2-sided BW=2 MHz)	L1	1	1	1	1	1	1	1	1
		L1 + SBAS	1	0.999	1	0.998	1	0.991	1	0.979
		L1 + L5	1	1	1	1	1	1	1	1
	L1 BPSK(1) (2-sided BW=20 MHz)	L1	1	1	1	1	1	1	1	1
		L1 + SBAS	0.997	0.971	0.995	0.967	0.966	0.746	0.947	0.715
		L1 + L5	1	0.997	1	0.995	1	0.970	1	0.950
	L1 BOC(1,1)	L1	1	1	1	1	1	1	1	1
		L1 + SBAS	0.997	0.974	0.996	0.969	0.974	0.768	0.960	0.735
		L1 + L5	1	0.998	1	0.996	1	0.980	1	0.964
	L1 TMBOC(6,1,4/33)	L1	1	1	1	1	1	1	1	1
		L1 + SBAS	0.981	0.946	0.975	0.939	0.803	0.597	0.757	0.565
		L1 + L5	0.996	0.971	0.995	0.967	0.964	0.748	0.946	0.717
	L5 BPSK(10)	L5	1	1	1	1	1	1	1	1
		L5 + SBAS	0.977	0.940	0.971	0.933	0.763	0.567	0.727	0.540

Table E.6 (a). Unavailability ratio of the WLSR RAIM with a constant $P_{FA} = 5 \cdot 10^{-3}$ ($p\{HPL > HAL\}$). Equivalently, probability that the WLSR RAIM variable P_{FA} exceeds $5 \cdot 10^{-3}$ ($p\{P_{FA} > 5 \cdot 10^{-3}\}$). Galileo receivers. RAIM: Fault exclusion (Fault detection in the worst subgroup).

Navigation solution (observation matrix)	GNSS signals	Pseudorange nominal error model	Environment							
			Urban				Rural			
			P_{MD}							
			$5 \cdot 10^{-5}$		10^{-3}		$5 \cdot 10^{-5}$		10^{-3}	
			HAL (m)							
			25	50	25	50	25	50	25	50
3 variables: • 2D position • $T_{rcx}/Galileo$	E1 BOC(1.1)	E1	1	1	1	0.999	1	0.999	1	0.993
		E1 + SBAS	0.987	0.959	0.982	0.951	0.893	0.724	0.836	0.695
		E1 + E5a	1	0.990	0.999	0.983	0.997	0.922	0.997	0.858
	E1 CBOC(6.1.1/11.+)	E1	1	1	1	0.999	1	0.999	1	0.990
		E1 + SBAS	0.966	0.916	0.959	0.906	0.754	0.530	0.718	0.479
		E1 + E5a	0.988	0.962	0.983	0.954	0.914	0.739	0.846	0.708
	E1 CBOC(6.1.1/11.-)	E1	1	1	1	0.999	1	0.999	1	0.990
		E1 + SBAS	0.961	0.908	0.954	0.898	0.726	0.489	0.695	0.442
		E1 + E5a	0.983	0.954	0.978	0.946	0.843	0.707	0.806	0.678
	E5a BPSK(10)	E5a	1	1	1	1	1	1	1	1
E5a + SBAS		0.954	0.897	0.946	0.886	0.690	0.431	0.661	0.394	
4 variables: • 3D position • $T_{rcx}/Galileo$	E1 BOC(1.1)	E1	1	1	1	1	1	1	1	0.998
		E1 + SBAS	0.997	0.982	0.996	0.977	0.972	0.798	0.945	0.757
		E1 + E5a	1	0.998	1	0.997	1	0.980	0.999	0.962
	E1 CBOC(6.1.1/11.+)	E1	1	1	1	1	1	0.999	1	0.998
		E1 + SBAS	0.987	0.960	0.982	0.956	0.825	0.663	0.787	0.646
		E1 + E5a	0.998	0.984	0.996	0.980	0.976	0.817	0.955	0.777
	E1 CBOC(6.1.1/11.-)	E1	1	1	1	1	1	0.999	1	0.998
		E1 + SBAS	0.984	0.957	0.979	0.954	0.796	0.651	0.758	0.634
		E1 + E5a	0.996	0.979	0.994	0.973	0.954	0.776	0.918	0.734
	E5a BPSK(10)	E5a	1	1	1	1	1	1	1	1
E5a + SBAS		0.979	0.954	0.974	0.950	0.754	0.631	0.721	0.614	

Table E.6 (b). Unavailability ratio of the WLSR RAIM with a constant $P_{FA} = 5 \cdot 10^{-3}$ ($p\{HPL > HAL\}$). Equivalently, probability that the WLSR RAIM variable P_{FA} exceeds $5 \cdot 10^{-3}$ ($p\{P_{FA} > 5 \cdot 10^{-3}\}$). Galileo receivers. RAIM: Fault exclusion (Fault detection in the worst subgroup).

Navigation solution (observation matrix)	GNSS signals	Pseudorange nominal error model	Environment							
			Urban				Rural			
			P _{MD}							
			5 · 10 ⁻⁵		10 ⁻³		5 · 10 ⁻⁵		10 ⁻³	
			HAL (m)							
			25	50	25	50	25	50	25	50
4 variables: • 3D position • T _{rcx} /Galileo Hybridization external altitude σ _{alt} = 5 m	E1 BOC(1.1)	E1	1	1	1	1	1	0.999	1	0.995
		E1 + SBAS	0.989	0.962	0.984	0.955	0.916	0.737	0.853	0.707
		E1 + E5a	1	0.991	1	0.985	0.998	0.928	0.997	0.876
	E1 CBOC(6.1.1/11.+)	E1	1	1	1	0.999	1	0.999	1	0.992
		E1 + SBAS	0.970	0.924	0.964	0.914	0.769	0.564	0.740	0.519
		E1 + E5a	0.990	0.964	0.985	0.957	0.925	0.749	0.868	0.719
	E1 CBOC(6.1.1/11.-)	E1	1	1	1	0.999	1	0.999	1	0.992
		E1 + SBAS	0.966	0.917	0.960	0.908	0.750	0.530	0.716	0.486
		E1 + E5a	0.985	0.957	0.980	0.950	0.866	0.719	0.822	0.692
E5a BPSK(10)	E5a	1	1	1	1	1	1	1	1	
	E5a + SBAS	0.960	0.907	0.954	0.899	0.712	0.479	0.684	0.440	

Appendix F

Simulation Results (II): Missed Road Segment Rate

F.1. Minimum trajectory duration

The following tables contain, for all receiver configurations under study, the minimum duration (T_{\min}) of a user trajectory through a geo-object in the fault-free case described in section 5.4.4.2.1, from which the required probability of missed road segment recognition with $N_{Th} = 1$ is met, i.e. $p\{N_{\text{valid pos IN}} = 0 \mid T \geq T_{\min}\} \leq 5 \cdot 10^{-5}$, where T is the total trajectory duration.

- Table F.1. - Minimum trajectory duration for dual constellation GPS & Galileo users.
- Table F.2. - Minimum trajectory duration for GPS users.
- Table F.3. - Minimum trajectory duration for Galileo users.

Table F.1(a). Minimum user trajectory duration through a geo-object T_{\min} (seconds) from which the required probability of missed road segment recognition with $N_{Th} = 1$ is met, i.e. $p\{N_{\text{valid pos IN}} = 0 \mid T \geq T_{\min}\} \leq 5 \cdot 10^{-5}$. Red crosses indicate $T_{\min} > 40$ seconds. Fault free case. Dual constellation GPS & Galileo users.

Navigation solution (observation matrix)	GNSS signals	Pseudorange nominal error model	WLSR RAIM															
			Civil aviation ($P_{FA} = 5 \cdot 10^{-3}$)								Variable P_{FA} (HPL = HAL)							
			Environment															
			Urban				Rural				Urban				Rural			
			P_{MD}															
			$5 \cdot 10^{-5}$		10^{-3}		$5 \cdot 10^{-5}$		10^{-3}		$5 \cdot 10^{-5}$		10^{-3}		$5 \cdot 10^{-5}$		10^{-3}	
			HAL (m)															
			25	50	25	50	25	50	25	50	25	50	25	50	25	50	25	50
3 variables: • 2D position • $T_{rcx}/GNSS$	L1 BOC(1,1) E1 BOC(1,1)	L1/E1	x	x	x	x	x	16	x	14	x	x	x	40	25	7	18	6
		L1/E1 + SBAS	x	17	x	16	7	2	5	2	25	14	18	13	4	1	3	1
		L1/E1 + L5/E5a	x	x	x	x	23	7	19	6	x	29	x	20	11	5	8	4
	L1 TMBOC(6,1,4/33) E1 CBOC(6,1,1/11,+)	L1/E1	x	x	x	x	x	15	x	13	x	x	x	36	24	7	17	5
		L1/E1 + SBAS	18	13	16	12	2	2	2	2	14	10	13	10	1	1	1	1
		L1/E1 + L5/E5a	x	17	x	16	6	2	5	2	25	14	19	13	4	1	3	1
	L1 TMBOC(6,1,4/33) E1 CBOC(6,1,1/11,-)	L1/E1	x	x	x	x	x	15	x	13	x	x	x	36	24	7	17	5
		L1/E1 + SBAS	17	12	16	11	2	2	2	2	14	10	13	10	1	1	1	1
		L1/E1 + L5/E5a	x	16	x	15	5	2	5	2	22	14	17	12	4	1	3	1
	L5 BPSK(10) E5a BPSK(10)	L5/E5a	x	x	x	x	x	x	x	x	x	x	x	x	x	20	x	14
L5/E5a + SBAS		16	11	15	10	2	2	2	2	13	10	11	10	1	1	1	1	
4 variables: • 2D position • T_{rcx}/GPS • $T_{rcx}/Galileo$	L1 BOC(1,1) E1 BOC(1,1)	L1/E1	x	x	x	x	x	18	x	14	x	x	x	x	32	9	19	7
		L1/E1 + SBAS	x	24	x	23	8	4	7	4	37	17	26	16	5	2	4	2
		L1/E1 + L5/E5a	x	x	x	x	26	8	22	7	x	x	x	27	12	5	9	4
	L1 TMBOC(6,1,4/33) E1 CBOC(6,1,1/11,+)	L1/E1	x	x	x	x	x	17	x	14	x	x	x	x	29	8	18	7
		L1/E1 + SBAS	25	15	23	15	4	2	4	2	17	14	16	14	2	1	2	1
		L1/E1 + L5/E5a	x	24	x	21	7	4	6	3	35	17	26	16	5	2	4	2
	L1 TMBOC(6,1,4/33) E1 CBOC(6,1,1/11,-)	L1/E1	x	x	x	x	x	17	x	14	x	x	x	x	29	8	18	7
		L1/E1 + SBAS	24	15	22	15	4	2	4	2	17	14	16	14	2	1	2	1
		L1/E1 + L5/E5a	x	24	x	20	7	4	6	3	30	16	24	15	5	2	4	2
	L5 BPSK(10) E5a BPSK(10)	L5/E5a	x	x	x	x	x	x	x	x	x	x	x	x	x	21	x	15
		L5/E5a + SBAS	22	15	19	14	4	2	3	2	16	14	15	14	2	1	1	1

Table F.1(b). Minimum user trajectory duration through a geo-object T_{\min} (seconds) from which the required probability of missed road segment recognition with $N_{Th} = 1$ is met, i.e. $p\{N_{\text{valid pos IN}} = 0 \mid T \geq T_{\min}\} \leq 5 \cdot 10^{-5}$. Red crosses indicate $T_{\min} > 40$ seconds. Fault-free case. Dual constellation GPS & Galileo users.

Navigation solution (observation matrix)	GNSS signals	Pseudorange nominal error model	WLSR RAIM															
			Civil aviation ($P_{FA} = 5 \cdot 10^{-3}$)								Variable P_{FA} (HPL = HAL)							
			Environment															
			Urban				Rural				Urban				Rural			
			P_{MD}															
			$5 \cdot 10^{-5}$		10^{-3}		$5 \cdot 10^{-5}$		10^{-3}		$5 \cdot 10^{-5}$		10^{-3}		$5 \cdot 10^{-5}$		10^{-3}	
			HAL (m)															
			25	50	25	50	25	50	25	50	25	50	25	50	25	50	25	50
4 variables: • 3D position • $T_{rcx}/GNSS$	L1 BOC(1,1) E1 BOC(1,1)	L1/E1	x	x	x	x	x	20	x	17	x	x	x	x	x	10	23	7
		L1/E1 + SBAS	x	29	x	26	9	3	8	3	x	22	31	20	5	2	4	2
		L1/E1 + L5/E5a	x	x	x	x	x	10	28	8	x	x	x	36	15	5	12	4
	L1 TMBOC(6,1,4/33) E1 CBOC(6,1,1/11,+)	L1/E1	x	x	x	x	x	18	x	17	x	x	x	x	x	9	22	6
		L1/E1 + SBAS	28	19	28	19	3	2	3	2	22	16	20	15	2	1	2	1
		L1/E1 + L5/E5a	x	29	x	26	8	3	8	3	x	22	32	20	5	2	4	2
	L1 TMBOC(6,1,4/33) E1 CBOC(6,1,1/11,-)	L1/E1	x	x	x	x	x	18	x	17	x	x	x	x	x	9	22	6
		L1/E1 + SBAS	28	19	24	19	3	2	3	2	21	16	19	15	2	1	2	1
		L1/E1 + L5/E5a	x	28	x	24	8	3	7	3	39	21	29	19	5	2	4	2
	L5 BPSK(10) E5a BPSK(10)	L5/E5a	x	x	x	x	x	x	x	x	x	x	x	x	x	27	x	17
L5/E5a + SBAS		23	19	22	17	2	2	2	2	20	15	18	14	2	1	1	1	
4 variables: • 3D position • $T_{rcx}/GNSS$ Hybridization external altitude $\sigma_{alt} = 5$ m.	L1 BOC(1,1) E1 BOC(1,1)	L1/E1	x	x	x	x	x	17	x	14	x	x	x	x	26	8	18	6
		L1/E1 + SBAS	x	20	x	17	8	3	6	2	29	15	21	13	5	1	4	1
		L1/E1 + L5/E5a	x	x	x	x	25	8	20	6	x	30	x	21	12	5	9	4
	L1 TMBOC(6,1,4/33) E1 CBOC(6,1,1/11,+)	L1/E1	x	x	x	x	x	16	x	14	x	x	x	37	24	7	18	5
		L1/E1 + SBAS	23	14	20	13	3	2	2	2	16	11	14	10	1	1	1	1
		L1/E1 + L5/E5a	x	20	x	17	7	3	6	2	28	15	21	13	4	1	4	1
	L1 TMBOC(6,1,4/33) E1 CBOC(6,1,1/11,-)	L1/E1	x	x	x	x	x	16	x	14	x	x	x	37	24	7	18	5
		L1/E1 + SBAS	21	14	19	12	2	2	2	2	16	11	14	10	1	1	1	1
		L1/E1 + L5/E5a	x	18	x	16	7	2	6	2	26	14	19	13	4	1	3	1
	L5 BPSK(10) E5a BPSK(10)	L5/E5a	x	x	x	x	x	x	x	x	x	x	x	x	x	20	x	15
		L5/E5a + SBAS	19	12	18	11	2	2	2	2	15	10	13	10	1	1	1	1

Table F.1(c). Minimum user trajectory duration through a geo-object T_{\min} (seconds) from which the required probability of missed road segment recognition with $N_{Th} = 1$ is met, i.e. $p\{N_{\text{valid pos IN}} = 0 \mid T \geq T_{\min}\} \leq 5 \cdot 10^{-5}$. Red crosses indicate $T_{\min} > 40$ seconds. Fault-free case. Dual constellation GPS & Galileo users.

Navigation solution (observation matrix)	GNSS signals	Pseudorange nominal error model	WLSR RAIM															
			Civil aviation ($P_{FA} = 5 \cdot 10^{-3}$)								Variable P_{FA} (HPL = HAL)							
			Environment															
			Urban				Rural				Urban				Rural			
			P_{MD}															
			$5 \cdot 10^{-5}$		10^{-3}		$5 \cdot 10^{-5}$		10^{-3}		$5 \cdot 10^{-5}$		10^{-3}		$5 \cdot 10^{-5}$		10^{-3}	
			HAL (m)															
			25	50	25	50	25	50	25	50	25	50	25	50	25	50	25	50
5 variables: • 3D position • T_{rcx}/GPS • $T_{rcx}/Galileo$	L1 BOC(1,1) E1 BOC(1,1)	L1/E1	x	x	x	x	x	23	x	18	x	x	x	x	x	12	27	9
		L1/E1 + SBAS	x	x	x	34	10	5	9	4	x	28	x	24	6	4	5	3
		L1/E1 + L5/E5a	x	x	x	x	x	11	40	10	x	x	x	x	16	7	12	5
	L1 TMBOC(6,1,4/33) E1 CBOC(6,1,1/11,+)	L1/E1	x	x	x	x	x	22	x	18	x	x	x	x	x	11	25	9
		L1/E1 + SBAS	x	24	31	22	6	3	5	3	28	20	24	19	4	2	3	2
		L1/E1 + L5/E5a	x	x	x	34	10	5	8	4	x	28	x	24	6	4	5	3
	L1 TMBOC(6,1,4/33) E1 CBOC(6,1,1/11,-)	L1/E1	x	x	x	x	x	22	x	18	x	x	x	x	x	11	25	9
		L1/E1 + SBAS	x	22	31	21	5	3	4	3	27	19	23	19	4	2	3	2
		L1/E1 + L5/E5a	x	40	x	31	10	5	8	4	x	27	x	23	6	3	5	3
	L5 BPSK(10) E5a BPSK(10)	L5/E5a	x	x	x	x	x	x	x	x	x	x	x	x	x	32	x	19
L5/E5a + SBAS		31	21	30	20	4	3	4	3	24	19	22	18	3	2	3	2	
5 variables: • 3D position • T_{rcx}/GPS • $T_{rcx}/Galileo$ Hybridization external altitude $\sigma_{alt} = 5$ m.	L1 BOC(1,1) E1 BOC(1,1)	L1/E1	x	x	x	x	x	18	x	15	x	x	x	x	35	9	20	7
		L1/E1 + SBAS	x	26	x	25	9	4	8	4	x	18	29	16	6	2	4	2
		L1/E1 + L5/E5a	x	x	x	x	29	8	23	7	x	x	x	29	13	5	10	5
	L1 TMBOC(6,1,4/33) E1 CBOC(6,1,1/11,+)	L1/E1	x	x	x	x	x	18	x	15	x	x	x	x	31	9	19	7
		L1/E1 + SBAS	36	17	27	16	5	3	4	2	20	15	18	15	3	1	2	1
		L1/E1 + L5/E5a	x	26	x	25	8	4	7	3	x	18	29	16	5	2	4	2
	L1 TMBOC(6,1,4/33) E1 CBOC(6,1,1/11,-)	L1/E1	x	x	x	x	x	18	x	15	x	x	x	x	31	9	19	7
		L1/E1 + SBAS	30	17	27	16	5	2	4	2	19	15	17	15	3	1	2	1
		L1/E1 + L5/E5a	x	25	x	21	8	4	7	3	x	17	27	16	5	2	4	2
	L5 BPSK(10) E5a BPSK(10)	L5/E5a	x	x	x	x	x	x	x	x	x	x	x	x	x	22	x	16
L5/E5a + SBAS		29	16	26	16	4	2	3	2	18	15	17	15	2	1	2	1	

Table F.2(a). Minimum user trajectory duration through a geo-object T_{\min} (seconds) from which the required probability of missed road segment recognition with $N_{Th} = 1$ is met, i.e. $p\{N_{\text{valid pos IN}} = 0 \mid T \geq T_{\min}\} \leq 5 \cdot 10^{-5}$. Red crosses indicate $T_{\min} > 40$ seconds. Fault-free case. GPS users.

Navigation solution (observation matrix)	GNSS signals	Pseudorange nominal error model	WLSR RAIM															
			Civil aviation ($P_{FA} = 5 \cdot 10^{-3}$)								Variable P_{FA} (HPL = HAL)							
			Environment															
			Urban				Rural				Urban				Rural			
			P_{MD}															
			$5 \cdot 10^{-5}$		10^{-3}		$5 \cdot 10^{-5}$		10^{-3}		$5 \cdot 10^{-5}$		10^{-3}		$5 \cdot 10^{-5}$		10^{-3}	
			HAL (m)															
			25	50	25	50	25	50	25	50	25	50	25	50	25	50	25	50
3 variables: • 2D position • T_{rcx}/GPS	L1 BPSK(1) (2-sided BW=2 MHz)	L1	x	x	x	x	x	x	x	x	x	x	x	x	x	x	x	x
		L1 + SBAS	x	x	x	x	x	x	x	x	x	x	x	x	x	x	x	28
		L1 + L5	x	x	x	x	x	x	x	x	x	x	x	x	x	x	x	x
	L1 BPSK(1) (2-sided BW=20 MHz)	L1	x	x	x	x	x	x	x	x	x	x	x	x	x	x	x	x
		L1 + SBAS	x	x	x	x	x	25	x	24	x	x	x	x	28	22	25	21
		L1 + L5	x	x	x	x	x	x	x	x	x	x	x	x	x	28	x	26
	L1 BOC(1,1)	L1	x	x	x	x	x	x	x	x	x	x	x	x	x	x	x	x
		L1 + SBAS	x	x	x	x	x	27	x	24	x	x	x	x	29	22	26	21
		L1 + L5	x	x	x	x	x	x	x	x	x	x	x	x	x	31	x	27
	L1 TMBOC(6,1,4/33)	L1	x	x	x	x	x	x	x	x	x	x	x	x	x	x	x	x
		L1 + SBAS	x	x	x	x	28	22	25	21	x	x	x	x	23	19	22	18
		L1 + L5	x	x	x	x	x	24	x	24	x	x	x	x	28	22	25	21
L5 BPSK(10)	L5	x	x	x	x	x	x	x	x	x	x	x	x	x	x	x	x	
	L5 + SBAS	x	x	x	x	25	21	24	21	x	x	x	x	22	19	21	18	

Table F.2(b). Minimum user trajectory duration through a geo-object T_{\min} (seconds) from which the required probability of missed road segment recognition with $N_{Th} = 1$ is met, i.e. $p\{N_{\text{valid pos IN}} = 0 \mid T \geq T_{\min}\} \leq 5 \cdot 10^{-5}$. Red crosses indicate $T_{\min} > 40$ seconds. Fault-free case. GPS users.

[illegible]

Table F.2(c). Minimum user trajectory duration through a geo-object T_{\min} (seconds) from which the required probability of missed road segment recognition with $N_{Th} = 1$ is met, i.e. $p\{N_{\text{valid pos IN}} = 0 \mid T \geq T_{\min}\} \leq 5 \cdot 10^{-5}$. Red crosses indicate $T_{\min} > 40$ seconds. Fault-free case. GPS users.

Navigation solution (observation matrix)	GNSS signals	Pseudorange nominal error model	WLSR RAIM															
			Civil aviation ($P_{FA} = 5 \cdot 10^{-3}$)								Variable P_{FA} (HPL = HAL)							
			Environment															
			Urban				Rural				Urban				Rural			
			P_{MD}															
			$5 \cdot 10^{-5}$		10^{-3}		$5 \cdot 10^{-5}$		10^{-3}		$5 \cdot 10^{-5}$		10^{-3}		$5 \cdot 10^{-5}$		10^{-3}	
			HAL (m)															
			25	50	25	50	25	50	25	50	25	50	25	50	25	50	25	50
4 variables: • 3D position • T_{rcx}/GPS Hybridization external altitude $\sigma_{alt} = 5$ m.	L1 BPSK(1) (2-sided BW=2 MHz)	L1	x	x	x	x	x	x	x	x	x	x	x	x	x	x	x	x
		L1 + SBAS	x	x	x	x	x	x	x	x	x	x	x	x	x	x	x	29
		L1 + L5	x	x	x	x	x	x	x	x	x	x	x	x	x	x	x	x
	L1 BPSK(1) (2-sided BW=20 MHz)	L1	x	x	x	x	x	x	x	x	x	x	x	x	x	x	x	x
		L1 + SBAS	x	x	x	x	x	28	x	28	x	x	x	x	x	23	28	22
		L1 + L5	x	x	x	x	x	x	x	x	x	x	x	x	x	29	x	27
	L1 BOC(1,1)	L1	x	x	x	x	x	x	x	x	x	x	x	x	x	x	x	x
		L1 + SBAS	x	x	x	x	x	28	x	28	x	x	x	x	x	23	29	22
		L1 + L5	x	x	x	x	x	x	x	x	x	x	x	x	x	34	x	28
	L1 TMBOC(6,1,4/33)	L1	x	x	x	x	x	x	x	x	x	x	x	x	x	x	x	x
		L1 + SBAS	x	x	x	x	x	24	x	23	x	x	x	x	27	21	23	19
		L1 + L5	x	x	x	x	x	28	x	28	x	x	x	x	x	23	28	22
	L5 BPSK(10)	L5	x	x	x	x	x	x	x	x	x	x	x	x	x	x	x	x
		L5 + SBAS	x	x	x	x	x	23	x	23	x	x	x	x	25	20	23	19

Table F.3(a). Minimum user trajectory duration through a geo-object T_{\min} (seconds) from which the required probability of missed road segment recognition with $N_{Th} = 1$ is met, i.e. $p\{N_{\text{valid pos IN}} = 0 \mid T \geq T_{\min}\} \leq 5 \cdot 10^{-5}$. Red crosses indicate $T_{\min} > 40$ seconds. Fault-free case. Galileo users.

Navigation solution (observation matrix)	GNSS signals	Pseudorange nominal error model	WLSR RAIM															
			Civil aviation ($P_{FA} = 5 \cdot 10^{-3}$)								Variable P_{FA} (HPL = HAL)							
			Environment															
			Urban				Rural				Urban				Rural			
			P_{MD}															
			$5 \cdot 10^{-5}$		10^{-3}		$5 \cdot 10^{-5}$		10^{-3}		$5 \cdot 10^{-5}$		10^{-3}		$5 \cdot 10^{-5}$		10^{-3}	
			HAL (m)															
			25	50	25	50	25	50	25	50	25	50	25	50	25	50	25	50
3 variables: • 2D position • $T_{rcx}/Galileo$	E1 BOC(1,1)	E1	x	x	x	x	x	x	x	x	x	x	x	x	x	x	x	x
		E1 + SBAS	x	x	x	x	x	25	30	25	x	x	x	x	25	16	23	13
		E1 + E5a	x	x	x	x	x	x	x	35	x	x	x	x	x	26	x	23
	E1 CBOC(6,1,1/11,+)	E1	x	x	x	x	x	x	x	x	x	x	x	x	x	x	x	x
		E1 + SBAS	x	x	x	x	25	15	25	15	x	x	x	x	18	10	15	9
		E1 + E5a	x	x	x	x	x	25	33	25	x	x	x	x	26	16	23	14
	E1 CBOC(6,1,1/11,-)	E1	x	x	x	x	x	x	x	x	x	x	x	x	x	x	x	x
		E1 + SBAS	x	x	x	x	25	15	25	14	x	x	x	x	17	10	14	8
		E1 + E5a	x	x	x	x	33	25	30	21	x	x	x	x	25	15	22	12
	E5a BPSK(10)	E5a	x	x	x	x	x	x	x	x	x	x	x	x	x	x	x	x
		E5a + SBAS	x	x	x	x	20	14	19	11	x	x	x	x	15	9	12	8
	4 variables: • 3D position • $T_{rcx}/Galileo$	E1 BOC(1,1)	E1	x	x	x	x	x	x	x	x	x	x	x	x	x	x	x
E1 + SBAS			x	x	x	x	x	26	x	25	x	x	x	x	30	23	26	22
E1 + E5a			x	x	x	x	x	x	x	x	x	x	x	x	x	34	x	27
E1 CBOC(6,1,1/11,+)		E1	x	x	x	x	x	x	x	x	x	x	x	x	x	x	x	x
		E1 + SBAS	x	x	x	x	27	22	26	22	x	x	x	x	23	19	22	19
		E1 + E5a	x	x	x	x	x	26	x	26	x	x	x	x	32	23	27	22
E1 CBOC(6,1,1/11,-)		E1	x	x	x	x	x	x	x	x	x	x	x	x	x	x	x	x
		E1 + SBAS	x	x	x	x	26	22	24	21	x	x	x	x	22	19	21	18
		E1 + E5a	x	x	x	x	x	26	x	25	x	x	x	x	28	22	25	22
E5a BPSK(10)		E5a	x	x	x	x	x	x	x	x	x	x	x	x	x	x	x	x
		E5a + SBAS	x	x	x	x	24	21	23	20	x	x	x	x	22	19	20	18

Table F.3(b). Minimum user trajectory duration through a geo-object T_{\min} (seconds) from which the required probability of missed road segment recognition with $N_{Th} = 1$ is met, i.e. $p\{N_{\text{valid pos IN}} = 0 \mid T \geq T_{\min}\} \leq 5 \cdot 10^{-5}$. Red crosses indicate $T_{\min} > 40$ seconds. Fault-free case. Galileo users.

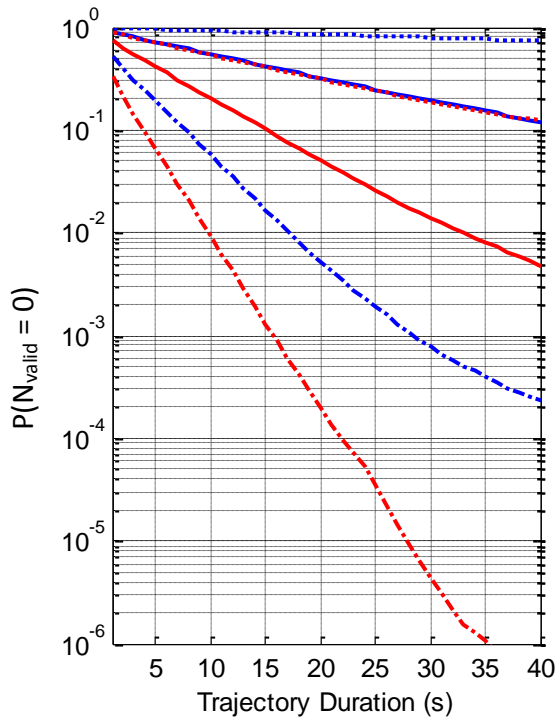
Navigation solution (observation matrix)	GNSS signals	Pseudorange nominal error model	Environment															
			Rural															
			WLSR RAIM															
			Civil aviation ($P_{FA} = 5 \cdot 10^{-3}$)								Variable P_{FA} (HPL = HAL)							
			Failure case															
			Fault-free (FD)				Faulty (FDE)				Fault-free (FD)				Faulty (FDE)			
			P_{MD}															
			$5 \cdot 10^{-5}$		10^{-3}		$5 \cdot 10^{-5}$		10^{-3}		$5 \cdot 10^{-5}$		10^{-3}		$5 \cdot 10^{-5}$		10^{-3}	
			HAL (m)															
			25	50	25	50	25	50	25	50	25	50	25	50	25	50	25	50
4 variables: • 3D position • $T_{rcx}/Galileo$ Hybridization external altitude $\sigma_{alt} = 5$ m.	E1 BOC(1,1)	E1	x	x	x	x	x	x	x	x	x	x	x	x	x	x	x	
		E1 + SBAS	x	x	x	x	x	25	x	25	x	x	x	x	27	19	24	18
		E1 + E5a	x	x	x	x	x	x	x	x	x	x	x	x	x	26	x	24
	E1 CBOC(6,1,1/11,+)	E1	x	x	x	x	x	x	x	x	x	x	x	x	x	x	x	x
		E1 + SBAS	x	x	x	x	27	19	26	19	x	x	x	x	19	18	18	15
		E1 + E5a	x	x	x	x	x	25	x	25	x	x	x	x	28	19	24	18
	E1 CBOC(6,1,1/11,-)	E1	x	x	x	x	x	x	x	x	x	x	x	x	x	x	x	x
		E1 + SBAS	x	x	x	x	26	19	25	18	x	x	x	x	19	17	18	15
		E1 + E5a	x	x	x	x	x	25	x	25	x	x	x	x	26	19	23	17
	E5a BPSK(10)	E5a	x	x	x	x	x	x	x	x	x	x	x	x	x	x	x	x
E5a + SBAS		x	x	x	x	23	18	21	18	x	x	x	x	19	17	18	14	

F.2. Probability of zero valid positions

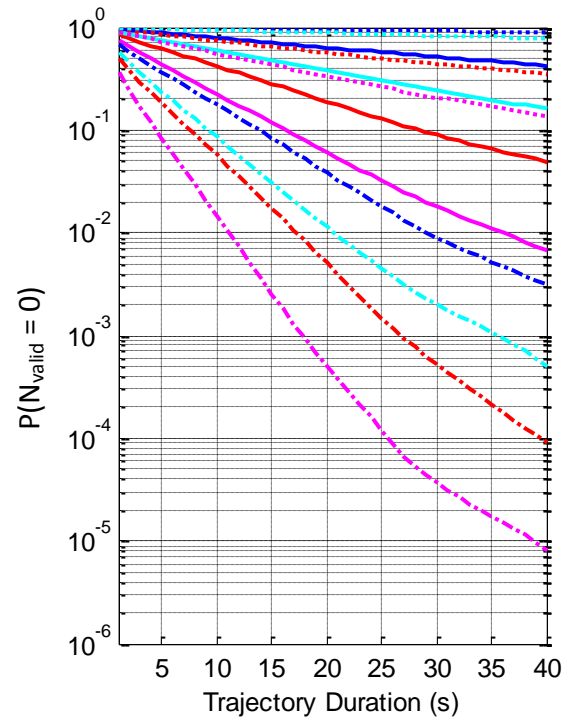
The following figures depict the evolution of the average probability of having zero valid positions during the trajectory of a user along a geo-object (and thus fail to recognize the corresponding road segment) as a function of the trajectory duration. All dual constellation GPS & Galileo receivers under study are analyzed in the fault-free case described in section 5.4.4.2.1 with $P_{MD} = 5 \cdot 10^{-5}$, $P_{FA} = 5 \cdot 10^{-3}$ and HAL equal to 25 and 50 meters:

- Figure F.1. - Average probability of $N_{\text{valid pos IN}} = 0$ for L1/E1 BOC(1,1) - iono-free with L5/E5a BPSK(10) - users with HAL=25 m. in urban environments.
- Figure F.2. - Average probability of $N_{\text{valid pos IN}} = 0$ for L1/E1 BOC(1,1) - iono-free with L5/E5a BPSK(10) - users with HAL=50 m. in urban environments.
- Figure F.3. - Average probability of $N_{\text{valid pos IN}} = 0$ for L1 TMBOC(6,1,4/33) & E1 CBOC(6,1,1/11,+) - iono-free with L5/E5a BPSK(10) - users with HAL=25 m. in urban environments.
- Figure F.4. - Average probability of $N_{\text{valid pos IN}} = 0$ for L1 TMBOC(6,1,4/33) & E1 CBOC(6,1,1/11,+) - iono-free with L5/E5a BPSK(10) - users with HAL=50 m. in urban environments.
- Figure F.5. - Average probability of $N_{\text{valid pos IN}} = 0$ for L1 TMBOC(6,1,4/33) & E1 CBOC(6,1,1/11,-) - iono-free with L5/E5a BPSK(10) - users with HAL=25 m. in urban environments.
- Figure F.6. - Average probability of $N_{\text{valid pos IN}} = 0$ for L1 TMBOC(6,1,4/33) & E1 CBOC(6,1,1/11,-) - iono-free with L5/E5a BPSK(10) - users with HAL=50 m. in urban environments.
- Figure F.7. - Average probability of $N_{\text{valid pos IN}} = 0$ for L5/E5a BPSK(10) users with HAL=25 m. in urban environments.
- Figure F.8. - Average probability of $N_{\text{valid pos IN}} = 0$ for L5/E5a BPSK(10) users with HAL=50 m. in urban environments.
- Figure F.9. - Average probability of $N_{\text{valid pos IN}} = 0$ for L1/E1 BOC(1,1) - iono-free with L5/E5a BPSK(10) - users with HAL=25 m. in rural environments.
- Figure F.10. - Average probability of $N_{\text{valid pos IN}} = 0$ for L1/E1 BOC(1,1) - iono-free with L5/E5a BPSK(10) - users with HAL=50 m. in rural environments.
- Figure F.11. - Average probability of $N_{\text{valid pos IN}} = 0$ for L1 TMBOC(6,1,4/33) & E1 CBOC(6,1,1/11,+) - iono-free with L5/E5a BPSK(10) - users with HAL=25 m. in rural environments.
- Figure F.12. - Average probability of $N_{\text{valid pos IN}} = 0$ for L1 TMBOC(6,1,4/33) & E1 CBOC(6,1,1/11,+) - iono-free with L5/E5a BPSK(10) - users with HAL=50 m. in rural environments.
- Figure F.13. - Average probability of $N_{\text{valid pos IN}} = 0$ for L1 TMBOC(6,1,4/33) & E1 CBOC(6,1,1/11,-) - iono-free with L5/E5a BPSK(10) - users with HAL=25 m. in rural environments.
- Figure F.14. - Average probability of $N_{\text{valid pos IN}} = 0$ for L1 TMBOC(6,1,4/33) & E1 CBOC(6,1,1/11,-) - iono-free with L5/E5a BPSK(10) - users with HAL=50 m. in rural environments.

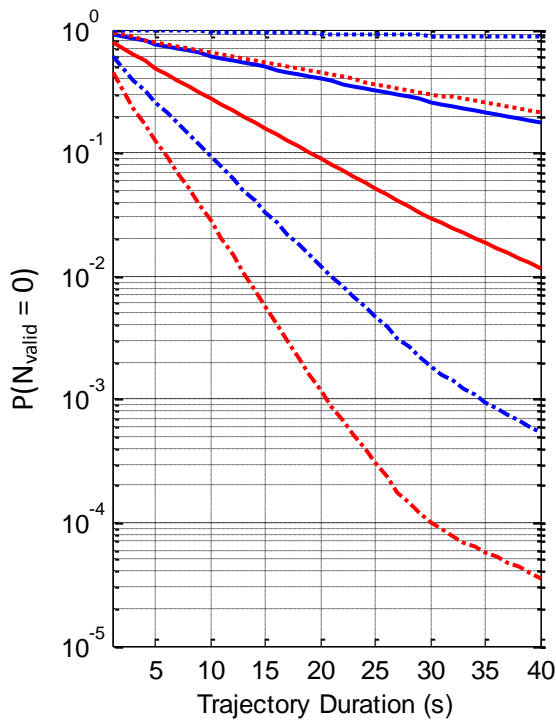
- Figure F.15. - Average probability of $N_{\text{valid pos IN}} = 0$ for L5/E5a BPSK(10) users with HAL=25 m. in rural environments.
- Figure F.16. - Average probability of $N_{\text{valid pos IN}} = 0$ for L5/E5a BPSK(10) users with HAL=50 m. in rural environments.



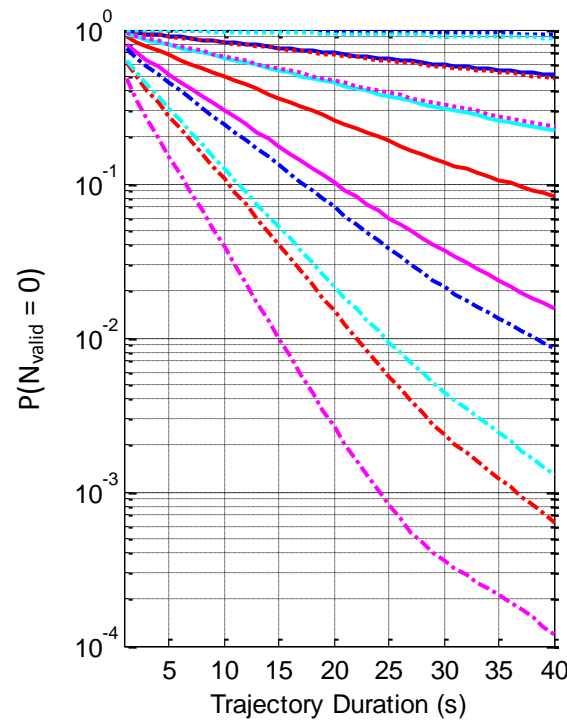
a) 2D position (known inter-GNSS delay)



b) 3D position (known inter-GNSS delay)



c) 2D position (unknown inter-GNSS delay)



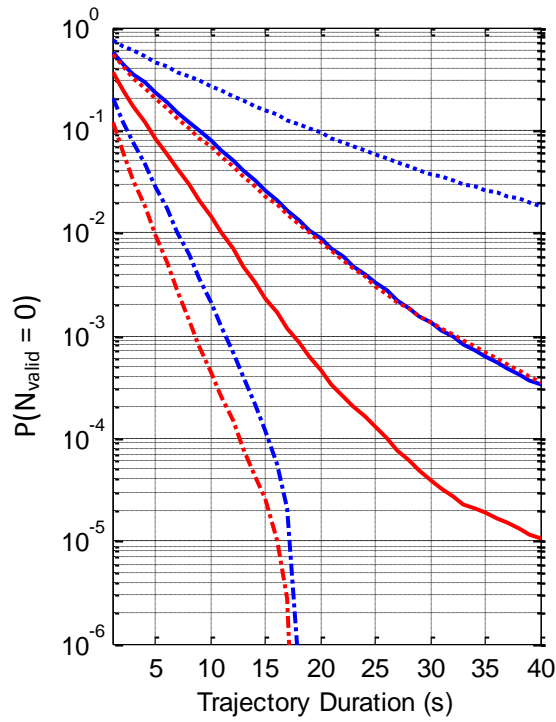
d) 3D position (unknown inter-GNSS delay)

— constant- P_{FA} WLSR RAIM ($P_{FA} = 5 \cdot 10^{-3}$)
 — constant- P_{FA} WLSR RAIM + external altitude $\sigma_{alt} = 5$ m.
 — variable- P_{FA} WLSR RAIM
 — variable- P_{FA} WLSR RAIM + external altitude $\sigma_{alt} = 5$ m.

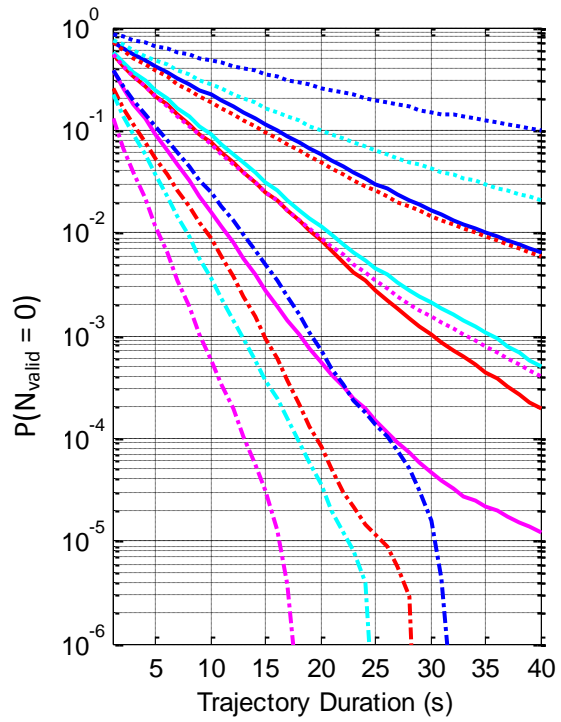
Dotted line: L1/E1
 Dashed line: L1/E1 + SBAS corrections
 Solid line: iono-free L1/E1 - L5/E5a

Figure F.1

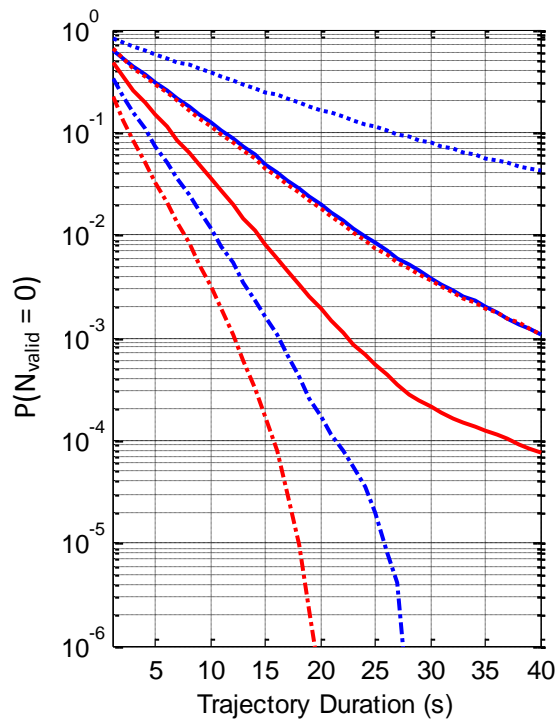
- Measurements: nominal (fault-free) - Signals: • L1/E1 BOC(1,1)
 - $P_{MD} = 5 \cdot 10^{-5}$ - Environment: urban • iono-free with L5/E5a BPSK(10)
 - HAL = 25 m. - Constellation: GPS & Galileo



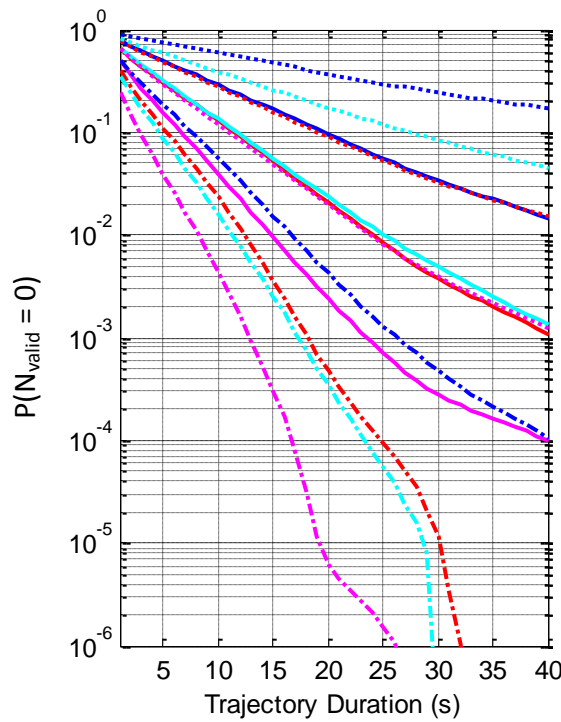
a) 2D position (known inter-GNSS delay)



b) 3D position (known inter-GNSS delay)



c) 2D position (unknown inter-GNSS delay)



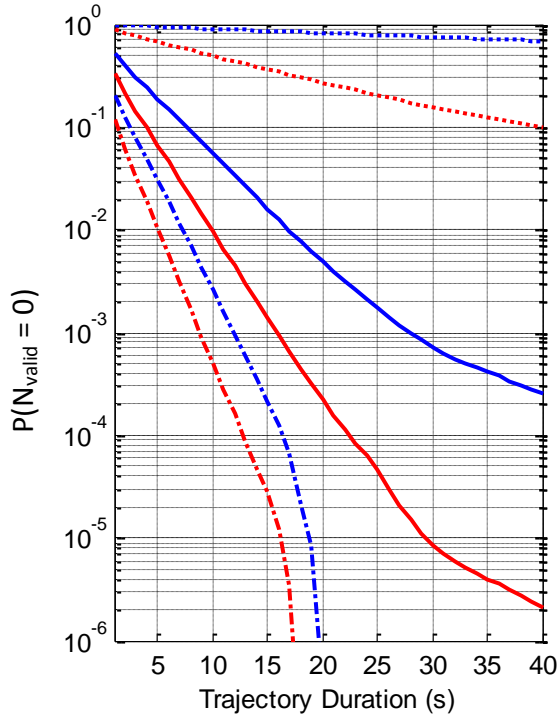
d) 3D position (unknown inter-GNSS delay)

— constant- P_{FA} WLSR RAIM ($P_{FA} = 5 \cdot 10^{-3}$)
 — constant- P_{FA} WLSR RAIM + external altitude $\sigma_{alt} = 5$ m.
 — variable- P_{FA} WLSR RAIM
 — variable- P_{FA} WLSR RAIM + external altitude $\sigma_{alt} = 5$ m.

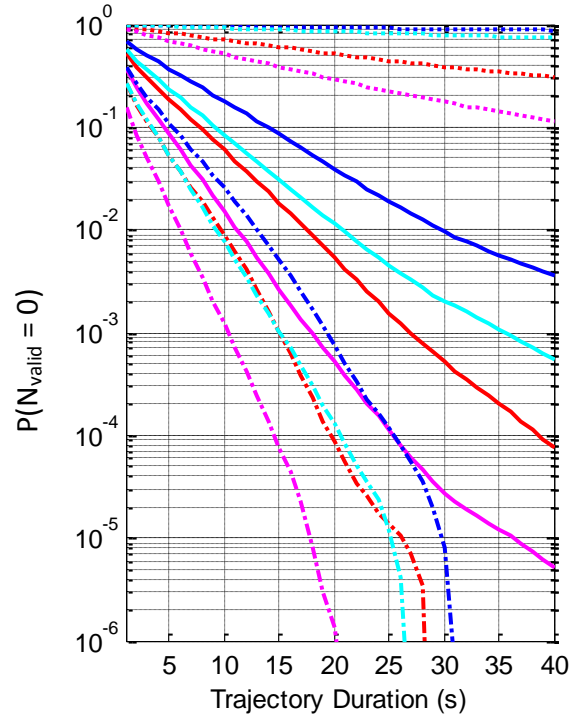
Dotted line: L1/E1
 Dashed line: L1/E1 + SBAS corrections
 Solid line: iono-free L1/E1 - L5/E5a

Figure F.2

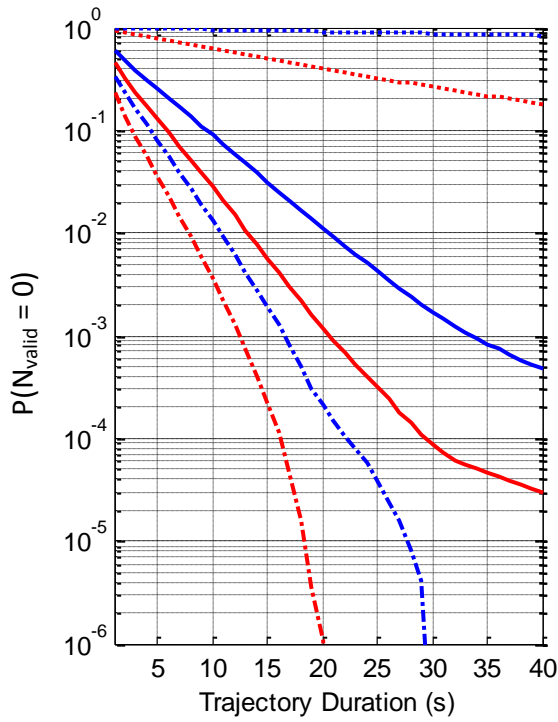
- Measurements: nominal (fault-free) - Signals: • L1/E1 BOC(1,1)
 - $P_{MD} = 5 \cdot 10^{-5}$ - Environment: urban • iono-free with L5/E5a BPSK(10)
 - HAL = 50 m. - Constellation: GPS & Galileo



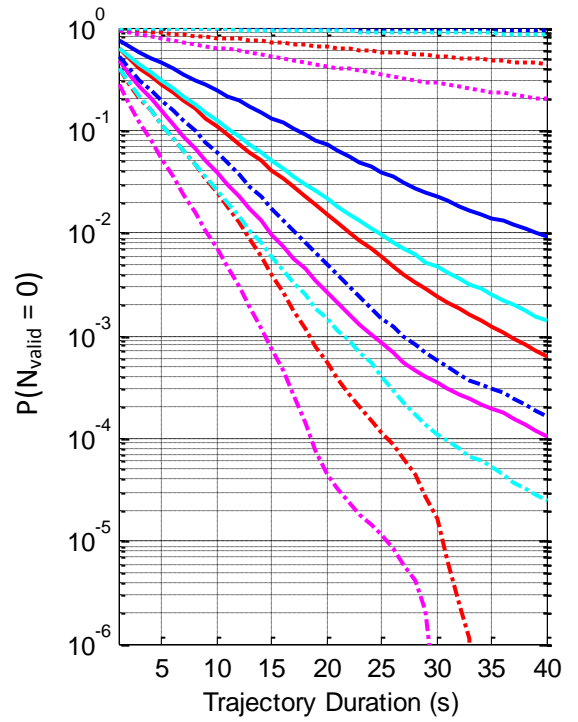
a) 2D position (known inter-GNSS delay)



b) 3D position (known inter-GNSS delay)



c) 2D position (unknown inter-GNSS delay)

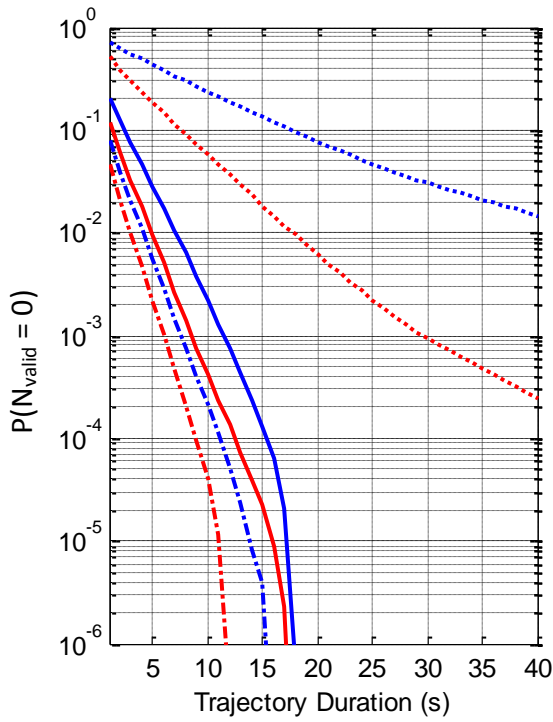


d) 3D position (unknown inter-GNSS delay)

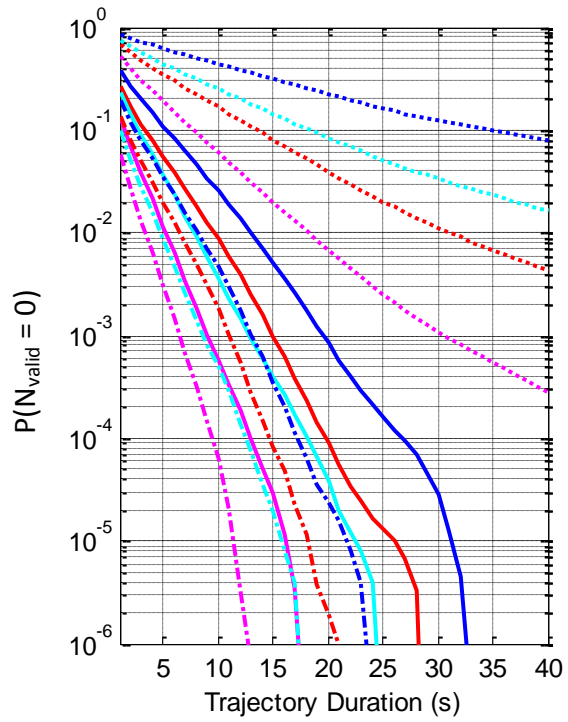
— constant- P_{FA} WLSR RAIM ($P_{FA} = 5 \cdot 10^{-3}$)	Dotted line: L1/E1
— constant- P_{FA} WLSR RAIM + external altitude $\sigma_{alt} = 5$ m.	Dashed line: L1/E1 + SBAS corrections
— variable- P_{FA} WLSR RAIM	Solid line: iono-free L1/E1 - L5/E5a
— variable- P_{FA} WLSR RAIM + external altitude $\sigma_{alt} = 5$ m.	

Figure F.3

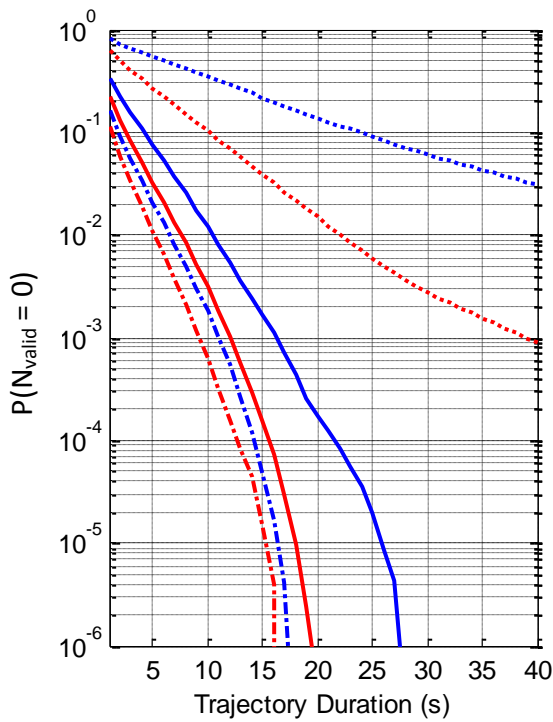
- $P_{MD} = 5 \cdot 10^{-5}$
- HAL = 25 m.
- Measurements: nominal (fault-free)
- Environment: urban
- Constellation: GPS & Galileo
- Signals: • L1 TMBOC(6,1,4/33)
- E1 CBOC(6,1,1/11,+)
- iono-free with L5/E5a BPSK(10)



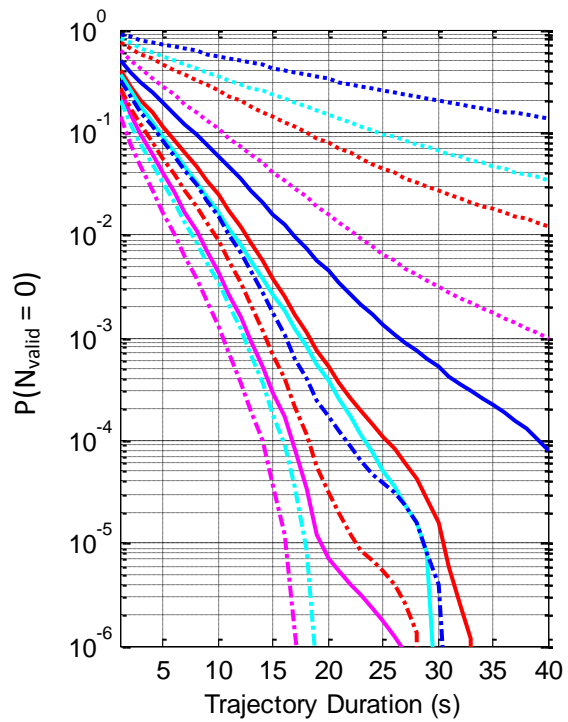
a) 2D position (known inter-GNSS delay)



b) 3D position (known inter-GNSS delay)



c) 2D position (unknown inter-GNSS delay)



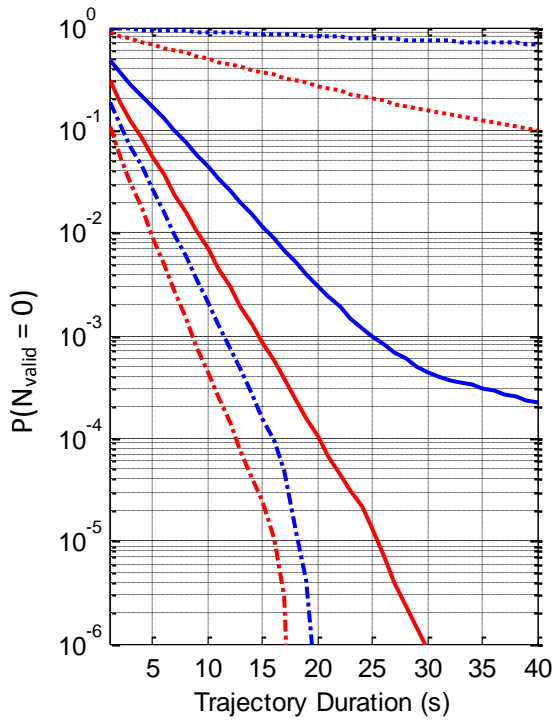
d) 3D position (unknown inter-GNSS delay)

— constant- P_{FA} WLSR RAIM ($P_{FA} = 5 \cdot 10^{-3}$)
 — constant- P_{FA} WLSR RAIM + external altitude $\sigma_{alt} = 5$ m.
 — variable- P_{FA} WLSR RAIM
 — variable- P_{FA} WLSR RAIM + external altitude $\sigma_{alt} = 5$ m.

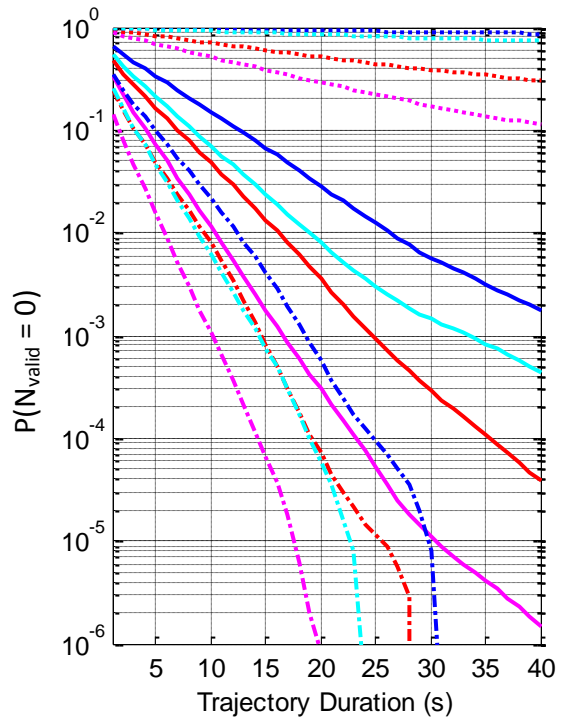
Dotted line: L1/E1
 Dashed line: L1/E1 + SBAS corrections
 Solid line: iono-free L1/E1 - L5/E5a

Figure F.4

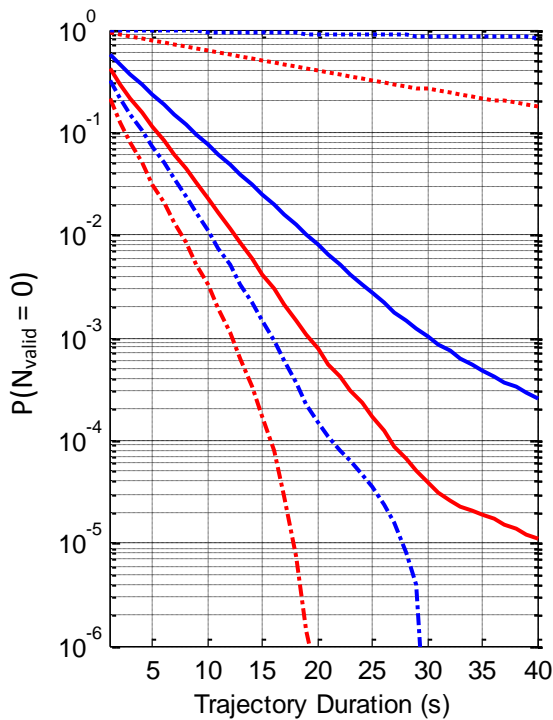
- Measurements: nominal (fault-free) - Signals: • L1 TMBOC(6,1,4/33)
 - $P_{MD} = 5 \cdot 10^{-5}$ - Environment: urban • E1 CBOC(6,1,1/11,+)
 - HAL = 50 m. - Constellation: GPS & Galileo • iono-free with L5/E5a BPSK(10)



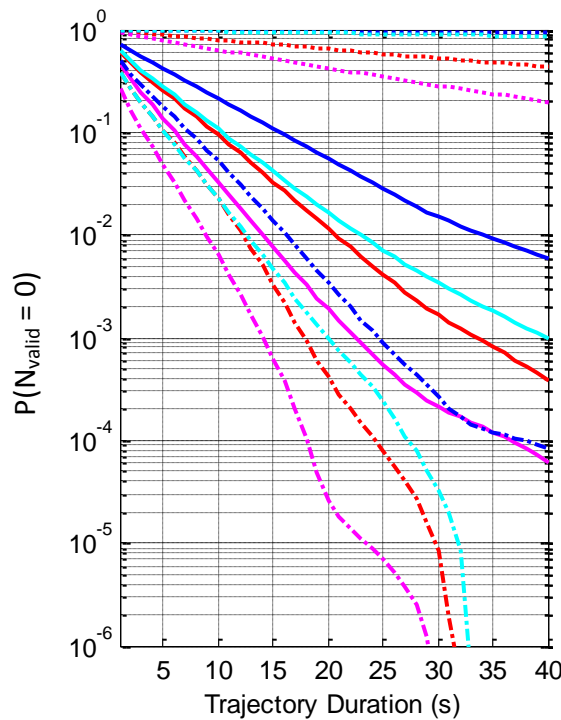
a) 2D position (known inter-GNSS delay)



b) 3D position (known inter-GNSS delay)



c) 2D position (unknown inter-GNSS delay)



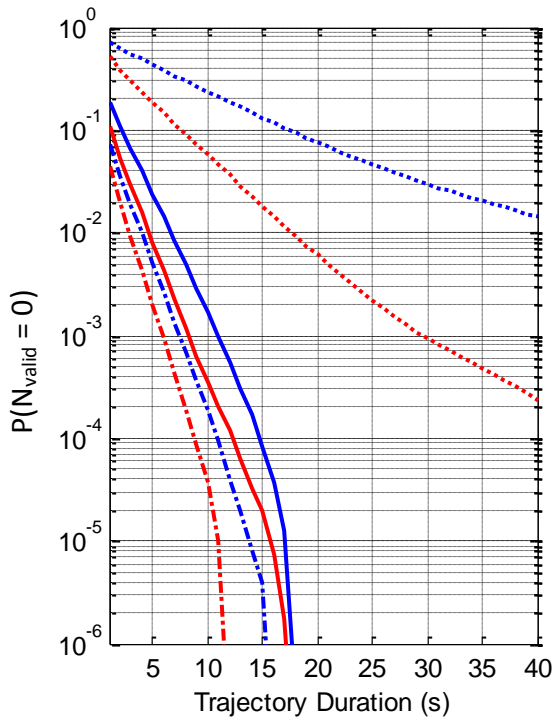
d) 3D position (unknown inter-GNSS delay)

— constant- P_{FA} WLSR RAIM ($P_{FA} = 5 \cdot 10^{-3}$)
 — constant- P_{FA} WLSR RAIM + external altitude $\sigma_{alt} = 5$ m.
 — variable- P_{FA} WLSR RAIM
 — variable- P_{FA} WLSR RAIM + external altitude $\sigma_{alt} = 5$ m.

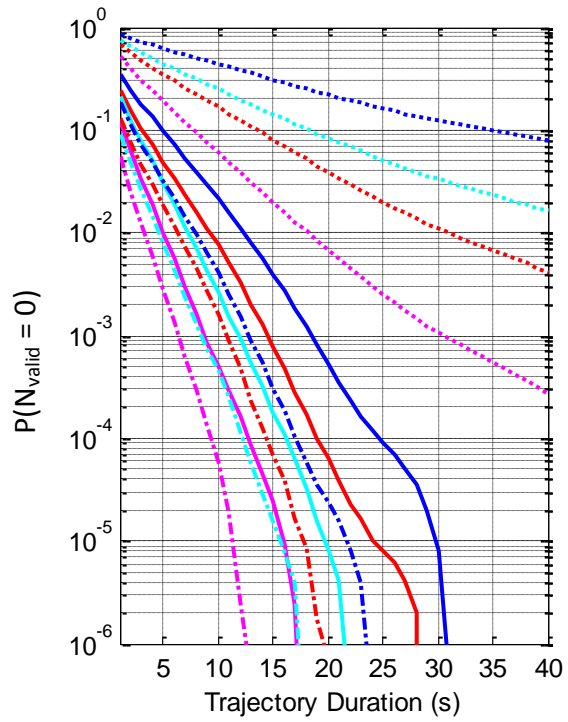
Dotted line: L1/E1
 Dashed line: L1/E1 + SBAS corrections
 Solid line: iono-free L1/E1 - L5/E5a

Figure F.5

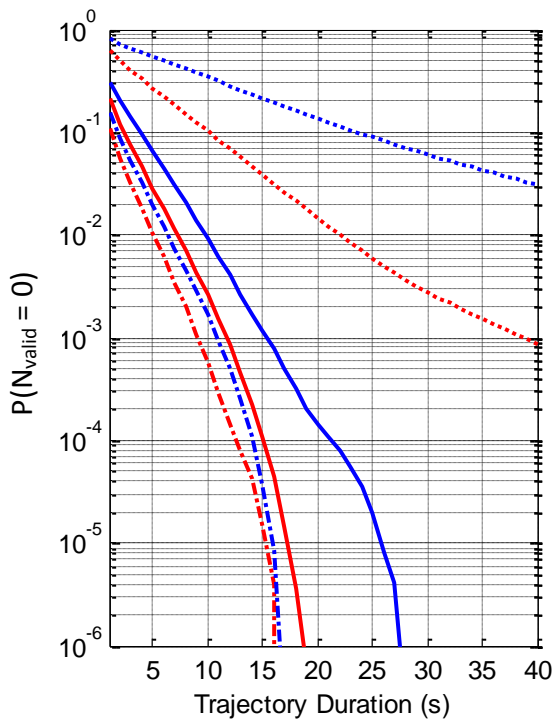
- Measurements: nominal (fault-free)
- $P_{MD} = 5 \cdot 10^{-5}$
- Environment: urban
- HAL = 25 m.
- Constellation: GPS & Galileo
- Signals: • L1 TMBOC(6,1,4/33)
- E1 CBOC(6,1,1/11,-)
- iono-free with L5/E5a BPSK(10)



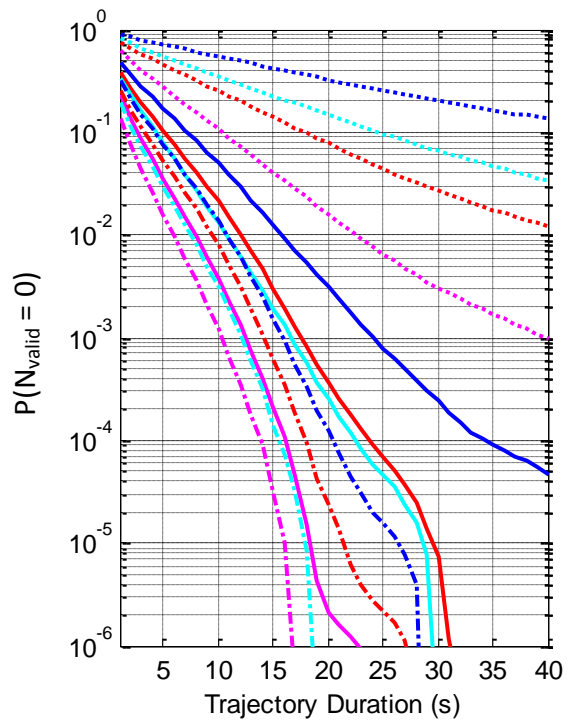
a) 2D position (known inter-GNSS delay)



b) 3D position (known inter-GNSS delay)



c) 2D position (unknown inter-GNSS delay)



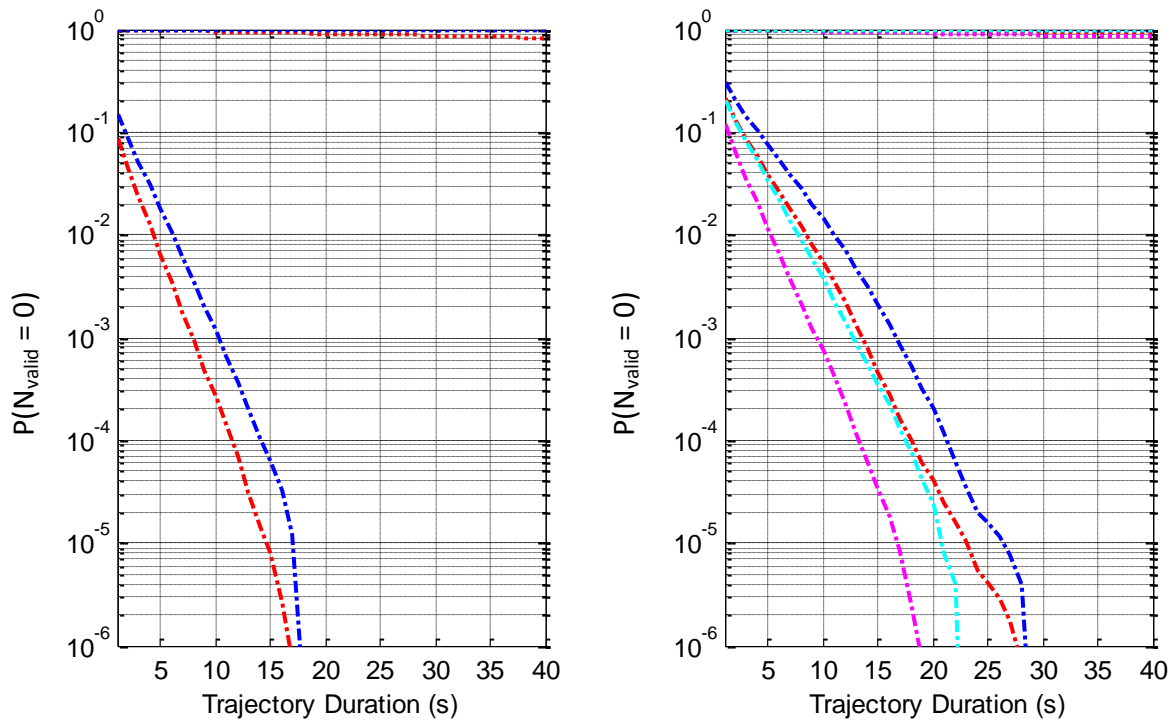
d) 3D position (unknown inter-GNSS delay)

— constant- P_{FA} WLSR RAIM ($P_{FA} = 5 \cdot 10^{-3}$)
 — constant- P_{FA} WLSR RAIM + external altitude $\sigma_{alt} = 5$ m.
 — variable- P_{FA} WLSR RAIM
 — variable- P_{FA} WLSR RAIM + external altitude $\sigma_{alt} = 5$ m.

Dotted line: L1/E1
 Dashed line: L1/E1 + SBAS corrections
 Solid line: iono-free L1/E1 - L5/E5a

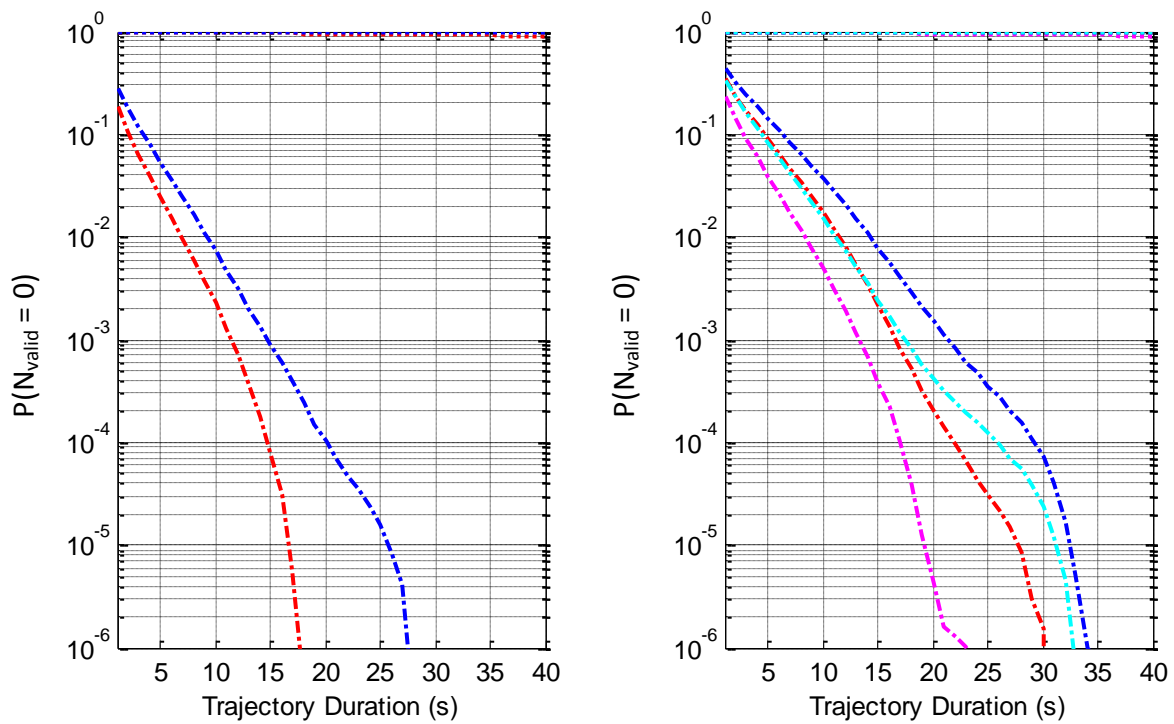
Figure F.6

- Measurements: nominal (fault-free) - Signals: • L1 TMBOC(6,1,4/33)
 - $P_{MD} = 5 \cdot 10^{-5}$ - Environment: urban • E1 CBOC(6,1,1/11,-)
 - HAL = 50 m. - Constellation: GPS & Galileo • iono-free with L5/E5a BPSK(10)



a) 2D position (known inter-GNSS delay)

b) 3D position (known inter-GNSS delay)



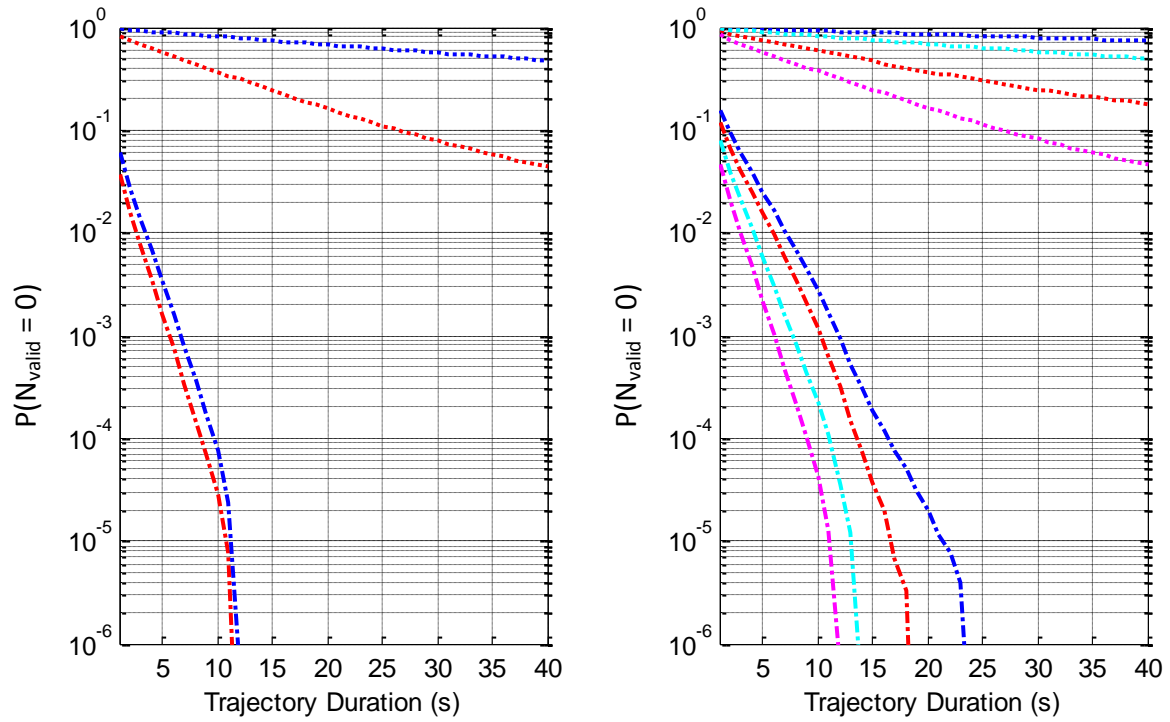
c) 2D position (unknown inter-GNSS delay)

d) 3D position (unknown inter-GNSS delay)

— constant- P_{FA} WLSR RAIM ($P_{FA} = 5 \cdot 10^{-3}$)	Dotted line: L1/E1
— constant- P_{FA} WLSR RAIM + external altitude $\sigma_{alt} = 5$ m.	Dashed line: L1/E1 + SBAS corrections
— variable- P_{FA} WLSR RAIM	
— variable- P_{FA} WLSR RAIM + external altitude $\sigma_{alt} = 5$ m.	

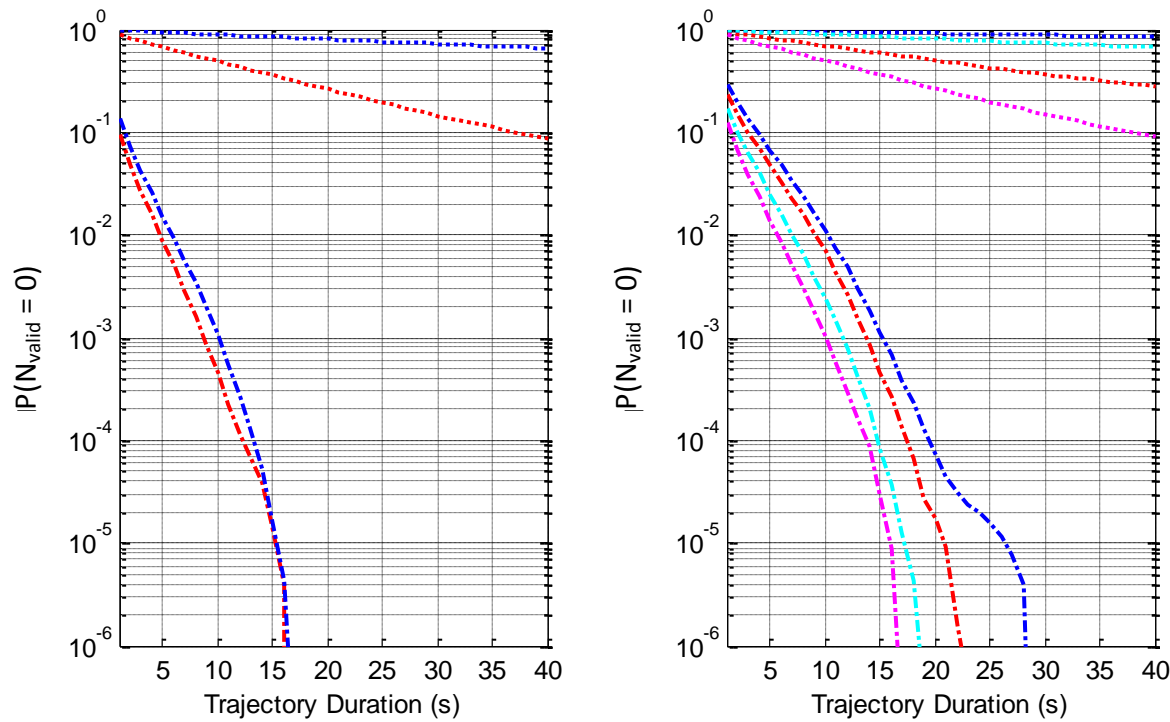
Figure F.7

- Measurements: nominal (fault-free)
- Signals: • L5/E5a BPSK(10)
- $P_{MD} = 5 \cdot 10^{-5}$
- Environment: urban
- HAL = 25 m.
- Constellation: GPS & Galileo



a) 2D position (known inter-GNSS delay)

b) 3D position (known inter-GNSS delay)



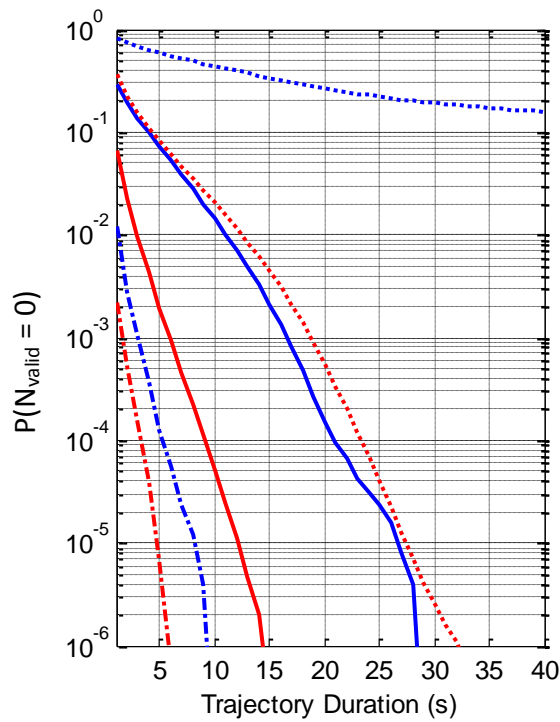
c) 2D position (unknown inter-GNSS delay)

d) 3D position (unknown inter-GNSS delay)

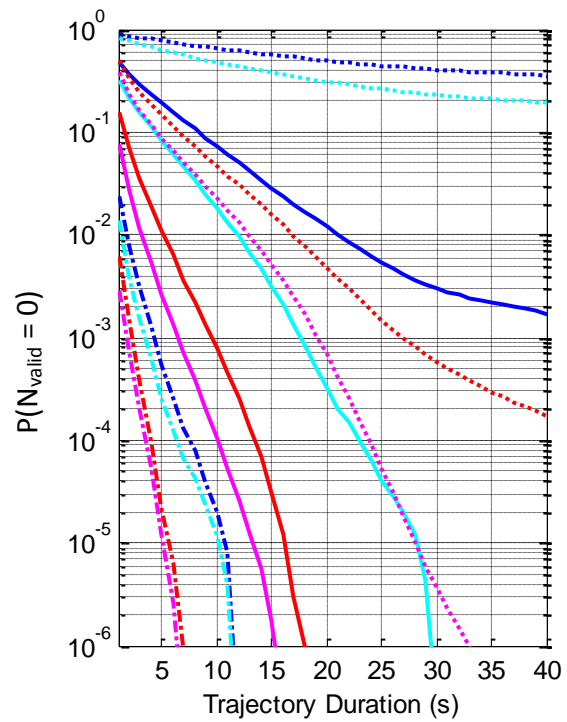
— constant- P_{FA} WLSR RAIM ($P_{FA} = 5 \cdot 10^{-3}$)	Dotted line: L1/E1
— constant- P_{FA} WLSR RAIM + external altitude $\sigma_{alt} = 5$ m.	Dashed line: L1/E1 + SBAS corrections
— variable- P_{FA} WLSR RAIM	
— variable- P_{FA} WLSR RAIM + external altitude $\sigma_{alt} = 5$ m.	

Figure F.8

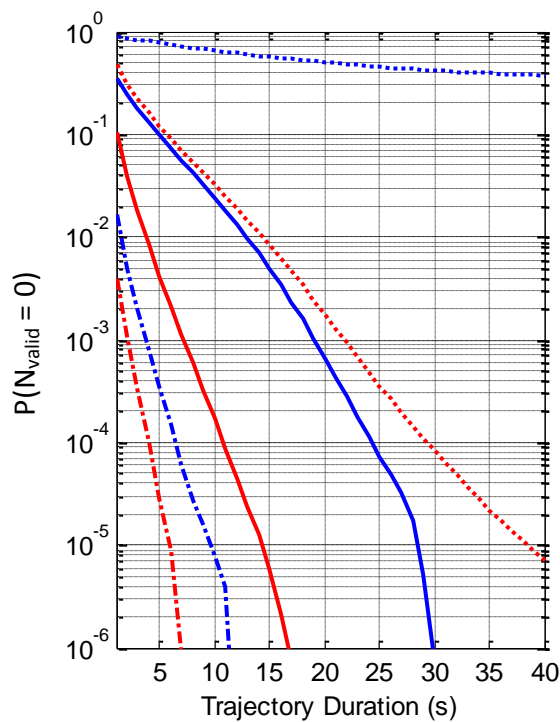
- Measurements: nominal (fault-free)
- Signals: • L5/E5a BPSK(10)
- $P_{MD} = 5 \cdot 10^{-5}$
- Environment: urban
- HAL = 50 m.
- Constellation: GPS & Galileo



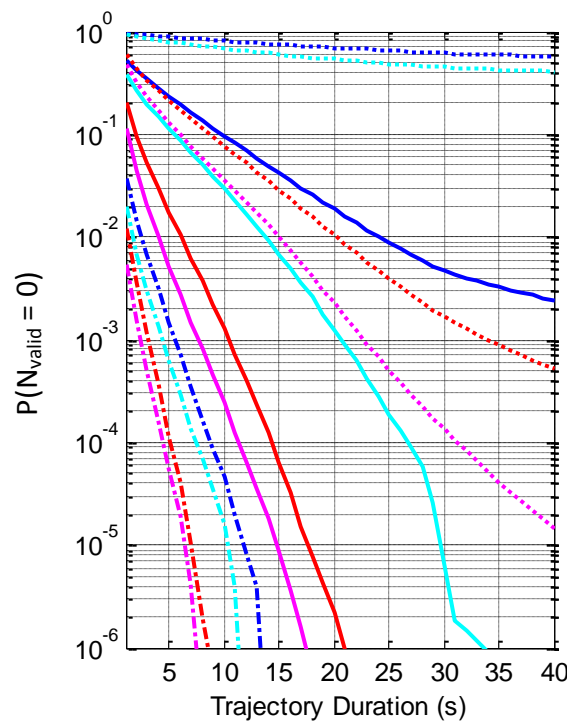
a) 2D position (known inter-GNSS delay)



b) 3D position (known inter-GNSS delay)



c) 2D position (unknown inter-GNSS delay)



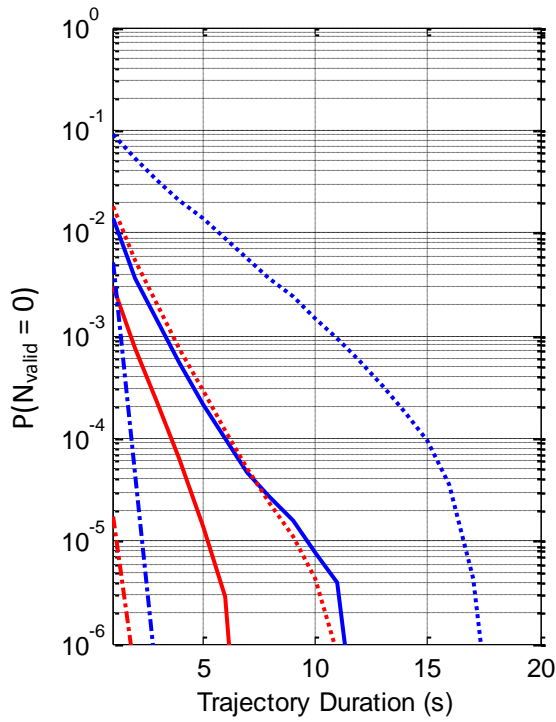
d) 3D position (unknown inter-GNSS delay)

— constant- P_{FA} WLSR RAIM ($P_{FA} = 5 \cdot 10^{-3}$)
 - - constant- P_{FA} WLSR RAIM + external altitude $\sigma_{alt} = 5$ m.
 — variable- P_{FA} WLSR RAIM
 - - variable- P_{FA} WLSR RAIM + external altitude $\sigma_{alt} = 5$ m.

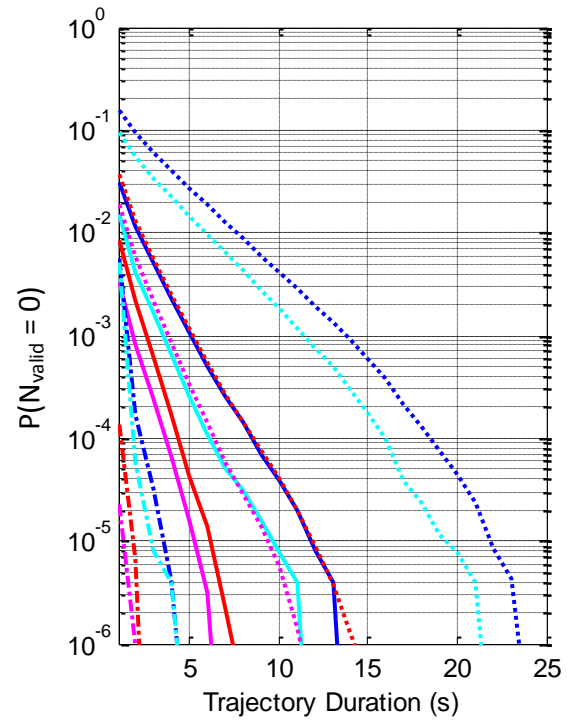
Dotted line: L1/E1
 Dashed line: L1/E1 + SBAS corrections
 Solid line: iono-free L1/E1 - L5/E5a

Figure F.9

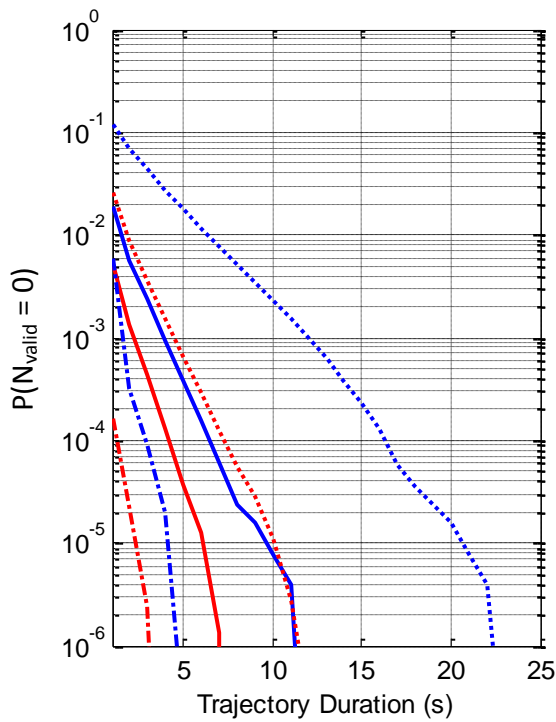
- $P_{MD} = 5 \cdot 10^{-5}$
- HAL = 25 m.
- Measurements: nominal (fault-free)
- Environment: rural
- Constellation: GPS & Galileo
- Signals: • L1/E1 BOC(1,1)
- iono-free with L5/E5a BPSK(10)



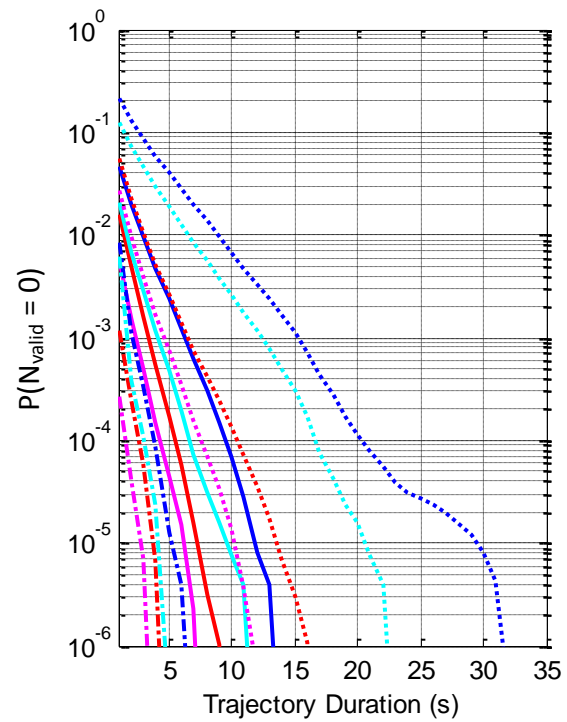
a) 2D position (known inter-GNSS delay)



b) 3D position (known inter-GNSS delay)



c) 2D position (unknown inter-GNSS delay)



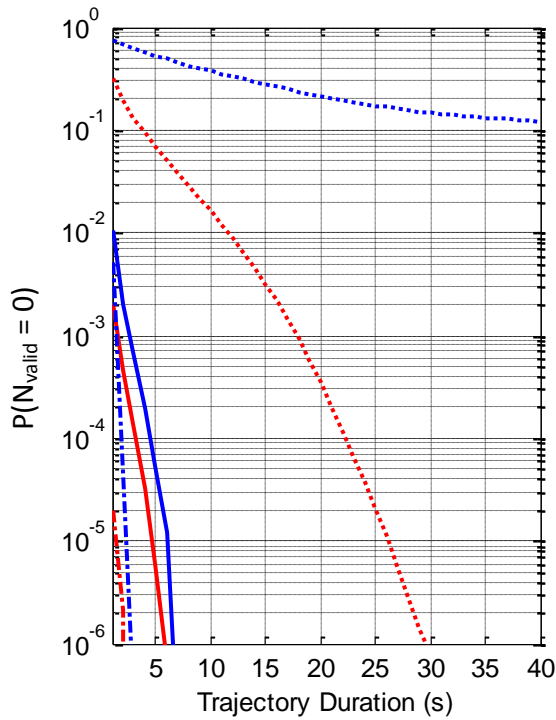
d) 3D position (unknown inter-GNSS delay)

— constant- P_{FA} WLSR RAIM ($P_{FA} = 5 \cdot 10^{-3}$)
 — constant- P_{FA} WLSR RAIM + external altitude $\sigma_{alt} = 5$ m.
 — variable- P_{FA} WLSR RAIM
 — variable- P_{FA} WLSR RAIM + external altitude $\sigma_{alt} = 5$ m.

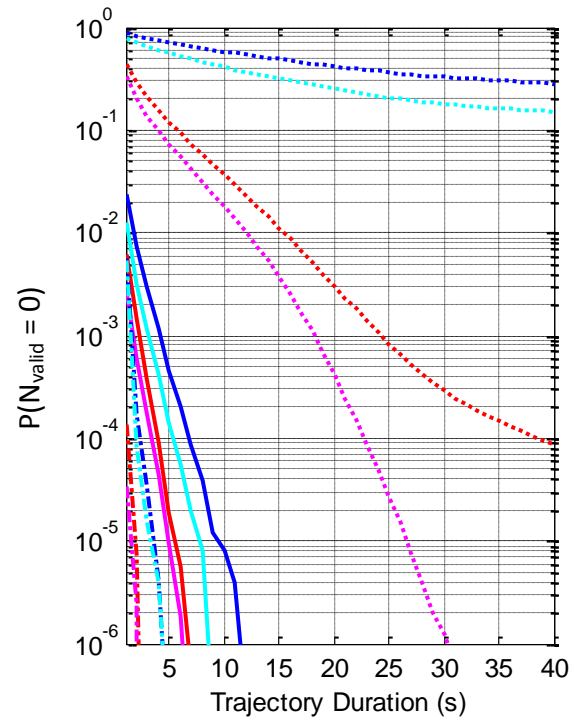
Dotted line: L1/E1
 Dashed line: L1/E1 + SBAS corrections
 Solid line: iono-free L1/E1 - L5/E5a

Figure F.10

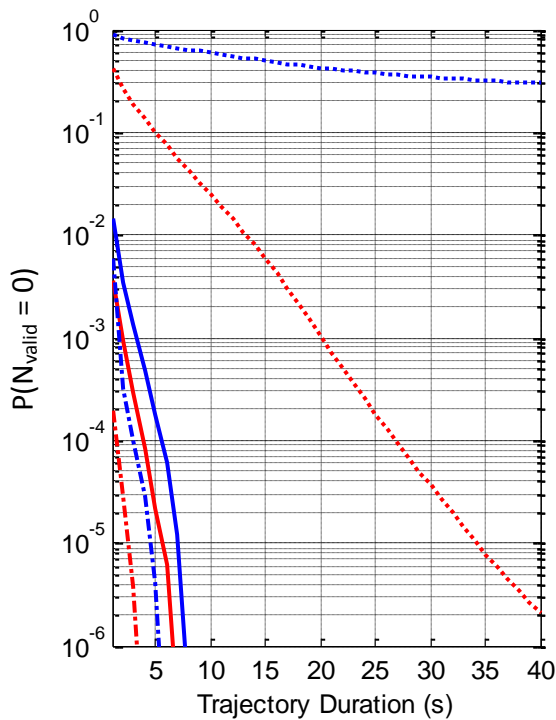
- Measurements: nominal (fault-free)
- Signals: • L1/E1 BOC(1,1)
- $P_{MD} = 5 \cdot 10^{-5}$
- Environment: rural
- HAL = 50 m.
- Constellation: GPS & Galileo
- • iono-free with L5/E5a BPSK(10)



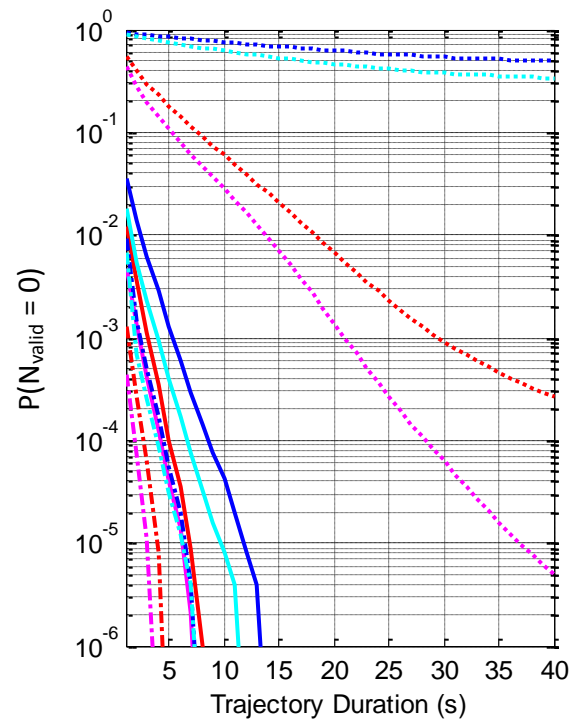
a) 2D position (known inter-GNSS delay)



b) 3D position (known inter-GNSS delay)



c) 2D position (unknown inter-GNSS delay)



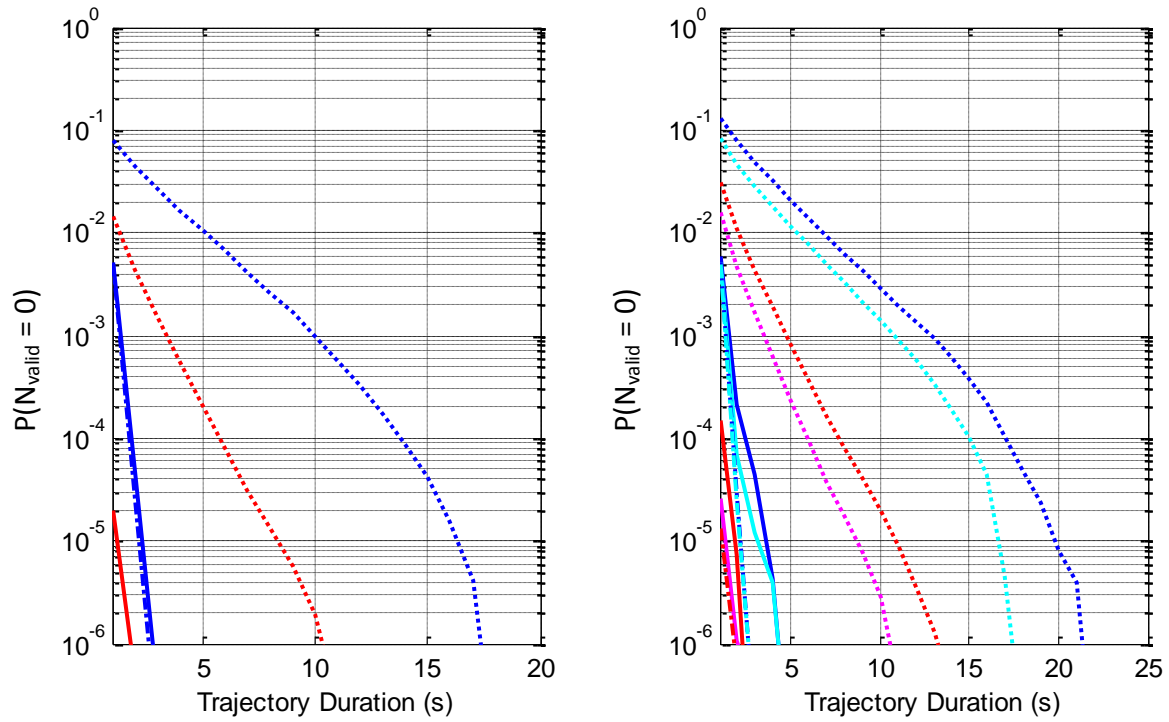
d) 3D position (unknown inter-GNSS delay)

— constant- P_{FA} WLSR RAIM ($P_{FA} = 5 \cdot 10^{-3}$)
 - - constant- P_{FA} WLSR RAIM + external altitude $\sigma_{alt} = 5$ m.
 — variable- P_{FA} WLSR RAIM
 - - variable- P_{FA} WLSR RAIM + external altitude $\sigma_{alt} = 5$ m.

Dotted line: L1/E1
 Dashed line: L1/E1 + SBAS corrections
 Solid line: iono-free L1/E1 - L5/E5a

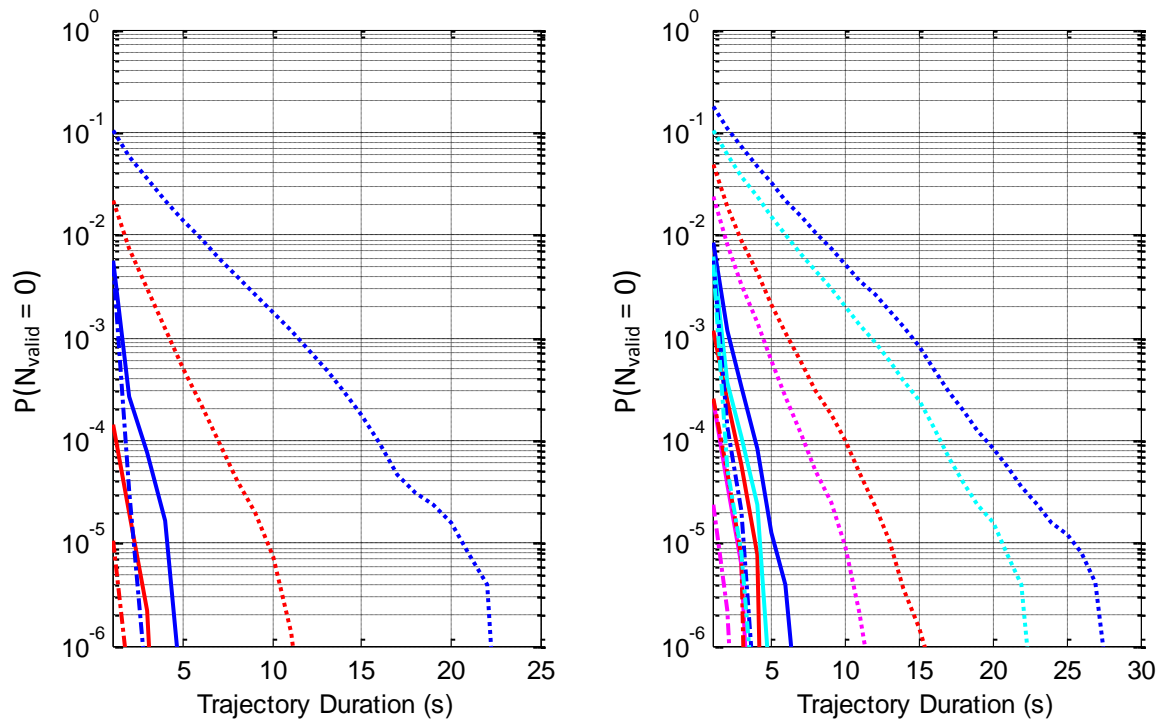
Figure F.11

- Measurements: nominal (fault-free) - Signals: • L1 TMBOC(6,1,4/33)
 - $P_{MD} = 5 \cdot 10^{-5}$ - Environment: rural • E1 CBOC(6,1,1/11,+)
 - HAL = 25 m. - Constellation: GPS & Galileo • iono-free with L5/E5a BPSK(10)



a) 2D position (known inter-GNSS delay)

b) 3D position (known inter-GNSS delay)



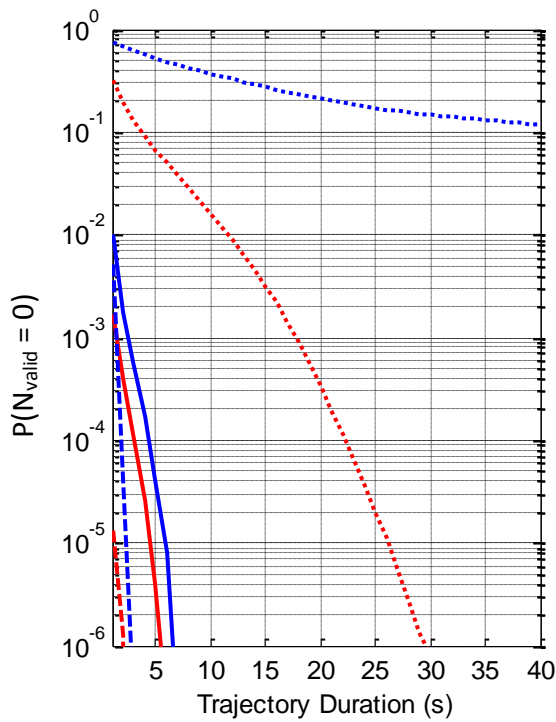
c) 2D position (unknown inter-GNSS delay)

d) 3D position (unknown inter-GNSS delay)

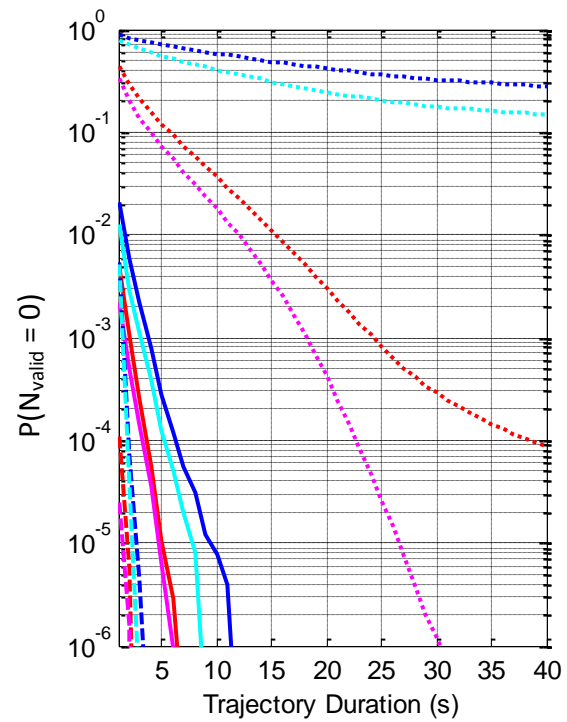
— constant- P_{FA} WLSR RAIM ($P_{FA} = 5 \cdot 10^{-3}$)	Dotted line: L1/E1
— constant- P_{FA} WLSR RAIM + external altitude $\sigma_{alt} = 5$ m.	Dashed line: L1/E1 + SBAS corrections
— variable- P_{FA} WLSR RAIM	Solid line: iono-free L1/E1 - L5/E5a
— variable- P_{FA} WLSR RAIM + external altitude $\sigma_{alt} = 5$ m.	

Figure F.12

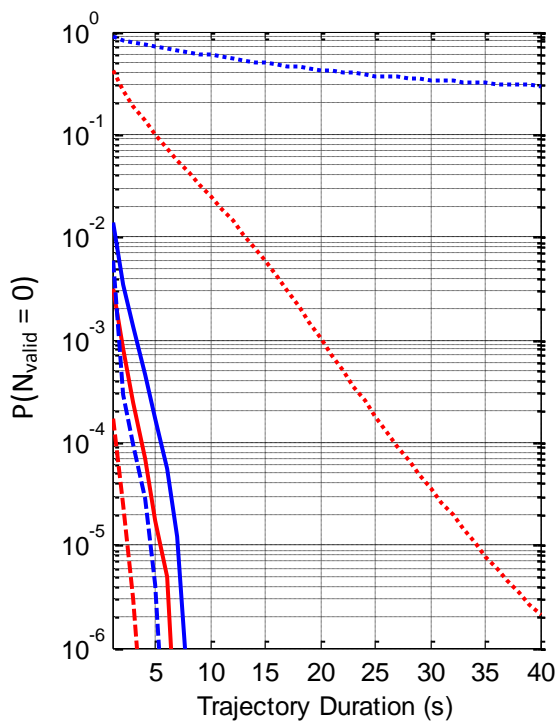
- $P_{MD} = 5 \cdot 10^{-5}$
- $HAL = 50$ m.
- Measurements: nominal (fault-free)
- Environment: rural
- Constellation: GPS & Galileo
- Signals: • L1 TMBOC(6,1,4/33)
- E1 CBOC(6,1,1/11,+)
- iono-free with L5/E5a BPSK(10)



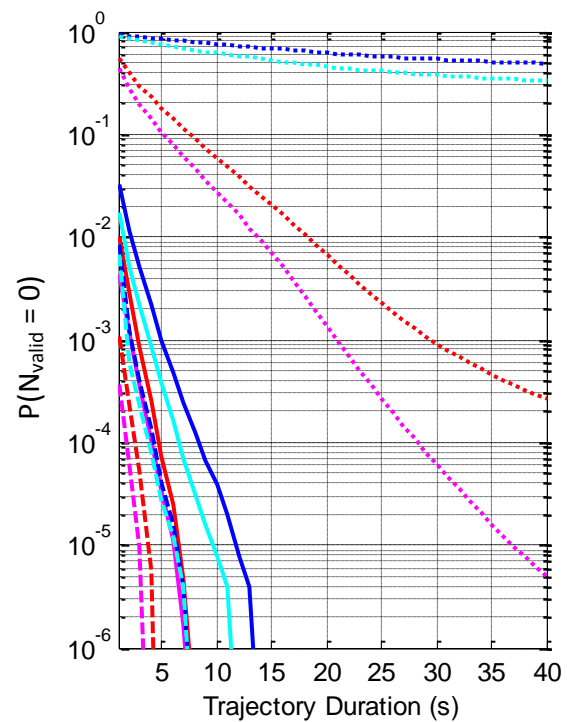
a) 2D position (known inter-GNSS delay)



b) 3D position (known inter-GNSS delay)



c) 2D position (unknown inter-GNSS delay)



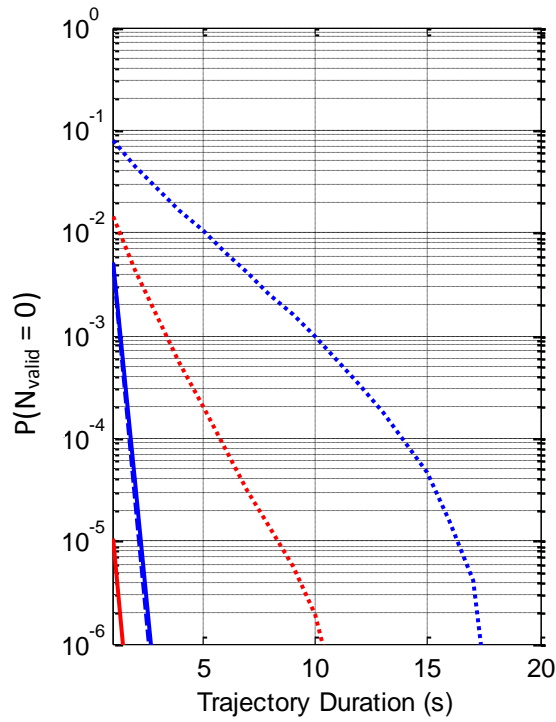
d) 3D position (unknown inter-GNSS delay)

— constant- P_{FA} WLSR RAIM ($P_{FA} = 5 \cdot 10^{-3}$)
 - - constant- P_{FA} WLSR RAIM + external altitude $\sigma_{alt} = 5$ m.
 — variable- P_{FA} WLSR RAIM
 - - variable- P_{FA} WLSR RAIM + external altitude $\sigma_{alt} = 5$ m.

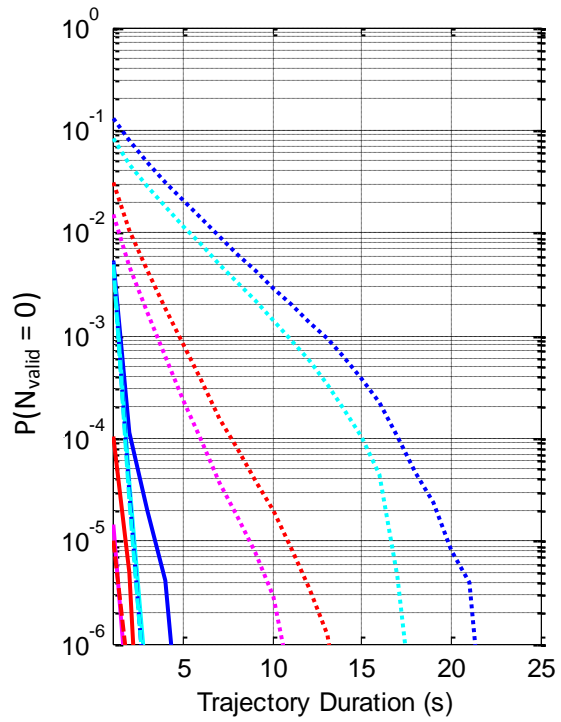
Dotted line: L1/E1
 Dashed line: L1/E1 + SBAS corrections
 Solid line: iono-free L1/E1 - L5/E5a

Figure F.13

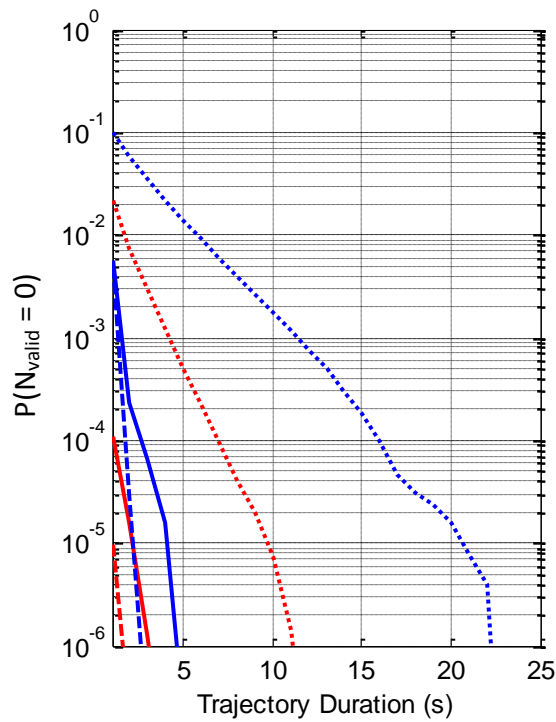
- $P_{MD} = 5 \cdot 10^{-5}$
- $HAL = 25$ m.
- Measurements: nominal (fault-free)
- Environment: rural
- Constellation: GPS & Galileo
- Signals: • L1 TMBOC(6,1,4/33)
- E1 CBOC(6,1,1/11,-)
- iono-free with L5/E5a BPSK(10)



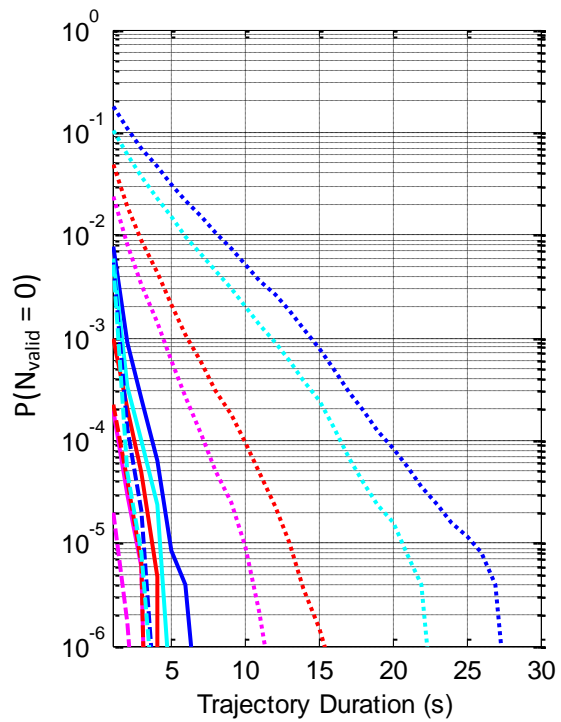
a) 2D position (known inter-GNSS delay)



b) 3D position (known inter-GNSS delay)



c) 2D position (unknown inter-GNSS delay)



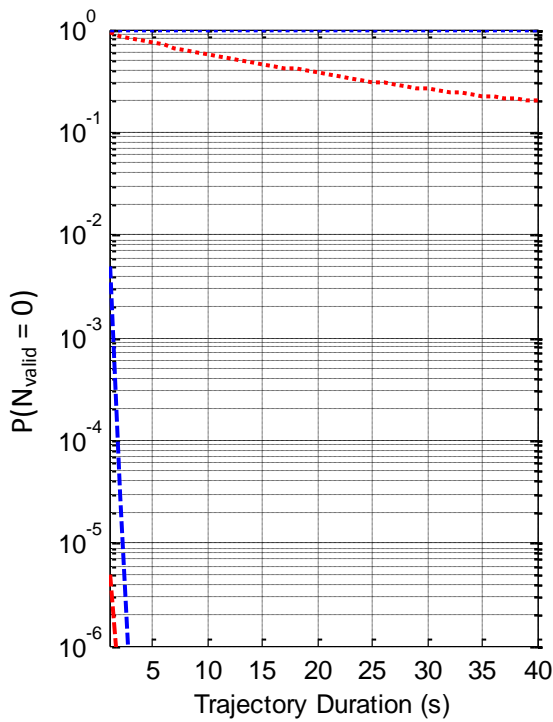
d) 3D position (unknown inter-GNSS delay)

— constant- P_{FA} WLSR RAIM ($P_{FA} = 5 \cdot 10^{-3}$)
 — constant- P_{FA} WLSR RAIM + external altitude $\sigma_{alt} = 5$ m.
 - - variable- P_{FA} WLSR RAIM
 - - variable- P_{FA} WLSR RAIM + external altitude $\sigma_{alt} = 5$ m.

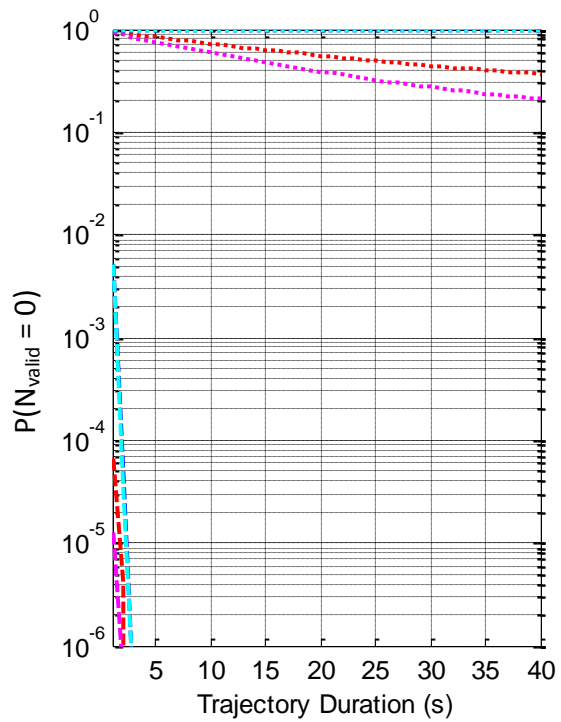
Dotted line: L1/E1
 Dashed line: L1/E1 + SBAS corrections
 Solid line: iono-free L1/E1 - L5/E5a

Figure F.14

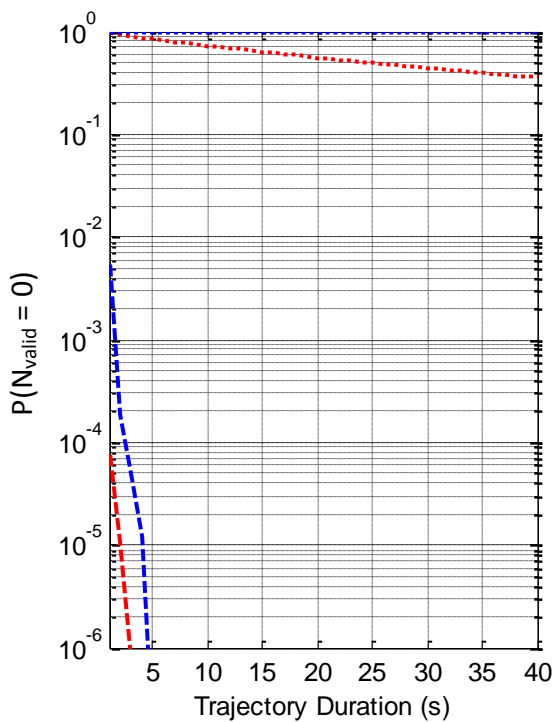
- Measurements: nominal (fault-free) - Signals: • L1 TMBOC(6,1,4/33)
 - $P_{MD} = 5 \cdot 10^{-5}$ - Environment: rural • E1 CBOC(6,1,1/11,-)
 - HAL = 50 m. - Constellation: GPS & Galileo • iono-free with L5/E5a BPSK(10)



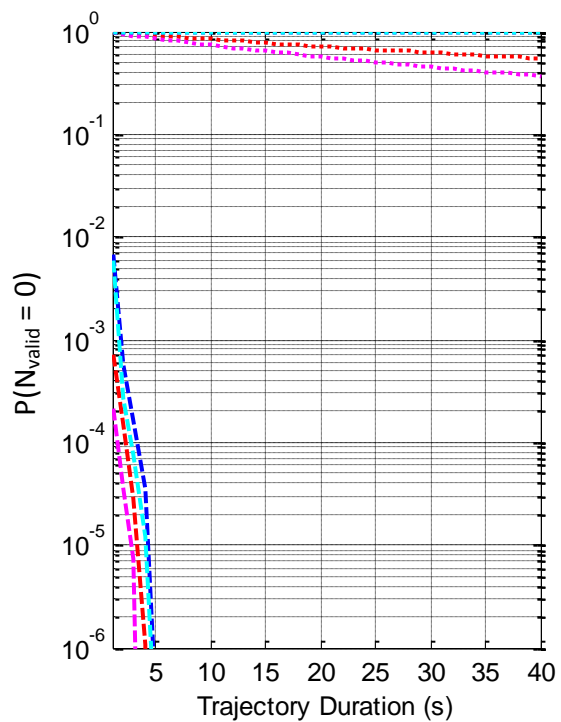
a) 2D position (known inter-GNSS delay)



b) 3D position (known inter-GNSS delay)



c) 2D position (unknown inter-GNSS delay)

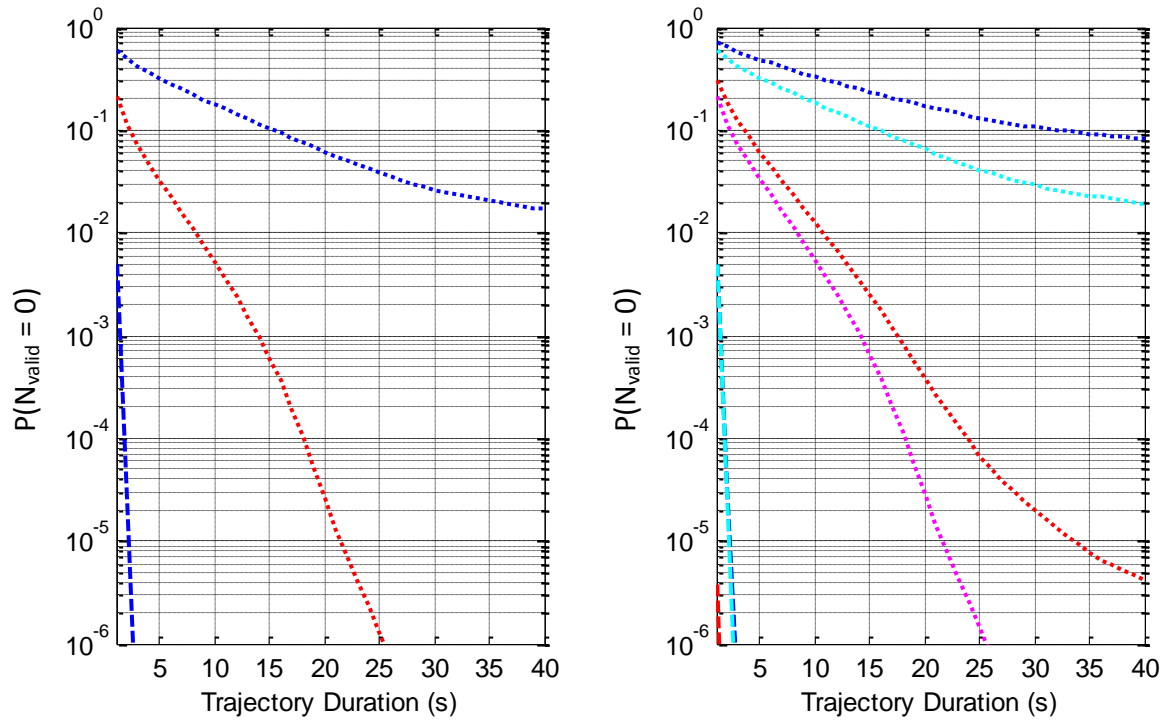


d) 3D position (unknown inter-GNSS delay)

— constant- P_{FA} WLSR RAIM ($P_{FA} = 5 \cdot 10^{-3}$)	Dotted line: L1/E1
— constant- P_{FA} WLSR RAIM + external altitude $\sigma_{alt} = 5$ m.	Dashed line: L1/E1 + SBAS corrections
— variable- P_{FA} WLSR RAIM	
— variable- P_{FA} WLSR RAIM + external altitude $\sigma_{alt} = 5$ m.	

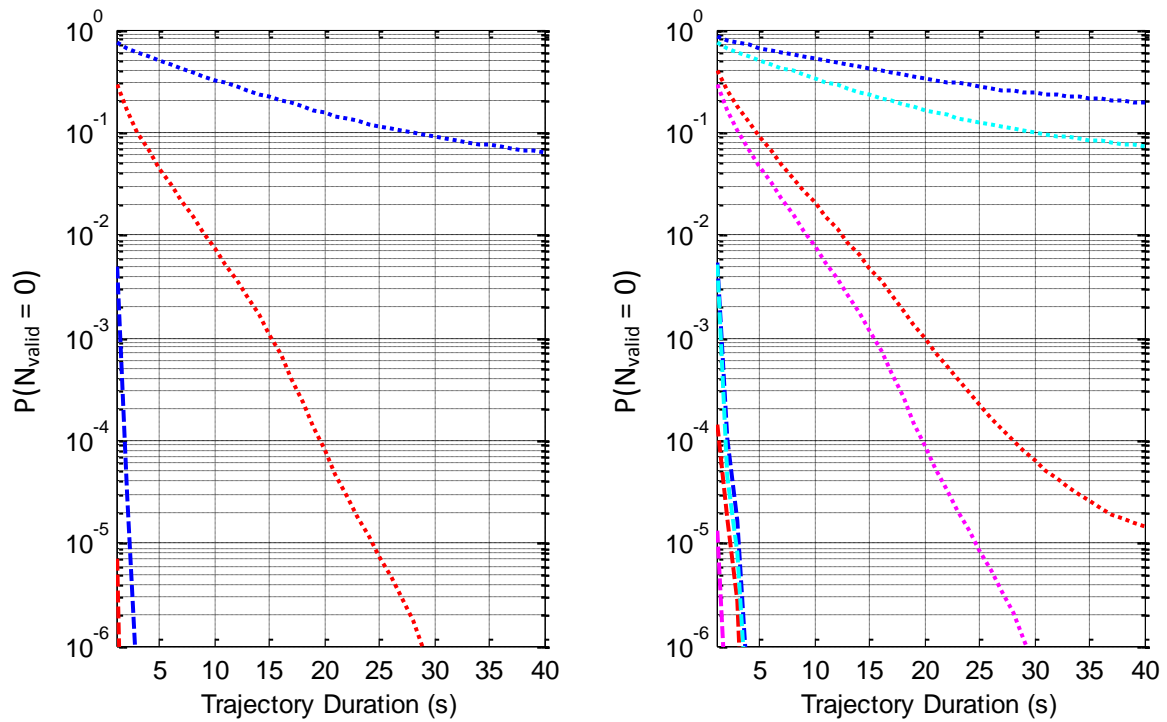
Figure F.15

- Measurements: nominal (fault-free)
- Signals: • L5/E5a BPSK(10)
- $P_{MD} = 5 \cdot 10^{-5}$
- Environment: rural
- HAL = 25 m.
- Constellation: GPS & Galileo



a) 2D position (known inter-GNSS delay)

b) 3D position (known inter-GNSS delay)



c) 2D position (unknown inter-GNSS delay)

d) 3D position (unknown inter-GNSS delay)

— constant- P_{FA} WLSR RAIM ($P_{\text{FA}} = 5 \cdot 10^{-3}$)	Dotted line: L1/E1
— constant- P_{FA} WLSR RAIM + external altitude $\sigma_{\text{alt}} = 5$ m.	Dashed line: L1/E1 + SBAS corrections
— variable- P_{FA} WLSR RAIM	
— variable- P_{FA} WLSR RAIM + external altitude $\sigma_{\text{alt}} = 5$ m.	

Figure F.16

- Measurements: nominal (fault-free)
- Signals: • L5/E5a BPSK(10)
- $P_{\text{MD}} = 5 \cdot 10^{-5}$
- Environment: rural
- HAL = 50 m.
- Constellation: GPS & Galileo